



**Scuola Internazionale Superiore di Studi Avanzati - Trieste**



**Development of small-molecule  
libraries for neurodegenerative  
protein misfolding diseases**

Candidate:

**Annachiara Gandini**

Supervisors:

**Prof. Maria Laura Bolognesi**

**Prof. Giuseppe Legname**

A thesis submitted for the degree of  
*Doctor of Philosophy* in  
Functional and Structural Genomics  
October 2018

**SISSA - Via Bonomea 265 - 34136 TRIESTE - ITALY**



**Scuola Internazionale Superiore Studi Avanzati  
(SISSA)**



**Development of small-molecule  
libraries for neurodegenerative  
protein misfolding diseases**

Candidate:

**Annachiara Gandini**

Supervisors:

**Prof. Maria Laura Bolognesi**

**Prof. Giuseppe Legname**

A thesis submitted for the degree of  
*Doctor of Philosophy*  
in Functional and Structural Genomics  
October 2018



# TABLE OF CONTENTS

**Abstract**

**List of publications**

**List of abbreviations**

## **Chapter I**

**Protein Misfolding Diseases: focus on Alzheimer's and prion diseases** 1

**1.1 Protein misfolding diseases** 2

1.1.1 Structures and properties of the amyloid fibrils 4

1.1.2 The mechanism of amyloid formation 6

1.1.3 Protein aggregates-related pathogenicity 7

1.1.4 Neurodegenerative PMDs 8

**1.2 Alzheimer's disease** 10

1.2.1 Drug development in Alzheimer's disease 10

1.2.2 AD as a multifactorial disorder 12

**1.3 Prion diseases** 18

1.3.1 Human prion diseases 19

1.3.2 PrP<sup>c</sup> and PrP<sup>Sc</sup> 20

1.3.3 Mechanisms of prion toxicity 22

**1.4 Drug discovery strategies targeting PMDs** 24

## **Chapter II**

**Objectives** 27

## **Chapter III**

<b>Tau centric multi-target approach for Alzheimer’s disease: development of first-in-class dual GSK-3<math>\beta</math> and tau-aggregation inhibitors</b>	<b>32</b>
<b>3.1 The “multi-target-directed ligand” approach in Alzheimer’s disease</b>	<b>33</b>
<b>3.2 Target selection for a MTDL drug discovery project: GSK-3<math>\beta</math> and tau protein</b>	<b>35</b>
3.2.1 GSK-3 $\beta$ : a crucial kinase for AD	35
3.2.1.1 The role of GSK-3 $\beta$ in AD	37
3.2.1.2 GSK-3 $\beta$ inhibitors	39
3.2.2 Tau protein as a promising target for AD	44
3.2.2.1 Tau protein in AD	46
3.2.2.2 Tau aggregation inhibitors	48
<b>3.3 Design of dual GSK-3<math>\beta</math> and tau aggregation inhibitors</b>	<b>53</b>
<b>3.4 Chemistry</b>	<b>58</b>
<b>3.5 Results and discussion</b>	<b>61</b>
3.5.1 GSK-3 $\beta$ inhibition assays	62
3.5.2 Retrospective docking simulations on GSK-3 $\beta$	66
3.5.3 Blood brain barrier permeation	69
3.5.4 Neuro- and hepato-toxicity assessment	71
3.5.5 AcPHF6 aggregation and inhibition studies by Thioflavin T (ThT) fluorescence, circular dichroism spectroscopy and atomic force microscopy	73
3.5.6 K18 and full-length tau aggregation	76
3.5.7 Okadaic acid-induced tau hyperphosphorylation cell model	78
3.5.8 Inhibitory activity profile towards casein kinase 1 (CK1) $\delta$ and $\epsilon$ , and cell division cycle 7 (Cdc7)	79

<b>Chapter IV</b>	
<b>Fluorescent bivalent ligands with potential combined therapeutic and diagnostic activities against Alzheimer's disease</b>	<b>82</b>
<b>4.1 Diagnostics in Alzheimer's disease</b>	<b>83</b>
<b>4.1.1 Imaging of amyloid plaques and NFTs by fluorescent tracers</b>	<b>85</b>
4.1.1.1 Small molecules fluorescent probes for in vivo A $\beta$ plaques imaging	86
4.1.1.2 Small molecules fluorescent probes for in vivo NFTs imaging	89
<b>4.2 The theranostic approach in Alzheimer's disease</b>	<b>92</b>
4.2.1 Theranostic small molecules in AD	94
<b>4.3 Design of fluorescent bivalent ligands</b>	<b>98</b>
<b>4.4 Chemistry</b>	<b>102</b>
<b>4.5 Native fluorescence studies</b>	<b>105</b>
<b>4.6 Results and discussion</b>	<b>109</b>
4.6.1 Inhibition of A $\beta$ <sub>42</sub> and tau aggregation in intact <i>E. coli</i> cells	111
<b>Chapter V</b>	
<b>Development of a focused library of antiprion compounds built around Compound 1</b>	<b>114</b>
<b>5.1 Therapy in prion diseases</b>	<b>115</b>
5.1.1 Clinical drug candidates	115
5.1.2 Preclinical drug candidates	118
<b>5.2 Design of a small library of antiprion compounds</b>	<b>123</b>

<b>5.3 Chemistry</b>	125
<b>Chapter VI</b>	
<b>Conclusions</b>	129
<b>Chapter VII</b>	
<b>Experimental section</b>	133
<b>7.1 Tau centric multi-target approach for Alzheimer's disease: development of first-in-class dual GSK-3<math>\beta</math> and tau-aggregation inhibitors</b>	134
7.1.1 Chemistry	134
7.1.2 K18 aggregation and inhibition studies	145
7.1.3 Full-length 2N4R tau aggregation and inhibition studies	145
<b>7.2 Fluorescent bivalent ligands with combined therapeutic and diagnostic activities against Alzheimer's disease</b>	147
7.2.1 Chemistry	147
7.2.2 Native fluorescence studies	155
<b>7.3 Development of a focused library of antiprion compounds built around Compound 1</b>	156
7.3.1 Chemistry	156
<b>Appendix I</b>	163
<b>Bibliography</b>	174





## **Abstract**

Protein misfolding diseases (PMDs) are chronic and progressively degenerative disorders, characterized by the accumulation of insoluble aggregates of misfolded proteins. Particularly, amyloid- $\beta$  and tau protein in Alzheimer's disease, prion protein in prion diseases, and  $\alpha$ -synuclein in Parkinson disease are prototypical misfolded proteins that aggregate and accumulate in the brain, being responsible for the respective neurodegenerative disease. In the last decades, neurodegenerative PMDs have drawn public and scientific attention due to an increasing number of cases, becoming a critical issue in terms of healthcare and social costs. Moreover, while the list of neurodegenerative PMDs is long and growing, the pipeline of disease-modifying drugs is dry. In light of this clear unmet medical need, the present PhD thesis has been devoted to the development of three small-molecule libraries for neurodegenerative PMDs, through different and innovative strategies. First, we applied the multi-target directed ligand approach and we developed the first class of multi-target compounds able to hit the tau cascade at two different hubs. The synthesized 2,4-thiazolidinedione derivatives were able to concomitantly inhibit the phosphorylating tau kinase GSK-3 $\beta$ , as well as the tau aggregation process. Thus, these multi-target compounds could be promising tools for the validation of a completely new tau-centric approach as a disease-modifying strategy to treat Alzheimer's disease. Secondly, we applied the theranostic approach and we designed and synthesized a library of fluorescent bivalent derivatives. These bivalent compounds could be able, in principle, to stain A $\beta$  and tau protein aggregates and to inhibit the protein aggregation process. If we will be able to further demonstrate their theranostic profile in vitro and in vivo, these compounds could serve as innovative tools to potentially diagnose, deliver therapy, and monitor response to therapy in PMDs. Finally, we designed a focused library of compounds with the aim of optimizing the drug-like properties of a previously identified antiprion compound. Namely, we inserted on a position amenable to derivatization solubilizing groups, specifically tailored for CNS drug optimization. If our design strategy will be successful, we will have improved the pharmacokinetic properties of a promising antiprion compound, making possible its progression to further in vivo studies.

## **List of publications**

All the work reported herein arises from my own experiments or as a result of joint collaborations with other groups. Some data are published in the following articles:

- **Gandini, A.**; Bartolini, M.; Tedesco, D.; Martinez-Gonzalez, L.; Roca, C.; Campillo, N.E.; Zaldivar-Diez, J.; Perez, C.; Zuccheri, G.; Miti, A.; Feoli, A.; Castellano, S.; Petralla, S.; Monti B.; Rossi, M.; Moda, F.; Legname, G.; Martinez, A.; Bolognesi, M.L. Tau-Centric Multi-Target Approach for Alzheimer's Disease: Development of First-in-Class Dual Glycogen Synthase Kinase 3 $\beta$  and Tau-Aggregation Inhibitors. *J Med Chem* **2018**, 61, 7640-7656.

Author contribution: performed the synthesis and the characterization of the compounds, contributed to performing some experiments, and writing the paper.

- **Gandini, A.**; Bolognesi, M.L. Therapeutic Approaches to Prion Diseases. *Prog Mol Biol Transl Sci* **2017**, 150, 433-453.

Author contribution: contributed to writing the chapter.

- Bolognesi, M.L.; **Gandini, A.**; Prati, F.; Uliassi, E. From companion diagnostics to theranostics: a new avenue for Alzheimer's disease? *J Med Chem* **2016**, 59, 7759-7770.

Author contribution: contributed to writing the paper.

### **Other publications not cited here**

**Gandini, A.**; Prati, F.; Uliassi, E.; Bolognesi, M.L. Drug discovery strategies for the generation of multitarget ligands against neglected tropical diseases. (Book chapter) *Drug Selectivity: An Evolving Concept in Medicinal Chemistry* **2017**, 135-159.

Author contribution: contributed to writing the chapter.

Uliassi, E.; **Gandini, A.**; Perone, R.C.; Bolognesi, M.L. Neuroregeneration versus neurodegeneration: toward a paradigm shift in Alzheimer's disease drug discovery. *Future Med Chem* **2017**, 9 (10), 995-1013.

Author contribution: contributed to writing the paper.

## **List of abbreviations**

$\alpha$ -syn:	$\alpha$ -synuclein
A $\beta$ :	amyloid- $\beta$
ACh:	acetylcholine
AChE:	acetylcholinesterase
AD:	Alzheimer's disease
AFM:	atomic force microscopy
ALS:	amyotrophic lateral sclerosis
APP:	amyloid precursor protein
ATP:	adenosine 5'-triphosphate
ATPZ:	aminothienopyridazines
BACE-1:	$\beta$ -secretase
BBB:	blood-brain barrier
BSE:	bovine spongiform encephalopathy
CD:	Circular dichroism
Cdc7:	cell division cycle 7
CDK-5:	cyclin-dependent kinase 5
CGNs:	cerebellar granule neurons
CK1:	casein kinase 1
CNS:	central nervous system
CJD:	Creutzfeldt-Jakob disease
CR:	Congo red
CSF:	cerebrospinal fluid
CT:	computed tomography
CWD:	chronic wasting disease
<i>E. coli</i> :	<i>Escherichia coli</i>
EDDA:	ethylenediamine diacetate
FAD:	familial Alzheimer's disease
FDA:	Food and Drug Administration
FFI:	fatal familial insomnia
FL:	full length
FTDP-17:	frontotemporal dementia with parkinsonism-17

GPI:	glycosylphosphatidylinositol
GSK-3:	glycogen synthase kinase 3
GSK-3 $\beta$ :	glycogen synthase kinase 3 $\beta$
GSS:	Gerstmann-Sträussler-Scheinker
HepG2:	human hepatoma cell line
HMKs:	halomethylketones
HMTA:	hexamethylenetetramine
IBs:	inclusions bodies
IPTG:	1-thio- $\beta$ -D-galactopyranoside
LCPs:	luminescent conjugated polythiophenes
LMTM:	leuco-methylthionium bis(hydromethanesulphonate)
MAP:	microtubule-associated protein
MAPK1:	mitogen-activated protein kinase 1
<i>MAPT</i> :	microtubule associated protein tau gene
MARK1:	microtubule affinity regulating kinase 1
MB:	methylene blue
MRI:	magnetic resonance imaging
MSFI:	multispectral fluorescence imaging
MTDL:	multi-target directed ligand
MTT:	3-(4,5-dimethylthiazol-2-yl)-2,5-diphenyltetrazolium bromide
MWI:	microwave irradiation
NIR:	near-infrared
NFTs:	neurofibrillary tangles
NMDA:	N-methyl-D-aspartate
OA:	okadaic acid
PAINS:	Pan Assay Interference Compounds
PAMPA:	Parallel Artificial Membrane Permeability Assay
PD:	Parkinson disease
Pe:	effective permeability
PET:	positron emission tomography
PHF:	paired helical filaments
PIO:	pioglitazone

PMDs:	protein misfolding diseases
PPIs:	protein-protein interactions
PPS:	pentosane polysulfate
PrDs:	prion diseases
PRM:	protein recognition motifs
<i>PRNP</i> :	human prion protein gene
PrP:	prion protein
PrP <sup>C</sup> :	physiological cellular form of PrP
PrP <sup>Sc</sup> :	misfolded, pathogenic form of PrP <sup>C</sup> , also denoted as prion
PSP:	progressive supranuclear palsy
PTHs:	phenylthiazolyl-hydrazides
QY:	quantum yield
RML:	Rocky mountain laboratory
RT-QuIC:	Real-Time Quaking-Induced Conversion
SAD:	sporadic Alzheimer's disease
SAR:	structure-activity relationship
SOD1:	Cu, Zn superoxide dismutase 1
SPECT:	single-photon emission computed tomography
T7RP:	T7 RNA polymerase
TDP-43:	TAR DNA-binding protein 43
TDZDs:	thiadiazolidinediones
Tg:	transgenic
ThS:	thioflavin S
ThT:	thioflavin T
TMS:	tetramethylsilane
TR-FRET:	Time-Resolved Fluorescence Energy Transfer
TSE:	transmissible spongiform encephalopathies
TTR:	transthyretin
TZD:	2,4-thiazolidinedione



## **Chapter I**

### **Protein Misfolding Diseases:**

**focus on Alzheimer's and prion diseases**



## **1.1 Protein misfolding diseases**

A broad range of human diseases arises from the failure of a specific peptide or protein to adopt, or remain in its native functional conformational state. These pathological conditions are generally referred to as protein misfolding diseases (PMDs).<sup>1</sup> The hallmark event in PMDs is the change in the secondary and/or tertiary structure of a physiological protein without alteration in its primary structure. This conformational change will then promote the disease by gain of a toxic activity or by the lack of the biological function of the natively folded protein.<sup>2</sup>

The majority of PMDs can be either inherited or sporadic. In familial cases, a mutation promotes the misfolding of the protein which starts to accumulate, thus triggering the disease process. On the other side, in sporadic cases, the balance between the normal and the pathological protein conformation can be altered by environmental fluctuation (e.g. pH, metal ions, oxidative stress, etc.), changes in the protein concentration, or by the effect of physiological and pathological chaperone proteins.<sup>3</sup>

Interestingly, there is no evident sequence or structural homology among all the proteins involved in PMDs. However, the pathological conformer of most of them is rich in a particular secondary structure motif, i.e. the  $\beta$ -sheet conformation.  $\beta$ -sheets consist of alternating pleated strands linked by hydrogen bonding between NH and CO groups of the peptidic bond.<sup>2</sup> The  $\beta$ -sheet conformation is stabilized by protein oligomerization or aggregation. These highly organized fibrillary aggregates are generally described as amyloid fibrils, or plaques, when they accumulate extracellularly. On the other hand, intracellular inclusions are fibrils morphologically and structurally related to extracellular amyloid that form inside the cell.<sup>4</sup>

The correlation and co-localization of protein aggregates with degenerating tissues and disease symptoms is a strong indication of the involvement of amyloid deposition in the pathogenesis of PMDs.<sup>5</sup> However, it is still unclear whether these aggregates are the culprit of the disease or its epiphenomenon. Nevertheless, protein aggregates have become a typical signature of PMDs, and their presence is used for definitive diagnosis.<sup>6</sup>

To date, 37 peptides or proteins have been found to form amyloid deposits in human diseases. Among them, eight proteins associated with PMDs form deposits in the

central nervous system (CNS), giving rise to neurodegenerative diseases such as Alzheimer’s disease (AD), Creutzfeldt-Jakob disease (CJD), Parkinson disease (PD), and many others (see Table 1.1). On the other side, several proteins form deposits in other tissues including heart, spleen, liver, and kidney, and the resulting diseases are non-neuropathic.<sup>7</sup>

**Table 1.1.** Neurodegenerative protein misfolding diseases (modified from Goedert, 2010).<sup>8</sup>

Misfolded protein	Human disease
<b>Prion protein</b>	Kuru Creutzfeldt-Jakob disease Gerstmann-Sträussler-Scheinker disease Fatal familial insomnia
<b>Amyloid-β</b>	Alzheimer’s disease
<b>Tau</b>	Alzheimer’s disease Gerstmann-Sträussler-Scheinker disease British dementia Danish dementia Pick’s disease Progressive supranuclear palsy Corticobasal degeneration Argyrophilic grain disease Guam Parkinsonism-dementia complex Tangle-only dementia White matter tauopathy with globular glial inclusions Frontotemporal dementia and Parkinsonism linked to chromosome 17
<b>α-synuclein</b>	Parkinson’s disease Dementia with Lewy bodies Multiple system atrophy Pure autonomic failure Lewy body dysphagia
<b>Superoxide dismutase 1</b>	Amyotrophic lateral sclerosis

<b>TAR DNA-binding protein 43</b>	Amyotrophic lateral sclerosis Frontotemporal dementia
<b>Fused in sarcoma</b>	Amyotrophic lateral sclerosis Frontotemporal dementia
<b>Huntingtin</b>	Huntington's disease

### 1.1.1 Structures and properties of the amyloid fibrils

Amyloid fibrils are insoluble and heterogeneous. Thus, their structure determination with the commonly used methods is very complicated. Nevertheless, the large number of structural models, and the high-resolution atomic structures of amyloid fibrils that are becoming available in the years, makes it possible to identify and to rationalize their common and distinctive features.<sup>7</sup> The signature of amyloid fibrils is the cross- $\beta$  fiber X-ray diffraction pattern, with  $\beta$ -strands oriented perpendicularly to the fibril axis (Figure 1.1).<sup>9</sup>



**Figure 1.1.** Model of the common core protofilaments structure of amyloid fibrils. In this illustration, four  $\beta$ -sheets make up the protofilaments structure. These sheets run parallel to the axis of the protofilaments. With twisting of the  $\beta$ -strands, the  $\beta$ -sheets twist around a common helical axis, corresponding with the protofilament axis, giving a helical repeat of 115.5 Å (modified from Sunde, 1997).<sup>10</sup>

Electron and atomic force microscopy (AFM) have given insight into their macromolecular structures, showing that fibrils are long, straight and unbranched, and are made up of individual subunits named “protofilaments”.<sup>11-13</sup> Amyloid fibrils generally comprise 2-8 protofilaments, each approximately 2-7 nm in diameter, which often twist around each other or associate laterally as flat ribbons 2-7 nm high and up to 30 nm wide. However, mono-protofilament fibrils have also been observed.<sup>14, 15</sup>

The presence of amyloid fibrils is characteristically monitored by the binding of dyes, such as Thioflavin T (ThT), Congo red (CR), or their derivatives, which are thought to form ordered arrays along the lengths of the fibrils that give rise to specific spectral responses.<sup>16</sup>

Importantly, cross- $\beta$  structures, fibrillary morphology, and peculiar tinctorial properties are universally accepted as the hallmarks of amyloid structures. Therefore, any protein aggregate needs to display all of them to be classified as such.<sup>7</sup>

An intriguing aspect of the amyloids is the morphological and structural similarity of the fibrils formed by different polypeptide chains. This evidence, together with the finding that they can be formed by a range of different polypeptide sequences, led to the hypothesis that the amyloid configuration is a generic, widely accessible, stable structure of the proteins.<sup>1, 17</sup> However, this is in contrast with the situation of the native states of proteins, where structure is strongly dependent on the specific amino acid sequence, and complex environments or careful regulation are frequently required for their correct self-assembly into folded structures. This consideration led the scientific community to investigate the nature of the interactions that stabilize the amyloid forms of proteins. It has been shown that the major contribution to their rigidity and stability stems from a generic interbackbone hydrogen-bonding network that is modulated by variable side-chain interactions.<sup>18</sup>

Another evident feature of amyloid aggregates is their polymorphism. Indeed, it is frequent that the same protein sequence gives rise to fibrils that differ both in the molecular structures of their protofilaments and in the overall morphology of the mature fibrils.<sup>19</sup> Polymorphism is an intrinsic consequence of the ability of polypeptide chains to form amyloid fibrils. Unlike native folds, selected throughout evolution and

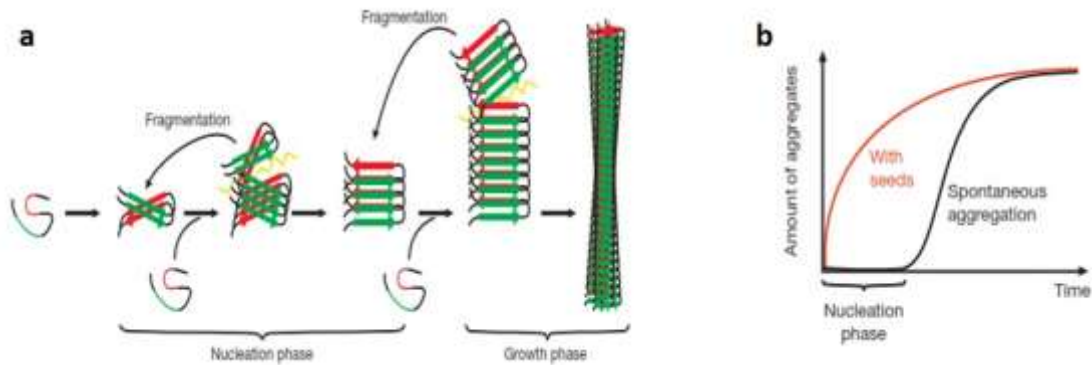
encoded in their amino acid sequence, the amyloid architecture is simply a consequence of the physicochemical properties of a polypeptide chain. Thus, a given sequence can be incorporated in such structures in multiple different ways. Once a given type of assembly has been initiated, however, it will propagate thanks to the inherent stability of repetitive structures in highly organized systems, and the high kinetic barriers that exist in the interconversion between polymorphs.<sup>7</sup>

### **1.1.2 The mechanism of amyloid formation**

Studying the mechanism of formation of amyloid fibrils is of utmost importance. Understanding the mechanism underlying polymerization of soluble, monomeric peptides into insoluble fibrils may provide researchers with possible therapeutic approaches to halting, reversing or avoiding fibril formation.<sup>20</sup>

Several information on the possible mechanism of amyloid-like fibril formation derive from *in vitro* aggregation kinetics studies.<sup>21-23</sup> It is thought that four major steps are involved in fibril formation (Figure 1.2a). The first step is a slow nucleation phase (the aggregation of the protein into a seed) that may go through several intermediates states until the initial segment of the amyloid spine is formed. Monomeric or oligomeric structures are then attached to the ends of the initial amyloid seed by conformational conversion, starting the elongation step. Although nucleation and elongation could be sufficient for describing fibrillation, secondary processes such as fibril fragmentation and secondary nucleation are extremely important.<sup>21</sup> Indeed, the growing fibril can break spontaneously or actively through cellular processes. Thus, amyloid formation becomes self-propagating through the generation and spread of new amyloid seeds, leading to a faster elongation. This process is referred to as secondary nucleation.

Fibril growth may be diagrammatically represented as a lag exponential growth curve where the phase is considerably shortened in the presence of seeds (Figure 1.2b).<sup>24</sup>



**Figure 1.2.** (a) Schematic representation of the amyloid formation process. (b) Representation of the kinetic of amyloid formation (modified from Jucker, 2013).<sup>24</sup>

### 1.1.3 Protein aggregates-related pathogenicity

The presence of highly organized and stable fibrillary deposits in the organs of patients suffering from PMDs, initially led to the hypothesis that these aggregates were the causative agents of such disorders. However, in PMDs involving the CNS, it is now increasingly accepted that the pathogenicity arises from the oligomeric forms generated in the aggregation process.<sup>25-28</sup> Nevertheless, also fibrils show toxicity, as they can deplete key components of the protein homeostasis network, they can act as a reservoir of protein oligomers that can be released, and, most importantly, they are potent catalysts for the generation of new toxic oligomers through secondary nucleation.

To definitively identify which is the key culprit between oligomers and/or fibrils is particularly challenging because of their transient nature and their variability in terms of size and structure. Nevertheless, intense structural research has elucidated some factors responsible for their toxicity. Indeed, one of the major determinants of oligomer-mediated toxicity is the exposure of hydrophobic groups on the oligomer surface, that are normally hidden in globular proteins or that are highly dispersed in intrinsically disordered proteins. Moreover, most of these misfolded oligomeric species are likely to be toxic to some degree because of their small size.<sup>7</sup> A possible explanation for the importance of small size in oligomer toxicity is the high diffusion

coefficient exhibited by these species, which allow them to diffuse more rapidly, thus forming aberrant interactions more easily.<sup>29</sup> The oligomers have also been reported to interact with a large number of molecular species, leading to a variety of mechanism of toxicity, and to a long list of possible molecular targets for such aberrant species. Moreover, it is important to understand that is unlikely to have a single toxic agent associated with a disease. The network of aberrant interactions that such species can generate indicates that it is improbable to have a unique molecular interaction, a unique mechanism of action, or a unique cascade of cellular events associated with a given disease. Indeed, oligomers' toxicity is likely to be the result of their intrinsic misfolded nature and their structural heterogeneity.<sup>7</sup>

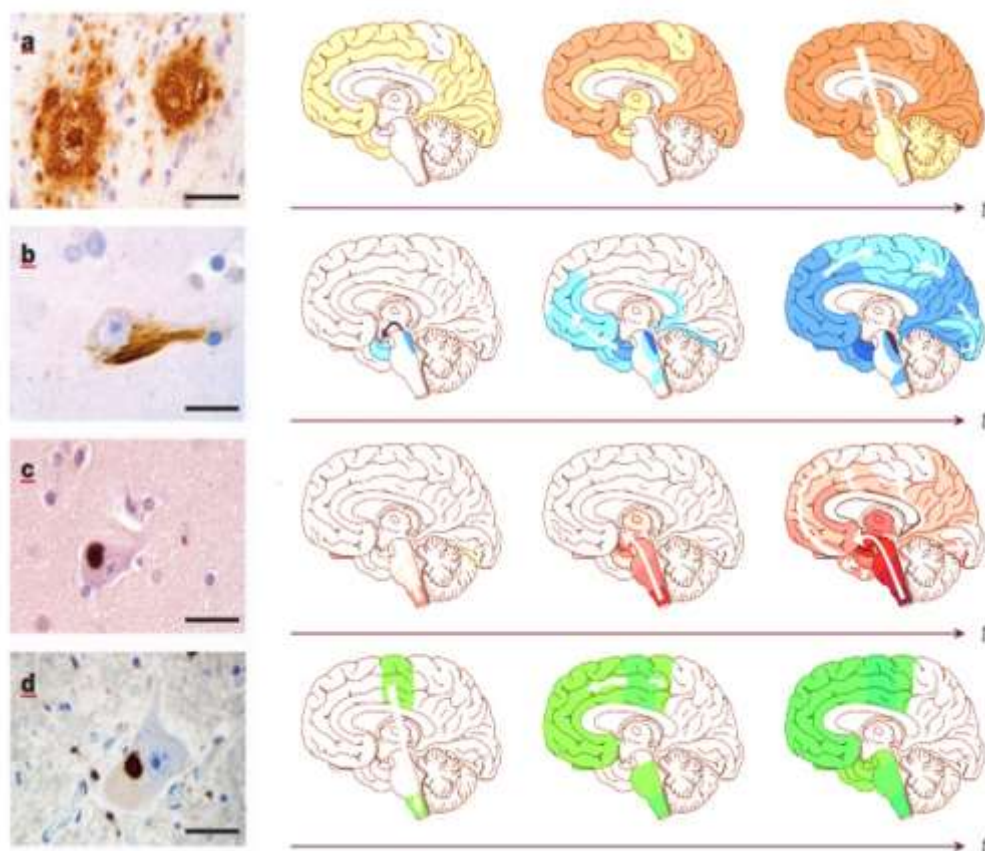
#### **1.1.4 Neurodegenerative PMDs**

In the last decades, neurodegenerative PMDs draw public and scientific attention due to an increasing number of cases, becoming a serious issue in terms of healthcare and economic costs. To date, 50 million people worldwide are affected by some form of neurodegeneration, and in 2030 the affected are expected to reach 75 million.<sup>30</sup> Furthermore, the list of PMDs is long and growing, while the pipeline of disease modifying drugs is almost dry. Thus, treatment of such misfolding maladies is considered as one of the most important therapeutic challenges of the 21<sup>st</sup> century.<sup>31</sup>

Alzheimer's disease (AD), prion diseases (PrDs), Parkinson's disease (PD), and amyotrophic lateral sclerosis (ALS) are prominent examples of PMDs.<sup>24</sup> The finding that all these diseases might share a common key pathological hallmark, i.e. the misfolding of a specific protein, has importantly contributed towards their understanding, but many aspects still remain unclear. The misfolding proteins responsible for neurodegenerative PMDs are: amyloid- $\beta$  (A $\beta$ ) and tau protein in AD; prion protein (PrP) in PrDs;  $\alpha$ -synuclein ( $\alpha$ -syn) in PD; and Cu, Zn superoxide dismutase 1 (SOD1) and TAR DNA-binding protein 43 (TDP-43) in ALS.<sup>8</sup>

Importantly, in recent years, prion diseases have received ample recognition as a prototype of neurodegenerative PMDs.<sup>24</sup> Briefly, the central molecular event during

PrDs is the self-propagating conformational conversion of the cellular prion protein ( $\text{PrP}^c$ ) to its pathological isoform ( $\text{PrP}^{\text{Sc}}$ ). This postulate is known as the “protein-only hypothesis”.<sup>32</sup> Nowadays, an increasing body of evidence reveals that several other proteins follow a similar general molecular mechanism of self-perpetuating seeded aggregation, and a similar cell-to-cell spreading in vitro, in cell cultures, and in vivo in animal models. Indeed,  $\text{A}\beta$  and tau protein in AD,  $\alpha$ -syn in PD, SOD1 and TDP-43 in ALS are now commonly referred to as prion-like proteins (Figure 1.3).<sup>24</sup>



**Figure 1.3.** Amyloid- $\beta$  deposits (a), tau inclusion as a neurofibrillary tangle (b),  $\alpha$ -synuclein inclusion (c), TDP-43 inclusions (d), and characteristic progression of the lesions over time (modified from Jucker, 2013).<sup>24</sup>



## **1.2 Alzheimer's disease**

Alzheimer's disease is the most common cause of dementia worldwide and the most prevalent neurodegenerative disorder. Since the first description provided by Alois Alzheimer in 1906, scientists have made remarkable improvements in understanding its molecular roots, although the two key pathological hallmarks, amyloid- $\beta$  and tau protein, were not molecularly identified until the 1980s.<sup>33</sup>

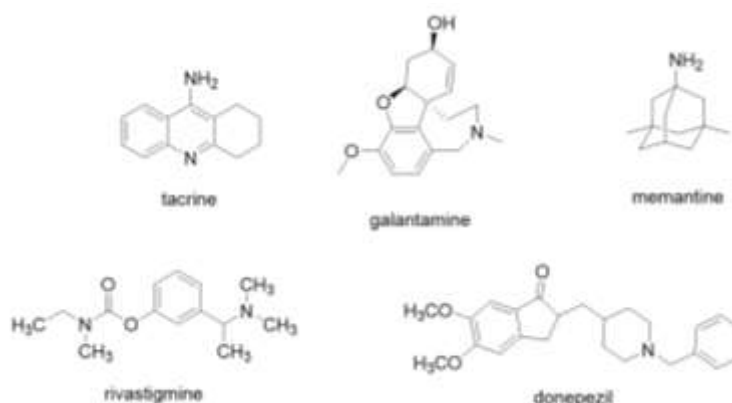
Today, AD is the most common dementia in late life, and it is becoming increasingly common as the global population ages. It is currently estimated that 50 million people worldwide have dementia, with an estimated global cost of dementia care at 1 trillion US\$ in 2018. In the absence of effective therapies, the numbers are estimated to increase to 82 million people by 2030, and 152 by 2050.<sup>34</sup> Global leaders have set a deadline of 2025 for finding an effective way to treat or prevent AD.<sup>35</sup> In 2014, the G8 stated that dementia should be made a global priority with the aim of a cure or approve disease-modifying therapy available by 2025.<sup>36</sup> Indeed, it has been estimated that the overall frequency of AD would be decreased by nearly 50% if the onset could be delayed by 5 years.<sup>37</sup>

### **1.2.1 Drug development in Alzheimer's disease**

AD drug development has proven to be extremely difficult. Despite the evaluation of several potential treatments in clinical trials, only four cholinesterase inhibitors (tacrine, donepezil, rivastigmine, galantamine) and an N-methyl-D-aspartate (NMDA) receptor antagonist (memantine) have shown sufficient safety and efficacy to allow marketing approval (Figure 1.4).<sup>38</sup>

Acetylcholinesterase inhibitor tacrine was approved by the FDA in 1993 but was then discontinued in some states, due to concerns over safety. Then, donepezil was approved in 1996, rivastigmine in 1998, galantamine in 2001, and NMDA receptor blocker memantine in 2003. These five drugs, however, are only symptomatic treatments, temporarily ameliorating memory and thinking problems. Indeed, their clinical effect is modest as they do not treat the underlying causes of AD, neither slow

the rate of decline. Unfortunately, no new treatments have been approved since 2003. Analyzing the period from 2002 to 2012, a very high attrition rate was found, with an overall success rate of 0.4% (99.6% failure), thus making AD one of the most unsuccessful therapeutic areas of drug discovery.<sup>39</sup>



**Figure 1.4.** Chemical structures of the AD-approved drugs.

What is even more discouraging is that despite the enormous social and economic reward of a successful treatment, big pharma are pulling out of AD research.<sup>40</sup>

The failures in AD drug development have occurred with both small molecules and immunotherapies, both failing to show a drug/placebo difference or having an unacceptable toxicity. The efforts to bring new AD drugs to market have been hindered by a number of challenges, such as the still incomplete understanding of AD pathogenesis, its multifactorial etiology and complex pathophysiology, its slowly progressive nature, and the high level of comorbidities occurring in the elderly people.<sup>41</sup> Moreover, clinical symptoms are not evident until considerable changes have occurred within the brain, making difficult in the clinical trial environment the establishment of the most appropriate outcomes to measure.<sup>42</sup>

### 1.2.2 AD as a multifactorial disorder

Two different forms of AD can be distinguished: familial AD (FAD, early-onset AD), and sporadic AD (SAD, late-onset AD). FAD represents less than 1% of AD cases, and it is caused by mutations in three different transmembrane proteins: APP, presenilin 1, and presenilin 2.<sup>43</sup> While SAD is the most common one, representing the 99% of AD cases, usually diagnosed in people over 65 years. SAD occurs in unpredictable manner and it is not associated with any known mutation.<sup>44</sup>

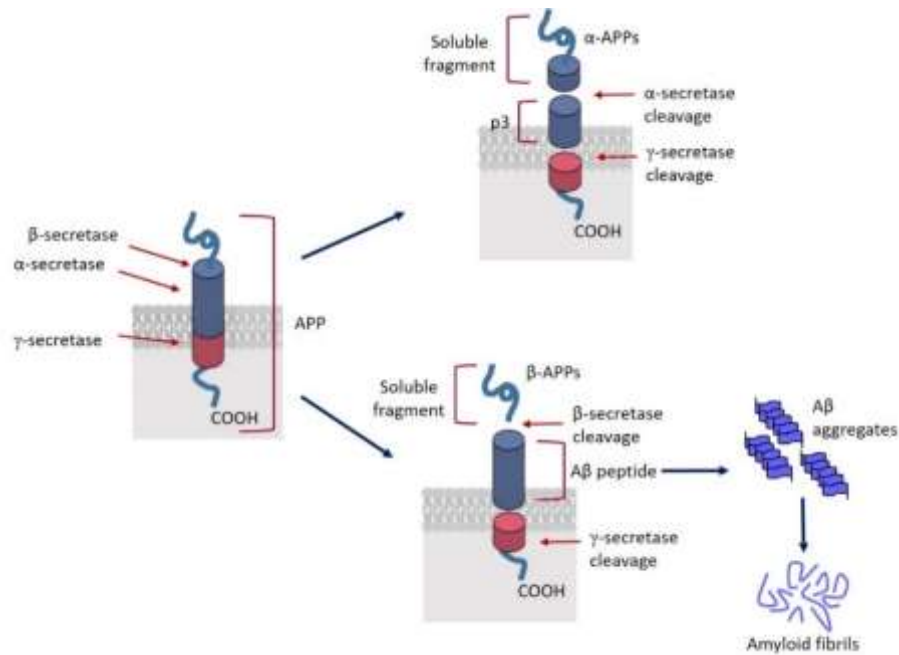
Although the etiology of AD is still not fully understood, the scientific community has recognized it as a multifactorial and complex disorder. AD is histopathologically characterized by brain  $\beta$ -amyloidosis, neurofibrillary degeneration, and loss of neuronal synapses and pyramidal neurons. All these changes result in the development of the typical AD symptomatology, namely a progressive impairment of cognitive function, together with behavioral disturbances such as aggression, depression and wandering.  $\beta$ -Amyloidosis encompasses plaques of extracellular deposits of amyloid- $\beta$  protein -derived from the amyloid precursor protein (APP)- in the brain parenchyma and in the cerebral blood vessels. Conversely, neurofibrillary degeneration is observed in the cell soma as neurofibrillary tangles (NFTs) composed of hyperphosphorylated tau proteins in paired helical filaments (PHF).<sup>44</sup> In both cases, the accumulating proteins assume a tertiary structure that is unusually rich in  $\beta$ -sheets, which in turn promote the self-assembly of protein molecules into small oligomeric and larger fibrillary assemblies, with neurotoxic properties.<sup>45</sup>

Since the discovery of AD, several single-factor theories try to explain its etiology, but to date, no one can adequately account for all the aspects of this disease. The “multiple combinations of co-factors” theory of AD was proposed by McDonald in 2002<sup>46</sup> and, during the years, appears as the most plausible model that could open the door to novel treatment strategies. However, despite significant advances in understanding AD pathophysiologic determinants (e.g. A $\beta$ , tau protein, neuroinflammation, oxidative stress, and synaptic dysfunctions), we still lack a detailed understanding of the causal role of this phenomena and the interactions between them.

In the mid-1970s, reports on the increasing loss of cholinergic neurons and synapses in the basal forebrain, together with the emerging role of acetylcholine (ACh) in learning and memory, led to the cholinergic hypothesis of AD.<sup>47</sup> It was proposed that degeneration of cholinergic neurons and the associated loss of cholinergic neurotransmission in the cerebral cortex contributed significantly to the deterioration in cognitive function of AD patients. The cholinergic hypothesis was the first proposed theory, and it led to the development of the acetylcholinesterase (AChE) inhibitors currently approved for the treatment of mild to moderate AD (see above).<sup>48</sup> However, the failure of AChE inhibitors to effectively cure AD was seen as disproving the cholinergic hypothesis, and the focus of AD research shifted towards A $\beta$  deposition and abnormalities in tau protein production.

In 1992, the “amyloid cascade hypothesis” was proposed,<sup>49, 50</sup> according to which the generation of the neurotoxic A $\beta$  peptide derive from the consecutive post-translational proteolysis of APP (Figure 1.5). Then, A $\beta$  peptides deposit and/or aggregate in extracellular insoluble plaques.

In the proteolytic process of the APP, as first step,  $\beta$ -secretase (BACE-1) cleaves APP at the NH<sub>2</sub> terminus to provide a soluble peptide ( $\beta$ -APP) and a 99-residue COOH-terminal fragment (C99), which remains bound to the membrane. Alternatively,  $\alpha$ -secretase cuts within the A $\beta$  region to produce  $\alpha$ -APPs and an 83-residue COOH-terminal fragment (C83). Secondly,  $\gamma$ -secretase, a second proteolytic enzyme, perform an unusual cut within the transmembrane domain to produce the amyloidogenic A $\beta$  from C99, and a non-amyloidogenic one (p3) from C83.  $\gamma$ -secretase' proteolysis is heterogeneous, the majority of the A $\beta$  species produced are 40-residue peptides (A $\beta$ <sub>40</sub>), while a small portion is a 42-residue (A $\beta$ <sub>42</sub>).<sup>51</sup> Importantly, A $\beta$ <sub>42</sub> is longer, more hydrophobic, and more prone to fibril formation compared to A $\beta$ <sub>40</sub>. However, A $\beta$ <sub>40</sub> and A $\beta$ <sub>42</sub> are not the only pathological APP-deriving peptides. Indeed, cerebrospinal fluid (CSF) of AD patients showed high levels of another isoform of A $\beta$ , the 38-residue peptide (A $\beta$ <sub>38</sub>).



**Figure 1.5.** Schematic depiction of the amyloid cascade (modified from Bolognesi, 2017).<sup>52</sup>

Considerable research now supports the conclusion that A $\beta$  aggregates and spreads in the brain by a prion-like mechanism.<sup>45</sup> AD involves a clinically silent period of intracerebral protein aggregation that precedes dementia by decades.<sup>53-55</sup> Thus, the seeding model of A $\beta$  deposition substantiates a primary role for A $\beta$  aggregation in the early stages of AD and reinforces the logic of therapeutically targeting A $\beta$  seeds,<sup>56</sup> preferably early in the pathogenic cascade.

During the years, several experimental evidence have consolidated the “amyloid hypothesis”, showing that fibrillogenic A $\beta$  is increased in the majority of mutations causing FAD. Moreover, A $\beta$  peptides impairs neuronal functions in a variety of experimental models.<sup>57</sup>

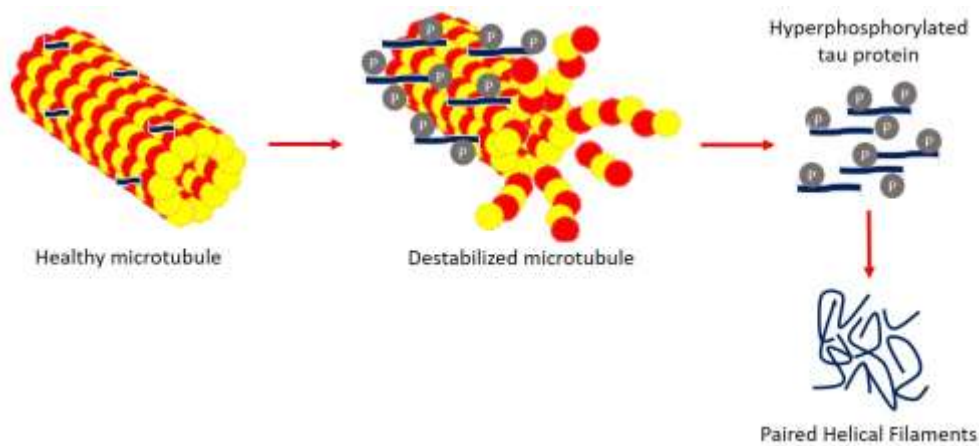
Nevertheless, understanding the nature of the neurotoxic A $\beta$  species is still very difficult. Initially, only plaques were thought to be neurotoxic, but now A $\beta$  oligomers has been suggested as the most harmful species.<sup>58, 59</sup> Moreover, it is widely recognized that A $\beta$  exerts its neurotoxic effect also through several other mechanisms as, for example, disrupting synaptic mitochondrial function, activating microglial cells and enhancing the expression of pro-inflammatory genes, increasing reactive oxygen species (ROS) formation, triggering the conversion of tau protein into a pathologic

state, etc.<sup>60, 61</sup> Thus, the aggregation of A $\beta$  peptide might initiate a vicious cycle, only ultimately leading to neuronal death and to the disruption of memory and cognitive functions that characterize AD.

Several efforts have been made to develop A $\beta$ -based therapies, with some of them now being tested in ongoing clinical trials.<sup>37, 62</sup> However, the recent failures of A $\beta$ -based drug candidates, have caused many scientists to question the “amyloid hypothesis”. Indeed, although the presence of A $\beta$  aggregates has been clearly associated with AD pathology, there is still an active discussion as to whether their presence closely correlates with disease severity and progression. In contrast, mounting evidence are now suggesting that the density and neocortical spread of NFTs better correlate with the neuronal degeneration and cognitive impairment.<sup>63</sup>

In light of this, in recent years, researchers have focused their attention towards tau protein, as the second pathological hallmark of AD is represented by neurofibrillary tangles. Tau is a neuronal microtubule-associated protein involved in microtubules stabilization,<sup>64</sup> and playing an important physiological role in microtubule dynamics and axonal transport.<sup>65</sup> Tau functions can be regulated by its phosphorylation state at more than 40 phosphorylatable sites, including serine, threonine, and tyrosine.<sup>66</sup> Under pathological conditions, tau proteins became hyperphosphorylated and start to accumulate and aggregate forming NFTs. NFTs interfere with axonal transport leading to atrophy of axons and dendrites, and eventually, to neuronal death.<sup>67</sup>

Abnormally phosphorylated tau was found in the brain of AD patients, and there are strong evidence supporting that tau hyperphosphorylation is an early event in the development of neurofibrillary pathology. Importantly, dephosphorylation of tau isolated from NFTs restores its ability to bind neuronal microtubules, indicating that the mechanism regulating phosphorylation/dephosphorylation kinetics are perturbed in AD.<sup>66</sup>



**Figure 1.6.** Schematic depiction of the tau cascade (modified from Bolognesi, 2017).<sup>52</sup>

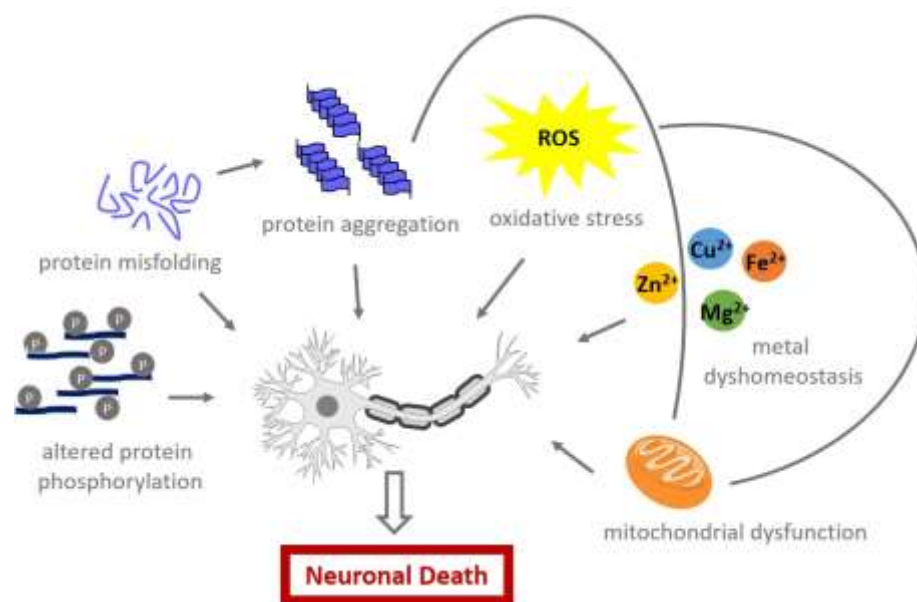
Several kinases have been shown to be capable of phosphorylating tau in vitro, including proline-directed kinases such as mitogen-activated protein kinase 1 (MAPK1), glycogen synthase kinase-3 (GSK-3) and cyclin-dependent kinase 5 (CDK5), as well as non-proline-directed enzymes such as casein kinase 1, protein kinase A, and MAP/microtubule affinity-regulating kinase 1 (MARK1).<sup>68</sup> Recent studies have demonstrated that the majority of tau protein phosphorylation sites can be modified by GSK-3. Furthermore, overexpression of GSK-3 results in tau hyperphosphorylation and disrupted microtubules in transgenic (Tg) mice, suggesting a major role for this kinase as a validated therapeutic target for AD.

NFTs originate in subcortical areas of the brain, predominantly in the hippocampus, and spread out to cortical areas. Similarly to A $\beta$ , tau protein was recognized few years ago as a prion-like protein.<sup>69</sup> Monomers of tau are unfolded and can dimerize without a substantial change in secondary structure. However, when the nucleus of aggregation is formed, an increase of  $\beta$ -sheet take place and the nucleus can be elongated to build PHFs. Moreover, the intracerebral injection of brain extracts containing aggregated tau induces tauopathy in tau-transgenic host mice, and the lesions propagate from the injection site to axonally connected areas, consistent with neuronal uptake, transport, and release of tau seeds.<sup>70</sup>

Although A $\beta$  and tau exert their toxicity through separate mechanisms, several evidence suggest that there is a strict correlation between them. A $\beta$  aggregation and deposition seems to be an early event, which can trigger tau pathology. However, it is

important to remind that  $A\beta$  does not correlate with the presence of NFTs, cell loss or dementia. To date, one hypothesis is that  $A\beta$  aggregation and deposition triggers a process that leads to neuronal loss through formation of PHF of tau. Nevertheless, it remains to be clarified how  $A\beta$  aggregates can trigger or accelerates tau pathology, and how tau pathology ultimately leads to neuronal loss.<sup>62</sup>

Several other hypothesis have been proposed to explain the pathogenesis of AD, including oxidative stress, metal ion dyshomeostasis, and inflammation.<sup>71</sup> It is important to highlight that all the aforementioned hypothesis of AD pathogenesis are not mutually exclusive. Rather, they complement each other, intersecting at a high level of complexity.<sup>72</sup>



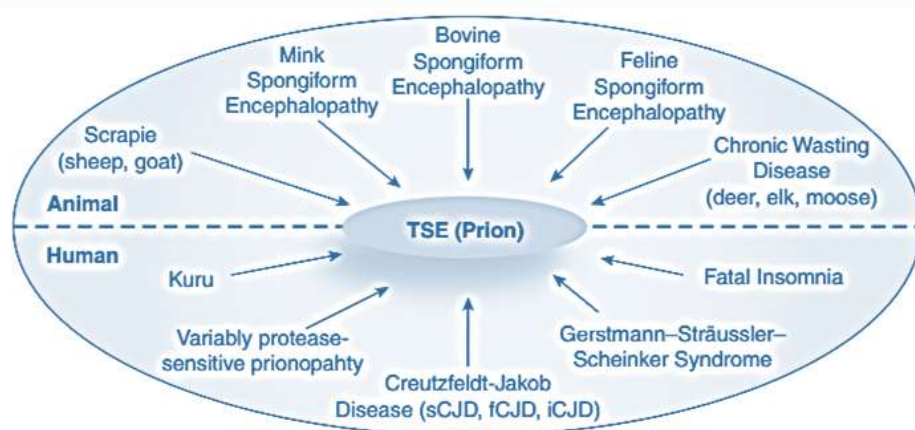
**Figure 1.7.** Schematic depiction of the multifactorial events leading to neuronal death in AD (modified from Cavalli, 2008).<sup>72</sup>



### **1.3 Prion diseases**

Prion diseases (PrDs), also known as transmissible spongiform encephalopathies (TSE), are a group of neurological disorders affecting both animals and humans (Figure 1.8).<sup>32, 73</sup> They include: bovine spongiform encephalopathy (BSE) of cattle; scrapie of sheep; chronic wasting disease (CWD) of deer, moose, and elk; kuru, Creutzfeldt-Jacob (CJD), fatal familial insomnia (FFI), and Gerstmann-Sträussler-Scheinker (GSS) diseases of humans.<sup>74</sup>

PrDs are characterized by widespread neurodegeneration, with clinical symptoms of both cognitive and motor dysfunction. The typical microscopic features is represented by vacuolation of the grey matter of the CNS, prominent neuronal loss, and reactive astrogliosis.<sup>32, 73</sup>



**Figure 1.8.** Animal and human TSEs (modified from Saá, 2016).<sup>75</sup>

Since Cuillé and Chelle successfully transmitted scrapie between sheep, in 1963, and Gajdusek transmitted kuru and CJD to chimpanzee in 1966 and 1968 respectively, the nature of the agents causing these “slow virus diseases” remains unknown.<sup>76</sup>

In 1982, S. Prusiner called them “PRIONS” (acronym of PRoteinaceous Infective ONLY particles), to distinguish the infectious pathogen that causes PrDs from viruses and viroids.<sup>77</sup> Indeed, it was surprising to discover that unlike viruses and bacteria, prions were composed only of protein, and were capable of replicating in the absence of any nucleic acid.<sup>78</sup>

Now it is known that prion diseases are caused by the conversion of the normal prion protein (PrP<sup>C</sup>, the cellular form of the protein) with an  $\alpha$ -helical structure, into an

abnormal amyloidogenic isoform, called the scrapie prion protein (PrP<sup>Sc</sup>, in which Sc stands for scrapie), showing an high content of  $\beta$ -sheet secondary structures.

### 1.3.1 Human prion diseases

Creutzfeldt-Jacob disease is the most common disease among human PrDs, and it can be sporadic, genetic, or acquired. Around 85-90% of CJD cases occur sporadically and affect 1-1.5 people per million annually. Familial/genetic CJD (fCJD/gCJD) account for about 10% of CJD cases worldwide. While acquired PrDs include variant CJD (vCJD) and iatrogenic CJD (iCJD), and are observed in 2-5% of CJD cases. Depending on the origin of the causative agent, human PrDs can be divided in: caused by prions originating internally (fCJD, gCJD, FFI, and GSS), or infected by external prions (kuru, iCJD, and vCJD).<sup>79</sup>

As there are no specific therapeutic and prophylactic interventions available for PrDs, active surveillance is critical for the control and prevention of these disorders, particularly for those caused by external prions.

Kuru was described in cannibalistic tribes of Papua New Guinea, however, after decimating almost the entire population, has almost disappear. Different is the case of vCJD. Indeed, in the '90s, more than 280000 cattle suffering from BSE provoked a worldwide food crisis with huge economic consequences for the European Union and other countries. The subsequent consumption of diseased cattle by humans lead to the emergence of vCJD, causing around 140 deaths in the United Kingdom and few cases in France, Italy, and Canada.<sup>80</sup> The suggested mechanism of infection is defined in three phases: (i) after ingestion, the PrP<sup>Sc</sup> agent is uptaken from the intestinal lumen; (ii) after incubation in lymphoid tissues the PrP<sup>Sc</sup> spreads to the CNS via the enteric nervous system; (iii) the final phase is the infection of the spinal cord and brain, leading to the characteristic spongiform degeneration and astroglial activation.<sup>81</sup> Finally, iatrogenic transmission of CJD has principally occurred through improperly sterilized neurosurgical instruments, transplants of *dura mater*, and administration of pituitary hormones of cadaveric origin.<sup>75</sup> These routes of transmission no longer pose a major threat; however, recently, the transmission of vCJD has been reported in four

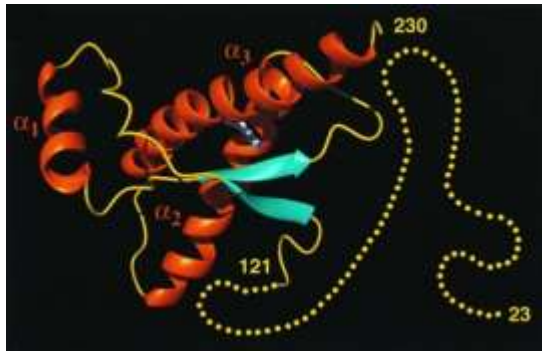
instances through the therapeutic use of non leukoreduced red blood cell concentrates.<sup>82, 83</sup>

### 1.3.2 PrP<sup>C</sup> and PrP<sup>Sc</sup>

The cellular prion protein is a cell surface glycoprotein, expressed in a variety of different organs and tissues, with high expression levels in the central and peripheral nervous system. In humans, PrP<sup>C</sup> is a 253 amino acid protein encoded by the *PRNP* (human PRion Protein) gene, and it is linked to the plasma membrane by a glycosylphosphatidylinositol (GPI) anchor. PrP<sup>C</sup> precursor protein contains two signal peptides. The 22 amino acids at the N-terminus targets the protein to the endoplasmic reticulum; while the 23 amino acid sequence at the C-terminus is essential for the addition of the GPI anchor.<sup>77</sup> Peptide 1-22 is cleaved as signal peptide during trafficking, while peptide 230-253 is replaced by the GPI anchor. After the cleavage of the signal peptides, PrP<sup>C</sup> is exported to the cell surface as an N-glycosylated protein.

PrP<sup>C</sup> is formed by an amino flexible, random coil sequence containing two hexarepeats and five octarepeats, and a C-terminal globular domain of about 100 amino acids (Figure 1.9). The N-terminal domain contains: a repetitive sequence of eight amino acids, the so-called octapeptide repeats (PHGGGWGQ) that appear five times in most mammalian species; a neurotoxic central region; and a hydrophobic domain. Through the octarepeats-containing flexible tail, PrP<sup>C</sup> can bind divalent cations such as copper and zinc, and it can interact with a plethora of different proteins. These interactions have been taken to reflect its putative role in several cellular processes, but they may also simply be a consequence of the unstructured, flexible conformation of the N-terminus of PrP<sup>C</sup>.

The physiological role of PrP<sup>C</sup> is still under debate, and defining its cellular role is complicated by the lack of major anatomical or developmental deficits observed in early studies with PrP<sup>C</sup> knock-out mice.<sup>84, 85</sup> To date, PrP<sup>C</sup> seems to be involved in several processes such as: neurite outgrowth; neuronal survival; synapse formation, maintenance, and function; and maintenance of myelinated fibers.<sup>86</sup>



**Figure 1.9.** Cartoon of the three-dimensional structure of the intact hPrP (23-230). Helices are depicted in orange,  $\beta$ -strands in cyan, the segments with non-regular secondary structure in the C-terminal domain in yellow, and the octarepeats-containing flexible tail is represented by yellow dots (modified from Zahn, 2000).<sup>87</sup>

Moreover, numerous putative neuroprotective functions have been attributed to PrP<sup>C</sup>, including cell surface signaling, and antioxidant and anti-apoptotic effects.<sup>88</sup> Finally, it seems to be implicated in autophagy regulation and metal ions trafficking.<sup>89, 90</sup>

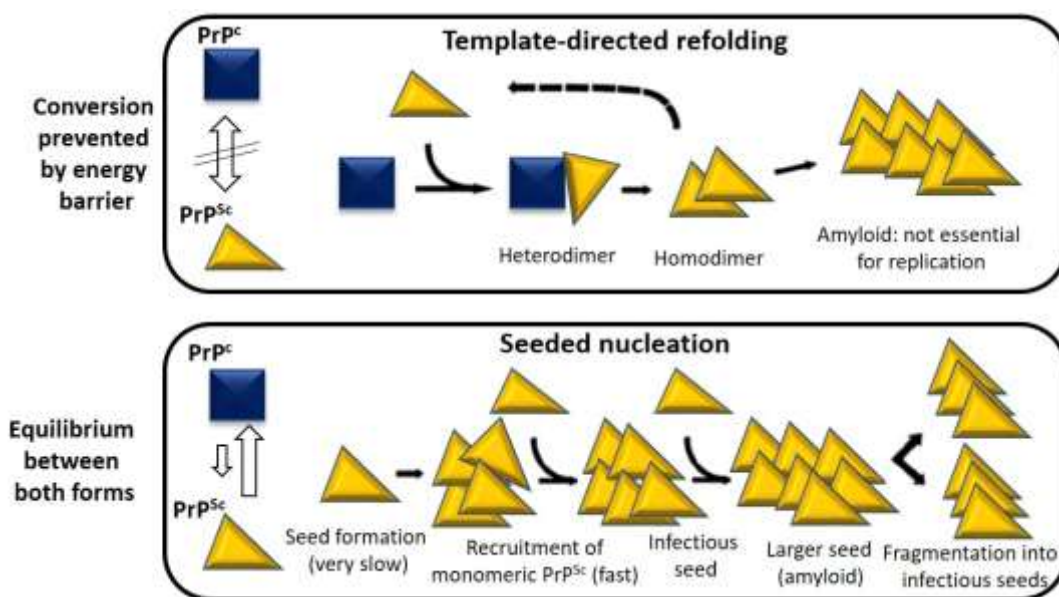
Despite their rare incidence, PrDs have captured broad consideration from the scientific community thanks to the unconventional mechanism by which they are transmitted. According to the “protein-only hypothesis”, PrP<sup>C</sup> is converted into the pathological PrP<sup>Sc</sup> in the brain of the infected host.<sup>32</sup> Subsequently, PrP<sup>Sc</sup> acts as a template, for the conversion of other PrP<sup>C</sup> molecules. Such conversion is associated with conformational changes of its secondary structure from  $\alpha$ -helices to  $\beta$ -sheets.

Two different models have been proposed to explain the conformational conversion from PrP<sup>C</sup> to PrP<sup>Sc</sup>: the “template-directed refolding” and the “seeded nucleation” hypothesis (Figure 1.10).<sup>80</sup>

The “refolding” model postulates an interaction between exogenously introduced PrP<sup>Sc</sup> and endogenous PrP<sup>C</sup>, which is induced to transform itself into further PrP<sup>Sc</sup>. A high energy barrier may prevent the spontaneous conversion of PrP<sup>C</sup> into PrP<sup>Sc</sup>.

On the other side, the “seeding” model proposes that PrP<sup>C</sup> and PrP<sup>Sc</sup> are in a reversible thermodynamic equilibrium. Such equilibrium would be heavily shifted toward PrP<sup>C</sup>, so that only small amounts of PrP<sup>Sc</sup> would coexist with PrP<sup>C</sup>. In this case, PrP<sup>Sc</sup> could not possibly represent the infectious agent, since it would be ubiquitous. However, if several monomeric PrP<sup>Sc</sup> molecules are aggregated into a highly ordered seed, further

monomeric PrP<sup>Sc</sup> can be recruited and, eventually, aggregates to amyloid. Within such a crystal-like seed, PrP<sup>Sc</sup> becomes stabilized. Then, fragmentation of PrP<sup>Sc</sup> aggregates increases the number of nuclei that can recruit further PrP<sup>Sc</sup>, thus accelerating the replication process, the prion accumulation, and finally giving rise to the disease.<sup>80</sup> Testing these hypotheses requires precise knowledge of the structural features of both PrP<sup>C</sup> and PrP<sup>Sc</sup>. To date, such knowledge has not progressed to a state that would allow for resolution of this question. The structure of PrP<sup>C</sup> has been studied extensively with high-resolution methods, yielded detailed insights into its arrangement at the atomic level. PrP<sup>Sc</sup>, however, has been amenable only to low-resolution structural methods, as insoluble aggregates are resilient to most of the available technologies for the determination of protein structure. All we know about PrP<sup>Sc</sup> is that it consists mainly of  $\beta$ -pleated sheet, and its aggregates expose a remarkably ordered structure.



**Figure 1.10.** Proposed models for the conformational conversion from PrP<sup>C</sup> to PrP<sup>Sc</sup> (modified from Aguzzi, 2004).<sup>80</sup>

### 1.3.3 Mechanisms of prion toxicity

PrP<sup>Sc</sup> accumulation in the brain is the hallmark of PrDs, but it is still unknown whether PrP<sup>Sc</sup> is also directly responsible for the devastating CNS pathology. Surely, the accumulation of amyloid in the CNS is likely to be generally unhealthy, as exemplified

by Alzheimer's disease. On the other hand, chronic deposition of PrP<sup>Sc</sup> does not damage PRNP knock-out brains,<sup>91</sup> and depletion of PrP<sup>C</sup> from neurons of scrapie-infected mice prevents the disease.<sup>92</sup>

In the past decades, three different mechanisms on how PrP<sup>Sc</sup> aggregates might exert their toxicity were proposed: the "loss-of-function", the "gain of function", and the "subversion of function" mechanisms.<sup>93</sup>

In the first case, prion neurodegeneration is related to "loss of function" of PrP<sup>C</sup>. However, as highlighted before, the discovery that the inactivation of the PrP<sup>C</sup> gene in mice or cows does not cause neurodegeneration, indicates that prion pathogenesis cannot be due to loss of PrP<sup>C</sup> function.

The most widely discussed hypothesis is the "gain of function" one, in which a toxic and infectious fragment is produced during the conversion of PrP<sup>C</sup> to PrP<sup>Sc</sup>. In this view, PrP<sup>Sc</sup> possesses novel toxic properties not related to the normal, physiological function of PrP<sup>C</sup>. Indeed, PrP<sup>Sc</sup> may block axonal transport, interfere with synaptic functions, or trigger apoptotic pathways.

Finally, the third possible hypothesis for prion pathogenesis involves a subversion of the normal neuroprotective function of PrP<sup>C</sup>. In this mechanism, interaction with PrP<sup>Sc</sup> converts PrP<sup>C</sup> from a transducer of neuroprotective signals into a transducer of neurotoxic signals. Consistent with this model, there are now a number of experimental situations in which expression of PrP<sup>C</sup> in neurons, rather than being neuroprotective, appears to be essential for conferring sensitivity to PrP-related neurotoxic insults.<sup>91, 92, 94</sup> For example, scrapie-inoculated mice expressing GPI-negative version of PrP, develop a minimal brain pathology and neurological dysfunction, despite the high accumulation of amyloid plaques containing PrP<sup>Sc</sup>.<sup>95</sup>

We are still far away from the understanding of the mechanisms underlying prion toxicity. However, it is now clear that alterations in the normal function of PrP<sup>C</sup> may play a crucial role in causing or contributing to the disease phenotype. Indeed, elucidating the physiological activity of PrP<sup>C</sup>, identifying physiologically relevant PrP-interacting partners and the cellular pathways in which they participate, has become a major priority in the prion field.

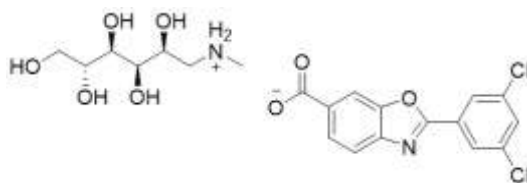
## **1.4 Drug discovery strategies targeting PMDs**

The challenge of PMDs needs to be met at several levels. However, the greatest unmet need is the availability of therapeutic interventions that are effective in slowing or preventing progression of the neurodegeneration. The development of drugs targeting protein misfolding or aggregation has been challenging due to the lack of certainty about which form/s of a given disease protein is primarily responsible for the disease. The situation is further complicated by the existence of a variety of intermediate species that exist during the folding and oligomerization processes, and by the existence of different conformational variants, or “strains”, with different levels of neurotoxicity.<sup>96</sup> In general, drug discovery strategies that restore protein folding and function can be grouped into three different groups:<sup>97</sup>

- I. Stabilization of a specific misfolding-prone or mutant protein using pharmacological chaperones. Chaperones are involved in all aspects of proteostasis, thus they offer potential therapeutic entry points to each step in the processing of a pathogenic protein. One approach to therapeutically targeting the chaperone system has been to develop small molecule inhibitors or activators of specific chaperones.<sup>98</sup> However, none of these compounds have yet entered clinical trials due to issues of low brain penetration and/or peripheral cytotoxicity, but active effort in this area is continuing. A second approach to developing chaperone-based therapeutics has been through protein engineering.<sup>99, 100</sup>
- II. Inhibition of the aggregation of a specific amyloid-prone protein that stabilizes the native state or the partially folded state and prevents the formation of oligomers or amyloids. One strategy is to look for molecules that bind to the soluble oligomers in order to preclude them from interacting with cell surface receptors or other oligomers, thus preventing the aggregation process. Another method is to remove the toxic oligomer via its conversion into a non-toxic aggregate.<sup>97</sup> Importantly, amyloid aggregation inhibitors were able to reach clinical trials for AD.<sup>37</sup>
- III. Targeting degradation and extracellular clearance. Defects in both the ubiquitin proteasome system and autophagy pathways of protein degradation are often

seen in PMDs. A number of small molecules that upregulate components of the ubiquitin proteasome system, promote the degradation of pathological proteins and have neuroprotective effects on cultured cells have been identified, but few have shown to be effective in vivo. One of the best-explored examples of targeting clearance of misfolded proteins has been the use of antibodies to promote, for example, the clearance of A $\beta$ . However, current challenges in the use of A $\beta$  antibodies include low rates of BBB penetration, and uncertainty as to which antibodies engage clinically relevant forms of A $\beta$ .<sup>96, 101, 102</sup>

To date, no drugs able to stop or prevent the progression of neurodegenerative PMDs have been approved. However, the approval of tafamidis for transthyretin amyloidosis give hope to medicinal chemists working in the field of PMDs.<sup>103</sup> Transthyretin amyloidosis are rare and fatal PMDs characterized by the aggregation of transthyretin (TTR), a natively tetrameric protein involved in the transport of thyroxine and the vitamin A–retinol-binding protein complex. The TTR amyloidosis present with a spectrum of manifestations, encompassing progressive neuropathy and/or cardiomyopathy.<sup>104</sup> In the mid1990s Kelly’s group began searching for TTR-aggregation inhibitors, and few years later they began to focus on benzoxazole as TTR-binding compounds. Kelly’s work resulted in the marketing approval of tafamidis meglumine (Figure 1.11), a rationally designed non-steroidal anti-inflammatory derivative of benzoxazole, able to bind to TTR and preventing it from deviating from its natural, functional form into the amyloid state.<sup>105</sup> Tafamidis is able to kinetically stabilize the tetramer, slowing monomer formation, misfolding, and amyloidogenesis.<sup>106, 107</sup> Thus, tafamidis represents the first and only clinically approved anti-amyloid drug. Importantly, the approval of tafamidis proved the effectiveness of small molecules-amyloid aggregation inhibitors for the treatment of PMDs.



**Figure 1.11.** Chemical structure of tafamidis meglumine.





## **Chapter II**

### **Objectives**

Considering the undoubted medical needs discussed in Chapter I, this PhD project has been devoted to the development of small molecules for neurodegenerative protein misfolding diseases. Starting from this, the present thesis has the following specific objectives:

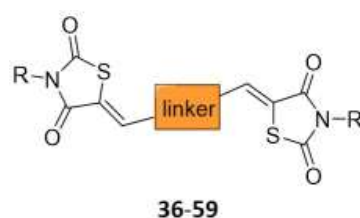
1. In the first project, we applied the Multi Target Directed Ligand (MTDL) approach in order to develop the first class of multi-target compounds able to hit the tau cascade at two different hubs. Indeed, several evidence suggested the altered tau protein network as a promising target for Alzheimer's disease. With the aim to develop multi-target compounds, we envisaged that targeting a phosphorylating tau kinase (i.e. GSK-3 $\beta$ ) and the tau aggregation process could be a favorable approach for the treatment of AD. Looking at the literature, several GSK-3 $\beta$  inhibitors and several tau aggregation inhibitors share a common 5-membered heterocyclic structure. On this basis, we selected the 2,4-thiazolidinedione (TZD) scaffold, and we develop a library of 35 5-arylidene-TZD derivatives (**1-35**, Figure 2.1), through a simple solvent-free Knoevenagel condensation, performed under microwave irradiation.



**Figure 2.1.** General chemical structure of dual GSK-3 $\beta$  and tau aggregation inhibitors **1-35**.

2. Building on the theranostic approach, in the second project we aimed to develop fluorescent bivalent ligands, with combined therapeutic and diagnostic properties for Alzheimer's disease. These bivalent compounds could be able, in principle, to stain A $\beta$  and tau protein aggregates and to inhibit the protein aggregation process. Thus, we designed and synthesized a library of dimeric compounds consisting

of two protein recognition motifs (PRM) joined via appropriate spacers. As PRM, we selected the TZD scaffold, while six different lipophilic and aromatic groups were selected as linkers. Moreover, in order to expand the structure-activity relationships, and to improve the drug-likeness of our compounds, we inserted three different substituents on the nitrogen of the TZD. The aim of these substitutions was to understand if different degrees of protonation could influence the interaction of our compounds with fibrillar structures and their fluorescence properties, as well their physicochemical properties. The combination of four TZD-derivatives with six linkers, allow us to develop a combinatorial library of 24 bivalent derivatives (**36-59**, Figure 2.2).



**Figure 2.2.** General chemical structure of the bivalent derivatives **36-59**.

3. The aim of the third project was the optimization of a previously identified antiprion compound, i.e. compound 1 (Figure 2.3). Compound 1 is a hybrid molecule, composed of a phenothiazine and a 7-chloroquinoline moieties, joined by a hydrazone linker. After the discovery of compound 1 as promising hit compound for prion diseases, we wanted to improve its drug-likeness properties, with a focus on its solubility. Thus, we designed and synthesized a small library of five derivatives (**60-64**, Figure 2.3), in which the nitrogen of the phenothiazine was substituted with five different solubilizing groups. Importantly, the solubilizing groups were carefully selected among those more frequently used for the optimization of CNS drugs.



**Figure 2.3.** Chemical structures of Compound 1 and its derivatives **60-64**.



## Chapter III

Tau centric multi-target approach for Alzheimer's disease:

development of first-in-class dual GSK-3 $\beta$

and tau-aggregation inhibitors

### **3.1 The “multi-target-directed ligand” approach in Alzheimer’s disease**

Alzheimer’s disease is one of the most challenging area in the drug discovery field. The tremendous difficulty in developing effective drugs has been attributed to several factors. First, despite significant advances in understanding its etiology, we still lack a detailed understanding of the causal roles and the interactions between them.<sup>108</sup> Second, as for any drug targeting the CNS, AD drugs must cross the blood brain barrier (BBB) and reach their targets at a concentration sufficient to exert the desired effect. However, it is estimated that the 98% of systemically administered small molecules do not possess the physicochemical properties for an optimal brain exposure.<sup>109</sup> Moreover, these drugs must be non-toxic or prone to developing drug-drug interactions, as elderly people show multiple comorbidities and concomitant treatments. Finally, the lack of proper biomarkers for earlier diagnosis and follow-up of disease progression, lead to inadequate trials design and to the administration of the drug candidates too late in the course of the cognitive decline, leading to a higher risk of clinical failure.<sup>36</sup>

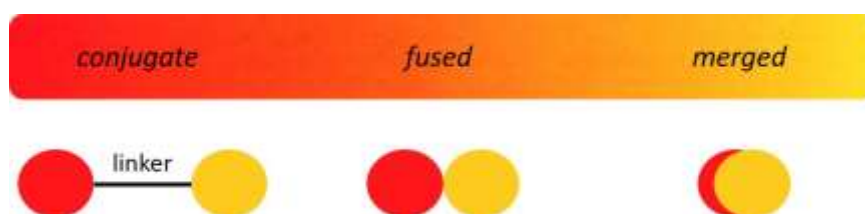
Fundamentally, the therapeutic paradigm “one compound-one target” has failed so far. AD, as many other neurodegenerative diseases, have a multifactorial nature that can hardly be “cured” by the specific modulation of a single target. The multifactorial processes leading to neurodegeneration involve multiple signaling pathways, therefore, there is a growing consensus that such a multi-factorial disease is approached more successfully with a polypharmacological strategy.<sup>110</sup> This strategy can be achieved by combination therapies consisting of several single-target specific drugs (polytherapy), or by using a single multi-target drug that addresses several biological targets and produces additive or synergistic effects. In the second case, compounds that are effective in treating complex diseases because of their ability to interact with multiple targets responsible for the disease pathogenesis are defined “multi-target-directed ligands” (MTDLs).<sup>72, 111, 112</sup>

The development of MTDLs offers many advantages over combination therapies, resulting in a reduction in: treatment complexity, drug side effects, pharmacokinetic complexity, and drug-drug interactions; while increasing the patient compliance. Indeed, non-compliance with prescribed medication regimens represents a general



problem for effective treatments, especially for forgetful AD patients. Consequently, a simplified therapeutic regimen may increase treatment adherence. Furthermore, the therapeutic efficacy achieved through the modulation of multiple targets, and the resulting synergies, may allow to lower the concentration of the active compound. This, in turn, can reduce side effects mediated by full engagement on the individual targets, without losing the therapeutic efficacy, and it can broaden the therapeutic window. Finally, the development of MTDLs can also offer economic advantages, since the clinical development of a single compound requires less clinical trials than multiple single-target drugs.

MTDLs can be classified in three general types, according to their molecular and pharmacophore architecture, as impeccably described by Morphy and Rankovic (Figure 3.1).<sup>113</sup>



**Figure 3.1.** Different strategies in the design of MTDLs (adapted from Morphy, 2005).<sup>113</sup>

The simplest way of combining multiple activities is the conjugation of pharmacophores with a linking group. Such linked pharmacophores usually show large molecular weights. Conjugation of two (or more) individual pharmacophores without a linking group produces fused multiple ligands that are also prone of having high molecular weights and high lipophilicity. Finally, the most elegant, demanding but also most fruitful way to design small molecules that modulate more than one target is merging their pharmacophore. Particularly, in such merged MTDLs, the key features required for the interaction with the targets are combined in one single pharmacophore.

## **3.2 Target selection for a MTDL drug discovery project: GSK-3 $\beta$ and tau protein**

To discover and to develop effective MTDLs, a central issue is the selection of combinations of targets that might produce additive effects, or even synergies. In principle, every combination of targets is thinkable, however, the chemical feasibility of the multi-target ligand must be taken into account. Clearly, the design of a MTDL is easier for highly related targets -sharing similarity in their binding sites-, while it is more challenging for unrelated targets. Generally speaking, the target selection process is particularly complicated in the case of multifactorial disorders, such as AD, in which there is a confusing plethora of putative targets, with no one with a clear validation.

The following paragraphs will describe two interrelated targets, which were selected by us for the development of new MTDLs towards AD: GSK-3 $\beta$  and tau protein.

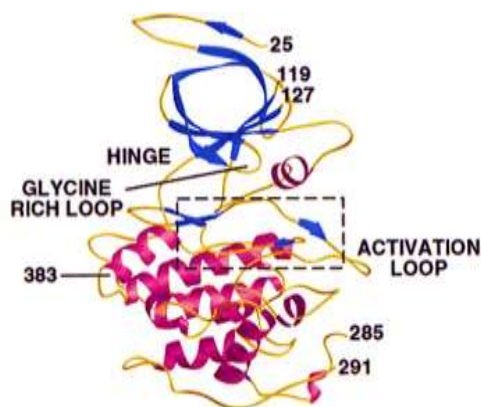
### **3.2.1 GSK-3 $\beta$ : a crucial kinase for AD**

Glycogen synthase kinase-3 (GSK-3) is the archaic name of two genomically independent encoded isozymes, GSK-3 $\alpha$  and GSK-3 $\beta$ , which functions as multifunctional serine/threonine kinase in metabolic signaling pathways, cytoskeletal organization, and transcriptional control. The two human GSK-3 isoenzymes are encoded by two different genes located on chromosome 3 (GSK-3 $\beta$ ) and 19 (GSK-3 $\alpha$ ), but they share 98% sequence identity in the catalytic domain, and 84% overall. GSK-3 $\beta$  is composed of 420 aa translating into a 47-kDa protein, whereas the 483 aa of GSK-3 $\alpha$  result in the larger 51-kDa protein, with the major difference being a glycine-rich N-terminal domain.<sup>114</sup>

GSK-3 $\beta$  is widely expressed in all tissues, but mainly in the developing and adult brain, and it is most abundant in neurons. Particularly, in adult neurons it is predominantly found in perikarya and proximal portion of the dendrites; while during development it is also localized in axons.<sup>115</sup> During embryonic development, GSK-3 $\beta$  acts as inhibitory

component of the Wnt signaling pathway in cell proliferation. Indeed, disruption of the murine GSK-3 $\beta$  gene resulted in embryonic lethality caused by severe liver degeneration.<sup>116</sup> Brain GSK-3 $\beta$  is proposed to be involved in response to cellular stress, regulation of long-term memory, apoptosis, and in maintenance of synaptic plasticity.<sup>117</sup> Moreover, a direct role of GSK-3 $\beta$  in long-term potentiation and long-term depression was also proposed.<sup>118, 119</sup>

The crystal structure of GSK-3 $\beta$  was determined in 2001, and provided insights into its catalytic mechanism.<sup>120-122</sup> GSK-3 $\beta$  has the typical two-domain kinase fold, with a  $\beta$ -strand domain in the N-terminal, and a  $\alpha$ -helical domain at the C-terminal end. The ATP-binding site is at the interface of the  $\alpha$ -helical and  $\beta$ -strand domains, and is bordered by the glycine-rich loop and the hinge region, while the activation loop runs along the surface of the substrate binding groove (Figure 3.2).



**Figure 3.2.** Structure of GSK-3 $\beta$ . The N-terminal domain (blue) correspond to the  $\beta$ -strand domain and encompasses residue 25-138. The  $\alpha$ -helical domain (magenta) corresponds to residues 139-349. The key features of the kinase fold such as hinge region, glycine-rich loop and activation loop are indicated (adapted from ter Haar, 2001).<sup>122</sup>

Generally, to enable the enzymatic activity of a serine/threonine kinase, its  $\beta$ -strand and  $\alpha$ -helical domains must be aligned in a catalytically active conformation.<sup>123</sup> For this purpose, most kinases need to be phosphorylated on their activation loop, at one or two specific amino acid residues, such as Thr or Tyr. The phosphate group can be

accommodated into an anionic binding site, thus the electrostatic interactions between the phosphate ion and the positively charged pocket, drive the proper alignment of the two catalytic domains.

However, GSK-3 $\beta$  shows some peculiarities, and it is considered an unusual kinase. In GSK-3 $\beta$ , despite the absence of any phosphorylation, the activation loop is arranged similarly to the correspondent one in the phosphorylated active form of serine/threonine kinases. Thus, it seems that GSK-3 $\beta$  may adopt a catalytically active conformation without phosphorylation of the activation loop. However, as other kinases, GSK-3 $\beta$  presents an anion binding site, pointing towards the activation loop. Hence, GSK-3 $\beta$  seems to depend on the same phospho-driven mechanism for optimally orientate the catalytic domains, but the phosphate group is not provided from its activation loop. The explanation of this came from the unusual behavior of GSK-3 $\beta$  for “primed” substrates, i.e. substrates pre-phosphorylated by a priming kinase.<sup>124</sup> However, it is important to consider that prior phosphorylation of the substrate is not always required, and not all GSK-3 $\beta$ 's substrates undergo primed phosphorylation. Moreover, like other kinases, GSK-3 $\beta$  can be phosphorylated on its activation loop, at the level of Tyr216, but such phosphorylation is not mandatory for kinase activity. Another peculiarity of GSK-3 $\beta$  is that its activity can be modulated by phosphorylation at Ser9, in the N-terminal domain. Phosphorylation of Ser9 creates a primed pseudo-substrate, thus preventing access of any other substrate into the substrate binding groove.<sup>121</sup>

### *3.2.1.1 The role of GSK-3 $\beta$ in AD*

In the nineties, when the tau-based hypothesis of AD was postulated, intensive research programs try to understand the mechanisms of aberrant tau phosphorylation. These lead to the discovery of two kinases, initially called TPK-I and TPK-II, responsible for in vivo tau hyperphosphorylation.<sup>125</sup> After cloning, they were identified as GSK-3 $\beta$  and cyclin dependent kinase 5 (CDK-5).<sup>126</sup> Then, ten years ago, the GSK-3 $\beta$  hypothesis for AD came out.<sup>127</sup>

Particularly, the GSK-3 $\beta$  hypothesis ascribe to this key kinase the link between amyloid and tau cascade. Moreover, it has been suggested that long-term aberrant Wnt or

insulin signaling result in increased GSK-3 $\beta$  activity, leading to the AD fatal events. Such hypothesis gained relevance after growing evidence suggested a brain insulin signaling deficit as the cause of AD.<sup>128</sup>

Today there is no doubt about the GSK-3 $\beta$  up-regulation in the brains of AD patients, and it is well-recognized that increased in GSK-3 $\beta$  activity may induce increased  $\beta$ -amyloid formation and toxicity of senile plaques. On the other hand, A $\beta$  accumulation has been reported to induce GSK-3 $\beta$  activity.

In accordance with the cholinergic deficit, it was also found that GSK-3 $\beta$  is able to reduce acetylcholine synthesis.<sup>129</sup> Moreover, GSK-3 $\beta$  is a key mediator of apoptosis, thereby directly contributing to neuronal loss.<sup>130</sup> Evidence also suggest that GSK-3 $\beta$  can phosphorylate and inhibit cAMP responsive element-binding protein, a universal modulator of memory,<sup>131</sup> and that can promote actin and tubulin assembly, processes required for synaptic reorganization during memory formation.

As well as being implicated in the core pathogenic events of AD (eg. increased formation of A $\beta$ , tau hyperphosphorylation, and memory impairment), it has been hypothesized that GSK-3 $\beta$  might also play a role in inflammatory processes. In the periphery, it is known that the regulation of GSK-3 $\beta$  activity is critical for inflammatory cell differentiation, inflammatory cell migration, and the secretion of pro-inflammatory cytokines. However, little is known about the function of GSK-3 $\beta$  in the cerebral inflammatory response.<sup>127</sup>

Taken together, all these observations point directly to GSK-3 $\beta$  as an excellent target to effectively treat AD. Moreover, in various cell cultures, in invertebrate, and in mammalian models of AD, increasing in GSK-3 $\beta$  activity leads to the hyperphosphorylation of tau, increased A $\beta$  generation, and deficit in learning and memory, together with neurodegeneration. Most importantly, inhibiting GSK-3 $\beta$  activity reverse some of the pathological effects.<sup>132, 133</sup>

In summary, GSK-3 $\beta$  is a validated pharmacological target for AD, and mild GSK-3 $\beta$  inhibitors may be real drug candidates in the next future. Indeed, the last decades has witnessed an intensive research on GSK-3 $\beta$  inhibitors, with some small molecule candidates reaching clinical trials.<sup>134</sup>

### 3.2.1.2 GSK-3 $\beta$ inhibitors

Over the past ten years, a number of chemically diverse families of GSK-3 inhibitors have been discovered. These compounds include inhibitors isolated from natural sources, cations, synthetic small molecules, and also peptides. In the AD drug discovery field, in particular, several small molecules GSK-3 $\beta$  inhibitors have been reported, showing different potency of in vitro inhibition, different selectivity, and different enzyme binding mode. Such inhibitors, with very different chemical structures, have also proven to ameliorate cognitive deficit and some pathological features such as neuronal death,  $\beta$ -amyloid levels, and tau phosphorylation in different specific AD transgenic models. Indeed, over the years, different methodologies to guide the design of new GSK-3 $\beta$  inhibitors, to enhance their potency and to optimize their drug-like properties have been described. However, it is now increasingly recognized that a moderate inhibition of GSK-3 $\beta$ , particularly for long-term treatments, provides more favorable outcome than strong, complete inhibition. Based on this, the main challenge in the design of GSK-3 $\beta$  inhibitors, to date, is the kinase selectivity, more than the potency.<sup>134</sup>

Lithium was the first “natural” GSK-3 $\beta$  inhibitor discovered, and it is an ATP non-competitive inhibitor.<sup>135</sup> Lithium is a mood stabilizer long used in treatment of bipolar disorders. Lithium inhibit GSK-3 $\beta$  directly by competition with magnesium ions,<sup>136</sup> and indirectly by enhancing serine phosphorylation and autoregulation.<sup>137, 138</sup> The use of lithium as AD therapy has been tested in several animal models, demonstrating that inhibition of GSK-3 $\beta$  with lithium inhibits A $\beta$ -induced neurodegeneration of cortical and hippocampal primary neurons.<sup>139</sup> Lithium was also able to block the accumulation of A $\beta$  peptides in the brains of mice overexpressing APP,<sup>133</sup> and to prevent tau phosphorylation in several mouse models of tauopathies.<sup>132, 140</sup> In most of these models, lithium was able to prevent the development of tau pathology, but only when administered early in disease progression. However, lithium could not inhibit only GSK-3 $\beta$ , but also several other enzymes, that is why researchers focused their attention on the discovery of more selective GSK-3 $\beta$  inhibitors.<sup>141</sup> Moreover, lithium entered several clinical trials for AD, but they were all discontinued because of toxic side effects in some elderly patients.<sup>142</sup>

Interestingly, other metal ions such as beryllium, zinc, mercury, and copper are potent GSK-3 $\beta$  inhibitors, and they are even more potent than lithium.<sup>143, 144</sup>

Beside cationic inhibitors, much effort was done in the discovery and development of small molecules GSK-3 $\beta$  inhibitors in the last years. Nowadays, several chemical families of GSK-3 $\beta$  inhibitors have emerged, including great chemical variability. Some GSK-3 $\beta$  inhibitors have synthetic origins, but others have been derived directly or indirectly from natural molecules, obtained in particular from the marine environment.

Most of the newly reported GSK-3 $\beta$  inhibitors act via an ATP-competitive mechanism of action.

The first synthetic small molecule GSK-3 $\beta$  inhibitors reported were the purine analogs aminopyrimidines. The potent inhibitors CHIR98014, and CHIR99021 (Figure 3.3) inhibit GSK-3 $\beta$  within the nanomolar concentration range.<sup>145</sup>

Highly selective GSK-3 $\beta$  inhibitors were developed by GlaxoSmithKline. The arylindolemaleimides SB-216763 and SB-415286 (Figure 3.3) show an IC<sub>50</sub> within the low nanomolar range.<sup>146</sup> Several studies demonstrated the neuroprotective effects of SBs against several pro-apoptotic conditions. Moreover, the therapeutic activity of SBs has been further tested in several in vivo models. In an AD model of mice injected with A $\beta$  peptide, SB216763 reduced A $\beta$  neurotoxic effects, including reduction in tau phosphorylation, caspase-3, and the activity of the stress activated kinase JNK. However, SB216763 also produced neurodegenerative-like effects and behavior deficits in healthy mice.<sup>147</sup> This demonstrated that over-inhibition of GSK-3 $\beta$  may result in conditions that prevent neurons from operating normally.

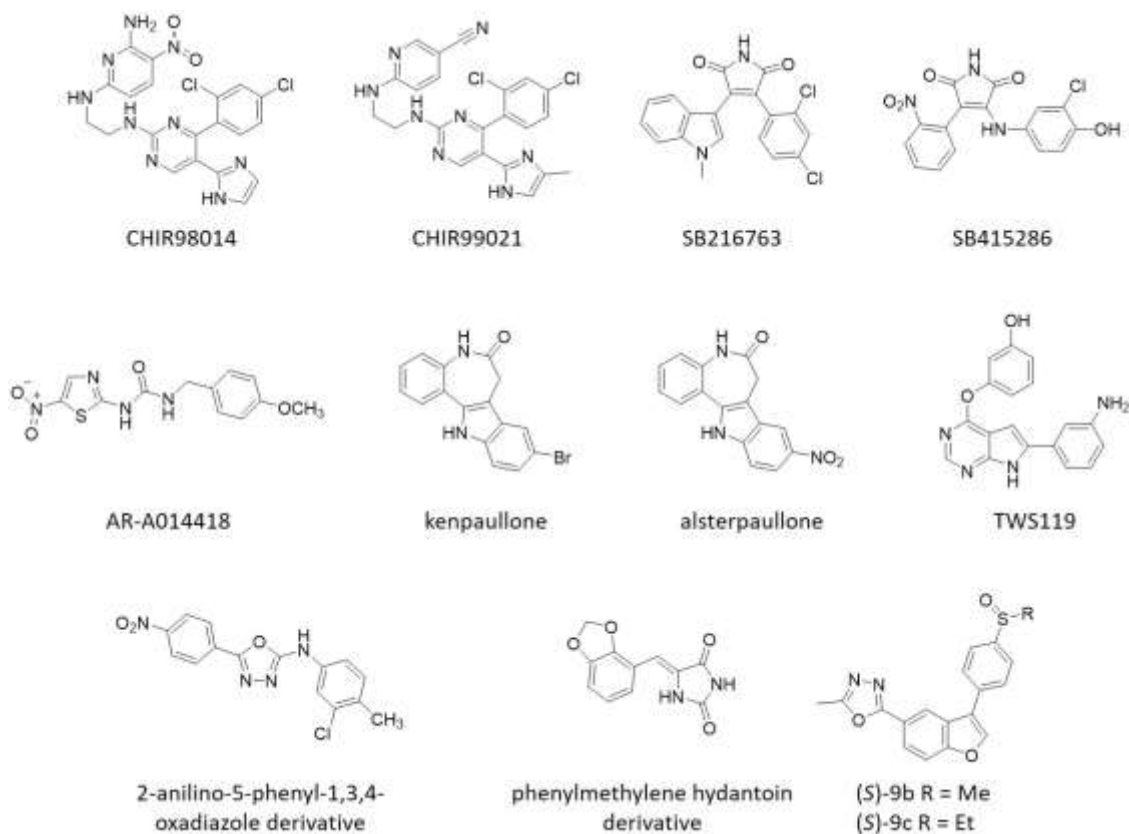
Another selective GSK-3 $\beta$  inhibitor was developed by AstraZeneca, the amino thiazole AR-A014418 (Figure 3.3).<sup>148</sup> AR-A014418 reduced levels of aggregated insoluble tau in the brainstem of transgenic mice overexpressing mutant human tau; it also attenuated motor neuron death and improved cognition in an ALS-transgenic mouse model.<sup>149</sup> Unexpectedly, however, AR-A014418 showed no effect on tau phosphorylation in the cortex or hippocampus in a postnatal rat model.<sup>150</sup> A structurally related compound, AZD-1080 entered into clinical trials phase I for AD in 2006, but the development has been discontinued.

The group of paullone compounds, in particular kenpaullone and alsterpaullone, are widely used GSK-3 $\beta$  inhibitors (Figure 3.3). Paullones are fused tetracyclic compounds that inhibit both GSK-3 $\beta$  and CDKs within the nanomolar concentration range.<sup>151, 152</sup> Kenpaullone decreased A $\beta$  production in cells overexpressing APP,<sup>153</sup> while alsterpaullone was shown to reduce tau phosphorylation in cultured neurons.<sup>150, 152</sup> However, reports of kenpaullone or alsterpaullone in in vivo systems are limited. One study demonstrated the ability of alsterpaullone to reduce tau phosphorylation in the rat brain.<sup>150</sup> In 2003, also 4,6-disubstituted pyrrolopyrimidines were reported as GSK-3 $\beta$  inhibitors, with TWS119 being the most active compound (Figure 3.3).<sup>154</sup>

In 2010, a novel class of GSK-3 $\beta$  inhibitors was discovered using combined ligand- and structure-based virtual screening. The two most potent and selective validated hits were a 2-anilino-5-phenyl-1,3,4-oxadiazole, and a phenylmethylene hydantoin (Figure 3.3), both showing nanomolar affinity and selectivity towards GSK-3 $\beta$ .<sup>155</sup> These two compounds were further evaluated for their in vivo (mice) abilities to enhance hepatic glycogen reserves and to cross the BBB, with the oxadiazole analogue showing high in vivo activity and excellent BBB permeability. The oxadiazole scaffold was already been proposed in 2009, when the 2-{3-[4-(Alkylsulfinyl)phenyl]-1-benzofuran-5-yl}-5-methyl-1,3,4-oxadiazole derivatives (S)-9b and (S)-9c (Figure 3.3) exhibited highly selective and potent inhibitory activity against GSK-3 $\beta$ , but also good pharmacokinetic profiles. In addition, both compounds, when orally administered to mice, display a significant inhibition of cold water stress-induced tau hyperphosphorylation in mouse brain.<sup>156</sup>

However, hydantoin and oxadiazole derivatives are not the only GSK-3 $\beta$  inhibitors with a five-membered heterocyclic scaffold reported in the literature. Indeed, several other five-membered heterocyclic scaffold were identified, such as pyrrolidin-2-ones,<sup>157</sup> and iminothiazolidin-4-one<sup>158</sup>.



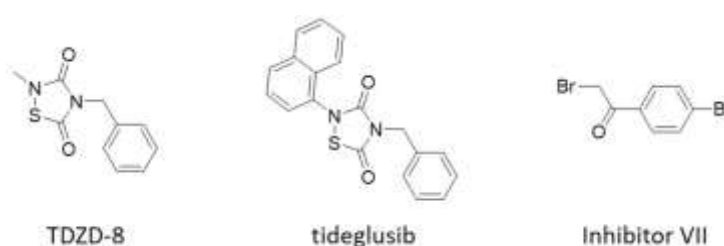


**Figure 3.3.** Chemical structures of ATP-competitive GSK-3 $\beta$  inhibitors.

Collectively, all these studies confirmed the importance of GSK-3 $\beta$  for maintenance of normal neuronal functions, but also demonstrated its important role in the etiology of AD. However, the general poor ability of GSK-3 $\beta$  ATP-competitive inhibitors to discriminate among a panel of kinases, represents a serious drawback for drug development. Indeed, GSK-3 $\beta$  non-ATP competitive inhibitors are likely to be more selective, since they should bind to unique regions within the kinase, providing a more subtle modulation of kinase activity, than simply blocking ATP entrance.

There are two different families of reported GSK-3 $\beta$  non-ATP competitive inhibitors. The first is the thiadiazolidindione family (TDZDs), described in 2002.<sup>159</sup> Two members of this family, TDZD-8 and tideglusib (Figure 3.4), have achieved particular relevance in the field. TDZD-8 is now commercially available from different sources, and it has been one of the most useful pharmacological tool in the chemical genetic approach followed by many scientists to explore GSK-3 $\beta$  functions. While tideglusib, described as an irreversible inhibitor of GSK-3 $\beta$ ,<sup>160</sup> reaches phase II of clinical development for AD.<sup>161</sup>

The second family of compounds known as GSK-3 $\beta$  non-ATP competitive inhibitors is the halomethylketones (HMKs) derivatives, reported as the first irreversible inhibitors of this enzyme.<sup>162</sup> HMKs show IC<sub>50</sub> values in the low micromolar range, they are able to decrease tau phosphorylation in cell cultures, show good kinase and neurotransmitter selectivity, and they are also able to cross the BBB.<sup>162, 163</sup> The HMK-derivative Inhibitor VII (Figure 3.4) is commercially available, confirming the importance of this series of compounds as pharmacological tools for the study of GSK-3 $\beta$  physiology and pathology.



**Figure 3.4.** Chemical structures of non-ATP competitive GSK-3 $\beta$  inhibitors.

Another strategy to achieve selectivity on GSK-3 $\beta$  is to target the priming substrate site.<sup>164</sup> Substrate competitive inhibitors can fulfill the requirement for selectivity and allow fine tuning of the degree of inhibition. To date, there are three families of compounds that binds GSK-3 $\beta$  through competition with the substrate: small peptides such as L803-mts,<sup>165</sup> heterocyclic compounds such 5-imino-1,2,4-thiadiazoles,<sup>166</sup> and the marine alkaloid manzamine<sup>167</sup> (Figure 3.5).

Finally, allosteric modulators of GSK-3 $\beta$  emerged as promising pharmacological tools for research. The heterocyclic compound VPO.7<sup>168</sup> and the marine sesquiterpene palinurin<sup>169</sup> bind to different allosteric sites on GSK-3 $\beta$  surface, with subtle modulation of its activity.

Taken together, all these results offer new opportunities for the design and development of new, selective GSK-3 $\beta$  inhibitors.

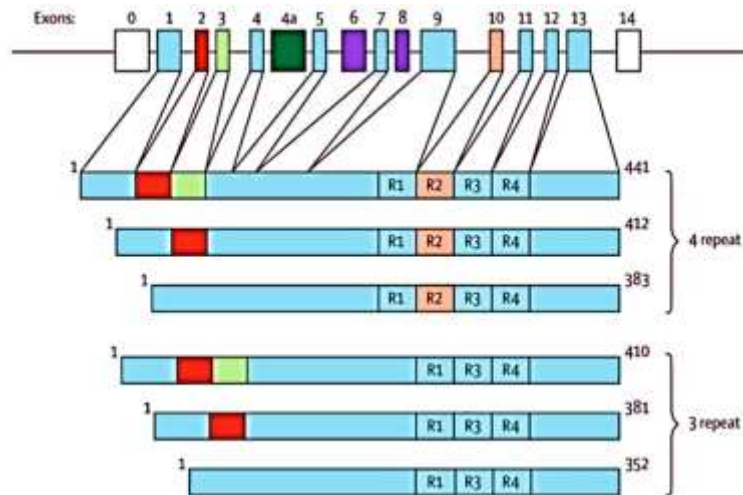
### 3.2.2 Tau protein as a promising target for AD

Tau protein was one of the first microtubule associated proteins (MAPs) to be characterized, named by Marc Kirschner in 1975, when his team was searching for factors that promote the self-assembly of tubulin into microtubules (hence tau = tubulin binding protein).<sup>64</sup> This started a line of research centered on the cell biological role of tau as a stabilizer of microtubules in neurons and other cells, with important roles in cell differentiation and polarization. A second line of tau research was triggered by basic neurological research to identify the components of the abnormal protein deposits found in the brains of AD patients. One of them, A $\beta$ , was identified as the core protein of extracellular amyloid plaques by molecular cloning, and the other, tau, as the core of intracellular fibrillary tangles by antibody reactivity. These discoveries led to concerted efforts by cell biologists and neuroscientists to elucidate the physiological and pathological properties of tau.<sup>170</sup>

Tau protein is the major microtubule associated protein of a normal mature neuron. The other two neuronal MAPs are MAP1 and MAP2. Tau is found as six molecular isoforms in human brain, coded by a single gene (*MAPT*) on chromosome 17, and generated by alternative splicing of its pre-mRNA.<sup>171</sup>

These six tau isoforms differ according to the contents of three (3R) or four (4R) tubulin binding domains (repeats, R) of 32 or 32 amino acids in the C-terminal part of tau protein, and one (1N), two (2N), or no inserts (0N) of 29 amino acids each in the N-terminal portion. These isoforms, which vary in size from 352 to 441 amino acid residues, are related to the presence or absence of sequences encoded by exons 2, 3, or 10 (Figure 3.5).

The 2N4R tau is the largest size human brain tau with a total of 441 amino acids (tau441) in length. The smallest size tau isoform, lacking both the two amino terminal inserts and the extra microtubule binding repeat (0N3R, tau352), is the only form that is expressed in fetal human brain.



**Figure 3.5.** Representation of the MAPT gene and the six tau isoforms expressed in human adult brain (modified from Goedert, 2017).<sup>172</sup>

The overall amino acid composition of tau is unusually hydrophobic, that is why tau does not adopt the compact folded structure typical of most cytosolic proteins. Indeed, evidence from several biophysical methods (circular dichroism, NMR and small angle X-ray scattering), show that tau is “natively unfolded” or “intrinsically disordered”.<sup>173, 174</sup> This means that the polypeptide chain is highly flexible and mobile, there is only a low content of secondary structures ( $\alpha$ -helix,  $\beta$ -strand, poly-proline II helix), which are also transient.

Tau is subject to a wide range of post-translational modifications, including phosphorylation, isomerization, glycation, nitration, addition of  $\beta$ -linked N-acetylglucosamine, acetylation, oxidation, polyamination, sumoylation, and ubiquitylation.<sup>175</sup> Phosphorylation is the most commonly described post-translational tau modification. Tau contains 85 putative phosphorylation sites, including 45 serine, 35 threonine, and five tyrosine residues, which comprise 53%, 41%, and 6% of the phosphorylatable residues on tau, respectively. Given the large number of potential phosphorylation sites, it is not surprising that phosphorylation has a profound impact on tau physiological function.<sup>176</sup> Moreover, tau is also a substrate for the ubiquitin-proteasome system, and for chaperone-mediated autophagy.<sup>177</sup>

To date, the only established function of tau is the promotion of the assembly of tubulin into microtubules, and the stabilization of their structure.<sup>64</sup> As highlighted before, the biological activity of tau is regulated by the degree of its phosphorylation. Normal brain tau contains 2-3 moles of phosphate per mole of the protein,<sup>178</sup> which appears to be optimal for its interaction with tubulin and the promotion of microtubule assembly. However, also the alternative splicing affects the biological activity of tau. Indeed, the extra repeat in the 4R tau and the amino terminal inserts (N1 and N2) enhance the binding of tau to tubulin, making 2N4R tau and 0N3R tau respectively, the most and the least effective in promoting microtubule assembly.<sup>179</sup>

Tau protein is also able to interact with other cytoskeletal components, such as spectrin and actin filaments, which may allow tau-stabilized microtubules to interconnect with neurofilaments that restrict the flexibility of the microtubule lattices. Another protein that can interact with tau is a peptidyl-prolyl cis/trans isomerase Pin 1. Pin 1 regulates functions of tau and APP, and it is important for protection against the degeneration that occurs during the ageing process. Finally, tau protein may interact with intracellular membranous elements such as the mitochondria, through its N-terminal projection.<sup>180</sup>

### *3.2.2.1 Tau protein in AD*

In Alzheimer's disease, the normal role of tau protein is ineffective to keep the cytoskeleton well organized in the axonal process, because tau loses its ability to bind microtubules. This abnormal behavior is promoted by conformational changes and misfolding in the normal structure of tau, leading to its aberrant aggregation into fibrillary structures, called neurofibrillary tangles (NFTs), inside the neurons. Importantly, neurofibrillary degeneration of abnormally phosphorylated tau not only occurs in AD brains, but is also seen in a family of related neurodegenerative disease called tauopathies. Examples of tauopathies are: fronto-temporal dementia with Parkinsonism linked to chromosome 17 (FTDP-17) caused by tau mutations, Pick disease, corticobasal degeneration, dementia pugilistica, and progressive supranuclear palsy (PSP).<sup>181</sup>

The mechanisms by which tau protein becomes a non-functional entity are still in debate. Abnormal post-translational modifications are proposed to be the main cause of this failure.<sup>3, 182</sup> Particularly, abnormal tau phosphorylation has been proposed to cause the loss of its normal function, and the gain of pathological features.

At cellular level, abnormal phosphorylation of tau introduces alterations in several processes which are directly regulated by the organization of the microtubule network. As already described, in a normal mature neuron, tubulin is present in over 10-fold excess of tau, indeed almost all tau protein is bounded to microtubules. Conversely, in AD neurons, abnormally phosphorylated cytosolic tau neither binds to tubulin, nor promotes microtubule assembly. Instead, hyperphosphorylated tau inhibits the assembly and disrupt the microtubule organization.<sup>183</sup> Moreover, it was reported that hyperphosphorylated tau disengages normal tau from microtubules into the cytosolic phase, and also removes MAP1 and MAP2 from microtubule lattice.<sup>184</sup> Importantly, this toxic feature of tau protein appears to be due only by its abnormal phosphorylation state, as dephosphorylation of hyperphosphorylated tau rescues this protein to perform its normal tasks.<sup>185</sup>

Tau protein is a natively unfolded protein, however, under pathological conditions, it becomes hyperphosphorylated and assembles into filaments, with the amino-terminal half and the carboxy-terminus forming the so-called fuzzy coat of the filaments. Moreover, tau filaments acquire a cross- $\beta$  structure, characteristic of all amyloid filaments.<sup>186</sup> The tau aggregation cascade, once initiated, is self-replicating, leading to the accumulation of NFTs and to neuronal death.<sup>187, 188</sup> NFTs have historically been considered the main hallmark in AD; however, they do not appear to be the main toxic species. Indeed, it is likely that intermediate tau species that form between tau monomers and NFTs (i.e. tau oligomers) are responsible for the onset of the disease.

Tau oligomers levels have been shown to be elevated and correlate with the onset of clinical symptoms in AD brains.<sup>189-191</sup> Additionally, when administered to wild-type mice, tau oligomers, but not monomers or tau fibrils, induce synaptic and mitochondrial dysfunction and cognitive deficits.<sup>192</sup> Experimentally, the fibrillization process does not occur spontaneously, therefore the mechanism of aggregation onset in AD has remained unknown. Evidence suggest that tau oligomers may be the most

efficient seeds for tau aggregation, through a process called oligomer-nucleated conformational induction, in which the tau monomer is first converted into an oligomeric state prior to the formation of fibrils. Post-translational modifications and the formation of disulfide bridges increase the ability of tau to form oligomers.<sup>193, 194</sup>

The seeding of tau with brain-derived oligomers results in highly toxic species, capable of propagating from affected to unaffected regions in cells and mice; however, fibrils are not able to propagate or induce toxic effects. All these results suggest a prion-like mechanism of the spread of tau pathology dependent upon oligomeric tau.<sup>69</sup>

All in all, these data suggest the importance of the tau cascade in the pathogenesis of AD. Indeed, tau cascade is now being recognized as a promising target for the development of drug candidates for the treatment of such disease.<sup>195-197</sup> Particularly, two major approaches are distinguishable for addressing tau aggregation. The first is the search for inhibitors of kinases that phosphorylate tau, as abnormally phosphorylated tau aggregates more readily. While the second approach is the search for direct inhibitors of the tau aggregation process.<sup>198</sup>

#### *3.2.2.2 Tau aggregation inhibitors*

Several research groups have taken advantage of the ability of full length tau or shorter tau fragments to form fibrils under defined conditions, and have conducted experiments to identify compounds that inhibits this fibrillization process. Importantly, the inhibition of protein-protein interactions occurring during fibril assembly is considered quite challenging with small molecules, due to the large protein surface involved. Nevertheless, a number of structurally unrelated compounds have been identified during the years, though many with features which are not consistent with drug-like candidates.

One of the first tau aggregation inhibitor reported was the phenothiazine dye methylene blue (MB, Figure 3.6).<sup>199</sup> MB was shown to partially disrupt the structure of isolated PHFs, and subsequent studies showed that MB could affect tau multimerization. Interestingly, MB was progressed into clinical trials for AD.<sup>200</sup>

Preliminary results of a phase II clinical trial indicated a lower rate of decline of cognitive functions compared to placebo. MB was orally administered in a double-blind, randomized parallel design phase II trial to 321 participants over 84 weeks. However, the blue urine staining properties of MB were not matched in the placebo group.<sup>201</sup> Lately, a newly developed form of the MB moiety, the leuco-methylthioninium bis(hydromethanesulphonate) (LMTM, Figure 3.6), was reported as tau anti-aggregating compound. LMTM has been taken forward for phase III clinical trial,<sup>202</sup> as it is able to stabilize the reduce form of the MT moiety in the solid state. Following absorption, the dissociated MT moiety is distributed and excreted in an equilibrium between oxidized and reduced forms, depending on the local pH and redox environment. After an 18-months phase III clinical trial conducted on 800 mild AD patients, it was suggested that LMTM might be effective as monotherapy, and that 4 mg twice a day may serve as well as higher doses.<sup>203</sup> However, a further suitably randomized trial is required to test this hypothesis.

Benzothiazole share with phenothiazines the characteristic positive charge and extensive aromatic conjugation. Indeed, benzothiazole-based inhibitors with excellent inhibitory potencies have been reported, such as the cyanine dye N744 (IC<sub>50</sub> 300 nm, Figure 3.6).<sup>204, 205</sup> An analysis of the time-course and dose-dependency of N744 suggested that it inhibits tau filament extension but not its nucleation. However, a loss of inhibitory activity with N744 has been reported at high concentrations, caused by the aggregation of the compound.<sup>204</sup>

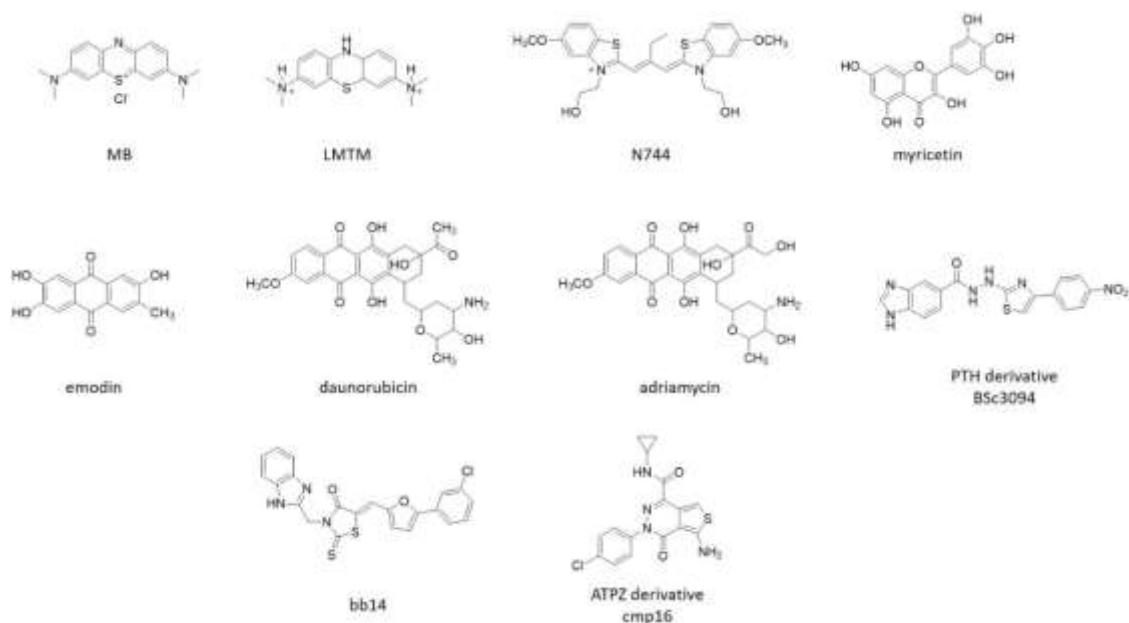
A number of other aggregation inhibitors have yielded promising preclinical results in decreasing tau toxicity.

In a small screen of 42 compounds, in 2005, Taniguchi et al. identified molecules from several chemical classes, able to inhibit fibrillization of full length tau, as proved by electron microscopy and thioflavin S (ThS) fluorescence.<sup>206</sup> These compounds included phenothiazines, polyphenols, and porphyrins. Particularly, myricetin (Figure 3.6) was reported as promising tau aggregation inhibitor (IC<sub>50</sub> = 1.2 μM), and the in vitro data indicate that it interferes with the elongation phase of fibril assembly.

Always in 2005, the Mandelkow research group conducted a large-scale screen of about 200,000 compounds, in an assay in which heparin promoted fibrillization of a



tau fragment composed only of three microtubule-binding repeats (termed K19) was monitored by ThS fluorescence.<sup>207</sup> A number of anthraquinones, including emodin, daunorubicin, and adriamycin (Figure 3.6), were identified as inhibitors of tau fibril formation. Anthraquinone derivatives were able to both preventing the formation of filaments, and dissolving preformed filaments. The abundant ring scaffolds in these compounds are thought to interfere with the formation of  $\beta$ -sheet structures. Moreover, anthraquinones do not interfere with native tau microtubule binding, and protect against cytotoxicity in cellular models of tauopathy.<sup>207</sup> Generally, anthraquinones could also induce disassembly of pre-formed tau fibrils, although in all cases the molecules were more effective in disaggregating the shorter tau fragments than the full length ones. Finally, emodin was demonstrated to reduce tau aggregates in N2a neuroblastoma cells over-expressing the K18 tau fragment containing an FTDL-17 mutation.<sup>208</sup> The same research group also demonstrated that certain N-phenylamines could inhibit the formation of tau aggregates and reduce pre-existing tau inclusions in the N2a cell model.<sup>208</sup>



**Figure 3.6.** Chemical structures of tau aggregation inhibitors.

Mandelkow team identified other two classes of tau aggregation inhibitors: phenylthiazolyl-hydrazides (PTHS, Figure 3.6) and rhodanines. Using a pharmacophore

model, a PTH compound was predicted to be active and was subsequently shown to prevent tau fibrillization.<sup>209</sup> Further medicinal chemistry efforts led to the synthesis of more active analogs, able to disassemble pre-existing K18 fibrils, and to prevent aggregation in the N2a cell model.

An additional rhodanine series of tau fibril inhibitors was identified.<sup>210</sup> In these experiments, rhodanine, thiohydantoin, thiooxooxazolidine, oxazolidinedione, and hydantoin were synthesized and screened for activity on tau aggregation inhibition and disaggregation of preformed tau aggregates. The rhodanine heterocycle appeared to be the most potent, highlighting the importance of the thioxo group. Moreover, the rhodanine derivative bb14 (Figure 3.6) prevented tau pathology development in a hippocampal slice model, as well as protected against Ca<sup>2+</sup> dyshomeostasis, dendritic spine loss, and cell death.<sup>211</sup>

Finally, a novel class of tau aggregation inhibitors was discovered: aminothienopyridazines (ATPZ).<sup>212</sup> ATPZ compounds effectively inhibit the formation of tau fibrils in vitro, similarly to MB, through a cysteine oxidation and the inhibition of the formation of disulfide linkages, rendering tau unable to fibrillize.<sup>213-215</sup> ATPZ derivative cmp16 (Figure 3.6) was also able to reverse the motor phenotype in a *C. elegans* tauopathy model.<sup>216</sup>

Tau protein has been considered for long times as an intractable drug target for small molecule drug discovery, due to the lack of a stable 3D structure. Indeed, for several years tau has been neglected by most small molecule drug design programs, and has been mostly targeted by specific monoclonal antibodies for immunotherapy. However, since tau is an intracellular protein, mainly localized in neurons, it is not clear whether antibodies will lead to efficacious treatments. Moreover, the economic cost of a potential immunotherapy for millions of patients with AD and, in general, tauopathies, will not likely be affordable for our society.<sup>217</sup>

Therefore, it is critical to explore alternative small molecule approaches targeting tau protein for the development of disease modifying drugs for AD. Altogether, the examples reported above, highlight that perceptible progress has been achieved after years of collective efforts aimed at deciphering the mode of action of tau aggregation

inhibitors, as well as developing compounds with improved pharmacokinetic properties. Importantly, all these efforts lead to the introduction of two tau aggregation inhibitors into clinical trials, i.e. MB and LMTM.<sup>37</sup>

### **3.3 Design of dual GSK-3 $\beta$ and tau aggregation inhibitors**

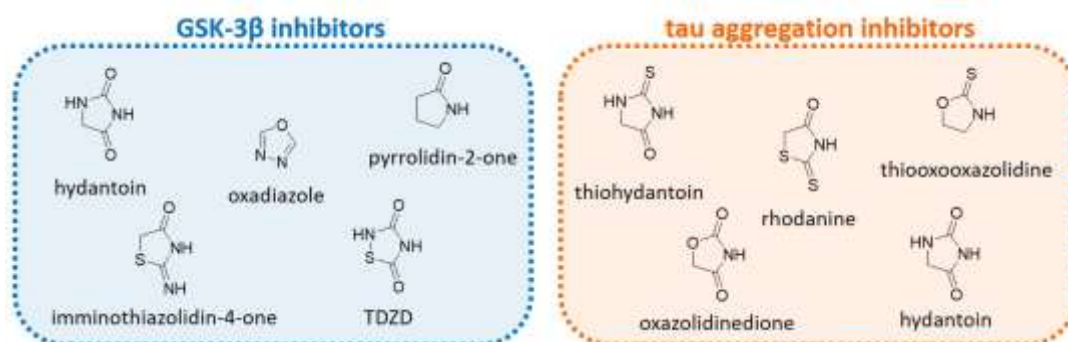
The aim of this project was the design and synthesis of the first class of multi-target compounds able to hit the altered tau protein cascade at two different validated hubs. Particularly, we envisaged that the simultaneous inhibition of GSK-3 $\beta$  and tau aggregation process, might pave the way for a completely novel treatment of Alzheimer's disease. As highlighted before, the very close spatial correlation between neuronal loss and tau aggregates in AD patients' brains, and the genetic evidence for the role of tau aggregation in a wide range of neurodegenerative disorders, due to mutations in the tau gene, provides a strong foundation for tau-targeted therapy. Moreover, such dual GSK-3 $\beta$  and tau aggregation inhibitors might show a higher efficacy compared to the combination of single-targeted drug candidates. Indeed, targeting two points of the tau network could generate a synergistic response and could eliminate compensatory reactions and feedback controls. Finally, dual inhibitors should possess a lower target-related toxicity, as even low-affinity dual inhibitors should be sufficient to achieve a significant anti-tau effect. On the other side, if the concentration of the dual inhibitor required to obtain the desired effect is lower with respect to single-targeted drugs, the risk for toxicity is reduced. This consideration greatly eases the constraints of druggability, a key issue for GSK-3 $\beta$ .<sup>197</sup>

Remarkably, although in the literature there are several examples of MTDLs that combine anti-tau activity with a second one useful for AD treatment (e.g. anti-amyloid, antioxidant, anti-inflammatory activity),<sup>218-228</sup> the development of dual GSK-3 $\beta$  and tau aggregation inhibitors has never been exploited so far.

Designing a ligand able to simultaneously bind two targets sharing no similarity in the binding sites, as it is the case of GSK-3 $\beta$  and tau protein, could be very challenging.<sup>229</sup> Similarly, combining the molecular frameworks of two CNS-directed single-target ligands in one small molecule, might not be an easy task and give rise to pharmacokinetic concerns.<sup>230</sup>

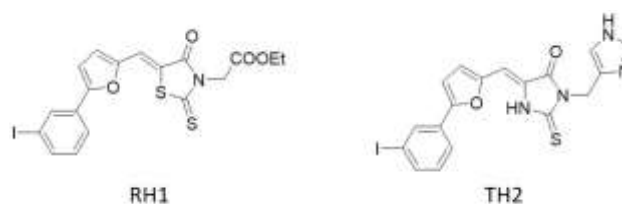
In light of this, 5-membered heterocyclic fragments caught our attention. As reported above, several known GSK-3 $\beta$  inhibitors carry 5-membered heterocyclic rings such as hydantoin, oxadiazole, pyrrolidin-2-ones, iminothiazolidin-4-one, and thiadiazolidinediones (Figure 3.7).<sup>155, 157-159</sup> On the other side, several 5-membered

heterocyclic fragments were discovered as effective anti-tau aggregation motifs. Rhodanine, thiohydantoin, thiooxooxazolidine, oxazolidinedione, and hydantoin (Figure 3.7) were screened for their ability to inhibit the tau aggregation process and to disaggregate preformed tau aggregates.<sup>210</sup> The rhodanine core appears to be the most active one, being able to inhibit the formation of tau aggregates in a dose-dependent manner, as well as destabilize preformed tau aggregates.



**Figure 3.7.** General chemical structures of 5-membered heterocyclic fragments reported as GSK-3 $\beta$  and tau aggregation inhibitors.

Finally, the ability of rhodanines and thiohydantoin to directly interact with tau aggregates has been confirmed by the tau imaging properties of derivatives RH1 and TH2 (Figure 3.8). The thiohydantoin derivative TH2, in particular, intensely stained neurofibrillary tangles in hippocampal sections obtained from AD patients.<sup>231</sup>



**Figure 3.8.** Chemical structures of the tau imaging probes RH1 and TH2.

Based on these evidence, we reasoned that the cross-talk between all these fragments could be favorably exploited for the identification of novel MTDLs directed towards the two selected targets: GSK-3 $\beta$  and the tau aggregation process.

As first, we focused our attention on rhodanines. In principle, being prone to bind a large number of targets with weak or moderate affinity, rhodanines might be an

optimal starting point for multi-target drug discovery projects. However, the validity of the rhodanine scaffold is questionable because of its notorious Pan Assay Interference Compounds (PAINS) behavior.<sup>232</sup> Although it is hard to draw the line between true multi-target activity and potential reactivity, which may or may not lead to assay interferences, we consider safer to disregard the rhodanine scaffold.

Thus, in our project, we selected a rhodanine isoster, the 2,4-thiazolidinedione (TZD, Figure 3.9), which has never been explored as either GSK-3 $\beta$  or tau aggregation inhibitor. Moreover, as highlighted by Baell and Pouliot, the TZD scaffold itself does not aggressively drive assay interference in the same way as rhodanine does.<sup>233-235</sup> Indeed, the TZD core is not identified as PAIN by computational filters. Finally, the drug-likeness of the TZD scaffold in AD is supported by the fact that the TZD-based antidiabetic drug pioglitazone (PIO) is currently in Phase III clinical trial, as anti-inflammatory drug in mild cognitive impaired patients.<sup>236</sup>

After the selection of the scaffold of our library, we decided to decorate the TZD at position 5, with different aromatic and heteroaromatic substituents, affording a 35-membered library of 5-arylidene-2,4-thiazolidinediones (**1-35**, Figure 3.9). The substitution of TZD at position 5, was based on previous studies showing that:

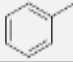
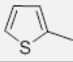
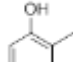
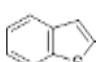
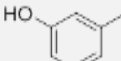
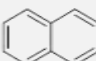
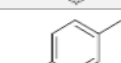
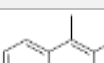
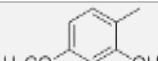
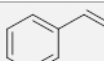
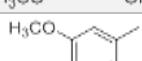

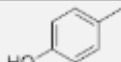

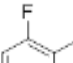
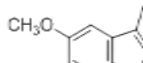
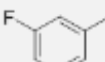
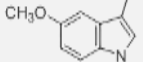
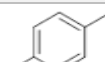
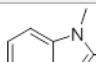
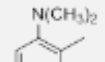
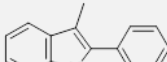
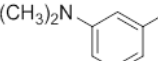
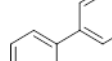

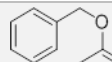
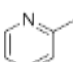
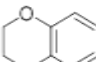
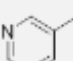
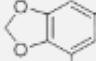
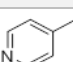
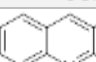
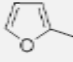
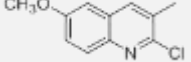
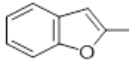
- 5-arylidene substitutions improved affinity in a series of 2-iminothiazolidin-4-one competitive GSK-3 $\beta$  inhibitors;<sup>158</sup>
- due to their volume and size, 5-arylidene substituted compounds should not fit in similar regions of homologous kinases, therefore showing selectivity towards GSK-3 $\beta$ ;<sup>158</sup>
- 5-arylidene substitution will allow to maintain the planarity and aromatic features, critical for the interaction with tau fibrils.<sup>237</sup>



**Figure 3.9.** General chemical structure of TZD derivatives **1-35**.

In order to explore the chemical space, starting from the simplest derivative **1**, we inserted different electron-withdrawing and electron-donating groups on the phenyl ring. Then, we also wanted to study the effect of different size substituents at position 5 of the TZD, by selecting different size aromatic and heteroaromatic groups. Particularly, among the possible heteroaromatic substituents, we include indoles, benzofurans and benzothiophenes, as they are already reported as effective anti-amyloid scaffolds.<sup>238</sup>

**Table 3.1.** Chemical structures and yields of the TZD-derivatives **1-35**.

Cmpd.	R	yields	Cmpd.	R	yields
<b>1</b>		87 %	<b>19</b>		92%
<b>2</b>		56%	<b>20</b>		54%
<b>3</b>		43%	<b>21</b>		37%
<b>4</b>		69%	<b>22</b>		18%
<b>5</b>		75%	<b>23</b>		36%
<b>6</b>		62%	<b>24</b>		58%
<b>7</b>		79%	<b>25</b>		45%
<b>8</b>		49%	<b>26</b>		47%
<b>9</b>		60%	<b>27</b>		44%
<b>10</b>		76%	<b>28</b>		48%
<b>11</b>		70%	<b>29</b>		22%
<b>12</b>		78%	<b>30</b>		55%
<b>13</b>		88%	<b>31</b>		61%
<b>14</b>		55%	<b>32</b>		75%
<b>15</b>		34%	<b>33</b>		58%
<b>16</b>		59%	<b>34</b>		45%
<b>17</b>		65%	<b>35</b>		32%
<b>18</b>		59%			



### 3.4 Chemistry

The synthesis of compounds **1-35** was easily achieved through a one-pot, optimized version of the Knoevenagel condensation. The conventional protocol is based on the condensation of equimolar amounts of TZD and different aromatic aldehydes, in the presence of catalytic amounts of pyridine and acetic acid, in refluxing toluene.<sup>239</sup> However, the reported protocol suffers from several disadvantages: (i) long reaction times; (ii) low to moderate yields; (iii) tedious work-up procedures; (iv) requirement of special apparatus; (v) use of toxic, organic solvents. Thus, taking inspiration from the literature, we moved to a green and solvent-free procedure using ethylenediamine diacetate (EDDA) as catalyst (Table 3.2).<sup>240</sup> In recent years, EDDA emerged as an effective catalyst for different reactions, being an inexpensive and effective Brønsted acid-base combined salt. Clearly, there are several advantages in using a green and solvent-free reaction, such as reduced pollution, lower costs, simplicity in process and handling, shorter reaction times, and higher yields. EDDA was easily synthesized through an acid-base reaction between ethylenediamine and glacial acetic acid (1:2) in dry ether. This second synthetic procedure allow us to shorter reaction times from 5-10 hours to 0.45-2 hours, but the reaction yields were not significantly improved.

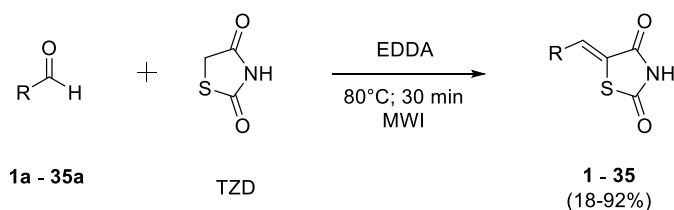
**Table 3.2.** Optimization of the Knoevenagel reaction.

	Time (h)	Temperature (°c)	Heating	Solvent	Catalyst	Yields (%)
<i>method 1</i>	5 - 10	116	conventional	toluene	benzoic acid, piperidine	5 - 52
<i>method 2</i>	0.45 - 2	80	conventional	-	EDDA	9 - 59
<i>method 3</i>	0.30	80	microwave	-	EDDA	18 - 92

With the aim of further improving the green chemistry aspects, we perform the same solvent-free reaction exploiting microwave irradiation (MWI) (Table 3.2). Importantly, microwave mediated synthesis using EDDA as catalyst, has never been exploited for the synthesis of 5-arylidene-2,4-thiazolidinediones.

Thus, our new optimized procedure is based on a one-step, green, and solvent-free condensation of aromatic aldehydes with an equimolar amount of TZD, in presence of EDDA (0.5 eq), for 30 minutes under MW irradiation (Scheme 3.1). The developed procedure was then apply to the vast array of aldehydes **1a-35a**, to obtain target compounds **1-35**. The yields vary from 18 to 92%. However, the lower 18% yield was obtained for compound **22**, which we was not able to synthesize with the first two synthetic procedures, thus proving the effective optimization of the synthetic protocol.

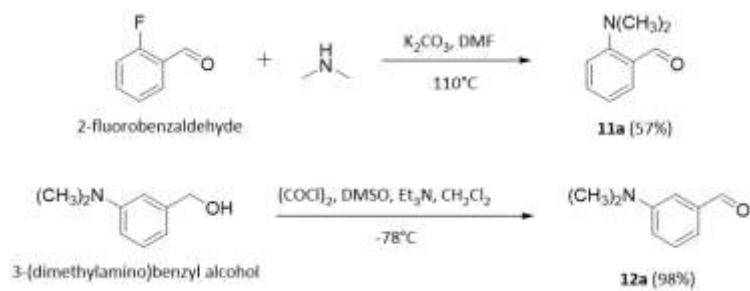
**Scheme 3.1.** Optimized Knoevenagel reaction for the synthesis of TZD-derivatives **1-35**.



Moreover, the wide applicability of our optimized procedure was further confirm by the successful obtaining of 35 structurally different TZD-derivatives. Indeed, as highlighted above, we select a vast array of aldehydes, with electron-withdrawing and electron-donating groups, heteroaromatic, conjugated and planar rings.

All the aromatic aldehydes were purchased from commercial vendors, except **11a** and **12a**. These aldehydes were synthesized by slightly modifying reported procedures (Scheme 3.2).<sup>241, 242</sup>

In the first case, 2-fluorobenzaldehyde was reacted with dimethylamine in the presence of potassium carbonate, to provide aldehyde **11a**. In the second case, the commercially available 3-(dimethylamino)benzyl alcohol was oxidized under Swern conditions, affording aldehyde **12a**.



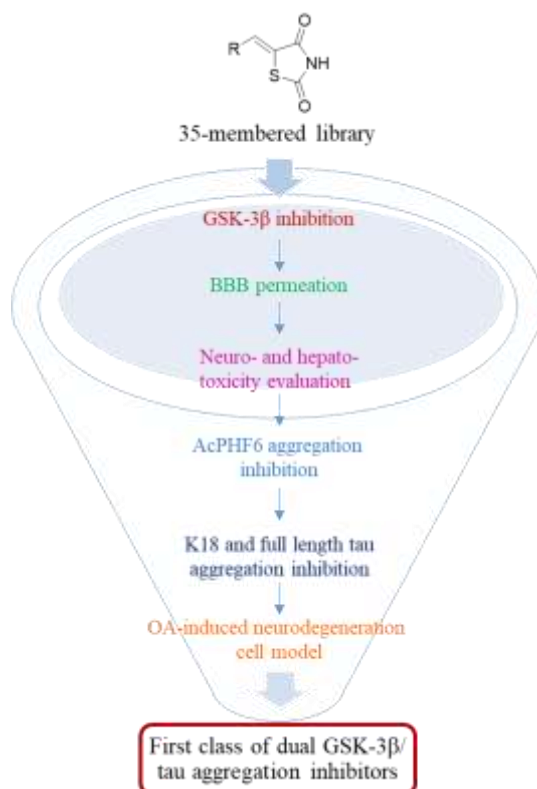
**Scheme 3.2.** Synthetic procedure for the synthesis of aldehydes **11a** and **12a**.

All compounds were characterized using analytical (HPLC) and spectroscopic data ( $^1\text{H}$ - and  $^{13}\text{C}$ -NMR, ESI-MS).

### 3.5 Results and discussion

The TZD derivatives **1-35** were designed and synthesized aiming at the development of MTDLs able to target the tau cascade at two different hubs. Thus, to verify the capability of **1-35** to simultaneously inhibit GSK-3 $\beta$  and the tau aggregation process, we exploited an appropriate screening pipeline, depicted in Figure 3.10.

As first step, we made a preliminary screening of all synthesized molecules for GSK-3 $\beta$  activity. Then, in order to understand their mechanism of action, we performed kinetic experiments, aiming at determining the competition with ATP. The results suggested that the TZD-derivatives represent a novel class of ATP-competitive GSK-3 $\beta$  inhibitors. Then, we developed docking studies, in order to obtain the theoretical binding mode of our compounds in the ATP-binding pocket of GSK-3 $\beta$ , and to relate their binding mode with the IC<sub>50</sub> values. The GSK-3 $\beta$  inhibitors were subsequently tested for their ability to cross the BBB, through a Parallel Artificial Membrane Permeability Assay (PAMPA).



**Figure 3.10.** Screening pipeline for the TZD-derivatives **1-35**.

With these results in our hands, we decided to filter out toxic compounds by testing their neuro- and hepatotoxicity in cerebellar granule neurons (CGNs) and HepG2 cells, respectively. Finally, the non-toxic compounds were tested for their ability to inhibit the aggregation of tau protein in three different assays, using three different tau constructs: the tau-derived hexapeptide AcPHF6, the K18 tau fragment, and the 2N4R full length tau.

The anti-tau activity of the best performing compounds was then assessed in a cellular context, the okadaic acid (OA)-induced neurodegeneration cell model.

### 3.5.1 GSK-3 $\beta$ inhibition assays

These experiments were performed by Carlos Roca, Josefa Zaldivar-Diez, and Concepción Perez under the supervision of Prof. Ana Martínez, at the Centro de Investigaciones Biológicas, CSIC, Madrid.

To characterize the ability of our compounds to inhibit GSK-3 $\beta$ , we performed a Kinase-Glo™ luminescent assay.<sup>40</sup> The Kinase-Glo luminescent assay quantifies the amount of ATP remaining in solution following a kinase reaction. This method is based on measuring the intensity of the “glow type” luminescence, generated by mono-oxygenation of beetle luciferin by luciferase, in the presence of Mg<sup>2+</sup>, ATP, and molecular oxygen. The luciferase-luciferin reaction consumes one ATP molecule and produces one photon per turnover. The luminescence signal is proportional to the amount of ATP present and inversely correlated to kinase activity.

All compounds were first tested at 10  $\mu$ M, and hits with percentage inhibition  $\geq$ 50% were further tested to obtain IC<sub>50</sub> values (determined by using the linear regression parameter). The TDZD derivative TDZD8<sup>159</sup> was used as reference compound. Encouragingly, sixteen compounds out of the starting 35 TZD derivatives, were able to inhibit GSK-3 $\beta$  with IC<sub>50</sub> values in the single-digit micromolar range (see Table 3.3). Above the sixteen GSK-3 $\beta$  inhibitors, compound **27** resulted as the most active one, with a submicromolar IC<sub>50</sub> of 0.89  $\pm$  0.21  $\mu$ M.

Structure-activity relationships (SAR) are discussed in comparison with compound **1** ( $IC_{50} > 10 \mu M$ ).

Hydroxyl substituents in ortho and meta positions of the phenyl ring did not increase enzyme inhibition, as evident for compounds **2** and **3**. On the other side, *para* hydroxyl substituted **4** shows a significant improvement in the inhibitory potency ( $8.99 \pm 0.78 \mu M$ ). Di-substitution of the phenyl ring in compounds **5-7** do not affect the activity, and the same was observed for the fluorine substitution in compounds **8-10**.

**Table 3.3.** GSK-3 $\beta$  inhibitory activity of TZD derivatives **1-35** and TDZD8.

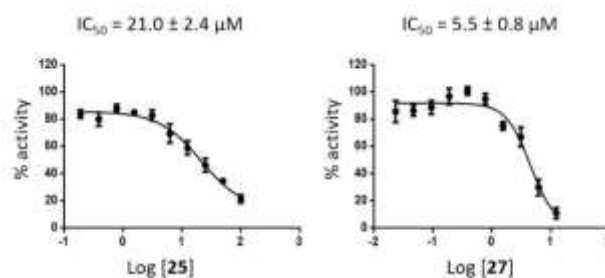
Cmpd.	GSK-3 $\beta$ IC <sub>50</sub> ( $\mu M$ )	Cmpd.	GSK-3 $\beta$ IC <sub>50</sub> ( $\mu M$ )	Cmpd.	GSK-3 $\beta$ IC <sub>50</sub> ( $\mu M$ )
<b>1</b>	> 10	<b>13</b>	> 10	<b>25</b>	$4.93 \pm 0.66$
<b>2</b>	> 10	<b>14</b>	> 10	<b>26</b>	> 10
<b>3</b>	> 10	<b>15</b>	$8.75 \pm 0.77$	<b>27</b>	$0.89 \pm 0.21$
<b>4</b>	$8.99 \pm 0.78$	<b>16</b>	$1.42 \pm 0.12$	<b>28</b>	> 10
<b>5</b>	$7.08 \pm 0.51$	<b>17</b>	> 10	<b>29</b>	$6.03 \pm 0.44$
<b>6</b>	$6.01 \pm 0.72$	<b>18</b>	> 10	<b>30</b>	> 10
<b>7</b>	$9.22 \pm 0.90$	<b>19</b>	$7.99 \pm 0.57$	<b>31</b>	> 10
<b>8</b>	> 10	<b>20</b>	$7.47 \pm 0.85$	<b>32</b>	$7.01 \pm 0.61$
<b>9</b>	> 10	<b>21</b>	> 10	<b>33</b>	> 10
<b>10</b>	> 10	<b>22</b>	> 10	<b>34</b>	$6.13 \pm 0.43$
<b>11</b>	$9.22 \pm 0.89$	<b>23</b>	> 10	<b>35</b>	$3.55 \pm 0.23$
<b>12</b>	$8.54 \pm 0.81$	<b>24</b>	> 10	<b>TDZD8</b>	$0.69 \pm 0.09$

Regarding the dimethylamino substituents, the favored positions are the *ortho* and *meta*, as shown by **11** ( $9.22 \pm 0.89 \mu M$ ) and **12** ( $8.54 \pm 0.81 \mu M$ ). Replacement of the phenyl ring of **1** with a 4-pyridil ring, as in **16**, led to an  $IC_{50}$  of  $1.42 \pm 0.12 \mu M$ . Thiophene (**19**) and benzothiophene (**20**) substitutions also resulted in a good inhibitory activity. While substitution with bulky substituents such as naphthyl, anthracene, phenylpropylen or biphenyl, as in **21-24**, **30**, and **31**, resulted in an inactivity of the compounds at  $10 \mu M$  of concentration. Interestingly, bicyclic N-

heterocycles, such as **25-29**, showed different behaviors. Probably, the lipophilic nature of the ligands can explain the IC<sub>50</sub> differences, being compounds **25** and **29** better GSK-3β inhibitors than **26**. Moreover, the insertion of a methyl group on the nitrogen atom of the indole, as in **27**, resulted in an important improvement in the inhibitory profile (0.89 ± 0.21 μM). This trend in activity was not surprising us, as it has been already described in published indolyl-maleimide GSK-3β inhibitors, in which the methylation of the indole nitrogen atom improves the IC<sub>50</sub> from 4.4 μM to 0.89 μM.<sup>243</sup>

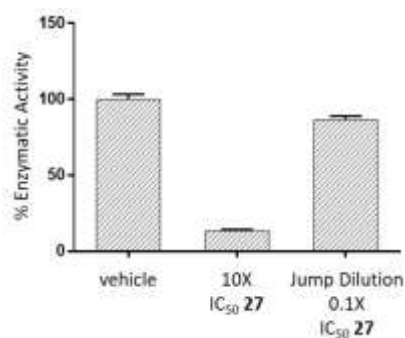
After these first results, we wanted to confirm the GSK-3β inhibitory activity of our compounds through a secondary assay. These experiments were performed by Alessandra Feoli, under the supervision of Prof. Sabrina Castellano, at the EpigeneticMedChemLab, UNISA, Fisciano.

We selected compounds **25** and **27** (that resulted as the best performing compounds in the following experiments), for a Time-Resolved Fluorescence Energy Transfer (TR-FRET) assay. LANCE® TR-FRET assay use a proprietary europium chelate donor dye, W-1024, with ULIGHT, a small molecular weight acceptor dye. The binding of an Eu-labeled anti-phospho-substrate antibody to the phosphorylated ULIGHT-labeled substrate, brings donor and acceptor molecules into close proximity. After irradiation of the kinase reaction at 320 nm, the energy from the Eu donor is transferred to the ULIGHT acceptor dye, which generates light at 665 nm. The intensity of the light emission is proportional to the level of ULIGHT-substrate phosphorylation. Thus, the two compounds were tested at ten different concentrations and the obtained IC<sub>50</sub> values for both **25** (21.0 ± 2.4 μM) and **27** (5.5 ± 0.8 μM) were in agreement with the ones obtained with the Kinase-Glo luminescent assay (Figure 3.11).



**Figure 3.11.** Dose-response curves of GSK-3 $\beta$  activity in the presence of **25** and **27**. Values are the means  $\pm$  SD determined for at least two independent experiments.

Moreover, aware of the potential covalent reactions that could arise from the alkylidene moiety, we also assess the reversibility of GSK-3 $\beta$  inhibition by **27** through a Jump dilution assay.<sup>244</sup> In details, **27** was first tested at 10 $\times$  its  $IC_{50}$  value, showing  $86 \pm 1$  % inhibition, the subsequent dilution at 0.1 $\times$  its  $IC_{50}$  lead to a  $13 \pm 2$  % inhibition (Figure 3.12). Thus, we were able to demonstrate that the enzymatic activity was restored after dilution, pointing to a reversible inhibition by **27**.

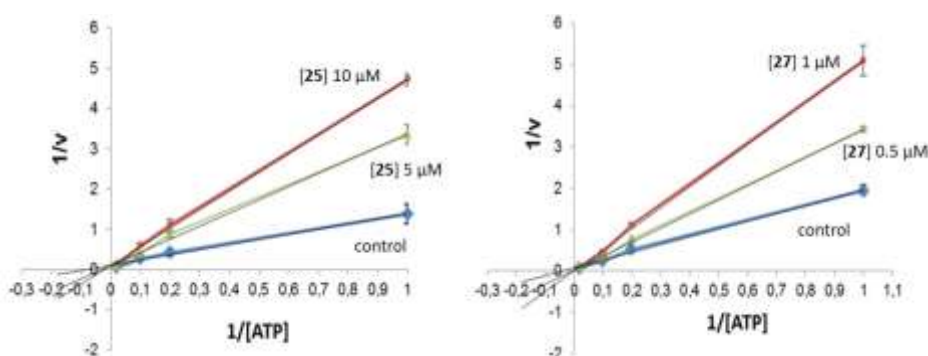


**Figure 3.12.** Jump dilution experiment for compound **27**. The residual enzymatic activity reported in graph are the mean values  $\pm$  SD of two separate experiments compared to the reaction performed with the vehicle.

To investigate the mechanism of action of the TZD-derivatives on GSK-3 $\beta$ , the selected compounds **25** and **27** were subjected to kinetic experiments. Particularly, we determined the competition with the ATP, varying both ATP and **25** and **27** concentrations with a constant concentration of GS-2, the substrate used in the



enzymatic reaction. As shown by the double-reciprocal plot reported in Figure 3.13, indicates that both **25** and **27** act as competitive inhibitors of ATP binding. Thus, we were able to claim that TZD derivatives represent a new chemical class of ATP-competitive GSK-3 $\beta$  inhibitors.



**Figure 3.13.** Kinetic data for the TZD-derivatives **25** and **27**. ATP concentration in the reaction mixture varied from 1 to 50  $\mu\text{M}$ . Compounds concentrations used are depicted in the plot, and the concentration of GS-2 was kept constant at 25  $\mu\text{M}$ . Each point is the mean of two different experiments, both analyzed in triplicate.

### 3.5.2 Retrospective docking simulations on GSK-3 $\beta$

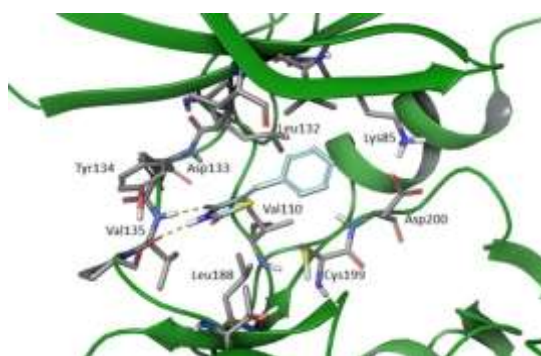
These experiments were performed by Dr. Nuria Campillo at the Centro de Investigaciones Biológicas, CSIC, Madrid.

The ATP-competitive GSK-3 $\beta$  inhibitors share a binding mode in the ATP binding pocket, making H-bonds interactions with the backbone atoms of Asp133 and Val135. These ligand-protein interactions allow the ligands to have the minimum interactions that allow them to bind to GSK-3 $\beta$  and with  $\text{IC}_{50}$  values in the micromolar range. Inhibitors that interact with both the flexible glycine-rich loop formed by Ile62, Gly63, Phe67 and Val70 or the ATP-binding pocket residues Lys85, Glu97, Glu137, Arg141, Gln185, Cys199 or Asp200 improve their inhibitory activity and the selectivity towards GSK-3 $\beta$  against other protein kinases.<sup>245, 246</sup>

In light of this, docking studies were developed in order to obtain the theoretical binding mode for the TZD-based GSK-3 $\beta$  inhibitors in the ATP-binding pocket, and to relate the binding mode with the IC<sub>50</sub> values. These studies were performed using AutoDock software, centring the grid into the hinge region of the ATP binding domain of GSK-3 $\beta$  (PDB ID 1Q3W).

As first, we study the interactions of **1** with GSK-3 $\beta$ . Docking study for this ligand show a typical binding mode, similar to other ATP-competitive inhibitors,<sup>155, 158, 247</sup> i.e. an H-bond donor interaction between the oxygen atom of Val135 backbone and the NH group of **1**, and an H-bond acceptor between the nitrogen atom of the backbone of Val135 and the carbonyl group in position 4 of the TZD. This pose orients the aromatic ring in the hydrophobic cavity of the ATP-binding pocket, where it establishes hydrophobic contacts with Val110, Leu132 and Leu188, but no direct interaction with catalytic residues Lys85 and Asp200 (Figure 3.14).

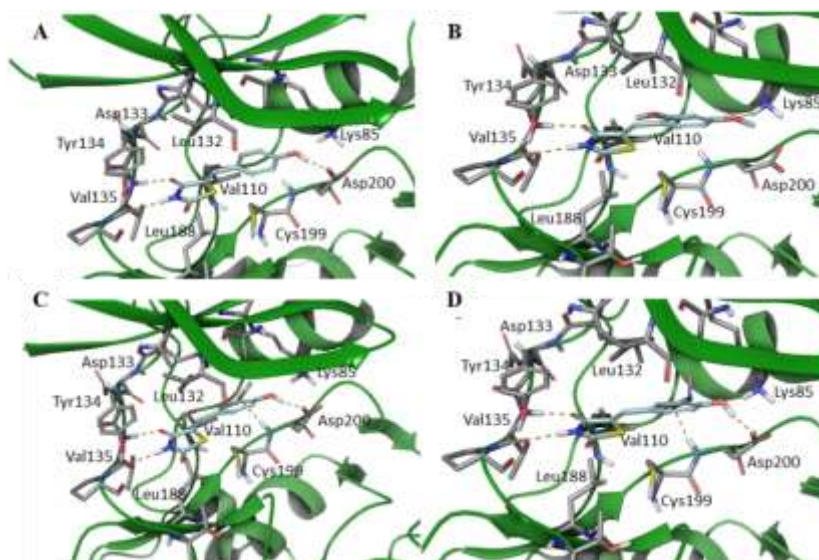
The poses generated for **2-35**, in which the phenyl ring is replaced by the different aromatic and heteroaromatic rings, may be clustered in three groups, according to their interaction with the hinge region. The first group includes those compounds that establish a double H-bond interaction with Val135 (**4-10**, **15-17**, **19**, **20**, and **27**). These compounds fit properly their aromatic nucleus into the hydrophobic binding pocket confirming our initial design hypothesis.



**Figure 3.14.** Suggested binding mode of **1** in the ATP-binding pocket of GSK-3 $\beta$  (PDB ID 1Q3W).

Among them, those than can interact with Lys85 or Asp200 show an improved affinity and, consequently, lower IC<sub>50</sub> values. This is the case of **4-7**, where acceptor, such as

methoxyl, or donor/acceptor groups, such as hydroxyl, can interact with the side chain of Lys85 or Asp200 through additional H-bond interactions (Figure 3.15).



**Figure 3.15.** Docking poses for compounds **4-7** (PDB ID 1Q3W).

Similarly, **16** orients the nitrogen atom of the pyridine towards the Lys85 residue, suggesting a favorable H-bond acceptor interaction.

On the other hand, isomers **11**, **12** and **13** are substituted with a dimethylamino group, which is not able to interact through donor H-bond interactions. Thus, these compounds are not able to interact directly with Lys85. Among them, compounds **11** and **12** fit in a better way into the cavity, due to the fact that the methyl groups are able to establish hydrophobic interactions with the target, whereas the less active **13** encounters steric hindrance.

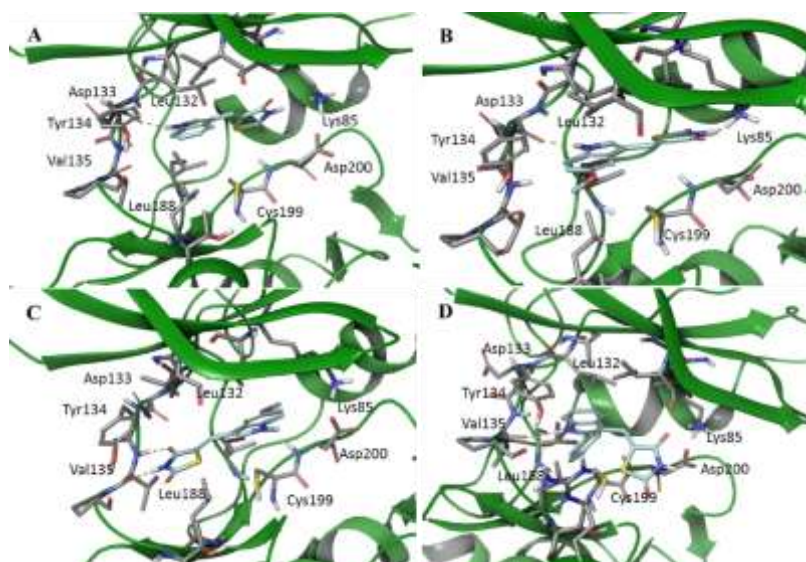
The second group encompasses compounds that interact with a donor H-bond with Asp133 and an acceptor H-bond with Val135. They (**2**, **3**, **18**) display generally higher IC<sub>50</sub> values than the previous ones, due to the poor fitting of the hydrophobic region of the ligands into the target.

Finally, the third group, i.e. compounds that interact with a donor hydrogen bridge with Asp133, are indole derivatives without substitution in the indole nitrogen (**25**, **26**,

**29**). These ligands change their binding mode, interacting with the hinge region through the indole ring and not through the TZD fragment (Figure 3.16).

Intriguingly, the most active N-methyl indole **27**, which loses the possibility of H-bonding through the indole nitrogen, re-orientates itself, as reported for the first group of GSK-3 $\beta$  inhibitors. Indeed, **27** make contacts between the TZD ring and Val135 through two H-bond interactions (Figure 3.16).

Importantly, compounds carrying bulky substituents (**21-24**, **30**, **31**) because of their steric hindrance, cannot fit properly into the ATP-binding pocket, and make specific H-bond interactions.



**Figure 3.16.** Best docking poses of indole-substituted TZDs: **25** (A), **26** (B), **27** (C), **29** (D) (PDB ID 1Q3W).

### 3.5.3 Blood brain barrier permeation

These experiments were performed by Loreto Martinez-Gonzales under the supervision of Prof. Ana Martinez at the Centro de Investigaciones Biológicas, CSIC, Madrid.

The BBB is a complex interface between blood and the CNS, that strictly controls the exchanges between the blood and brain compartments.<sup>248</sup> This barrier is composed by endothelial cells with tight junctions and it protect the brain from endogenous materials that could damage the brain tissues.<sup>249</sup> The majority of CNS drugs enter the brain by transcellular passive diffusion, due to the tight junction structure and limited transport pathways. Importantly, one of the main obstacles in the treatment of neurodegenerative diseases is the drug's penetration into the BBB, at therapeutic concentrations. Thus, in early drug discovery stage, evaluation of BBB penetration is of crucial importance to reduce attrition in the development process.

Indeed, we perform a Parallel Artificial Membrane Permeability Assay (PAMPA), in order to preliminary explore the capacity of the sixteen GSK-3 $\beta$  inhibitors to penetrate into the brain. PAMPA-BBB is a high throughput technique developed to predict BBB passive permeability. The *in vitro* permeability (Pe) of commercial drugs through lipid membrane extract, together with TZD-derivatives were determined and described in Table 3.4.

An assay validation was made comparing the reported permeability values of commercial drugs with the experimental data obtained employing this methodology. A good correlation between experimental-described values was obtained. From this equation and following the pattern established in the literature for BBB permeation prediction<sup>250</sup> we could classify compounds as CNS+ when they present a permeability > 3.07 x 10<sup>-6</sup> cm/s. Based on these results, compounds **11**, **12**, **20**, **25**, and **27** are able to cross the BBB by passive permeation, and thus were progressed for toxicity and tau anti-aggregation analysis.

**Table 3.4.** Effective permeability ( $P_e$   $10^{-6}$  cm  $s^{-1}$ ) in the PAMPA-BBB assay for the GSK-3 $\beta$  TZD-derivatives with their predictive penetration in the CNS.<sup>a</sup>

Compound	$P_e$ ( $10^{-6}$ cm $s^{-1}$ ) <sup>b</sup>	Prediction
4	0.3 $\pm$ 0.6	CNS -
5	1.5 $\pm$ 1	CNS + / CNS -
6	0.1 $\pm$ 1	CNS -
7	0.2 $\pm$ 0.1	CNS -
11	5.4 $\pm$ 0.8	CNS +
12	3.6 $\pm$ 0.4	CNS +
15	0.1 $\pm$ 0.1	CNS -
16	0.2 $\pm$ 0.1	CNS -
19	2.2 $\pm$ 1	CNS + / CNS -
20	5.7 $\pm$ 0.9	CNS +
25	5.4 $\pm$ 1.5	CNS +
27	5.8 $\pm$ 1	CNS +
29	2.6 $\pm$ 0.7	CNS + / CNS -
32	1.9 $\pm$ 0.1	CNS + / CNS -
34	1.9 $\pm$ 0.5	CNS + / CNS -
35	1.8 $\pm$ 0.3	CNS + / CNS -

<sup>a</sup> PBS:EtOH (70:30) was used as solvent. <sup>b</sup> Data are the mean  $\pm$  SD of two independent experiments.

#### 3.5.4 Neuro- and hepato-toxicity assessment

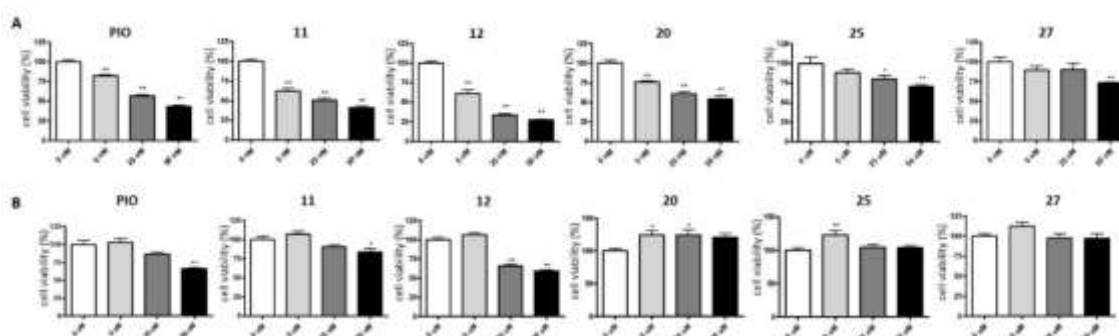
These experiments were performed by Dr. Sabrina Petralla, under the supervision of Prof. Barbara Monti, at the Department of Pharmacy and Biotechnology, UNIBO, Bologna.

The failure of several drug discovery approaches has been widely attributed not only to the lack of efficacy, but also to the toxicity of the drug candidates. The identification

of toxicity issues early in a drug discovery project, might reduce the attrition rate, allowing only compounds with optimal safety profiles to proceed to further studies. In light of this, and motivated by the promising *in vitro* results, we tested neurotoxicity of the five GSK-3 $\beta$  inhibitors predicted to cross the BBB (Figure 3.17), in comparison to PIO.

Primary cultures of cerebellar granule neurons (CGNs) were established a few decades ago, and since then have become one of the most useful *in vitro* models to study neuronal death. Indeed, cerebellum is engaged in cognition and learning and it affects AD patients' bodily control.<sup>251</sup> MTT (3-(4,5-dimethylthiazol-2-yl)-2,5-diphenyltetrazolium bromide) assessment of CGNs viability after 24h treatment with **11**, **12**, and **20** showed a clear cytotoxic effect for all the three compounds, as well as PIO, even at 5  $\mu$ M concentration. Notably, **25** and **27** showed a very low toxicity only at the highest tested concentrations (50  $\mu$ M).

Moreover, it is well-known that, for understanding the drug likeness of a chemical library, the assessment of hepatotoxicity is of utmost importance. In AD patients, aging, comorbidity, and subsequent polytherapy significantly contribute to increase the risk of drug-drug interactions and, indeed, hepatotoxicity. Moreover, although being effective therapeutic agents, some TZD derivatives have been reported to have hepatotoxicity.<sup>252</sup> To this end, parallel experiments were performed on **11**, **12**, **20**, **25**, **27** in human hepatoma cell line (HepG2), in comparison with PIO (Figure 3.17). After 24 h incubation at 0-50  $\mu$ M, a concentration-dependent decrease in cell viability was observed for PIO, **11**, and **12**. Encouragingly, compounds **20**, **25**, and **27** showed no hepatotoxicity, even at 50  $\mu$ M. On the basis of the toxicity profiles, indole derivatives **25** and **27** emerged as the most drug-like compounds, and were further progressed in the screening pipeline.



**Figure 3.17.** (A) Neurotoxicity on primary rat cerebellar granule neurons (CGNs) after 24 h treatment. (B) Hepatotoxicity on human hepatoma cells (HepG2) after 24 h treatment. Results are expressed as percentage of controls and are the mean  $\pm$  SE of at least 3 different experiments, each run in triplicate.

### 3.5.5 AcPHF6 aggregation and inhibition studies by Thioflavin T (ThT) fluorescence, circular dichroism spectroscopy and atomic force microscopy

These experiments were performed by Prof. Manuela Bartolini, Dr. Daniele Tedesco, Andrea Miti, and Dr. Giampaolo Zuccheri at the Department of Pharmacy and Biotechnology, UNIBO, Bologna.

Two hexapeptide motifs within tau protein were demonstrated to be crucial for tau aggregation into oligomers and NFTs: VQIVYK and VQIINK.<sup>253, 254</sup> Thus, to preliminary study the ability of our TZD-derivatives to interfere with tau aggregation, we selected the so-called AcPHF6 peptide (<sub>306</sub>VQIVYK<sub>311</sub>) as a model system for the in vitro aggregation of tau.

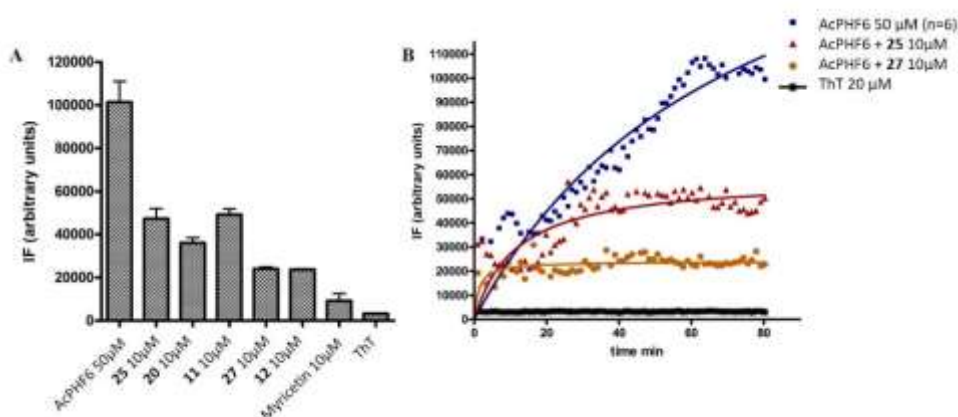
AcPHF6 is a short segment found in the third repeat domain of the microtubule-binding region of tau protein, and it is considered as a suitable model for the screening of small molecule tau aggregation inhibitors.<sup>255-260</sup>

Indeed, this tau derived hexapeptide is well characterized and it is known that it easily undergoes fibrillation in vitro, forming cross- $\beta$ -sheets structures. Moreover, cryo-electron microscopy recently demonstrated that the cores of PHFs are composed of eight  $\beta$ -sheets, adopting a C-shaped architecture. Importantly, the N-terminal part of



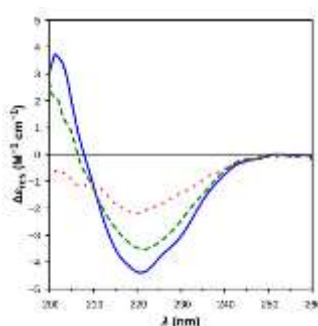
the cross- $\beta$  structure is formed by the hexapeptide AcPHF6, further demonstrating its essential role in the assembly of tau filaments.<sup>261</sup>

As for other  $\beta$ -sheet proteins, the aggregation process of AcPHF6 can be monitored by fluorescence in the presence of ThT, which displays a characteristic change in the emission spectrum in the presence of  $\beta$ -rich structures.<sup>262</sup> The anti-aggregating activity of **11**, **12**, **20**, **25**, and **27** was therefore monitored in phosphate buffer 50 mM at pH 7.4, using ThT as detection dye. As already reported in the literature,<sup>255-260</sup> AcPHF6 incubated alone, rapidly aggregated, as confirmed by the increase in the fluorescence intensity over a period of 80 min (Figure 3.18). Co-incubation of AcPHF6 with the selected compounds led to a significant (> 50%) decrease of the fluorescence intensities, indicating that all compounds could significantly interfere with AcPHF6 aggregation, even if at different extents (from 54.7% to 79.8%). In details, derivatives **12** and **27** showed the highest inhibitory potencies, reducing the fluorescent signal at plateau by almost 80% (79.5 and 79.8% respectively), and resulting only slightly less potent than the known inhibitor myricetin.<sup>206</sup> Figure 3.18B shows the details of the kinetic of aggregation of AcPHF6 incubated alone and in the presence of compounds **25** and **27**, the derivatives endowed with the best safety profile.



**Figure 3.18.** (A) Inhibition of AcPHF6 peptide (50  $\mu$ M) aggregation in the presence of selected derivatives (10  $\mu$ M) after 80 min incubation. The data are the mean of at least three repeats. (B) Kinetics of the AcPHF6 aggregation in the absence and in the presence of compounds **25** and **27** monitored by ThT fluorescence.

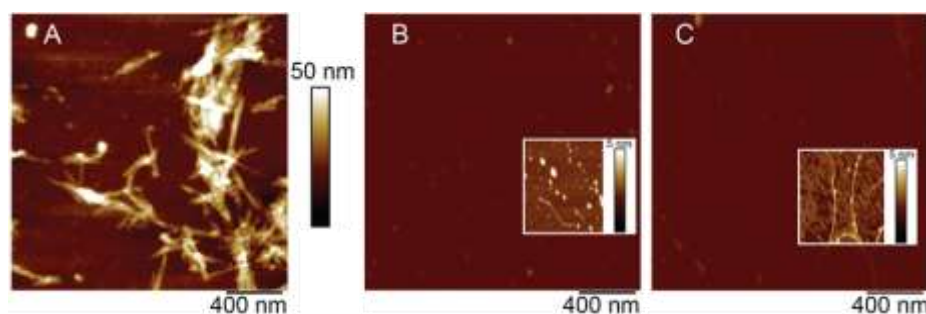
Circular dichroism (CD) studies were then carried out to gain further insights into the mechanism of inhibition of **25** and **27**, and to exclude false positive outcomes due to the possible displacement of bound ThT by the tested compounds. The CD spectrum of AcPHF6 (Figure 3.19) shows a negative band at 221 nm followed by a positive band at shorter wavelengths, both of which are typical features of  $\beta$ -sheet structures. A decrease in intensity was observed for the CD spectrum of AcPHF6 in the presence of **25**, suggesting that the abundance of  $\beta$ -sheet structures is lower. On the other hand, the CD profile of AcPHF6 in the presence of **27** lacks for the typical bands of  $\beta$ -sheet structures, with the peptide displaying an unordered conformation. Both behaviors are consistent with the inhibitory trends highlighted by the fluorescence-based assay; therefore, CD data confirm the inhibitory capacity of derivatives **25** and **27**, and suggest that their anti-aggregating activity is related to their ability to stabilize the AcPHF6 peptide in a less fibrillogenic conformation, with derivative **27** being much more effective in doing so.



**Figure 3.19.** CD spectra of AcPHF6 (100  $\mu$ M) in the absence (solid) and in the presence of **25** (20  $\mu$ M, dashed) or **27** (20  $\mu$ M, dotted), measured after 2 h incubation.

In order to better characterize the morphology of the fibrils formed by the AcPHF6 peptide alone and in the presence of **25** and **27**, we performed atomic force microscopy studies. Solutions of 50  $\mu$ M phosphate buffer with the AcPHF6 alone and in the presence of **25** and **27** were prepared in the same conditions employed for the ThT studies (but in the absence of ThT). After incubation, aliquots of the solutions were subjected to ultrafiltration to separate the low molecular weight un-polymerized peptide fraction from the high-molecular weight fiber fraction, and such high-

molecular weight fraction was adsorbed on the surface of mica for AFM imaging. As shown in Figure 3.20, long and thick amyloid fibrils were imaged after adsorbing on mica the solution of AcPHF6 incubated alone. Here, fibers with individual diameters of 10 nm or more (and lengths of several hundreds of nanometers) are found in bundles and higher-order aggregates (Figure 3.20A). On the other hand, the absorption of AcPHF6 incubated in the presence of **25** and **27**, displayed only much smaller structures (possibly oligomers or protofibrils, Figure 3.20 B and C).



**Figure 3.20.** AFM micrographs of amyloid fibers obtained from the aggregation of 50  $\mu$ M AcPHF6 peptide in phosphate buffer in the absence (A), and in the presence of 10  $\mu$ M **25** (B) and **27** (C).

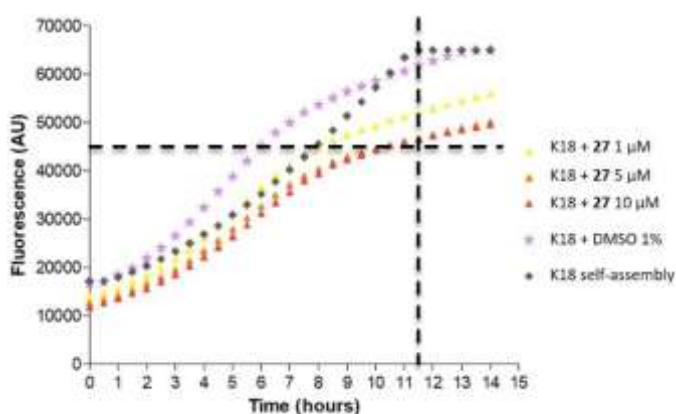
### 3.5.6 K18 and full-length tau aggregation and inhibition studies

These experiments were performed by me and Martina Rossi, under the supervision of Dr. Fabio Moda, at the Istituto Neurologico Carlo Besta, Milan.

Encouraged by the results obtained with the AcPHF6 peptide, we decided to test the anti-aggregating properties of **27** in more clinically relevant models of tau aggregation. As described before, the formation of insoluble tau fibrils seems to derive from a nucleation-elongation process, by which misfolded tau monomers slowly assembled into nucleating cores followed by a rapid elongation from the core to yield fibrils. Tau fibrillization process can be replicated in vitro, however, recombinant tau shows very little intrinsic tendency to aggregate due to the lack of a series of post-translational modifications required for its aggregation. Indeed, recombinant truncated tau isoforms

are more frequently used for in vitro tau aggregation, where the addition of anionic co-factors (e.g. heparin, arachidonic acid) results in the formation of fibrils that resemble those observed in the brains of AD patients.<sup>263, 264</sup>

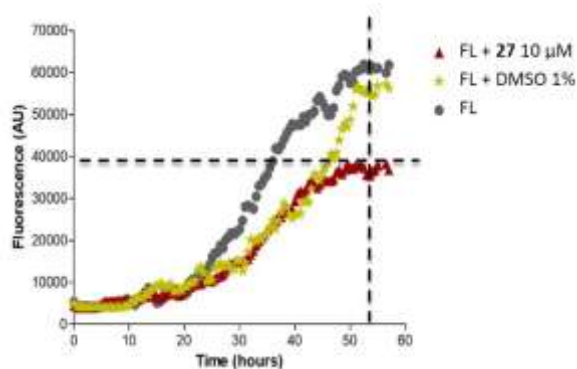
Thus, **27** was firstly evaluated in a heparin-induced tau assembly assay, in which the fibrillization of the truncated K18 tau fragment (comprising four microtubules-binding repeats) was monitored by ThT. The aggregation of the tau fragment K18 was achieved through the Real-Time Quaking-Induced Conversion (RT-QuIC) technique.<sup>265</sup> As shown in Figure 3.21, K18 alone was completely aggregated after 11-12 h and the fluorescence intensity reached the highest value. On the other side, the treatment of K18 with **27** at three different concentrations (1, 5, 10  $\mu$ M) resulted in a delay of K18 self-aggregation. Moreover, the analysis of the averaged fluorescence intensities at the plateau of the kinetic showed a 35% inhibition of the aggregation process.



**Figure 3.21.** RT-QuIC analysis of **27** activity on tau K18 self-aggregation monitored by ThT fluorescence.

Motivated by the promising results obtained with the K18 tau fragment, we also tested the inhibitory activity of **27** towards the heparin-induced self-aggregation of full-length 2N4R tau (FL), through RT-QuIC technique. Treatment of 2N4R tau with **27** (10  $\mu$ M) did not show a delay in the aggregation process, as can be seen from Figure 3.22. However, from the analysis of the averaged fluorescence intensities at the plateau of the kinetic, **27** shows a 30% inhibition of the aggregation process. Importantly, this

result is in agreement with that obtained with K18 fragment, confirming the potential of **27** as tau anti-aggregating compound.



**Figure 3.22.** RT-QuIC analysis of **27** activity on full-length tau self-aggregation monitored by ThT fluorescence.

### 3.5.7 Okadaic acid-induced tau hyperphosphorylation cell model

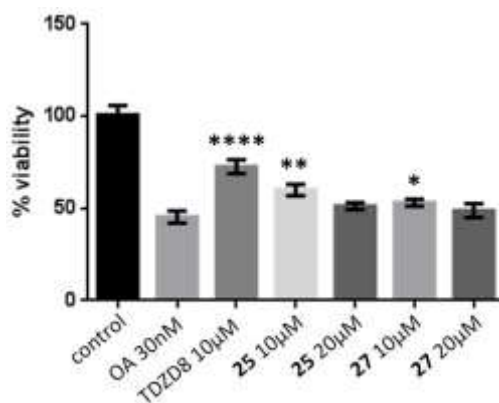
These experiments were performed under the supervision of Prof. Ana Martinez, at the Centro de Investigaciones Biológicas, CSIC, Madrid.

Increasing evidence has suggested that inhibition of phosphatases by okadaic acid (OA) represents the most robust way to induce PHF-like tau hyperphosphorylation. Moreover, OA was identified as a potent neurotoxin for cultured neuronal cells many years ago,<sup>266</sup> as it is able to induce time- and dose-dependent apoptotic changes in such cells.<sup>267</sup> Thus, different cell lines and primary neuronal cultures have been used to establish cellular models of OA-induced neurodegeneration.<sup>268-270</sup> In addition, OA-treated rodents recapitulate the morphological hallmarks of AD.<sup>269</sup>

To confirm the anti-tau profile of **25** and **27** in a cellular context, we further explored their rescue potential in the OA-induced neurodegeneration cell model, in comparison with TDZD8 (data provided by Prof. A. Martinez).

We studied the effect of **25**, **27** and TDZD8, at two different concentrations (10 and 20  $\mu$ M), in a human neuroblastoma cell line (SH-SY5Y) treated with OA (Figure 3.23). As

expected, OA induced a decrease in cell viability higher than 50%. Importantly, both **25** and **27** were able to increase the cell viability probably due to the decrease on tau phosphorylation by GSK-3 $\beta$  inhibition. Particularly, **25** was only slightly less effective than TDZD8. To note, other indole derivatives have been reported as effective in counteracting OA-induced neurotoxicity.<sup>225</sup>



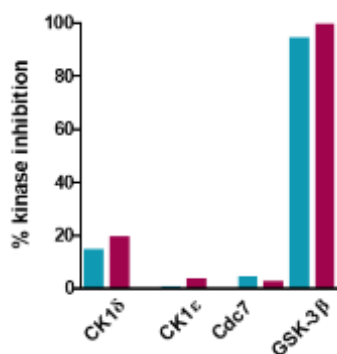
**Figure 3.23.** OA-induced neurodegeneration cell model. Effects of treatment with **25** and **27**. Results are mean value  $\pm$  SEM, represented as relatives to control value (=100), of n=6 from three independent experiments.

### 3.5.8 Inhibitory activity profile towards casein kinase 1 (CK1) $\delta$ and $\epsilon$ , and cell division cycle 7 (Cdc7)

These experiments were performed under the supervision of Professor Ana Martinez, at the Centro de Investigaciones Biológicas, CSIC, Madrid.

Finally, one of the main challenges to overcome when modulating a protein kinase is the selectivity over other protein kinases. Thus, to address this issue, we tested **25** and **27** on a small panel of 3 selected kinases: casein kinase 1 (CK1)  $\delta$  and  $\epsilon$ , and cell division cycle 7 (Cdc7). Cdc7 is another representative cell cycle regulation kinase,<sup>271</sup> which should show low binding affinity toward new GSK-3 $\beta$  hits to avoid possible toxicities. While CK1 $\delta$  and CK1 $\epsilon$  represent GSK-3 $\beta$  phylogenetically diverse kinases, able to phosphorylate tau.<sup>272</sup>

Therefore, the inhibition of **25** and **27** toward CK1 $\delta$ , CK1 $\epsilon$ , Cdc7 and GSK-3 $\beta$  were assessed at 10  $\mu$ M. Encouragingly, both compounds only poorly, or not inhibited at all, CK1 $\delta$ , CK1 $\epsilon$ , and Cdc7 (Figure 3.24), while they inhibited GSK-3 $\beta$  by 95% and 100%, respectively. This reveals a preliminary selectivity of both **25** and **27** towards GSK-3 $\beta$ .



**Figure 3.24.** Inhibitory activity profile of **25** (blue) and **27** (purple) towards human CK1 $\delta$ , CK1 $\epsilon$ , Cdc7 and GSK-3 $\beta$  kinases, at a fixed concentration of 10  $\mu$ M.





## **Chapter IV**

### **Fluorescent bivalent ligands**

**with potential combined therapeutic and diagnostic activities**

**against Alzheimer's disease**

## **4.1 Diagnostics in Alzheimer's disease**

Pre-mortem diagnosis of Alzheimer's disease, relies on clinically documenting decline in memory, cognition, and function over time. However, symptoms associated with cognitive decline are difficult to separate from those of normal ageing processes. Neurodegeneration is estimated to start 20 to 30 years before the first clinical symptoms appear. Thus, after AD diagnosis, the pathology has already caused severe brain damage.<sup>52</sup>

In addition, a definitive diagnosis can be obtained only following biopsy or autopsy, as it is only by looking at the affected brain that a pathologist can be able to see exactly what occurred in specific areas of the brain. Considering that brain biopsy is an invasive procedure, and that currently there is no effective treatment for AD, brain biopsy is rarely performed. Thus, a definitive AD diagnosis can be obtained only after clinical demonstration of dementia, and identification of the pathological hallmarks of the disease (i.e.  $\beta$ -amyloid plaques and neurofibrillary tangles) through autopsy.<sup>273</sup>

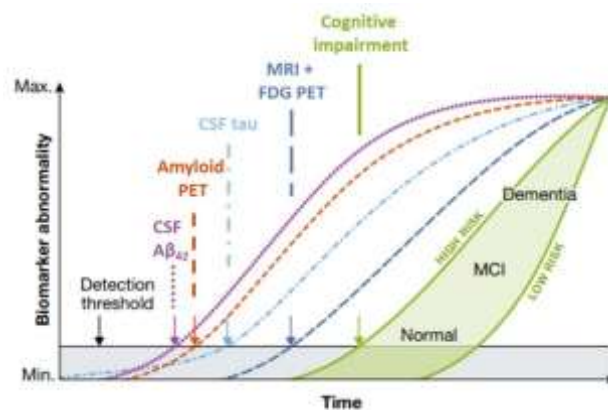
Unfortunately, the lack of an early diagnosis of AD, strongly impacts the development of effective drugs. The failure of many drug candidates has also been attributed to their late administration, when the pathology is too advanced. Based on this, while AD drug discovery has experienced a profound productivity crisis in recent years,<sup>39</sup> the field of diagnostics has been booming.

The first step to find an easy and accurate way to diagnose AD before clinical symptoms are evident, is to find the appropriate biomarkers. A biomarker is a "characteristic that is objectively measured and evaluated as an indicator of normal biological processes, pathogenic processes, or pharmacologic responses to a therapeutic intervention".<sup>274</sup> Importantly, identification of appropriate "diagnostic" biomarkers is essential for distinguishing individuals with prodromal signs of AD from healthy aging adults, or from patients suffering from other types of dementia. To date, there are no universally validated biomarkers for AD, but several candidates have been identified and began evaluating in preclinical models. Particularly, the defining and main pathological hallmarks of AD are extracellular A $\beta$  deposits and intracellular NFTs. Thus, these pathological hallmarks should precede clinical symptoms by several

years.<sup>275</sup> Based on this, in vivo imaging of A $\beta$  and tau seems to be particularly suitable for diagnosing patients at risk and for detecting AD before dementia occurs.

The tremendous advances in molecular imaging have allowed us to non-invasively visualize A $\beta$  deposition directly in AD patients, thanks to the current availability of several amyloid tracers.<sup>276</sup> However, although A $\beta$  aggregates have been clearly associated with AD pathology, there is still an active discussion as to whether their presence closely correlates with disease progression and severity. Indeed,  $\beta$ -amyloid imaging has not been approved for the diagnosis of AD but rather as a diagnostic method for the exclusion of AD in cognitively impaired and amyloid PET-negative patients. Conversely, it is being evaluated as a diagnostic tool for defining the preclinical stages of AD.<sup>277</sup> In contrast to A $\beta$ , the density and neocortical spread of NFTs very well correlate with progressive neuronal degeneration and cognitive impairment. These evidence potentially make imaging of NFTs as a more desirable biomarker for AD, with respect to A $\beta$ .<sup>63</sup>

In 2010, Jack et al. proposed the first biomarkers model of the AD pathological cascade. In this model, the vertical axis represented the severity of biomarker abnormality and the horizontal axis represented the progression along the AD pathophysiological pathway.<sup>53</sup> Few years later, based on the advanced published in the literature, the same authors revised their model (Figure 4.1).<sup>278</sup>



**Figure 4.1.** Hypothetical temporal model integrating AD biomarkers (modified from Jack, 2013).<sup>278</sup>

The new model shows the temporal evolution of AD biomarkers in relation to each other and to the progression of clinical symptoms. The horizontal axis is expressed as time, not clinical disease stage. Importantly, this model shows that the manifestation of tau pathology can precede A $\beta$  deposition in time, but only at a sub-threshold biomarker detection level. On the other side, A $\beta$  deposition occurs independently and rises above the biomarker detection threshold, inducing the acceleration of tauopathy.

All in all, these evidence might suggest that we should not focus on a single biomarker for AD, rather we should take advantage from the combined information coming from imaging probes directed towards both A $\beta$  and tau. Based on this, over the last decade, several small molecules have been suggested as potential A $\beta$  or tau imaging probes. Importantly, since A $\beta$  plaques and NFTs share a similar  $\beta$ -sheet structure, it is not surprising that structural similarities exist between imaging agents for both species.

#### **4.1.1 Imaging of amyloid plaques and NFTs by fluorescent tracers**

Through the years, great progresses have been made in the field of molecular imaging with the aim to detect abnormal amyloid deposits in vivo.

To date, positron emission tomography (PET) is one of the most popular clinical imaging techniques. PET imaging plays also a unique role in drug development because of its ability to quantify drug properties in vivo. By employing radiotracer principles, PET is capable of quantitatively measuring a variety of in vivo processes, without perturbing the biochemistry of the systems.<sup>279</sup> For these reasons, PET is considered a key molecular imaging technique, and it has revolutionized the ability to image molecular processes in the brain.<sup>280, 281</sup> To date, the United States Food and Drug Administration (FDA) has approved three PET probes for the estimation of A $\beta$  neuritic plaque density in adult patients with suspected AD or other causes of cognitive decline: florbetaben,<sup>282</sup> florbetapir,<sup>283</sup> and flutemetamol.<sup>284</sup> However, PET imaging suffers from many drawbacks. Its routine use for AD is unlikely, due to its financial and technical cost.<sup>285</sup> Moreover, the short half-lives of commonly used positron-emitting

isotopes requires the on-site synthesis of PET tracers and access to radiochemistry equipment and a cyclotron.

On the other side, optical imaging is emerging as a cheaper and non-invasive in vivo tool with improved sensitivity and resolution if compared with other routinely used methodologies, such as magnetic resonance imaging (MRI) and computed tomography (CT).<sup>286, 287</sup> However, until the very recent years, fluorescent microscopy application to the intact animal has been limited to imaging few hundreds micrometers below the surface. Therefore, the current ability to perform minimally invasive deep in vivo fluorescence imaging in intact-animal studies, has represented a breakthrough. Indeed, today there is a growing interest in fluorescence spectroscopy as a non-invasive alternative for early diagnosis, allowing the real-time visualization of biomolecules in living systems.

Importantly, fluorescent probes have to possess appropriate features for a potential in vivo application. Among all, a fluorescent probes should be able to emit fluorescence in the far-red or near-infrared (NIR) region (600-900 nm). NIR light is particularly suitable for the in vivo imaging of molecular processes due to its acceptable depth of penetration, non-invasive operation, minimal interferences from auto-fluorescence of biological matter, and minimal photo-damage to biological samples.<sup>288</sup> Moreover, in the NIR spectral range, the absorption of fluorescent signals by body tissues is minimal.

#### *4.1.1.1 Small molecules fluorescent probes for in vivo A $\beta$ plaques imaging*

Following the wide use of Thioflavin T (ThT, Figure 4.2)<sup>289</sup> and Congo Red (CR, Figure 4.2)<sup>290</sup> in histopathology, the first evidence of the possibility of a fluorescent staining directly in mouse models of AD, was provided in 2001.<sup>291</sup> In this study, a novel imaging approach was developed, using in vivo multiphoton microscopy and the Thioflavin S (ThS, Figure 4.2) dye, to image senile plaques in an AD mouse model. Although ThS was effectively able to visualize A $\beta$  plaques, it must be administered topically, because it does not cross the BBB.

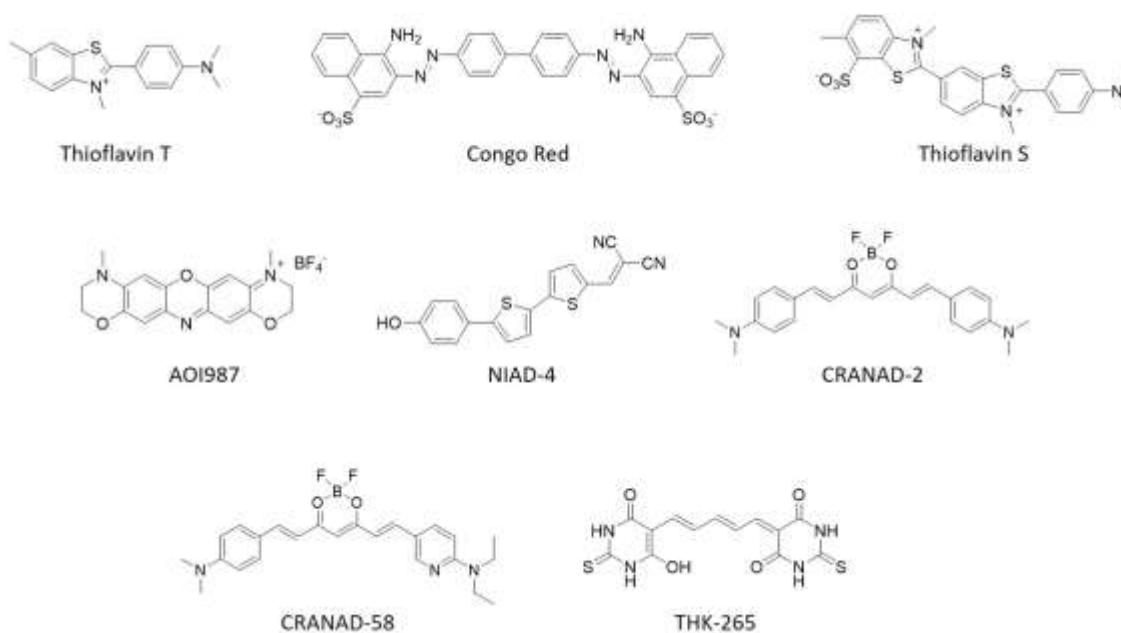
Thus, after the development of some ThT and CR derivatives, in which the permanent charge or their ionizable nature hindered their BBB crossing, it was clear that the

design of fluorescent dyes for in vivo applications needed to incorporate several other criteria. Among them: (i) a suitable wavelength interval of absorption and emission (NIR range) and a large Stokes shift; (ii) the ability to rapidly enter the brain after intravenous injection; (iii) specific labeling of the A $\beta$  deposits with concomitant rapid clearing of the unbound dye.<sup>52</sup>

In 2005, the oxazine derivative AOI987 (Figure 4.2) suggested, for the first time, the feasibility of non-invasively imaging cerebral  $\beta$ -amyloid deposits in living mice.<sup>292</sup> The compound readily penetrated the BBB, bound to A $\beta$  fibrils with a  $K_d$  of 220 nM, and showed promising fluorescence properties, with absorption and emission maxima at 650 and 670 nm. AOI987, after intravenous administration, was able to image A $\beta$  plaques in living APP23 mice, with intact cranium and BBB. For the first time, it was also possible to quantify the A $\beta$  load by spatial integration of fluorescence intensities. Importantly, the non-invasiveness of AOI987 imaging allowed repeated measurements over the life-time of the mouse, and provide an ideal tool for monitoring disease progression in AD animal models, and assessing the efficacy of the potential treatment.<sup>292</sup>

Since then, the use of molecular fluorescence-based neuroimaging, particularly near-infrared (NIR) imaging, has rapidly gained momentum.<sup>287</sup>

The bithiophene derivative NIAD-4 (Figure 4.2) represents the first rationally designed A $\beta$  probe.<sup>293</sup> Swager and co-workers merged the pharmacokinetic requirements with an electronic structure design to produce a compound possessing a suitable spectral range of the absorption and emission bands, with the explicit aim to develop a fluorescent probe to be used in vivo. In in vivo two-photon imaging experiments in transgenic mice, NIAD-4 readily crossed the BBB after intravenous injection, showed excellent binding affinity ( $K_d = 10$  nM) and a dramatic enhancement of the fluorescence intensity when labeling A $\beta$  aggregates.



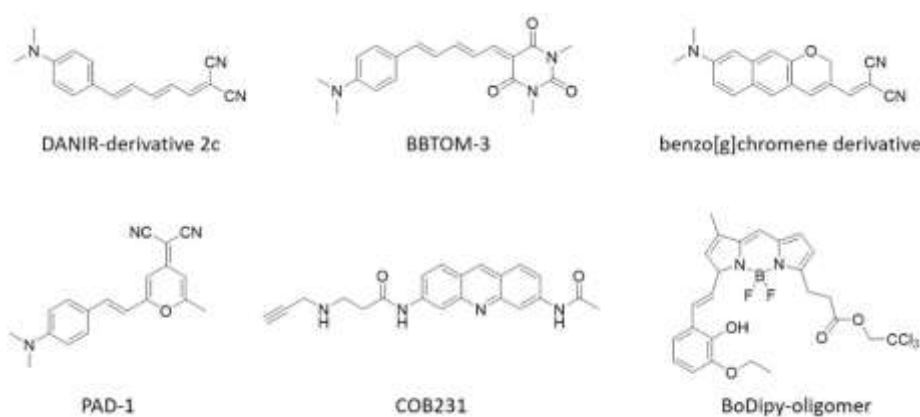
**Figure 4.2.** Chemical structures of the first developed A $\beta$  fluorescent probes.

In 2009, the first curcumin-based NIR probe CRANAD-2 (Figure 4.2) was developed. The rationale behind the design of CRANAD-2 started from curcumin, and was based on different considerations: (i) the red shift benefit of boron incorporation could be used to design boron-containing curcumin derivatives; (ii) the introduction of a difluoro-boronate moiety into curcumin should generate an appropriate red shift; (iii) replacing the phenolic hydroxyl groups with the N,N'-dimethyl group should further enable red-shifted absorption and, consequently, an additional red-shift emission.<sup>294</sup> The synthesis of several derivatives lead to the discovery of CRANAD-58 (Figure 4.2), showing excitation and emission into the NIR region, together with significant fluorescence property changes upon mixing with both soluble and insoluble A $\beta$  species. Importantly, *in vivo* NIR imaging revealed that CRANAD-58 was able of differentiating transgenic and wild-type mice, as young as 4-months old, the age that apparently lacks visible A $\beta$  plaques.<sup>295</sup>

Another example of A $\beta$  fluorescent probe, is represented by the thiopyridone dimer THK-265 (Figure 4.2).<sup>296</sup> THK-265 was discovered by screening a large pool of commercial NIR fluorescent dyes for their binding toward A $\beta$ . Based on promising preliminary *in vivo* studies, THK-265 was used to develop a systemic protocol for staging disease progression by evaluating different A $\beta$  aggregation levels in mice of different age. The

intensity of the fluorescent signal correlated well with the plaque burden, indicating the utility of THK-265 for direct monitoring A $\beta$  aggregation progression.<sup>297</sup>

More recently, several others A $\beta$  fluorescent probes were developed, such as: DANIR-derivatives,<sup>298-300</sup> BBTOM-3,<sup>301</sup> benzo[g]chromene derivatives,<sup>302</sup> the dicyanomethylene-4H-pyran-based dye PAD-1,<sup>303</sup> the proflavine COB231,<sup>304</sup> and the oligomer-specific BoDipy-Oligomer<sup>305</sup> (Figure 4.3).



**Figure 4.3.** Chemical structures of recently developed A $\beta$  fluorescent probes.

#### 4.1.1.2 Small molecules fluorescent probes for *in vivo* NFTs imaging

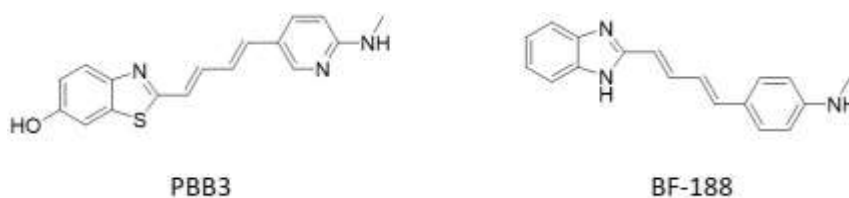
As highlighted before, there is an urgent need for tau imaging tools to complement A $\beta$  imaging tracers. To date, only few fluorescent probes for NFTs have been reported in the literature, likely due to the fact that tau tangles are present inside the neurons. Thus, tau has been less accessible and fewer fluorescent probes have been discovered, compared to A $\beta$  ones.

In 2013, the first series of fluorescent and BBB-penetrant compounds capable of detecting tau aggregates in AD and non-AD tauopathies was developed. The discovery of these compounds, named PBBs, was based on the finding that the affinity for tau inclusions of different compounds, could be attributed to a core structure with a specific extent ranging from 13 to 19 Å. Indeed, the derivative PBB3 (Figure 4.4), intravenously administrated in PS19 mice, was able to bind to intracellular tau



inclusions. Importantly, the corresponding radiolabeled derivative [ $^{11}\text{C}$ ]PBB3, was one of the first reported human PET tau imaging tracers.<sup>306</sup>

Another fluorescent probe, the benzimidazole BF-188 (Figure 4.4) was developed in 2014. Curiously, BF-188 emit a different color of fluorescence when bound to A $\beta$  and tau aggregates. Particularly, using multispectral fluorescence imaging (MSFI) it is possible to differentiate the deposits of the two proteins with a single fluorescent probe. BF-188 showed sufficient brain uptake and rapid wash-out in normal mice, thus it was very promising for further studies.<sup>307</sup>



**Figure 4.4.** Chemical structures of tau fluorescent probes.

Other selective tau probes have been developed, but their potential has been evaluated mostly in in vitro assays. Bis(arylvinyl)pyrazines, -pyrimidines, and -pyridazines were able to detect A $\beta$  and tau aggregates in human brain tissues, with some derivatives showing higher selectivity for aggregated tau.<sup>308</sup> Curcumin derivatives were able to detect tau aggregates in living SH-SY5Y cells, showing favorable fluorescence properties upon binding to tau fibrils, thus make them promising NIR fluorescent probes. A novel tau-selective NIR fluorescence probe was developed by combining previously identified core scaffolds: the 3,5-dimethoxy-N,N-dimethylanilin-4-yl moiety of DANIR-derivatives, with the characteristic donor- $\pi$ -acceptor architecture of the A $\beta$  probe MCAAD-3. These derivatives exhibited tau-selective fluorescence properties in the NIR range, and were able to detect tau aggregates in live SH-SY5Y cells and in human AD brain sections.<sup>309</sup> Finally, rhodanine and thiohydantoin derivatives has been studied for detecting tau pathology in AD patients brains.<sup>231</sup> Particularly, the thiohydantoin derivative TH2 (Figure 3.8) showed high specific binding to tau aggregates compared to the rhodanine derivatives.

However, as the fluorescence properties of the compounds were not optimal, the corresponding radiolabeled derivatives were further investigate.<sup>231</sup> Two years later, rhodanine-3-acetic acid derivatives were proposed as fluorescent probes for the imaging of NFTs in brain tissues of AD patients.<sup>310</sup>

## **4.2 The theranostic approach in Alzheimer's disease**

In traditional approaches, imaging probes and drugs are pursued separately, which is time-consuming and expensive. To overcome these disadvantages, developing agents that have potential for both therapy and imaging is highly desirable. These agents have already been developed at research level with the name of “theranostics”. Theranostics use single chemical entities to simultaneously deliver therapy and diagnosis, and represent a more recent and innovative way of implementing translational medicine and personalized approaches.<sup>311</sup>

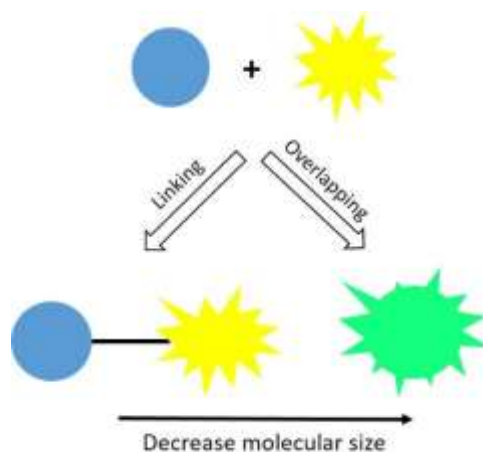
The term “theranostic” was first coined by John Funkhouser, in a press release from the company Cardiovascular Diagnostics in 1998, to describe a material that allows the combined diagnosis, treatment, and follow-up of a disease.<sup>312</sup> Since its first definition, the concept of theranosis has expanded, being nowadays quite broad in its meaning. The dedicated journal *Theranostics* says: “Theranostics is a concept that was originally raised to refer to the efforts of integrating imaging and therapy. As an emerging interdisciplinary, it is related to, but different from traditional imaging and therapeutics.”<sup>313</sup>

The field of theranostics, still in its beginning, has exploded over the last years, with agents reaching clinical trials, especially in the field of cancer.<sup>314</sup> Though CNS disorders does not match oncology due to a poorer understanding of the disease molecular origins, theranostic approaches against neurodegeneration begin to be intensively pursued.<sup>315</sup>

Indeed, in neurodegenerative diseases, and particularly in AD, the theranostic approach seems to be very promising as the pathological hallmarks of the disease overlap with the therapeutic targets. A $\beta$  aggregates and NFTs, are neuropathological hallmarks of the disease, and they are recognized as effective biomarkers for clinical diagnosis. Moreover, they are both considered as potential therapeutic targets for drug discovery endeavors. Thus, both A $\beta$  and tau proteins have been undoubtedly regarded from a double diagnostic and therapeutic perspectives.

From the examples reported in the literature, two main rational strategies for the design of theranostic compounds can be envisaged: (i) linking structural elements from

diagnostic and therapeutic agents, to make a new conjugate molecule; or (ii) overlapping or highly integrating the diagnostic and therapeutic moiety in a single chemical entity (Figure 4.5).<sup>311</sup>



**Figure 4.5.** Design strategy of theranostics (modified from Bolognesi, 2016).<sup>311</sup>

In the first case, conjugates ligands contain two starting units, one carrying the therapeutic properties, and the other carrying the diagnostic properties. On the other side, the second approach can show narrower applicability, as the fundamental prerequisite is that an imaging probe and a drug share a common structural scaffold. Importantly, in the case of AD, a particular strength is that there can be overlap between the molecular properties responsible for recognizing and consequently inhibiting the amyloid proteins, and those responsible for their fluorescence imaging. Indeed, extended  $\pi$ -conjugated flat systems are considered important features for binding and interfering with amyloids.<sup>293, 316</sup> Clearly, compounds deriving from a conjugating approach are more likely to have a high molecular weight and less likely to have favorable BBB permeation. While overlapped compounds are likely to have lower molecular weight and should have better drug-like properties.

#### 4.2.1 Theranostic small molecules in AD

Despite huge development is taking place in the field of AD theranostics, it was not until 2012 that the first examples appeared in the literature.

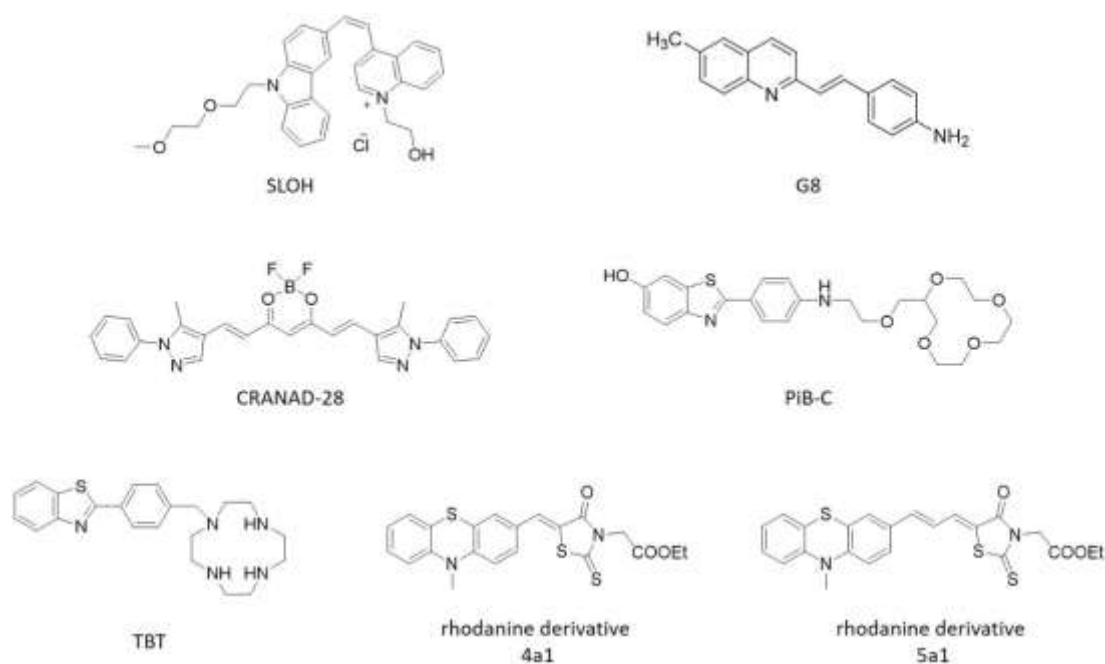
The first “multifunctional fluorophore” published in the literature was SLOH (Figure 4.6), a carbazole-based cyanine fluorophore, able to directly image the dynamics of A $\beta$  fibrillogenesis and to inhibit its aggregation.<sup>317</sup> SLOH showed an optimal intrinsic fluorescence, a strong progressive increase in fluorescence intensity and a blue shift in the emission maximum, upon binding to A $\beta$  fibrils. In parallel, SLOH was also able to inhibit A $\beta$  aggregation, interfering with both the nucleation and elongation processes. SLOH was also preliminary tested in vivo, and it was able to enter the brain of living transgenic mice and to specifically target A $\beta$  plaques.<sup>317</sup>

Another molecule intentionally proposed as an in vitro theranostic was the styrylquinoline G8 (Figure 4.6).<sup>318</sup> The starting point in the design of this compound was the finding that several styryl derivatives, developed to improve the CNS properties of Congo Red, were employed as AD imaging agents in vivo.<sup>319</sup> Moreover, in 2012, styryl-1H-indole and styrylquinoline derivatives were reported as SPECT (Single-Photon Emission Computed Tomography) imaging probes. Thus, the styryl moiety appears to be very promising for labeling and interfere with pathological fibrillary aggregates, while the quinoline moiety was selected for its “privileged scaffold” nature, displaying good pharmacokinetic properties and drug-likeness. Furthermore, an amino group was purposely introduced, in order to have an electron-releasing substituent conjugated with the quinoline nitrogen, as the goal was to develop a NIR fluorescent compound. G8 showed a strong hypsochromic shift of the emission maximum, together with a hyperchromic effect upon A $\beta$  binding. Moreover, G8 was a moderate inhibitor of the A $\beta$  aggregation process, as shown by ThT-based fluorometric assay. As the compound was also able to inhibit prion replication and to label prion fibrillary aggregates in living ScGT1 cells, it was proposed as promising starting point for the development of theranostic compounds for both AD and prion diseases.<sup>318</sup>

Another example of rationally designed theranostic agent is represented by the curcumin derivative CRANAD-28 (Figure 4.6).<sup>320</sup> The starting point for its discovery was a fluorescent curcumin derivative, CRANAD-2 (Figure 4.2), able to detect A $\beta$

aggregates, but showing a low quantum yield (QY).<sup>294</sup> The substitution of the phenyl ring of CRANAD-2 with a pyrazole, increased the QY of the compound, as the inductive electron-withdrawing effect of the nitrogen of pyrazole led to a low tendency of electron delocalization in the system. Then, substitution of the pyrazole with an N-1 phenyl pyrazole, led to the discovery of CRANAD-28. Thanks to the rational design, CRANAD-28 showed promising fluorescence properties in terms of optical range (emission peak at 578 nm) and QY. CRANAD-28 was able to label A $\beta$  plaques ex vivo, in brain slices. Then, as it was able to cross the BBB, it was evaluated for the two-photon imaging of A $\beta$  plaques in APP/PS1 mice. In parallel, CRANAD-28 was also able to inhibit natural and copper-induced A $\beta$  crosslinking.<sup>320</sup> Thus, despite its emission maximum is not within the NIR region, CRANAD-28 was the first theranostic providing an in vivo proof of principle in an AD mouse model.

The same research group proposed another useful strategy for the development of A $\beta$ -directed theranostics, inhibiting A $\beta$  aggregation through non-covalent modifications at its surface. Particularly, it is known that crown ethers can form stable complexes with protonated amines, through the formation of H-bonds. It is also known that the stabilization of misfolded A $\beta$  peptides derived from inter-sheet salt bridges and intra-peptide salt bridges.<sup>321</sup> Thus, breaking down these interactions should attenuate the aggregation process. With this in mind, the authors hypothesized that crown ethers could break down the salt bridges, attenuating the stability and, consequently, the A $\beta$  aggregation process. After confirming the effective ability of 12-crown-4-ether to form complexes with charged amino acids, and to efficiently inhibit A $\beta$  aggregation through ThT assay, the crown ether moiety was link to PiB, the widely used A $\beta$  PET ligand, to achieve a more selective effect.<sup>322</sup> The new conjugate, PiB-C (Figure 4.6) showed an A $\beta$ -aggregation inhibitory effect stronger than PiB, together with a neuroprotective ability in SH-SY5Y cells. Two-photon imaging analysis shown that PiB-C could clearly label plaques in APP/PS1 mouse brains ex vivo, but also in vivo.<sup>322</sup>



**Figure 4.6.** Chemical structures of theranostic compounds for AD.

A theranostic small molecule with a peculiar profile is TBT (Figure 4.6).<sup>323</sup> The inspiration for the design of TBT came from the therapeutic potential of metal chelators to reduce metal-induced A $\beta$  aggregation and neurotoxicity in AD.<sup>324</sup> Based on this, the authors hypothesized that proper modifications of chelators with sensing functions would be a promising strategy for developing a novel chelator as a dual functional probe and a disaggregating agent for A $\beta$  aggregation induced by Zn<sup>2+</sup> and Cu<sup>2+</sup>. Thus, they select a metal chelating 1,4,7,10-tetraazacyclododecane (cyclen) group, and the A $\beta$ -targeting 2-phenylbenzothiazole group, and following a linking strategy they develop a new theranostic compound. TBT was able to specifically inhibit Zn<sup>2+</sup>- and Cu<sup>2+</sup>-induced A $\beta$ <sub>40</sub> aggregation, and to monitor the disaggregation of A $\beta$ <sub>40</sub> aggregates in brain homogenates of APP<sup>swe</sup>/PSEN1 transgenic mice. Moreover, TBT showed specificity, neuroprotectivity, BBB permeability, and rapid wash out, highlighting its potential as theranostic tool for AD.<sup>323</sup> Needless to say, *in vivo* studies are now essential to evaluate the effective applicability of this compound.

Finally, the most recently proposed theranostic small molecules are phenothiazine-rhodanine-based compounds.<sup>325, 326</sup> Aiming to develop a theranostic agent for NIR fluorescence imaging, the authors selected the donor-acceptor architecture bridged by

a conjugated  $\pi$ -electron chain. After the synthesis of a series of derivatives, compound 4a1 (Figure 4.6) was selected for further studies. Indeed, compound 4a1 displayed a significant fluorescence intensity increase in the emission spectra upon binding A $\beta$  aggregates, with an emission maximum of 670 nm. Moreover, 4a1 was able to fluorescently stain A $\beta$  plaques in brain and eye slices in vitro, demonstrating its excellent targeting ability. 4a1 also showed high stability in mouse serum, together with a low toxicity in human neuronal cells. From a medicinal chemistry perspective, 4a1 offers advantages of a small molecule scaffold, easily amenable to further manipulation in order to improve its fluorescence properties and amyloid-binding properties.<sup>325</sup> Indeed, 4a1 was the starting point for the development of a new library of theranostic compounds. The most promising derivative was compound 5a1 (Figure 4.6), which differs from 4a1 only for the insertion of another double bond between the phenothiazine and the rhodanine moieties.<sup>326</sup> With compound 5a1 the authors were able to further shift the emission to the NIR region, to strengthen the binding affinity towards A $\beta$  aggregates, to enhance the inhibition potency, and to low cytotoxicity. Thus, 5a1 represents the last developed theranostic agents for NIR imaging of  $\beta$ -amyloid plaques and inhibition of  $\beta$ -amyloid aggregation.<sup>326</sup>

In the last ten years, several efforts have been made in the development and application of fluorescent theranostic small molecules for AD. The theranostic field in AD is still at its infancy, and no registered theranostics are available in the market. Importantly, many crucial issues need to be addressed and the translational potential of such compounds has been only marginally investigated. No one knows if theranostics will reach the clinics for AD; however, there are already promising evidence that these unconventional tools might increase the overall understanding of AD, and might be critical for finding and personalizing its treatment.<sup>311</sup>



### **4.3 Design of fluorescent bivalent ligands**

The aim of this project was the development of a small library of fluorescent bivalent ligands, as potential theranostic tools for Alzheimer's disease. As highlighted above, combining therapy and diagnosis in a single molecular entity seems particularly suitable in AD, as the pathological hallmarks overlap with the therapeutic targets.

Several evidence suggest that directly targeting the proteins involved in the fibrillization process could represent a valid therapeutic tool against PMDs.<sup>327</sup> Thus, several drug discovery approaches have been employed for developing small molecules able to interfere with protein-protein interactions (PPIs), in order to avoid propagation or to prevent fibril formation. However, the modulation of PPIs with small molecules is very challenging for medicinal chemists for several reasons. Most disease-modifying proteins lack druggable active site or pockets, and we also lack high-resolution structural information on amyloid fibrils and aggregates. Moreover, the contact surfaces between proteins usually involve a multitude of polar and hydrophobic interactions distributed across a large interface. Thus, a small molecule has difficulties in achieving a tight binding, due to insufficient interactions. Finally, the protein-protein interfaces are usually flat and this further limits the site of contact to only one side of a small molecule.<sup>328, 329</sup> Thus, anti-aggregating compounds should be designed, at least initially, starting from the structure of known inhibitors of the aggregation process.

Looking at the literature, several anti-aggregating compounds share a symmetrical bifunctional structure, consisting of two identical protein recognition motifs (PRMs) joined by an appropriate spacer (Figure 4.7). These symmetrical compounds have been described as bivalent compounds or "palindromic compounds", as their structure can be read in the same way in the forward or reverse directions.<sup>330</sup> Considering the oligomeric and repetitive structure of fibrillar aggregates, it has been hypothesized that bivalent compounds could interact simultaneously with two binding surfaces. Thus, bivalent ligands should allow to achieve a higher potency and to significantly enhance the recognition process. The synergy between two PRMs connected by a spacer is mainly due to two factors: (i) an increase in the local concentration of the

active moiety; (ii) since a bivalent ligand must first undergo univalent binding, in this bound-state the binding of the second pharmacophore to a neighboring recognition site is favored due to entropic factors.<sup>331</sup>

Several evidence suggest that lipophilic and aromatic residues able to provide van der Waals and  $\pi$ - $\pi$  stacking interactions, connected by a central core, might modulate PPIs. Indeed, many anti-aggregating bivalent compounds share a common chemical structure, consisting of planar  $\pi$ -conjugated rings. Importantly, extended  $\pi$ -conjugated flat systems are considered important features not only for binding and interfering with amyloids, but also for achieving optimal fluorescence properties.<sup>293</sup>



**Figure 4.7.** Schematic depiction of a bivalent compound, in which the two protein recognition motifs are joined by an appropriate linker.

In light of this, we focused on a bivalent strategy to identify novel ligands to combat AD, by designing and synthesizing a small library of bivalent 2,4-thiazolidinedione (TZD) derivatives (**36-59**, general structure in Figure 4.8). The selection of the TZD moiety as PRM was motivated by several observations:

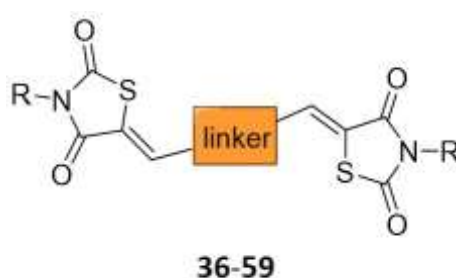
(i) TZD and other 5-membered heterocyclic scaffolds had been shown to have promising anti-aggregating potential, thus being able to selectively recognized fibrillar structures,<sup>210, 332</sup>

(ii) rhodanine and thiohydantoin derivatives have been shown to stained NFTs in hippocampal sections obtained from AD patients,<sup>231, 310</sup>

(iii) the most recently published theranostic small molecule for AD, is a rhodanine-based compound.<sup>325</sup>

After the selection of the PRM, we focused our attention on six structurally different lipophilic and aromatic linkers, aiming to evaluate their potential for the inhibition of the aggregation process. The selection was also based on their intrinsic fluorescence properties. First, we select a phenyl, a biphenyl, and a diphenylmethane linkers, in order to evaluate the importance of the conjugation both for the activity and the fluorescence properties of the compounds. Then, we specifically selected carbazole, fluorene, and bis-thiophene as recognized anti-aggregating and fluorescent moieties, in principle able to act both as therapeutic and diagnostic tools. Particularly: carbazole and fluorene derivatives have been reported as inhibitors of A $\beta$  aggregation<sup>333-335</sup> and as AD theranostic compounds,<sup>317</sup> while bis-thiophene and pentameric thiophene derivatives are well-known A $\beta$  and tau protein fluorescent probes.<sup>293, 336, 337</sup>

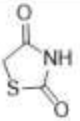
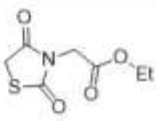
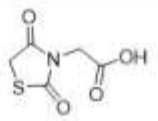
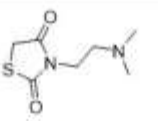
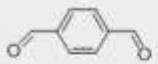
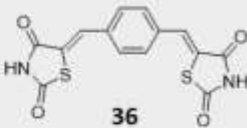
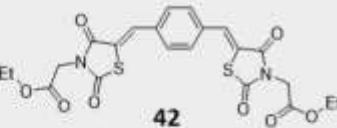
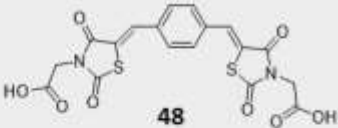
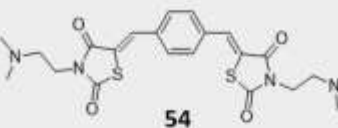
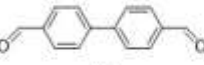
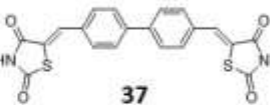
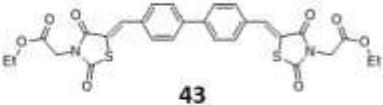
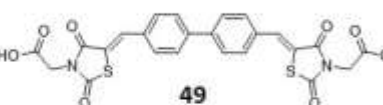
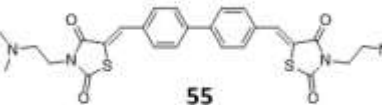
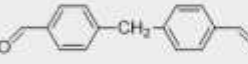
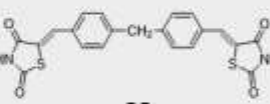
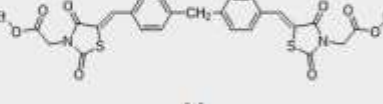
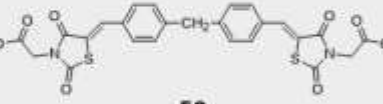
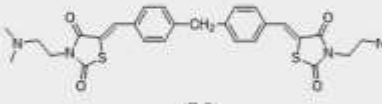
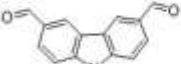
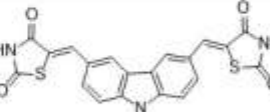
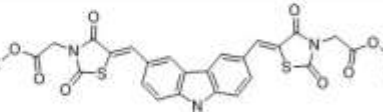
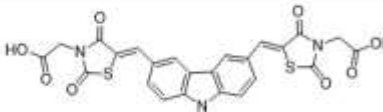
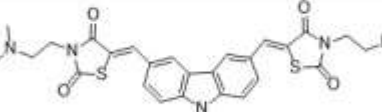

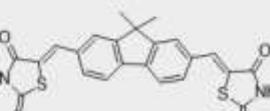
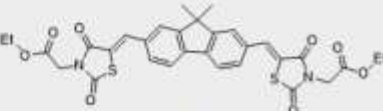
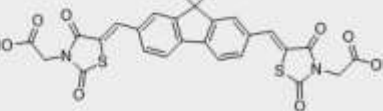
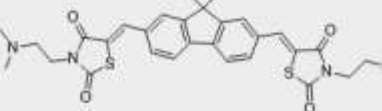
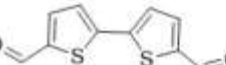
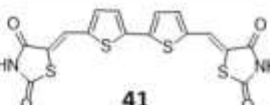
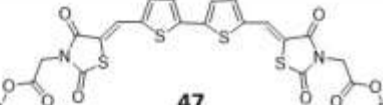
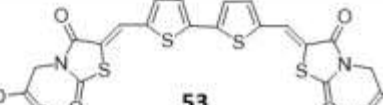
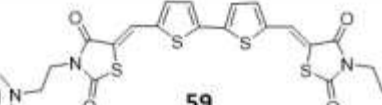
Finally, in order to expand the structure-activity relationships, and to improve the drug-likeness of our compounds, we decided to study the impact of side chain functionalization on the TZD core. Particularly, our aim was to investigate if different degrees of protonation could influence the interaction of the compounds with fibrillar structures, and their intrinsic fluorescence properties. Thus, we inserted an ester, a carboxyl and a secondary amine groups on the nitrogen of the TZD.



**Figure 4.8.** General structure of the bivalent TZD-derivatives **36-59**.

The combination of four different TZD-derivatives with six different aromatic linkers, led to the development of a small combinatorial library of 24 bivalent compounds (**36-59**, Table 4.1).

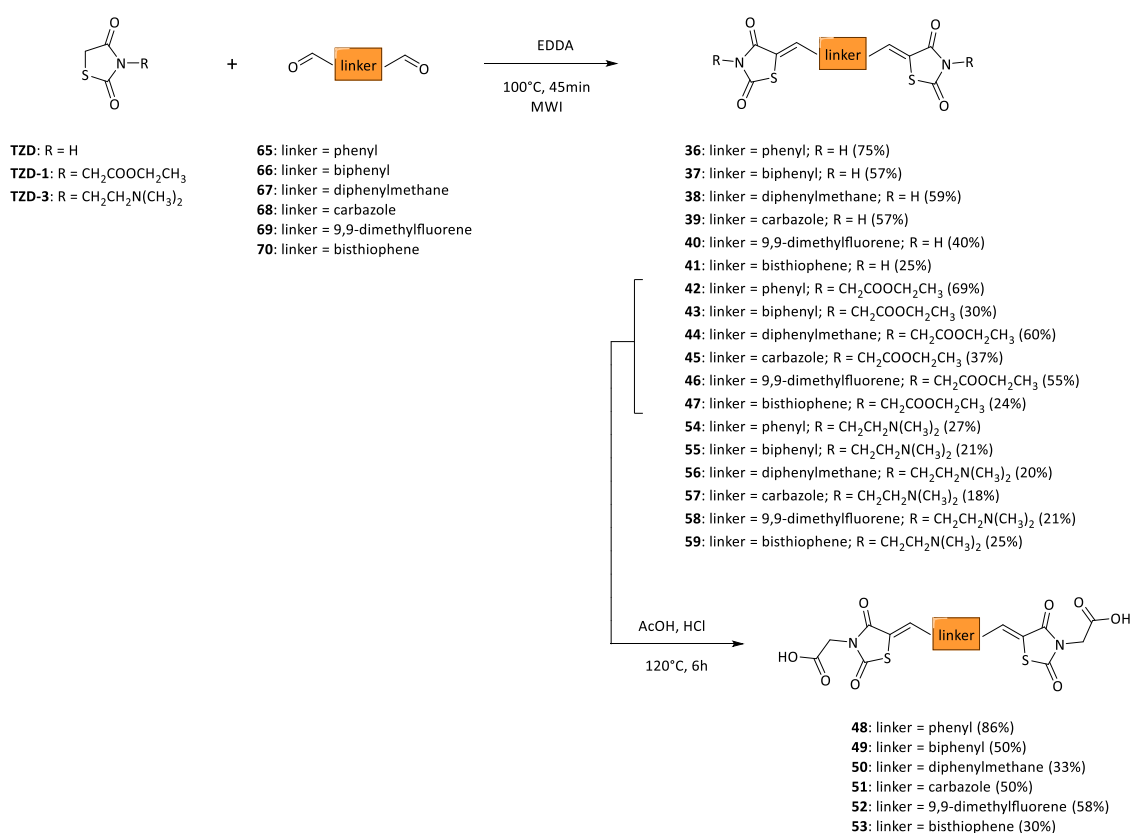
**Table 4.1.** Combinatorial library of the bivalent derivatives **36-59**.

<div style="text-align: center;">TZDs</div> <div style="text-align: center;">aldehydes</div>	 <b>TZD</b>	 <b>TZD-1</b>	 <b>TZD-2</b>	 <b>TZD-3</b>
 <b>65</b>	 <b>36</b>	 <b>42</b>	 <b>48</b>	 <b>54</b>
 <b>66</b>	 <b>37</b>	 <b>43</b>	 <b>49</b>	 <b>55</b>
 <b>67</b>	 <b>38</b>	 <b>44</b>	 <b>50</b>	 <b>56</b>
 <b>68</b>	 <b>39</b>	 <b>45</b>	 <b>51</b>	 <b>57</b>
 <b>69</b>	 <b>40</b>	 <b>46</b>	 <b>52</b>	 <b>58</b>
 <b>70</b>	 <b>41</b>	 <b>47</b>	 <b>53</b>	 <b>59</b>

## 4.4 Chemistry

The synthesis of the targeted compounds **36-59**, was achieved through a slightly modification of an optimized version of the Knoevenagel condensation (see paragraph 3.4).<sup>332</sup> The modified procedure is based on a green and solvent-free condensation of aromatic aldehydes with different TZD-derivatives, in the presence of EDDA under microwave irradiation at 100°C, for 45 minutes (Scheme 4.1).

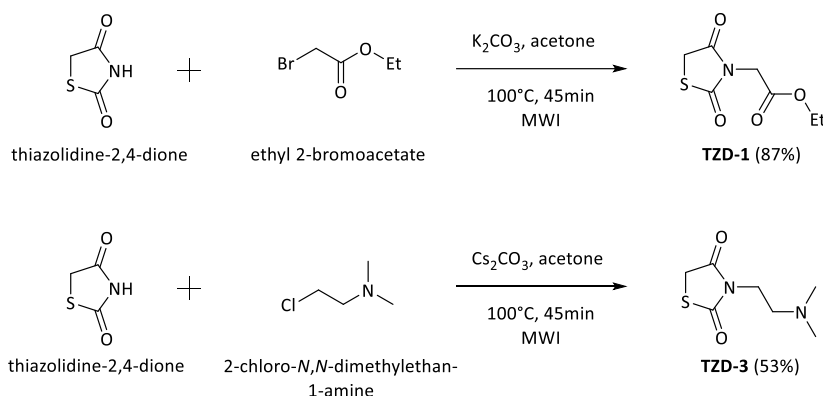
Particularly, the unsubstituted- (**36-41**), the ester- (**42-47**), and the amine-derivatives (**54-59**) were synthesized through the Knoevenagel condensation of 3 equivalents of the TZD derivatives (TZD, **TZD-1**, and **TZD-3**) and 1 equivalent of the six aromatic dialdehydes (**65-70**), with 0.5 equivalent of EDDA. The bivalent derivatives **36-47**, and **54-59** were obtained with yields varying from 15% to 69%. In some case, the yield was low because of the formation not only of the bivalent derivative, but also of the monosubstituted one.



**Scheme 4.1.** Synthetic procedure for the synthesis of target compounds **36-59**.

For the synthesis of the carboxyl-derivatives (**48-53**), the Knoevenagel reaction was followed by an acid catalyzed hydrolysis of the corresponding ester-derivatives (Scheme 4.1). **42-47** were refluxed in acetic acid and concentrated HCl overnight, yielding **48-53** in good yields (30-86%).

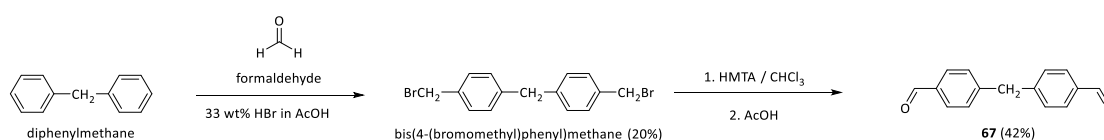
The *N*-substituted TZD derivatives were also synthesized. **TZD-1** was obtained upon *N*-alkylation of TZD with ethyl-2-bromoacetate, in the presence of  $K_2CO_3$  in acetone.<sup>338</sup> In the reported procedure the reaction is carried out for 12 h reflux, however, in order to reduce the reaction times, we performed the reaction using MW irradiation. Thus, the reaction of TZD (1 eq.) with ethyl-2-bromoacetate (1 eq.), and  $K_2CO_3$  (1.5 eq.) in acetone at 100°C for 50 minutes, gives **TZD-1** in good yield (87%, Scheme 4.2). The same optimized *N*-alkylation was applied for the synthesis of **TZD-3**. In this case, we change  $K_2CO_3$  to  $Cs_2CO_3$  and we were able to obtain **TZD-3** with 53% yield (Scheme 4.2).



**Scheme 4.2.** Synthetic procedure for the synthesis of *N*-substituted TZD derivatives **TZD-1** and **TZD-3**.

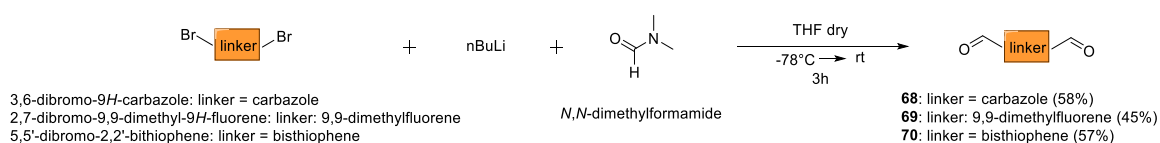
Dialdehydes **65** and **66** were commercially available, while dialdehydes **67-70** were synthesized as reported in Scheme 4.3 and 4.4. Synthesis of **67** was achieved through a two-step reaction (Scheme 4.3).<sup>339</sup> In the first step, dibromomethylation of diphenylmethane with formaldehyde and 33% wt solution of HBr in acetic acid, gives

the intermediate bis(4-(bromomethyl)phenyl)methane (20%). The second step was a Sommelet reaction in which, generally, a benzyl halide is converted to aldehyde using hexamethylenetetramine (HMTA).<sup>340</sup> Thus, after this two steps reaction, we were able to obtain **67** in good yield (42%).



**Scheme 4.3.** Synthetic procedure for the synthesis of dialdehyde **67**.

The synthesis of dialdehyde **68** was achieved through direct lithiation of the corresponding 3,6-dibromo-9*H*-carbazole, and subsequent formylation with dimethylformamide (DMF), as reported in Scheme 4.4.<sup>341</sup> **68** was obtained in a very good yield (58%), higher than that reported in the literature. As the reaction works well, we apply it also to the corresponding dibromo-fluorene and -bisthiophene derivatives (Scheme 4.4). To the best of our knowledge, this is the first case in which this reaction is exploited for the synthesis of fluorene and bisthiophene dialdehydes. Importantly, we were able to synthesize **69** and **70** in good yields (45-57%).



**Scheme 4.4.** Synthetic procedure for the synthesis of dialdehyde **68-70**.

All the final compounds **36-59** were characterized using analytical (HPLC) and spectroscopic data (<sup>1</sup>H- and <sup>13</sup>C-NMR, ESI-MS).

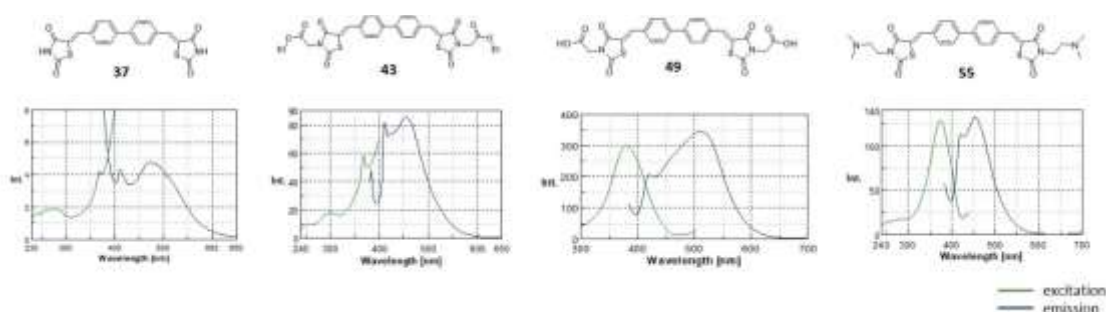
## 4.5 Native fluorescence studies

As mentioned above, the aim of this project was to develop fluorescent bivalent ligands, as theranostic tools for AD. Indeed, after the synthesis of the library, we studied the native fluorescence of all the 24 derivatives in ethanol, whose polarity mimics the protein environment. From these studies, we were able to select the best performing compounds in terms of fluorescent properties.

The fluorescence of all the compounds was strongly dependent on the nature of the linker; while, in some cases, the *N*-substitution seems not to affect it.

In details, the phenyl derivatives **36**, **42**, **48**, and **54** showed no fluorescence emission, probably due to the small degree of conjugation.

The biphenyl derivatives showed a better profile, with **49** and **55** showing an intense fluorescence emission at 513 nm and 452 nm respectively (Figure 4.9).



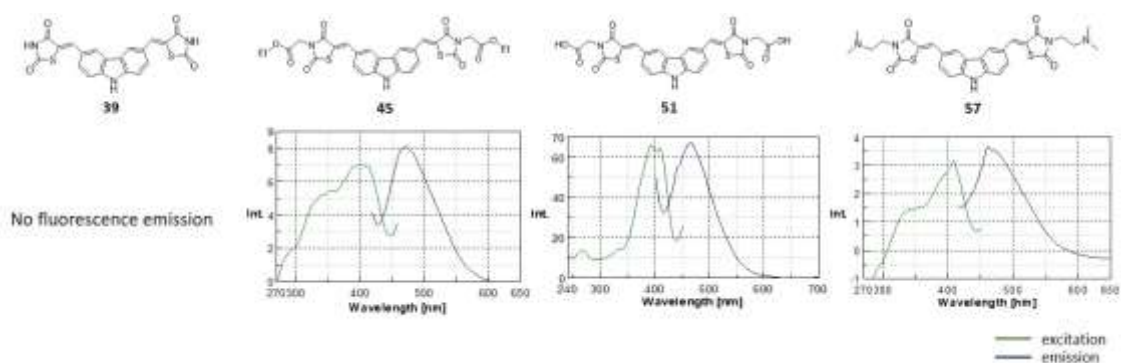
**Figure 4.9.** Fluorescence spectra of the biphenyl-derivatives **37**, **43**, **49**, and **55** in ethanol.

The lack of fluorescence emission for the diphenylmethane-derivatives confirm the importance of a conjugated and planar system for optimal fluorescence properties. Indeed, the loss of fluorescence signal in **38**, **44**, **50**, and **56** is due to the insertion of a methylene between the two phenyl rings and the resulting loss of conjugation.

The insertion of the carbazole linker, as in derivatives **39**, **45**, **51**, and **57**, displays different effects, based also on the *N*-substituent on the TZD core (Figure 4.10). Particularly, the *N*-unsubstituted **39** was not fluorescent, while ester- and amine-

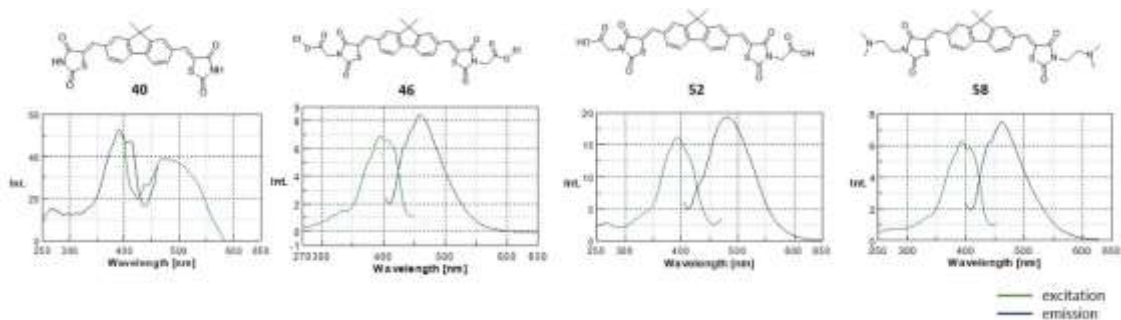


derivatives (**45** and **57**) show a very low fluorescence intensity with an emission wavelength ( $\lambda_{em}$ ) of 470 nm. The best compound in the carbazole series was the carboxyl-derivative **51**, with a higher intensity of fluorescence emission at 468 nm.



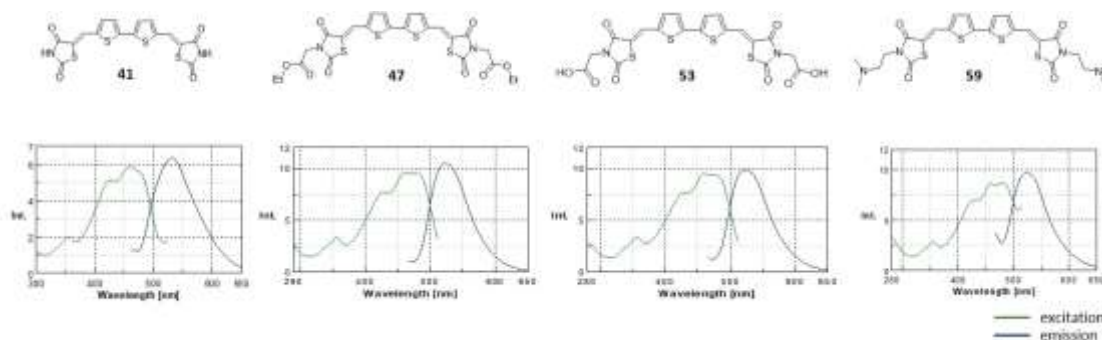
**Figure 4.10.** Fluorescence spectra of the carbazole-derivatives **39**, **45**, **51**, and **57** in ethanol.

The fluorene derivatives **40**, **46**, **52**, and **58** showed a very good fluorescence, in terms of both intensity and emission wavelength (Figure 4.11). **40** represent the most promising compound of this small series, with an intense fluorescence at 500 nm. The other derivatives ester- and amine-derivatives **46**, **52** and **58** showed a less intense fluorescent signal with a good  $\lambda_{em}$  of about 460-480 nm.



**Figure 4.11.** Fluorescence spectra of the fluorene-derivatives **40**, **46**, **52**, and **58** in ethanol.

Finally, the bithiophene derivatives represent the most promising compounds in terms of emission wavelength, as they were able to reach 520-530 nm (Figure 4.12). In this case, the fluorescence properties of all the four compounds seems not to be affected by the *N*-substitution of the TZD. Indeed, all the compounds displayed similar fluorescence intensity, as well as a similar emission wavelength.



**Figure 4.12.** Fluorescence spectra of the bithiophene-derivatives **41**, **47**, **53**, and **59** in ethanol.

In Table 4.2 are reported the excitation and emission wavelength of all the 24 bivalent derivatives. As it is clear, no compound shows an emission wavelength in the NIR region. However, the compounds displaying  $\lambda_{em}$  above 450 nm could represent promising candidates for *in vitro* studies, and good starting point for the development of derivatives with improved fluorescence properties. Importantly, in native fluorescence studies it is not possible to evaluate the importance of the protonation of the compounds in a protein environment. This could explain why we were not able to find strong differences in the emission spectra of ester-, carboxyl-, or amine-derivatives.

Compounds **40**, **47**, **49**, **51-53**, **55**, **59**, showing good fluorescence intensity and  $\lambda_{em}$  higher than 450 nm, were selected for further studies, in order to evaluate changes in their fluorescence properties after the interaction with A $\beta$  and tau fibers.

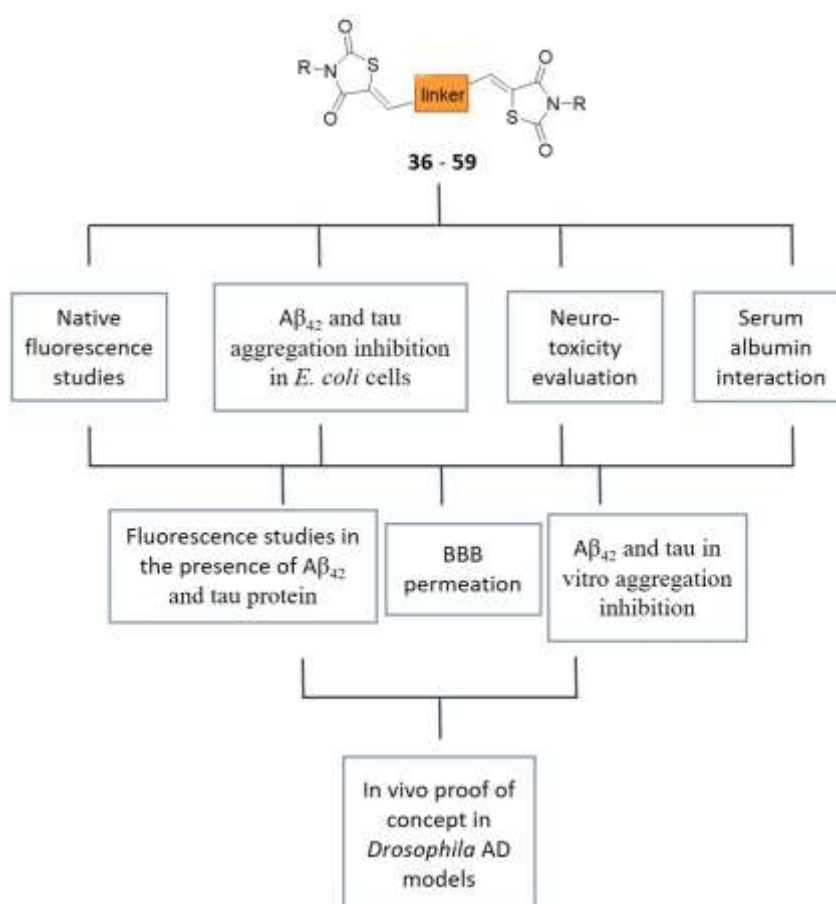
**Table 4.2.** Excitation and emission maxima of compounds **36-59**.

<b>Cmpd.</b>	$\lambda_{\text{ex}}$ (nm)	$\lambda_{\text{em}}$ (nm)	<b>Cmpd.</b>	$\lambda_{\text{ex}}$ (nm)	$\lambda_{\text{em}}$ (nm)
<b>36</b>	-	-	<b>48</b>	-	-
<b>37</b>	369	471	<b>49</b>	374	513
<b>38</b>	-	-	<b>50</b>	-	-
<b>39</b>	-	-	<b>51</b>	400	526
<b>40</b>	389	500	<b>52</b>	393	482
<b>41</b>	465	534	<b>53</b>	479	524
<b>42</b>	-	-	<b>54</b>	-	-
<b>43</b>	376	452	<b>55</b>	375	452
<b>44</b>	-	-	<b>56</b>	-	-
<b>45</b>	409	469	<b>57</b>	407	470
<b>46</b>	395	459	<b>58</b>	390	462
<b>47</b>	462	522	<b>59</b>	459	522

## 4.6 Results and discussion

After the synthesis and the native fluorescence studies, we designed a screening pipeline, depicted in Figure 4.13, to evaluate the theranostic profile of our bivalent derivatives **36-59**.

First, we plan to study the potential of our compounds as anti-aggregating agents towards A $\beta$  and tau protein in intact *Escherichia coli* (*E. coli*) cells overexpressing A $\beta$ <sub>42</sub> and 2N4R full-length tau. Secondly, we wanted to assess the neuro-toxicity of **36-59** in primary CGNs at two different concentrations, together with their interaction with serum albumin. The results from these preliminary assays will allow us to select the best performing compounds to be progressed for further studies.



**Figure 4.13.** Screening pipeline for the bivalent derivatives **36-59**.

Then, due to their potential application as amyloid probes, we will record the fluorescence emission spectra of the selected compounds in the presence of A $\beta$ <sub>42</sub> and tau protein. These experiments will allow us to evaluate changes in their fluorescence properties after the interaction with A $\beta$  and tau fibers. In parallel, we will confirm their antiaggregating potential performing A $\beta$ <sub>42</sub> and tau aggregation and inhibition studies by ThT fluorescence, and we will assess their ability to cross the BBB through a PAMPA-BBB assay.

Finally, the theranostic potential of our compounds will be confirmed *in vivo* in *Drosophila melanogaster* models of AD.

*Drosophila melanogaster* is a powerful platform for the screening of AD drug candidates.<sup>342-344</sup> In the last years, several transgenic flies expressing human A $\beta$ <sub>42</sub> and tau proteins have been developed, and they are now providing new insights into disease mechanisms, and assisting in the identification of novel AD drug candidates.<sup>258, 345-349</sup> Transgenic flies expressing the human A $\beta$ <sub>42</sub> protein in their nervous system display different symptoms reminiscent of AD, including defective locomotion and memory, as well as markedly reduced longevity. Moreover, their brains display characteristic amyloid plaques and amyloid pathology.<sup>350, 351</sup> *Drosophila* over-expressing the human tau protein are also of utmost importance, as they show key features of AD: adult onset, progressive neurodegeneration, early death, enhanced toxicity of mutant tau, and accumulation of abnormal tau. Human tau overexpression in neuronal tissues is neurotoxic, but neurodegeneration occurred without the formation of NFTs. However, human tau expression on the retina yields adult flies with a characteristic rough eye phenotype.<sup>352</sup>

Importantly, we will assess *Drosophila* longevity and locomotor activity, and we will analyze A $\beta$  and tau deposits, respectively in the brains and eyes of the flies. We will also perform fluorescent staining of our bivalent compounds on *Drosophila*, to demonstrate the effective labeling of A $\beta$ <sub>42</sub> and tau proteins by our compounds, thus confirming their diagnostic potential. Thus, the *Drosophila* AD models will provide us the proof of concept of our bivalent compounds as theranostic tools for AD.

#### 4.6.1 Inhibition of A $\beta$ <sub>42</sub> and tau aggregation in intact *Escherichia coli* cells

These experiments were performed by Dr. Raimon Sabaté at the Department of Pharmacy and Pharmaceutical Technology and Physical Chemistry, UB, Barcelona.

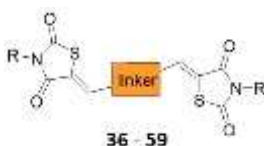
The aggregation of A $\beta$ , especially the most aggregation-prone and neurotoxic 42 amino acid form (A $\beta$ <sub>42</sub>), and tau protein represent an early pathogenic event in AD. Thus, based on this and on our interest in developing anti-aggregating compounds, all the 24 bivalent derivatives were tested in intact *E. coli* cells overexpressing these proteins.

In bacteria, protein aggregation occurs during the production of heterologous proteins, leading to the formation of insoluble inclusion bodies (IBs). IBs contain highly ordered amyloid-like structures, and their formation seems to share mechanistic features with amyloid self-assembly. Thus, bacteria have been proposed as a model to study amyloid aggregation.<sup>353, 354</sup> Taking advantage of the fact that amyloid aggregation can be followed in vivo, in bacteria, Muñoz-Torrero and Sabaté, recently developed a new methodology that allows the fast, easy, and inexpensive screening of putative inhibitors of the spontaneous aggregation of potentially any amyloidogenic protein that can be overexpressed in *E. coli* cells.<sup>355, 356</sup> The protein aggregates inside *E. coli* can be stained with ThS, and the extent of aggregation can be monitored measuring the variations of the fluorescence of ThS. Indeed, overexpression of recombinant amyloid prone proteins led to an increase in ThS fluorescence compared to bacteria that do not express the protein; while when bacteria are grown in the presence of amyloid aggregation inhibitors, the ThS fluorescence is clearly reduced. Moreover, as the ThS fluorescence is directly proportional to the amyloid amount, the anti-aggregating activity of each inhibitor can be easily determined by steady-state fluorescence. Importantly, this rapid in vivo screening has already been used for the screening of several libraries of anti-aggregating compounds.<sup>357-362</sup>

The preliminary screening of the nine bivalent derivatives **36-40**, **48**, **49**, **51**, and **52** in *E. coli* cells shows promising results, as reported in Table 4.3. The *N*-unsubstituted derivatives **36-38** show high IC<sub>50</sub> values. However, the substitution of the nitrogen of the TZD with a carboxyl group, as in compounds **48** and **49**, led to an important

decrease in their IC<sub>50</sub> values. The same behavior was observed with the carbazole derivatives **39** and **51**, and the fluorene derivatives **40** and **52**. The *N*-unsubstituted **39** and **40** showed a good IC<sub>50</sub> of about 22 μM and 26 μM, respectively for both Aβ<sub>42</sub> and tau protein. While the corresponding carboxyl-derivatives **51** and **52** showed a significant reduction of the IC<sub>50</sub> values, with compound **52** being the most active in this first nine tested derivatives. Indeed, **52** showed IC<sub>50</sub> values of 9.35 ± 0.01 μM towards Aβ<sub>42</sub>, and 8.15 ± 0.01 μM towards tau protein. Importantly, all the compounds seems equally active on both proteins, but this was not surprising us. As highlighted above, several anti-aggregating compounds share a common chemical structure, thus being effective in inhibiting the aggregation process of different amyloid proteins. Although preliminary, these results confirm the potential antiaggregating activity of our bivalent derivatives.

**Table 4.3.** Effect of the bivalent derivatives **36-40**, **48**, **49**, **51**, and **52** on *E. coli* cells overexpressing Aβ<sub>42</sub> or tau protein, monitored by ThS staining.



Cmpd	linker	R	Aβ <sub>42</sub> aggregation IC <sub>50</sub> (μM)	Tau aggregation IC <sub>50</sub> (μM)
<b>36</b>		-H	56.9 ± 0.06	51.4 ± 0.04
<b>37</b>		-H	44.3 ± 0.06	54.9 ± 0.03
<b>38</b>		-H	57.5 ± 0.05	56.6 ± 0.03
<b>39</b>		-H	22.7 ± 0.03	21.6 ± 0.02
<b>40</b>		-H	26.8 ± 0.02	25.9 ± 0.02
<b>48</b>		-CH <sub>2</sub> COOH	36.2 ± 0.02	24.3 ± 0.02
<b>49</b>		-CH <sub>2</sub> COOH	22.8 ± 0.06	30.0 ± 0.02
<b>51</b>		-CH <sub>2</sub> COOH	17.5 ± 0.01	15.1 ± 0.02
<b>52</b>		-CH <sub>2</sub> COOH	9.35 ± 0.01	8.15 ± 0.01





## **Chapter V**

### **Development of**

**a focused library of antiprion compounds**

**built around Compound 1**

## **5.1 Therapy in prion diseases**

Three decades after the discovery of prions as the cause of Creutzfeldt-Jakob disease and other transmissible spongiform encephalopathies, we are still far away from the discovery of an effective treatment for these disorders. The lack of a mechanistic understanding of how prions damage the brain, results in the lack of validated pharmacological targets. Moreover, several pharmacological interventions have attempted to target different stages of disease progression but none has significantly affected the course of the disease. Indeed, PrDs still represent an extremely challenging endeavor for medicinal chemists.<sup>363</sup>

Given the central role of PrP in prion propagation and pathology, this protein represents the best target currently available for antiprion drug discovery. Thus, possible strategies for interrupting prion formation act on different stages of prion biogenesis and PrP<sup>Sc</sup> formation and aggregation. Such strategies include: reducing PrP expression, preventing PrP<sup>C</sup> unfolding, blocking unfolded PrP binding to PrP<sup>Sc</sup>, blocking PrP<sup>Sc</sup> from recruiting PrP, breaking-up PrP<sup>Sc</sup>, and increasing PrP<sup>Sc</sup> degradation.<sup>364</sup>

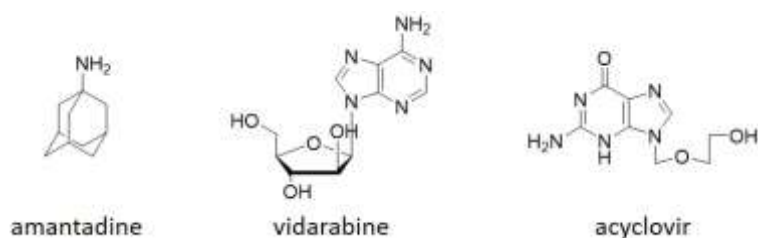
In the last decade, an increasing interest in PrDs, led to the discovery of several antiprion compounds, coming from both screening- and knowledge-based approaches. In the first case, cell-based high throughput in vitro assays have allowed the screening of several library of compounds. In many cases, the screenings were performed on libraries of approved drugs, providing repurposed candidates ready for clinical trials. On the other side, knowledge-based approaches originated from an ever-increasing understanding of the mechanisms underlying pathogenesis, and led to the discovery of several new preclinical compounds.<sup>363</sup>

### **5.1.1 Clinical drug candidates**

Starting from 1971, 14 drugs have been tested in clinical trials for the treatment of PrDs. Clinical drug candidates have varied over the years, and have been largely influenced by the ever-changing state of knowledge within the field. The tested drug candidates were antivirals, antimalarials, anticoagulants, antifungals, antidepressant, anticonvulsant and antioxidants. However, none of the tested drug candidates

reported positive results. Importantly, the failure of all these trials has been attributed to several factors, among them, the lack of validated outcome measures, and the small number of data deriving from prospective observational studies.<sup>365</sup>

The initial designation of prion diseases as “slow viral illnesses” led to the early evaluation of several antiviral treatments. Thus, amantadine,<sup>366, 367</sup> interferon,<sup>368</sup> vidarabine,<sup>369</sup> and acyclovir<sup>370, 371</sup> were assayed between 1971 and 1984 (Figure 5.1).



**Figure 5.1.** Chemical structures of amantadine, vidarabine, and acyclovir.

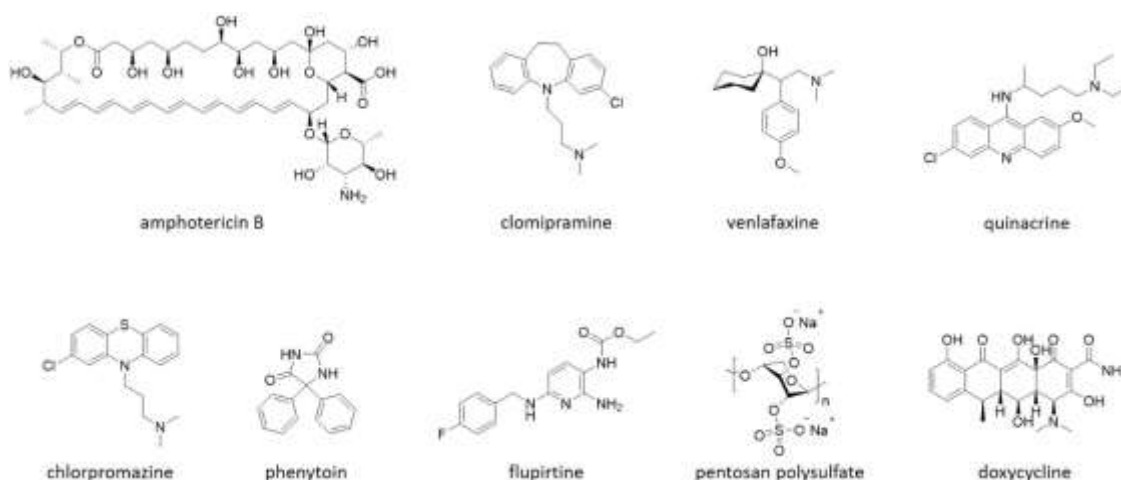
In 1992, two CJD patients were treated with the antifungal drug amphotericin B (Figure 5.2). However, also in this case, the treatment was unsuccessful.<sup>372</sup> In 2001, a vCJD patient was treated with clomipramine (Figure 5.2), a tricyclic antidepressant with an aliphatic side chain at the middle ring moiety, and venlafaxine (Figure 5.2), a serotonin and norepinephrine reuptake inhibitor. Again, no clinical improvement was observed, and the patient died 14 months after the onset of the symptoms.<sup>373</sup> In the same year, other tricyclic compounds with an aliphatic side chain at the middle ring moiety were reported as inhibitors of the PrP<sup>C</sup> conversion in scrapie-infected neuroblastoma cells.<sup>374</sup> Thus, several studies focused on the antimalarial drug quinacrine (Figure 5.2), an acridine derivative with a basic side-chain.

Four clinical trials have evaluated the potential of quinacrine in treating PrDs.<sup>369, 375-377</sup> The two most important trials were: PRION-1, conducted in the UK, and consisting of 107 patients;<sup>376</sup> and a trial conducted at the University of San Francisco, consisting of 425 patients.<sup>377</sup> In both cases, a dose of 300 mg of quinacrine daily was well tolerated, however, it did not significantly affect the clinical course of the disease. Moreover, in all the four clinical trials, lemon-yellow discoloration of skin, liver dysfunction, and

leucopenia were described as common side effects. However, in 2009 it was reported that treatment with quinacrine, both in vitro and in vivo, could at first reduce PrP<sup>Sc</sup>, but a continuous treatment resulted in strain selection of PrP resistant to the effect of quinacrine.<sup>378</sup> The failure of quinacrine in clinical trials was also ascribed to the focus upon single therapy approaches. Thus, quinacrine was administered in combination with the antipsychotic drug chlorpromazine (Figure 5.2) to four patients.<sup>379, 380</sup> Once more, no clinical improvements were found.

In 2003, anticonvulsants were also tested in patients affected by sCJD.<sup>381, 382</sup> One patient was treated with phenytoin (Figure 5.2), and then quinacrine and chlorpromazine were co-administered. Again, no evident clinical improvements were observed.

Another compound tested in clinical trials for PrDs was flupirtine (Figure 5.2). Flupirtine is a non-opioid analgesic, which has been shown to decrease neurotoxicity associated with prion diseases in vitro.<sup>383</sup> As flupirtine was a well-tolerated and clinically well-established drug, it was directly investigated in a clinical trial on 28 patients with probable CJD. The results showed less cognitive decline in patients treated with flupirtine, but no differences in the mean survival time.<sup>384</sup>



**Figure 5.2.** Chemical structures of drug candidates for PrDs.

A “controversial” compound of interest in PrDs was pentosan polysulfate (PPS, Figure 5.2). PPS was shown to inhibit scrapie infections in mice.<sup>385, 386</sup> However, as it is not BBB permeable, PPS was rejected as a possible treatment for CJD, as its intraventricular administration is invasive and the risk of complications is high.<sup>387</sup> Nevertheless, several studies on PPS treatment in patients were reported.<sup>388-393</sup> In all these cases reported on a clinical stabilization and a slow disease progression; however, surgical complications were common. Thus, PPS seems to represent a possible disease-modifying treatment for CJD patients, although the invasiveness of the treatment cannot be overlooked.

Finally, in recent years, the research has focused on the tetracycline doxycycline (Figure 5.2), thanks to several preliminary encouraging in vitro and in vivo studies. The first two observational studies reported a significantly prolonged survival times in patients treated with doxycycline.<sup>394, 395</sup> However, a subsequent trial conducted between 2007 and 2012, did not confirm the previous findings.<sup>396</sup> Indeed, doxycycline was well-tolerated, but efficacy analysis did not show any significant difference between doxycycline- and placebo-treated patients in terms of survival time or rate of disease progression.

The only active clinical trial, to date, is a preventive trial with doxycycline treatment in 30 patients belonging to an Italian FFI family.<sup>397, 398</sup> The volunteers have agreed to be exposed over a ten-years treatment to doxycycline. Hopefully, the study will be closed within 2023.

### **5.1.2 Preclinical drug candidates**

As highlighted before, the search of antiprion compounds is an extremely challenging area for medicinal chemists. As in all the other PMDs, the lack of an early diagnosis, the difficulties in developing BBB-permeable compounds, as well as the lack of structural information regarding the interactive surfaces of two proteins involved in a PPI, make even more difficult the discovery of effective disease-modifying treatments. Nevertheless, in the last decades, several drug discovery approaches have been

pursued in the PrDs field. The development of cell cultures in which prion infection is stable has surely provided a unique and efficient way for the identification of antiprion compounds. Thus, neuronal cell lines chronically infected with rodent prions are routinely used either to screen compounds inhibiting PrP<sup>Sc</sup> accumulation, as well as to confirm the antiprion effect of compounds discovered by biophysical methods. This type of screening has been very useful for identifying several antiprion drug candidates.<sup>399</sup> However, only few compounds were effectively progressed to in vivo animal studies. Indeed, starting from 2007, only five reported compounds were able to disrupt prion propagation in infected mice, and to extend the animals' life span.

The first orally available small molecule able to delay death in prion-infected animals was compound B (Figure 5.3).<sup>400</sup> Compound B was discovered as an orally available antiprion compound, effective in prolonging the incubation periods of mice cerebrally infected with Rocky Mountain Laboratory (RML) strain. However, a huge amount of compound B was necessary for in vivo efficacy. Indeed, its rapid washout from both the brain and the blood, together with some metabolic instability, might be responsible for its limited effectiveness and its loss of efficacy during long-term treatments. Thus, the optimization of its safety profile and pharmacokinetic properties are necessary before a clinical application.<sup>400</sup>

In 2013, two different research groups discovered other two promising compounds, both coming from high-throughput screening. The first compound, named anle138b (Figure 5.3) showed structure-dependent binding to pathological aggregates and strongly inhibited formation of oligomers in vitro and in vivo both for prion protein and  $\alpha$ -synuclein.<sup>401</sup> Anle138b did not show a detectable toxicity at therapeutic doses, while showing an excellent bioavailability and BBB permeation. Moreover, it was able to double the life span of prions infected mice.<sup>401</sup> Thus, anle138b represent a promising compound for PrDs treatment, but its activity as anti-aggregating compound is now being tested towards other prion-like proteins such as tau, SOD1, and TDP-43.

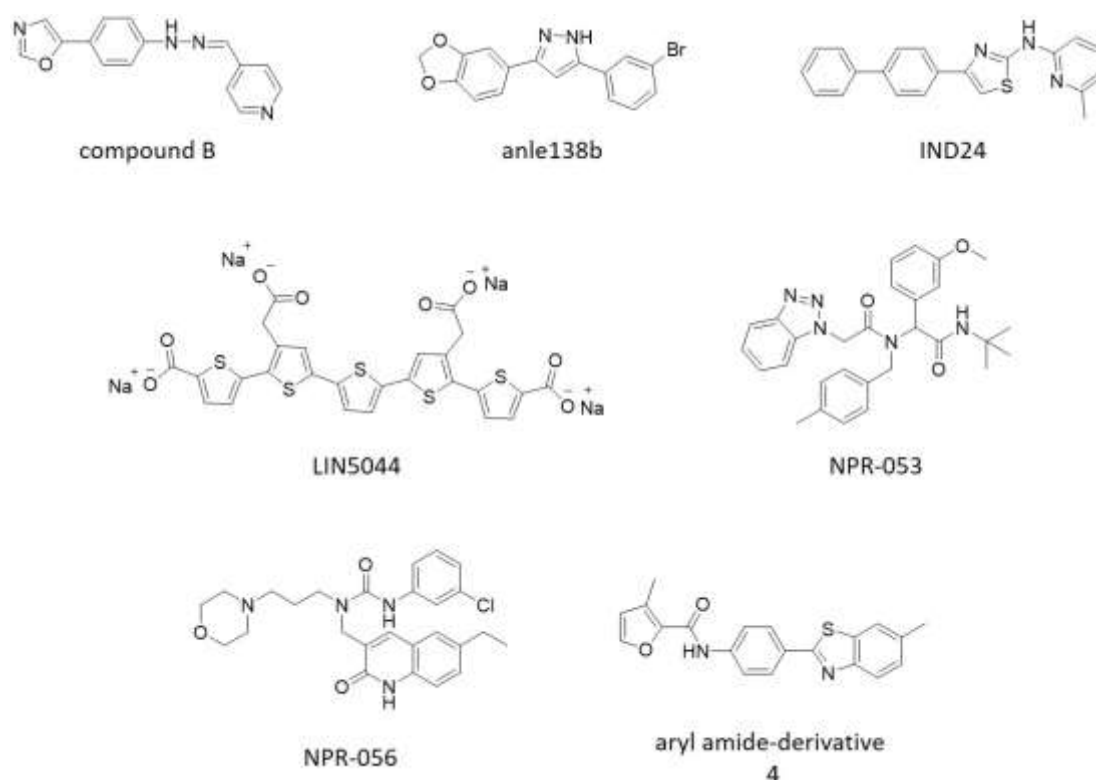
The second compound was developed by Prusiner' group, and it is called IND24 (Figure 5.3).<sup>402</sup> This compound doubled the survival times of scrapie-infected, wild-type mice. However, mice infected with the RML prion strain and treated with IND24, exhibited neurological dysfunction and died. Thus, the author demonstrated that prion strains

can acquire resistance upon exposure to IND24, and that this resistance can be lost upon strains passages in mice, in the absence of the compound. However, IND24 showed another limitation that was already seen for both compound B and Anle138b: all the three compounds are not effective against all prion strains. For example, compound B worked against a mouse prion strain but not against a hamster one. More importantly, to date, no antiprion compound has demonstrated the ability to slow the progression of human prion strains injected into animals. Indeed, IND24 was ineffective in slowing propagation of Creutzfeldt-Jakob disease prions in transgenic mice.<sup>402</sup>

In 2015, Aguzzi and colleagues reported the first rationally designed antiprion compound, able to attenuate PrP<sup>Sc</sup> toxicity in infected mice.<sup>403</sup> Particularly, the authors selected the mutant fungal prion HET-s as a plausible structural proxy of PrP. Indeed, HET-s represent the only available high resolution structure of a prion, and its stacked lysine residues are arranged in a single-layer repeat amyloid as expected for PrP<sup>Sc</sup>.<sup>15</sup> Based on this structure, they extract a set of rules that predicted the activity of a series of luminescent conjugated polythiophenes (LCPs). First, the backbone must contain at least five thiophene or selenophene moieties, as it seems to represent a minimal generic anti-amyloid LCP pharmacophore. Second, charged side groups are required for therapeutic efficacy, as carboxylic acids and acetic acids conferred effectiveness. Third, compounds bearing five thiophene or selenophene rings are effective only when bearing anionic side groups linked to the terminal thiophene rings. Based on this, LIN5044 (Figure 5.3) was proposed as the most active and promising compound. Administration of LIN5044 to prion-infected mice was effective not only for prophylaxis but also during the symptomatic phase of the disease, without showing toxicity. LIN5044 delayed prion replication, and reduced the efficiency of prion self-perpetuation. Moreover, the compound was active even after systemic administration, suggesting favorable pharmacodynamic and pharmacokinetic properties. Finally, the authors investigated whether LIN5044 was active also on mice infected with hamster prions, and the results were positive.<sup>403</sup>

In 2016, another class of antiprion compounds was developed through a structure-based drug discovery approach.<sup>404</sup> The best performing compounds NPR-053 and NPR-

056 (Figure 5.3) were tested in mice inoculated with the human-derived Fukuoka-1 GSS strain. The results showed that both compounds were able to suppress PrP<sup>Sc</sup> and gliosis levels in the brains of mice at onset, but they had no effect on survival. Thus, the authors hypothesized that the level of effective drugs left in the brain after treatment was very low. NPR-053 and NPR-056 could represent a good starting point for the development of antiprion compounds, however, a deeper understanding of their pharmacokinetics is required.<sup>404</sup>



**Figure 5.3.** Chemical structures of antiprion compounds tested in in vivo models.

In the same year, Prusiner' lab discover a novel class of antiprion compounds.<sup>405</sup> In 2013, an extended high throughput screening identified aryl amide as a promising antiprion scaffold.<sup>406</sup> Thus, starting from the benzothiazole hit 4 (Figure 5.3) four different series of aryl amide, differing in their N-linked aryl groups, were developed and tested in prion-infected mice, demonstrating to be able to double the survival time of the infected mice. Particularly, aryl amides were able to alter the prion strain



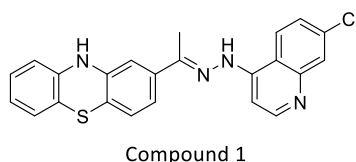
properties, as evident by the distinct patterns of neuropathological deposition of prion protein, and associated astrogliosis in the brain. Unfortunately, none of these compounds showed efficacy against CJD prions.<sup>406</sup> Nevertheless, aryl amide demonstrate for the first time that the development of drug resistance is not an inevitable consequence of efficacious anti-prion compounds.

All in all, it is clear that all the compounds tested in in vivo models of PrDs are able to disrupt prion propagation, and to extend the animals' life span. However, these molecules are not able to cure the disease, and none of these compounds are likely to make it into the clinic to treat human prion diseases. Indeed, none of these compounds work against human prions in humanized mice. Undoubtedly, the inadequacy of current cell culture models of human PrDs likely contributes to the translational failure of apparently promising antiprion compounds from the laboratory to clinical practice. Thus, developing a cell model for the replication of human CJD prions, remains a top priority for the development of drug candidates for PrDs.

A breakthrough in the field was obtained for the first time in 2017, when it was demonstrated that astrocytes derived from human induced pluripotent stem cells support the replication of prions from brain samples of CJD patients.<sup>407</sup> Importantly, this work represents a fundamental advance in modeling human PrDs by establishing a readily scalable system useful to address mechanistic aspects of human prion infections, and to facilitate drug discovery.<sup>407</sup>

## 5.2 Design of a small library of antiprion compounds

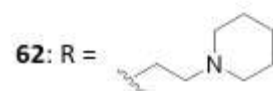
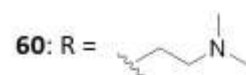
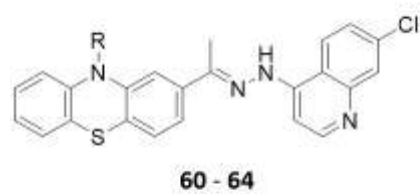
The aim of this project was the development of a focused library of antiprion compounds deriving from Compound 1 (Figure 5.4). Compound 1 came from an in silico screening, and its activity was then confirmed in in vitro studies (L. Zaccagnini' PhD thesis, SISSA, 2018). Chemically speaking, Compound 1 represent a hybrid compound, composed of a phenothiazine and a quinoline moieties, joined by a hydrazone linker. As it shown a very promising profile in terms of both activity and safety, the first step of this project was to resynthesize Compound 1, to validate the biological activity of the vendor-supplied sample, and to perform further studies to explore its potential as antiprion compound.



**Figure 5.4.** Chemical structure of Compound 1.

After the synthesis, we wanted to improve the drug-likeness of this compound, with a focus on its physico-chemical properties. Indeed, Compound 1 showed a very low solubility, which might negatively affect its absorption, and make difficult to perform further in vivo studies. In light of this, we decided to functionalize the nitrogen of the phenothiazine ring, through the insertion of polar groups. Derivatives **60-64** (Figure 5.5), bearing dimethylamino, piperidino, morpholino and methylpiperazino substituents, were synthesized. Importantly, the selected solubilizing groups were carefully selected among those more frequently employed for the design and optimization of CNS drugs.<sup>408</sup>

Then, in order to assess whether our design strategy was successful or not, the aqueous solubility of Compound 1, and derivatives **60-64** will be assessed.



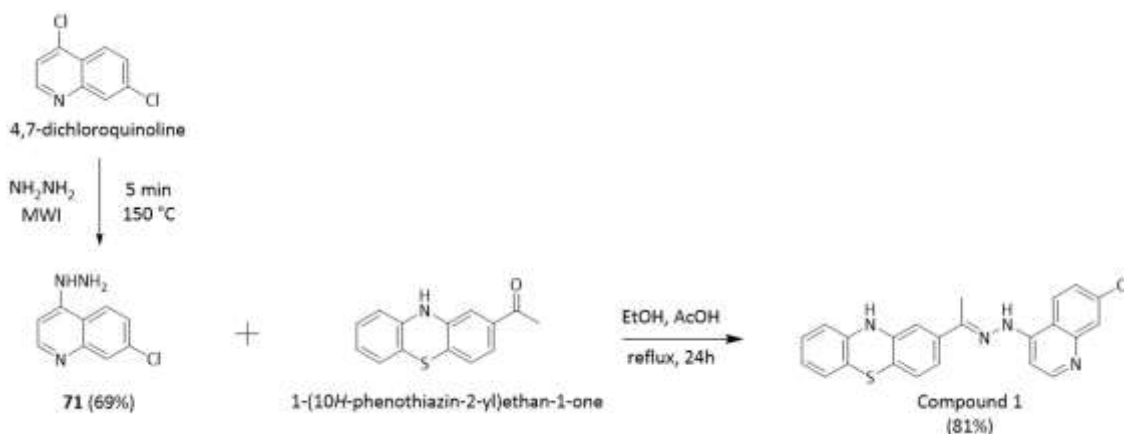
**Figure 5.5.** Chemical structures of derivatives **60-64**.

### 5.3 Chemistry

As first step, Compound 1 was resynthesized. Particularly, as no synthetic protocol was reported, we aimed to develop a versatile synthetic procedure that would allow us further chemical manipulation starting from easily accessible building blocks.

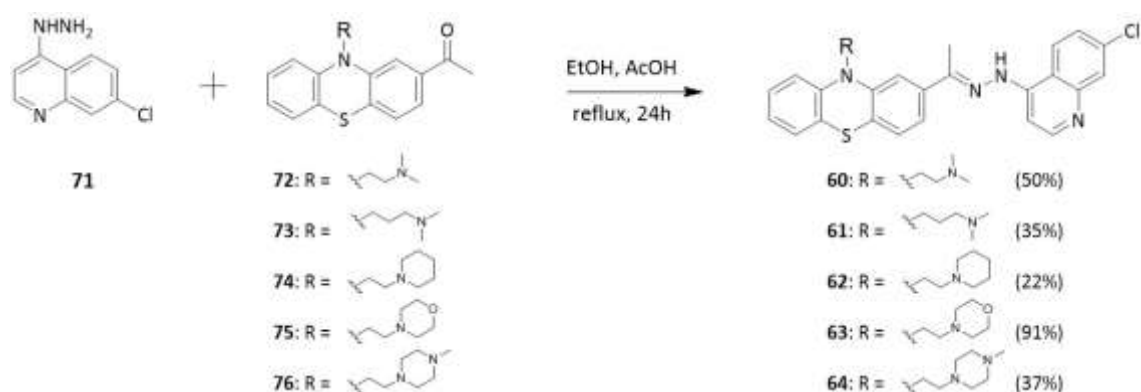
Thus, the synthesis of Compound 1 was achieved through a simple two-step reaction, depicted in Scheme 5.1. Hydrazine **71**, was synthesized through a solvent-free, nucleophilic substitution of 4,7-dichloroquinoline (1 eq) by hydrazine (2 eq) using microwave irradiation.<sup>409</sup> Then, **71** (1 eq) was condensed with 2-acetylphenothiazine (3 eq) in acetic acid and ethanol, affording Compound 1 in a good yield (81%).

Compound 1 identity was confirmed by analytical (HPLC), full scan MS (ESI+) and spectroscopic data (<sup>1</sup>H- and <sup>13</sup>C-NMR), which were identical to those of the commercial sample.



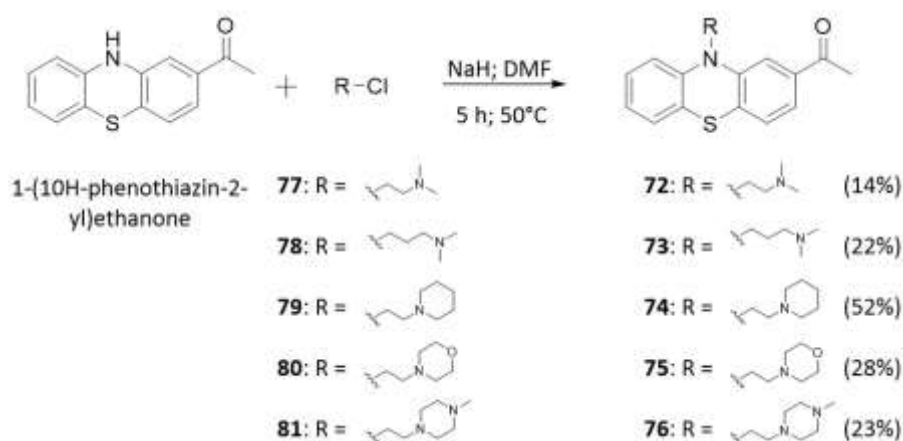
**Scheme 5.1.** Synthetic procedure for the synthesis of Compound 1.

After the synthesis of Compound 1, the same condensation reaction was applied for the synthesis of derivatives **60-64**. This part of the project was performed in collaboration with an undergraduate student, Luca Zambardi, who worked under my supervision. The different N-substituted phenothiazine derivatives **72-76** (1 eq) were reacted with **71** (1 eq) in acetic acid and ethanol, affording the corresponding final compounds **60-64** (Scheme 5.2) with yield varying from 22 to 91%.



**Scheme 5.2.** Synthetic procedure for the synthesis of derivatives **60-64**.

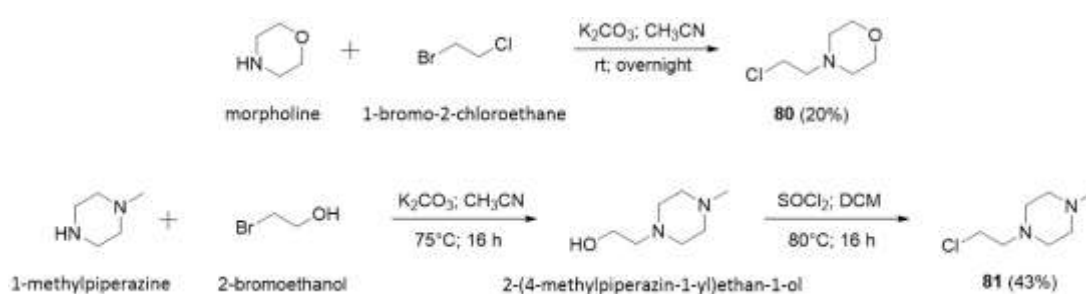
The N-substituted 2-acetylphenothiazine-derivatives **72-76** were synthesized through a simple N-alkylation of 2-acetylphenothiazine with the corresponding Cl-derivatives **77-81** (Scheme 5.3). In details, 2-acetylphenothiazine (1 eq) was reacted with **77-81** (2 eq), in the presence of NaH in DMF, affording **72-76** with low to good yields.



**Scheme 5.3.** Synthetic procedure for the synthesis of phenothiazine-derivatives **72-76**.

Among the Cl-derivatives, only **77-79** were commercially available. Thus, the synthesis of derivatives **80** and **81** was achieved through nucleophilic substitution, following two reported procedures (Scheme 5.4).<sup>410, 411</sup> In the first case, **80** was obtained through the reaction of morpholine (1 eq) with 1-bromo-2-chloroethane (2 eq) in the presence of

$K_2CO_3$  in acetonitrile. The same reaction was applied to 1-methylpiperazine, but no product was observed. Thus, **81** was synthesized through a two-step reaction. First, the reaction of 1-methylpiperazine (1 eq) with 2-bromoethanol (2 eq) and  $K_2CO_3$  in acetonitrile toluene at  $75^\circ C$  for 16 h give the intermediate 2-(4-methylpiperazin-1-yl)ethan-1-ol. Then, the crude product was reacted with  $SOCl_2$  in DCM at  $80^\circ C$  for 16 h, giving compound **81** in good yield.



**Scheme 5.4.** Synthetic procedure for the synthesis of **80** and **81**.

The final compounds **60-64** were characterized using analytical (HPLC) and spectroscopic data ( $^1H$ - and  $^{13}C$ -NMR).



## **Chapter VI**

## **Conclusions**



Protein misfolding diseases are a very challenging area for medicinal chemists. Several efforts have been made during the years; however, an effective treatment for these devastating diseases does not exist yet. PMDs are complex diseases, we still lack a complete understanding of all the mechanisms underlying them and how they are interconnected one to each other. Moreover, the neurodegeneration is estimated to start several years before the first clinical symptoms appeared. Importantly, the lack of an early diagnosis negatively affects the development of effective drugs.

Based on these considerations, this thesis was focused on the development of small molecule libraries for neurodegenerative PMDs, through different and innovative approaches.

1. Based on our interest in developing MTDLs for the treatment of Alzheimer's disease, and aiming to target the altered tau protein cascade, we have synthesized and tested a library of thirty-five TZD-derivatives. Among the developed compounds, two hit molecules (**25** and **27**) display features relevant in terms of MTDL drug discovery principles: (i) they are low molecular weight fragment hits; (ii) their activity towards the two selected targets is balanced; (iii) they show no significant toxicity, even towards mammalian primary neuronal cells.

**25** and **27** showed a low micromolar  $IC_{50}$  towards GSK-3 $\beta$ , together with the ability to inhibit AcPHF6 aggregation of 60% and 80%, respectively. Both compounds were predicted to cross the BBB through PAMPA-BBB assay, and showed a suitable cellular safety profile. Moreover, **27** displayed a good inhibition of the aggregation process of both K18 and full-length tau. Finally, both compounds were able to improve the cell viability in an okadaic acid-induced neurodegeneration cell model. Thus, **25** and **27** represent the first balanced, non-toxic, dual-acting compounds hitting the tau cascade at two different hubs.

Although preliminary and not yet confirmed by the in vivo proof of concept, our results showed that it is possible to design molecules that act specifically at two structurally different targets, like a kinase and a fibrillar protein. Importantly, these two hit

compounds could be promising tools to validate a completely new tau-centric approach as a potential disease-modifying strategy to treat Alzheimer's disease.

2. In the second project, we synthesized a library of 24 bivalent derivatives, with the aim to develop potential theranostic tools for Alzheimer's disease. Particularly, our design strategy resulted successful as fifteen compounds out of twenty-four were able to emit fluorescence. Among them, compounds **40**, **41**, **47**, **49**, **51**, **53**, and **59** showed an emission wavelength higher than 500 nm. Moreover, the preliminary tested compounds were also effective in inhibiting A $\beta$  and tau aggregation process in the *E. coli* model, showing IC<sub>50</sub> values in the low micromolar range. Thus, if the theranostic profile of the synthesized compounds will be confirmed through the designed assay cascade, they could emerge as innovative tools to potentially diagnose, deliver therapy, and monitor response to therapy in PMDs.

Although the clinical impact of theranostics is hard to predict, they currently represent a powerful emerging platform that could advance diagnostic and therapeutic treatment modalities, as well as streamline the entire drug development process.

3. In the third project we focused our attention on prion diseases. Particularly, we successfully developed an efficient synthetic route for the synthesis of target Compound 1 discovered at SISSA, Trieste. We applied the same reaction for the synthesis of five derivatives (**60-64**), designed to overcome the low solubility liability of Compound 1. Thus, we slightly modified its structure and we develop a focused library of five derivatives. After the synthesis, we will perform a solubility assay confirming our design strategy. The next step in the project will be testing the five derivatives in scrapie-infected cells, to assess whether the small modification could affect the activity. Importantly, the optimization of the drug-likeness of Compound 1 will allow us to select the best performing compound among its derivatives, to be progressed for further in vivo studies.



## **Chapter VII**

### **Experimental section**

## **7.1 Tau centric multi-target approach for Alzheimer's disease: development of first-in-class dual GSK-3 $\beta$ and tau-aggregation inhibitors**

### **7.1.1 Chemistry**

All the commercial available reagents and solvents were purchased from Sigma-Aldrich, Alpha Aesar, VWR, and TCI, and used without further purification. Reactions were followed by analytical thin layer chromatography (TLC), on pre-coated TLC plates (layer 0.20 mm silica gel60 with a fluorescent indicator UV254, from Sigma-Aldrich). Developed plates were air-dried and analyzed under a UV lamp (UV 254/365 nm). CEM Discover SP focused microwave reactor was used for microwave mediated reactions. Nuclear magnetic resonance (NMR) experiments were run on Varian VXR 400 (400 MHz for  $^1\text{H}$ , 100 MHz for  $^{13}\text{C}$ ).  $^1\text{H}$  and  $^{13}\text{C}$  NMR spectra were acquired at 300 K using deuterated dimethyl sulfoxide ( $(\text{CD}_3)_2\text{SO}$ ) and chloroform ( $\text{CDCl}_3$ ) as solvents. Chemical shifts ( $\delta$ ) are reported in parts per million (ppm) relative to tetramethylsilane (TMS) as internal reference, and coupling constants (J) are reported in hertz (Hz). The spin multiplicities are reported as s (singlet), br s (broad singlet), d (doublet), t (triplet), q (quartet), and m (multiplet). Mass spectra were recorded on a VG707EH-F apparatus, and electrospray ionization (ESI) both in positive and negative mode was applied. Compounds were named following IUPAC rules as applied by ChemBioDraw Ultra (version 14.0). All of the final compounds showed  $\geq 95\%$  purity by analytical HPLC. The purity of compounds **1-35** was determined using a Kinetex<sup>®</sup> 5 $\mu\text{m}$  EVO C18 100 Å, LC column 150 x 4.6 mm and a HPLC Jasco Corporation (Tokyo, Japan) instrument (PU-1585 UV equipped with a 20  $\mu\text{L}$  loop valve). HPLC parameters were the following: water with 0.05% trifluoroacetic acid (eluent A), and acetonitrile with 0.05% trifluoroacetic acid (eluent B); flow rate 1.00 mL/min; elution type isocratic with 75% of eluent A and 25% of eluent B; detection UV-Vis Abs at 254 nm. The samples were dissolved in MeOH or DMF (10  $\mu\text{g}/\text{mL}$ ).

As reported in literature,<sup>412</sup> the TZD-derivatives **1-35** were obtained as single Z isomers. Indeed, their  $^1\text{H}$ -NMR spectra shows only one signal attributable to the resonance of the 5-methylidene proton in the range 7.50-8.70 ppm; while in their  $^{13}\text{C}$ -

NMR spectra the 5-methylidene carbon and the C5 of the TZD ring resonated in the ranges 130.5-140.7 and 117.5-128.0 ppm, respectively.

### **PAINS analysis**

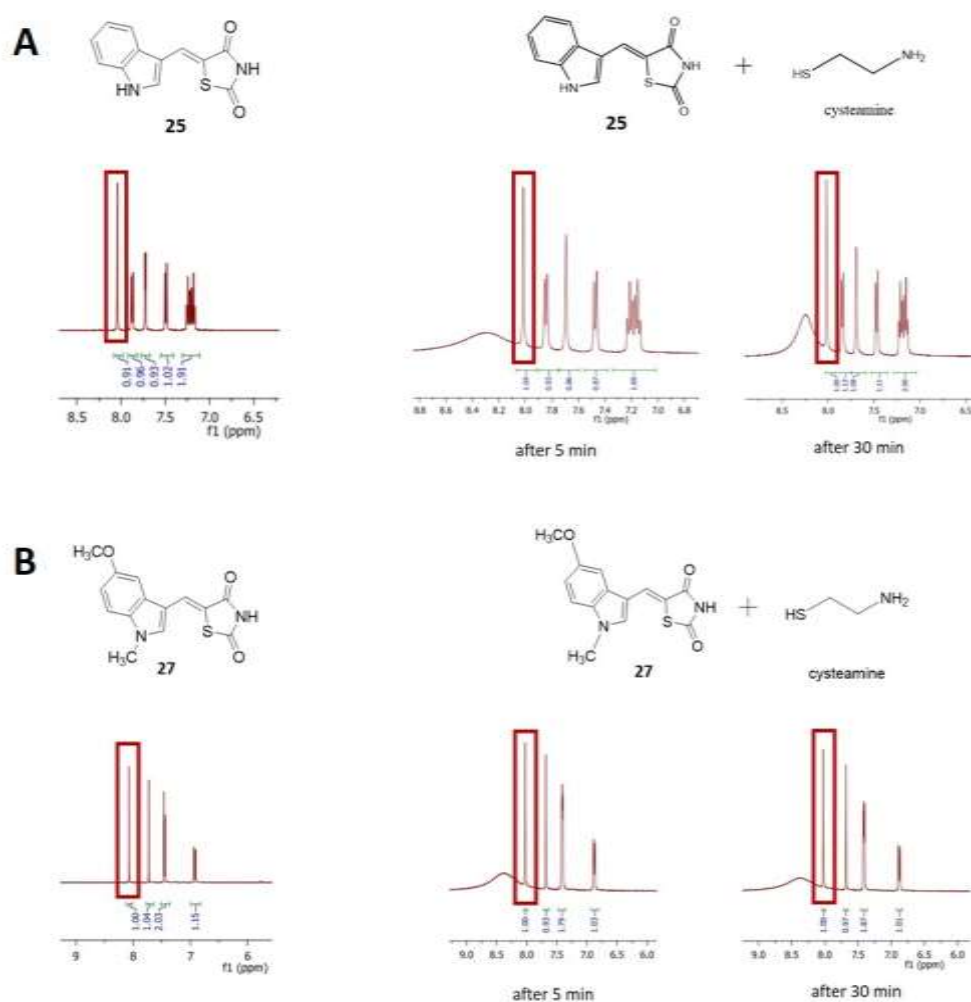
Aware of the liabilities that might arise from the alkylidene-TZD scaffold, we have analyzed **1-35** for known classes of assay interference compounds.<sup>413</sup> First, **1-35** were not recognized as PAINS according to the Free ADME-Tox Filtering Tool (FAF-Drugs4) program (<http://fafdrugs4.mti.univ-paris-diderot.fr/>), and to the “False Positive Remover” software (<http://www.cbligand.org/PAINS/>), neither as aggregators according to the software “Aggregator Advisor” (<http://advisor.bkslab.org/>). However, FAF-Drugs4 labeled them as covalent inhibitors due to their electrophilic nature. Thus, we provided evidence that the activities reported herein are highly likely not caused by pan assay interference.

First, the genuine GSK-3 $\beta$  inhibitory activity of **25** and **27** has been confirmed in two assays (i.e. Kinase-Glo and TR-FRET). Possible promiscuous kinase inhibition was preliminary ruled out by the fact that **25** and **27** do not inhibit similar kinases (CK1 $\delta$ , CK1 $\epsilon$ ) and Cdc7.

As regards tau aggregation inhibition, activities of **25** and **27** has been evaluated in three different assays (i.e. ThT-based fluorometric assay, CD, and AFM), which show consistent results.

Concerning the potential unspecific covalent reactions with proteins of alkylidene-TZD, we first investigated the thiol-trapping reactivity of **25** and **27** in a simple NMR-based assay.<sup>414</sup> Reaction of Michael acceptor-bearing compounds with two equivalents of 2-aminoethanethiol (cysteamine), a biologically relevant model thiol,<sup>415</sup> in DMSO should lead to the instantaneous formation of the corresponding Michael adduct and the simultaneous disappearance of the olefin signals. In contrast to what is reported for 5-benzylidene barbiturates,<sup>416</sup> reaction of **25** and **27** (0.01 mmol) with cysteamine (0.02 mmol), after 30 minutes, did not lead to the formation of the Michael adduct (Figure 7.1). The same was observed after 24 h. Thus, we can expect that the double bond of **25** and **27** did not react covalently with sulphur nucleophiles, with indiscriminate

reactivity. In addition, based on the results of the jump-dilution and the ATP-competition assays, we are confident that they did not react covalently with GSK-3 $\beta$  kinase.



**Figure 7.1.** Thiol trapping assay.  $^1\text{H-NMR}$  spectrum of **25** (A) and **27** (B) in  $\text{DMSO-}d_6$  and in  $\text{DMSO-}d_6$  with cysteamine (1:2). In the squares, the olefin signal is highlighted. No reaction occurs, even after 30 minutes.

#### General procedure for the synthesis of compounds 1-35.

The corresponding aldehydes (1 mmol) were reacted with 2,4-thiazolidinedione (1 mmol), using EDDA (0.5 mmol) under microwave irradiation at  $80^\circ\text{C}$  for 30 minutes. The reaction mixture was diluted with water and the solid was collected by filtration.

After washing it with water all the final compounds were purified through crystallization from ethanol/water.

*(Z)*-5-benzylidenethiazolidine-2,4-dione (**1**). The title compound **1** was obtained as a light yellow solid, according to general procedure using benzaldehyde (**1a**). Yield 87%. <sup>1</sup>H-NMR (401 MHz, DMSO-*d*<sub>6</sub>): δ 12.61 (br s, 1H); δ 7.79 (s, 1H); δ 7.61-7.46 (m, 5H). <sup>13</sup>C-NMR (101 MHz, DMSO-*d*<sub>6</sub>): δ 168.37; δ 167.89; δ 133.49; δ 132.10; δ 130.81; δ 130.41; δ 129.74; δ 124.11. MS (ESI<sup>-</sup>) *m/z*: 204 [M-H]<sup>-</sup>.

*(Z)*-5-(2-hydroxybenzylidene)thiazolidine-2,4-dione (**2**). The title compound **2** was obtained as a yellow solid, according to general procedure using 2-hydroxybenzaldehyde (**2a**). Yield 56%. <sup>1</sup>H-NMR (401 MHz, DMSO-*d*<sub>6</sub>): δ 12.48 (br s, exch, 1H); δ 10.48 (s, exch, 1H); δ 8.02 (s, 1H); δ 7.33-7.28 (m, 2H); δ 6.96-6.92 (m, 2H). <sup>13</sup>C-NMR (101 MHz, DMSO-*d*<sub>6</sub>): δ 168.60; δ 167.97; δ 157.69; δ 132.66; δ 128.73; δ 127.41; δ 122.36; δ 120.37; δ 120.11; δ 116.55. MS (ESI<sup>-</sup>) *m/z*: 220 [M-H]<sup>-</sup>.

*(Z)*-5-(3-hydroxybenzylidene)thiazolidine-2,4-dione (**3**). The title compound **3** was obtained as a white solid, according to general procedure using 3-hydroxybenzaldehyde (**3a**). Yield 43%. <sup>1</sup>H-NMR (401 MHz, DMSO-*d*<sub>6</sub>): δ 12.58 (br s, exch, 1H); δ 9.82 (s, exch, 1H); δ 7.68 (s, 1H); δ 7.32 (t, *J* = 7.9, 1H); δ 7.03 (d, *J* = 7.6, 1H); δ 6.97 (s, 1H); δ 6.87 (d, *J* = 8, 1H). <sup>13</sup>C-NMR (101 MHz, DMSO-*d*<sub>6</sub>): δ 168.38; δ 167.81; δ 158.29; δ 134.63; δ 132.37; δ 130.78; δ 123.78; δ 121.73; δ 118.14; δ 116.32. MS (ESI<sup>-</sup>) *m/z*: 220 [M-H]<sup>-</sup>.

*(Z)*-5-(4-hydroxybenzylidene)thiazolidine-2,4-dione (**4**). The title compound **4** was obtained as a yellow solid, according to general procedure using 4-hydroxybenzaldehyde (**4a**). Yield 69%. <sup>1</sup>H-NMR (401 MHz, DMSO-*d*<sub>6</sub>): δ 12.42 (br s, exch, 1H); δ 10.28 (s, exch, 1H); δ 7.69 (s, 1H); δ 7.45 (s, 1H); δ 6.91 (s, 1H). <sup>13</sup>C-NMR (101 MHz, DMSO-*d*<sub>6</sub>): δ 168.48; δ 167.94; δ 160.30; δ 132.79; δ 132.70; δ 124.36; δ 119.43; δ 116.73. MS (ESI<sup>-</sup>) *m/z*: 220 [M-H]<sup>-</sup>.

*(Z)*-5-(2-hydroxy-4-methoxybenzylidene)thiazolidine-2,4-dione (**5**). The title compound **5** was obtained as a yellow solid, according to general procedure using 2-hydroxy-4-methoxybenzaldehyde (**5a**). Yield 75%. <sup>1</sup>H-NMR (401 MHz, DMSO-*d*<sub>6</sub>): δ 12.39 (br s, exch, 1H); δ 10.64 (s, exch, 1H); δ 7.98 (s, 1H); δ 7.27 (d, *J* = 8.8, 1H); δ 6.59 (dd, *J* = 8.8,



2.5, 1H);  $\delta$  6.51 (d,  $J = 2.5$ , 1H);  $\delta$  3.77 (s, 3H).  $^{13}\text{C-NMR}$  (101 MHz,  $\text{DMSO-}d_6$ ):  $\delta$  168.24;  $\delta$  167.63;  $\delta$  162.66;  $\delta$  159.13;  $\delta$  129.72;  $\delta$  126.96;  $\delta$  118.38;  $\delta$  113.07;  $\delta$  106.56;  $\delta$  101.13;  $\delta$  55.32. MS (ESI<sup>+</sup>)  $m/z$ : 274 [M+Na]<sup>+</sup>.

*(Z)*-5-(4-hydroxy-3-methoxybenzylidene)thiazolidine-2,4-dione (**6**). The title compound **6** was obtained as a light yellow solid, according to general procedure using 4-hydroxy-3-methoxybenzaldehyde (**6a**). Yield 62%.  $^1\text{H-NMR}$  (401 MHz,  $\text{DMSO-}d_6$ ):  $\delta$  12.43 (br s, exch, 1H);  $\delta$  9.90 (s, exch, 1H);  $\delta$  7.71 (s, 1H);  $\delta$  7.17 (s, 1H);  $\delta$  7.08-7.05 (m, 1H);  $\delta$  6.94-6.90 (m, 1H);  $\delta$  3.83 (s, 3H).  $^{13}\text{C-NMR}$  (101 MHz,  $\text{DMSO-}d_6$ ):  $\delta$  168.51;  $\delta$  167.99;  $\delta$  149.84;  $\delta$  148.40;  $\delta$  132.96;  $\delta$  124.83;  $\delta$  124.54;  $\delta$  119.73;  $\delta$  116.60;  $\delta$  114.58;  $\delta$  56.07. MS (ESI<sup>-</sup>)  $m/z$ : 250 [M-H]<sup>-</sup>.

*(Z)*-5-(4-hydroxy-3-nitrobenzylidene)thiazolidine-2,4-dione (**7**). The title compound **7** was obtained as a light yellow solid, according to general procedure using 4-hydroxy-3-nitrobenzaldehyde (**7a**). Yield 79%.  $^1\text{H-NMR}$  (401 MHz,  $\text{DMSO-}d_6$ ):  $\delta$  8.14 (d,  $J = 2.3$  Hz, 1H);  $\delta$  7.76 (s, 1H);  $\delta$  7.72 (dd,  $J = 8.8$ , 2.3 Hz, 1H);  $\delta$  7.22 (d,  $J = 8.8$  Hz, 1H).  $^{13}\text{C-NMR}$  (101 MHz,  $\text{DMSO-}d_6$ ):  $\delta$  168.88;  $\delta$  168.61;  $\delta$  155.86;  $\delta$  137.81;  $\delta$  135.78;  $\delta$  130.09;  $\delta$  128.19;  $\delta$  123.16;  $\delta$  122.55;  $\delta$  121.57. MS (ESI<sup>-</sup>)  $m/z$ : 265 [M-H]<sup>-</sup>.

*(Z)*-5-(2-fluorobenzylidene)thiazolidine-2,4-dione (**8**). The title compound **8** was obtained as a pale yellow solid, according to general procedure using 2-fluorobenzaldehyde (**8a**). Yield 49%.  $^1\text{H-NMR}$  (401 MHz,  $\text{DMSO-}d_6$ ):  $\delta$  12.73 (br s, 1H);  $\delta$  7.79 (s, 1H);  $\delta$  7.56 (t,  $J = 6.9$ , 2H);  $\delta$  7.39 (t,  $J = 8.3$ , 2H).  $^{13}\text{C-NMR}$  (101 MHz,  $\text{DMSO-}d_6$ ):  $\delta$  168.05;  $\delta$  167.51;  $\delta$  160.93;  $\delta$  129.24;  $\delta$  126.81;  $\delta$  125.85;  $\delta$  123.10;  $\delta$  121.36;  $\delta$  116.66. MS (ESI<sup>+</sup>)  $m/z$ : 246 [M+Na]<sup>+</sup>.

*(Z)*-5-(3-fluorobenzylidene)thiazolidine-2,4-dione (**9**). The title compound **9** was obtained as a yellow solid, according to general procedure using 3-fluorobenzaldehyde (**9a**). Yield 60%.  $^1\text{H-NMR}$  (401 MHz,  $\text{DMSO-}d_6$ ):  $\delta$  12.73 (br s, 1H);  $\delta$  7.83 (s, 1H);  $\delta$  7.62 (dd,  $J = 14.5$ , 7.5, 1H);  $\delta$  7.48 (t,  $J = 9.9$ , 2H);  $\delta$  7.37 (t,  $J = 8.5$ , 1H).  $^{13}\text{C-NMR}$  (101 MHz,  $\text{DMSO-}d_6$ ):  $\delta$  167.67;  $\delta$  167.27;  $\delta$  162.28;  $\delta$  135.46;  $\delta$  131.41;  $\delta$  130.32;  $\delta$  125.56;  $\delta$  125.37;  $\delta$  117.19;  $\delta$  116.74. MS (ESI<sup>-</sup>)  $m/z$ : 222 [M-H]<sup>-</sup>.

*(Z)*-5-(4-fluorobenzylidene)thiazolidine-2,4-dione (**10**). The title compound **10** was obtained as a yellow solid, according to general procedure using 4-fluorobenzaldehyde

**(10a)**. Yield 76%.  $^1\text{H-NMR}$  (401 MHz,  $\text{DMSO-}d_6$ ):  $\delta$  12.63 (br s, exch, 1H);  $\delta$  7.81 (s, 1H);  $\delta$  7.67 (m, 2H);  $\delta$  7.39 (t,  $J = 8.7$ , 2H).  $^{13}\text{C-NMR}$  (101 MHz,  $\text{DMSO-}d_6$ ):  $\delta$  167.79;  $\delta$  167.32;  $\delta$  162.86;  $\delta$  132.48;  $\delta$  130.70;  $\delta$  129.74;  $\delta$  123.31;  $\delta$  116.51. MS (ESI $^-$ )  $m/z$ : 222 [M-H] $^-$ .

*(Z)*-5-(2-(dimethylamino)benzylidene)thiazolidine-2,4-dione (**11**). The title compound **11** was obtained as a yellow solid, according to general procedure using 2-(N,N-dimethylamino)benzaldehyde (**11a**). Yield 70%.  $^1\text{H-NMR}$  (401 MHz,  $\text{DMSO-}d_6$ ):  $\delta$  12.45 (br s, exch, 1H);  $\delta$  7.86 (s, 1H);  $\delta$  7.43 (dd,  $J = 12.9, 7.3$ , 2H);  $\delta$  7.18 (d,  $J = 8.1$ , 1H);  $\delta$  7.10 (t,  $J = 7.5$ , 1H);  $\delta$  2.68 (s, 6H).  $^{13}\text{C-NMR}$  (101 MHz,  $\text{DMSO-}d_6$ ):  $\delta$  168.65;  $\delta$  167.88;  $\delta$  153.28;  $\delta$  131.38;  $\delta$  130.53;  $\delta$  129.83;  $\delta$  125.65;  $\delta$  122.82;  $\delta$  122.08;  $\delta$  118.81;  $\delta$  44.15. MS (ESI $^-$ )  $m/z$ : 247 [M-H] $^-$ .

*(Z)*-5-(3-(dimethylamino)benzylidene)thiazolidine-2,4-dione (**12**). The title compound **12** was obtained as a yellow solid, according to general procedure using 3-(N,N-dimethylamino)benzaldehyde (**12a**). Yield 78%.  $^1\text{H-NMR}$  (401 MHz,  $\text{DMSO-}d_6$ ):  $\delta$  12.55 (br s, exch, 1H);  $\delta$  7.73 (s, 1H);  $\delta$  7.31 (t,  $J = 7.9$ , 1H);  $\delta$  6.87-6.81 (m, 3H);  $\delta$  2.93 (s, 6H).  $^{13}\text{C-NMR}$  (101 MHz,  $\text{DMSO-}d_6$ ):  $\delta$  168.45;  $\delta$  167.74;  $\delta$  151.06;  $\delta$  134.00;  $\delta$  133.51;  $\delta$  130.16;  $\delta$  123.16;  $\delta$  117.73;  $\delta$  114.79;  $\delta$  113.99;  $\delta$  40.33. MS (ESI $^-$ )  $m/z$ : 247 [M-H] $^-$ .

*(Z)*-5-(4-(dimethylamino)benzylidene)thiazolidine-2,4-dione (**13**). The title compound **13** was obtained as an orange solid, according to general procedure using 4-(N,N-dimethylamino)benzaldehyde (**13a**). Yield 88%.  $^1\text{H-NMR}$  (401 MHz,  $\text{DMSO-}d_6$ ):  $\delta$  12.29 (br s, exch, 1H);  $\delta$  7.66 (s, 1H);  $\delta$  7.42 (d,  $J = 8.9$ , 2H);  $\delta$  6.81 (d,  $J = 9$ , 2H);  $\delta$  3.01 (s, 6H).  $^{13}\text{C-NMR}$  (101 MHz,  $\text{DMSO-}d_6$ ):  $\delta$  168.10;  $\delta$  167.52;  $\delta$  151.42;  $\delta$  132.83;  $\delta$  132.06;  $\delta$  119.80;  $\delta$  115.71;  $\delta$  112.01;  $\delta$  30.63. MS (ESI $^-$ )  $m/z$ : 247 [M-H] $^-$ .

*(Z)*-5-(pyridin-2-ylmethylene)thiazolidine-2,4-dione (**14**). The title compound **14** was obtained as a yellow solid, according to general procedure using 2-pyridinecarbaldehyde (**14a**). Yield 55%.  $^1\text{H-NMR}$  (401 MHz,  $\text{DMSO-}d_6$ ):  $\delta$  12.43 (br s, 1H);  $\delta$  8.75 (d,  $J = 4.7$ , 1H);  $\delta$  7.93 (t,  $J = 7.6$ , 1H);  $\delta$  7.86-7.82 (m, 2H);  $\delta$  7.42 (dd,  $J = 6.7, 5.6$ , 1H).  $^{13}\text{C-NMR}$  (101 MHz,  $\text{DMSO-}d_6$ ):  $\delta$  172.13;  $\delta$  167.55;  $\delta$  151.33;  $\delta$  149.44;  $\delta$  137.61;  $\delta$  128.12;  $\delta$  127.88;  $\delta$  127.83;  $\delta$  124.03. MS (ESI $^-$ )  $m/z$ : 205 [M-H] $^-$ .

*(Z)*-5-(pyridin-3-ylmethylene)thiazolidine-2,4-dione (**15**). The title compound **15** was obtained as a pale yellow solid, according to general procedure using 3-pyridinecarbaldehyde (**15a**). Yield 34%. <sup>1</sup>H-NMR (401 MHz, DMSO-*d*<sub>6</sub>): δ 12.68 (br s, 1H); δ 8.80 (s, 1H); δ 8.59 (d, *J* = 4.7, 1H); δ 7.93 (d, *J* = 8.1, 1H); δ 7.80 (s, 1H); δ 7.52 (d, *J* = 5.6, 1H). <sup>13</sup>C-NMR (101 MHz, DMSO-*d*<sub>6</sub>): δ 167.57; δ 167.20; δ 151.31; δ 150.53; δ 135.98; δ 129.24; δ 128.38; δ 126.02; δ 124.23. MS (ESI<sup>-</sup>) *m/z*: 205 [M-H]<sup>-</sup>.

*(Z)*-5-(pyridin-4-ylmethylene)thiazolidine-2,4-dione (**16**). The title compound **16** was obtained as a pale pink solid, according to general procedure using 4-pyridinecarbaldehyde (**16a**). Yield 59%. <sup>1</sup>H-NMR (401 MHz, DMSO-*d*<sub>6</sub>): δ 12.79 (br s, 1H); δ 8.72 (d, *J* = 5.1, 2H); δ 7.75 (s, 1H); δ 7.54 (d, *J* = 5.2, 2H). <sup>13</sup>C-NMR (101 MHz, DMSO-*d*<sub>6</sub>): δ 167.82; δ 167.71; δ 150.81; δ 149.72; δ 140.50; δ 128.65; δ 123.59. MS (ESI<sup>-</sup>) *m/z*: 205 [M-H]<sup>-</sup>.

*(Z)*-5-(furan-2-ylmethylene)thiazolidine-2,4-dione (**17**). The title compound **17** was obtained as a brown solid, according to general procedure using 2-furaldehyde (**17a**). Yield 65%. <sup>1</sup>H-NMR (401 MHz, DMSO-*d*<sub>6</sub>): δ 12.44 (br s, exch, 1H); δ 8.05 (s, 1H); δ 7.61 (d, *J* = 5.3, 1H); δ 7.09 (d, *J* = 3.5, 1H); δ 6.76-6.75 (m, not resolved, 1H). <sup>13</sup>C-NMR (101 MHz, DMSO-*d*<sub>6</sub>): δ 168.59; δ 167.05; δ 149.21; δ 147.46; δ 120.39; δ 118.55; δ 118.40; δ 113.48. MS (ESI<sup>-</sup>) *m/z*: 194 [M-H]<sup>-</sup>.

*(Z)*-5-(benzofuran-2-ylmethylene)thiazolidine-2,4-dione (**18**). The title compound **18** was obtained as a dark yellow solid, according to general procedure using 2-benzofurancarboxaldehyde (**18a**). Yield 59%. <sup>1</sup>H-NMR (401 MHz, DMSO-*d*<sub>6</sub>): δ 12.58 (br s, exch, 1H); δ 7.78-7.75 (m, not resolved, 2H); δ 7.70-7.67 (m, not resolved, 1H); δ 7.51 (s, 1H); δ 7.45 (dd, *J* = 14.0, 7.3, 1H); δ 7.33 (dd, *J* = 13.7, 7.0, 1H). <sup>13</sup>C-NMR (101 MHz, DMSO-*d*<sub>6</sub>): δ 168.57; δ 166.97; δ 155.33; δ 150.89; δ 127.82; δ 127.11; δ 124.21; δ 123.98; δ 122.46; δ 118.54; δ 114.14; δ 111.50. MS (ESI<sup>-</sup>) *m/z*: 244 [M-H]<sup>-</sup>.

*(Z)*-5-(thiophen-2-ylmethylene)thiazolidine-2,4-dione (**19**). The title compound **19** was obtained as a grey solid, according to general procedure using 2-thiophenecarboxaldehyde (**19a**). Yield 92%. <sup>1</sup>H-NMR (401 MHz, DMSO-*d*<sub>6</sub>): δ 12.56 (br s, exch, 1H); δ 8.06 (s, 1H); δ 8.02 (d, *J* = 5.0, 1H); δ 7.68 (d, *J* = 3.6, 1H); δ 7.30-7.28 (m, 1H). <sup>13</sup>C-NMR (101 MHz, DMSO-*d*<sub>6</sub>): δ 166.99; δ 166.94; δ 137.15; δ 134.31; δ 132.89; δ 128.80; δ 125.00; δ 120.98. MS (ESI<sup>-</sup>) *m/z*: 210 [M-H]<sup>-</sup>.

*(Z)*-5-(benzothiophen-2-ylmethylene)thiazolidine-2,4-dione (**20**). The title compound **20** was obtained as a dark yellow solid, according to general procedure using benzo[b]thiophene-2-carboxaldehyde (**20a**). Yield 54%. <sup>1</sup>H-NMR (401 MHz, DMSO-*d*<sub>6</sub>): δ 12.61 (br s, exch, 1H); δ 8.14 (s, 1H); δ 8.12-8.08 (m, 1H); δ 8.00-7.96 (m, 2H); δ 7.50-7.45 (m, 2H). <sup>13</sup>C-NMR (101 MHz, DMSO-*d*<sub>6</sub>): δ 167.37; δ 167.34; δ 141.28; δ 138.83; δ 137.04; δ 131.29; δ 126.47; δ 125.46; δ 125.23; δ 125.02; δ 124.35; δ 122.90. MS (ESI<sup>-</sup>) *m/z*: 260 [M-H]<sup>-</sup>.

*(Z)*-5-(naphthalen-2-ylmethylene)thiazolidine-2,4-dione (**21**). The title compound **21** was obtained as a yellow solid, according to general procedure using 2-naphthaldehyde (**21a**). Yield 37%. <sup>1</sup>H-NMR (401 MHz, DMSO-*d*<sub>6</sub>): δ 12.65 (br s, exch, 1H); δ 8.18 (s, 1H); δ 8.06-8.04 (m, 2H); δ 7.98-7.94 (m, 2H); δ 7.69 (d, *J* = 8.6, 1H); δ 7.64-7.58 (m, 2H). <sup>13</sup>C-NMR (101 MHz, DMSO-*d*<sub>6</sub>): δ 168.38; δ 167.81; δ 133.68; δ 133.16; δ 132.18; δ 131.26; δ 131.06; δ 129.37; δ 129.13; δ 128.41; δ 128.13; δ 127.57; δ 126.42; δ 124.30. MS (ESI<sup>+</sup>) *m/z*: 254 [M+Na]<sup>+</sup>.

*(Z)*-5-(anthracen-9-ylmethylene)thiazolidine-2,4-dione (**22**). The title compound **22** was obtained as an orange solid, according to general procedure using anthracene-9-carbaldehyde (**22a**). Yield 18%. <sup>1</sup>H-NMR (401 MHz, CDCl<sub>3</sub>): δ 8.79 (s, 1H); δ 8.55 (s, 1H); δ 8.07 (d, *J* = 8.2, 2H); δ 7.98 (d, *J* = 8.8, 2H); 7.60-7.52 (m, 4H). <sup>13</sup>C-NMR (101 MHz, CDCl<sub>3</sub>): δ 166.87; δ 165.04; δ 133.38; δ 131.32; δ 131.11; δ 129.82; δ 129.41; δ 128.70; δ 127.23; δ 126.81; δ 125.89; δ 125.04. MS (ESI<sup>-</sup>) *m/z*: 304 [M-H]<sup>-</sup>.

*(Z)*-5-((*E*)-3-phenylallylidene)thiazolidine-2,4-dione (**23**). The title compound **23** was obtained as a pale yellow solid, according to general procedure using cinnamaldehyde (**23a**). Yield 36%. <sup>1</sup>H-NMR (401 MHz, DMSO-*d*<sub>6</sub>): δ 12.31 (br s, 1H); δ 7.67-7.65 (m, 2H); δ 7.47-7.35 (m, 4H); δ 7.27 (d, *J* = 15.3, 1H); δ 6.91 (dd, *J* = 15.3, 11.4, 1H). <sup>13</sup>C-NMR (101 MHz, DMSO-*d*<sub>6</sub>): δ 168.61; δ 143.33; δ 136.07; δ 131.94; δ 130.03; δ 129.34; δ 128.13; δ 124.09; δ 109.95. MS (ESI<sup>-</sup>) *m/z*: 230 [M-H]<sup>-</sup>.

*(Z)*-5-((*E*)-3-(4-(dimethylamino)phenyl)allylidene)thiazolidine-2,4-dione (**24**). The title compound **24** was obtained as a dark red solid, according to general procedure using (*E*)-3-(4-(dimethylamino)phenyl)acrylaldehyde (**24a**). Yield 58%. <sup>1</sup>H-NMR (401 MHz, DMSO-*d*<sub>6</sub>): δ 12.23 (br s, 1H); δ 7.47 (dd, *J* = 19.7, 10.2, 3H); δ 7.16 (d, *J* = 15.0, 1H); δ 6.72 (d, *J* = 8.9, 2H); δ 6.61 (dd, *J* = 15.0, 11.6, 1H); δ 2.99 (s, 6H). <sup>13</sup>C-NMR (101 MHz,

DMSO-*d*<sub>6</sub>): δ 168.23; δ 167.32; δ 151.79; δ 145.30; δ 133.96; δ 129.97; δ 123.61; δ 120.93; δ 118.50; δ 112.31; δ 40.13. MS (ESI<sup>-</sup>) *m/z*: 273 [M-H]<sup>-</sup>.

*(Z)*-5-((1*H*-indol-3-yl)methylene)thiazolidine-2,4-dione (**25**). The title compound **25** was obtained as a yellow solid, according to general procedure using 1*H*-indole-3-carbaldehyde (**25a**). Yield 45%. <sup>1</sup>H-NMR (401 MHz, DMSO-*d*<sub>6</sub>): δ 12.29 (br s, 1H); δ 12.12 (s, exch, 1H); δ 8.06 (s, 1H); δ 7.89 (d, *J* = 7.8, 1H); δ 7.74 (s, 1H); δ 7.50 (d, *J* = 7.9, 1H); δ 7.27-7.18 (m, 2H). <sup>13</sup>C-NMR (101 MHz, DMSO-*d*<sub>6</sub>): δ 168.09; δ 167.69; δ 136.62; δ 129.06; δ 127.19; δ 124.93; δ 123.49; δ 121.47; δ 118.75; δ 116.59; δ 112.82; δ 110.83. MS (ESI<sup>-</sup>) *m/z*: 243 [M-H]<sup>-</sup>.

*(Z)*-5-((5-methoxy-1*H*-indol-3-yl)methylene)thiazolidine-2,4-dione (**26**). The title compound **26** was obtained as a dark yellow solid, according to general procedure using 5-methoxy-1*H*-indole-3-carbaldehyde (**26a**). Yield 47%. <sup>1</sup>H-NMR (401 MHz, DMSO-*d*<sub>6</sub>): δ 12.25 (br s, 1H); δ 12.00 (s, 1H); δ 8.09 (s, 1H); δ 7.66 (d, *J* = 3.0, 1H), δ 7.40 (dd, *J* = 18.0, 5.5, 2H); δ 6.86 (dd, *J* = 8.8, 2.3, 1H); δ 3.82 (s, 3H). <sup>13</sup>C-NMR (101 MHz, DMSO-*d*<sub>6</sub>): δ 168.19; δ 167.77; δ 155.36; δ 131.43; δ 129.19; δ 128.05; δ 125.43; δ 115.76; δ 113.80; δ 113.59; δ 110.86; δ 100.47; δ 55.88. MS (ESI<sup>-</sup>) *m/z*: 273 [M-H]<sup>-</sup>.

*(Z)*-5-((5-methoxy-1-methyl-1*H*-indol-3-yl)methylene)thiazolidine-2,4-dione (**27**). The title compound **27** was obtained as an orange solid, according to general procedure using 5-methoxy-1-methyl-1*H*-indole-3-carbaldehyde (**27a**). Yield 44%. <sup>1</sup>H-NMR (401 MHz, DMSO-*d*<sub>6</sub>): δ 12.25 (br s, 1H); δ 8.07 (s, 1H); δ 7.73 (s, 1H); δ 7.52–7.44 (m, 2H); δ 6.92 (dd, *J* = 8.9, 2.3 Hz, 1H); δ 3.89 (s, 3H); δ 3.84 (s, 3H). <sup>13</sup>C-NMR (101 MHz, DMSO-*d*<sub>6</sub>): δ 168.20; δ 167.73; δ 155.68; δ 132.72; δ 132.20; δ 128.56; δ 124.96; δ 115.48; δ 113.73; δ 112.10; δ 109.72; δ 100.71; δ 55.95; δ 33.85. MS (ESI<sup>-</sup>) *m/z*: 287 [M-H]<sup>-</sup>.

*(Z)*-5-((1-methyl-1*H*-benzo[*d*]imidazol-2-yl)methylene)thiazolidine-2,4-dione (**28**). The title compound **28** was obtained as an orange solid, according to general procedure using 1-methyl-1*H*-benzo[*d*]imidazole-2-carbaldehyde (**28a**). Yield 48%. <sup>1</sup>H-NMR (401 MHz, DMSO-*d*<sub>6</sub>): δ 12.57 (br s, 1H); δ 7.84 (s, 1H); δ 7.75 (d, *J* = 8.0, 1H); δ 7.67 (d, *J* = 8.0, 1H); δ 7.34 (dt, *J* = 26.1, 7.1, 2H); δ 3.99 (s, 3H). <sup>13</sup>C-NMR (101 MHz, DMSO-*d*<sub>6</sub>): δ 171.21; δ 167.41; δ 147.97; δ 143.15; δ 136.28; δ 131.34; δ 124.48; δ 123.49; δ 120.04; δ 115.69; δ 111.43; δ 30.25. MS (ESI<sup>+</sup>) *m/z*: 260 [M+Na]<sup>+</sup>.

*(Z)*-5-((2-phenyl-1H-indol-3-yl)methylene)thiazolidine-2,4-dione (**29**). The title compound **29** was obtained as an orange solid, according to general procedure using 2-phenyl-1H-indole-3-carbaldehyde (**29a**). Yield 22%. <sup>1</sup>H-NMR (401 MHz, DMSO-*d*<sub>6</sub>): δ 12.31 (br s, 1H); δ 12.27 (s, exch 1H); δ 7.96 (s, 1H); δ 7.78 (d, *J* = 7.9, 1H); 7.63-7.49 (m, 6H); δ 7.29-7.19 (m, 2H). <sup>13</sup>C-NMR (101 MHz, DMSO-*d*<sub>6</sub>): δ 168.44; δ 142.21; δ 136.91; δ 131.44; δ 129.56; δ 129.44; δ 128.09; δ 126.01; δ 123.47; δ 121.18; δ 120.40; δ 120.28; δ 112.68; δ 107.31. MS (ESI<sup>-</sup>) *m/z*: 319 [M-H]<sup>-</sup>.

*(Z)*-5-([1,1'-biphenyl]-4-ylmethylene)thiazolidine-2,4-dione (**30**). The title compound **30** was obtained as a white solid, according to general procedure using [1,1'-biphenyl]-4-carbaldehyde (**30a**). Yield 55%. <sup>1</sup>H-NMR (401 MHz, DMSO-*d*<sub>6</sub>): δ 12.64 (br s, 1H); δ 7.86-7.83 (m, 3H); δ 7.72 (dd, *J* = 21.4, 8.0, 4H); δ 7.50 (t, *J* = 7.6, 2H); δ 7.41 (t, *J* = 7.3, 1H). <sup>13</sup>C-NMR (101 MHz, DMSO-*d*<sub>6</sub>): δ 168.28; δ 167.88; δ 142.15; δ 139.25; δ 132.52; δ 131.66; δ 131.10; δ 129.50; δ 128.63; δ 127.81; δ 127.21; δ 123.94. MS (ESI<sup>-</sup>) *m/z*: 280 [M-H]<sup>-</sup>.

*(Z)*-5-(2-(benzyloxy)benzylidene)thiazolidine-2,4-dione (**31**). The title compound **31** was obtained as a pale yellow solid, according to general procedure using 2-(benzyloxy)benzaldehyde (**31a**). Yield 61%. <sup>1</sup>H-NMR (401 MHz, DMSO-*d*<sub>6</sub>): δ 12.58 (br s, 1H); δ 8.03 (s, 1H); δ 7.48-7.42 (m, 6H); δ 7.36 (t, *J* = 6.5, 1H); δ 7.24 (d, *J* = 8.4, 1H); δ 7.11 (t, *J* = 7.5, 1H); δ 5.25 (s, 2H). <sup>13</sup>C-NMR (101 MHz, DMSO-*d*<sub>6</sub>): δ 168.43; δ 167.77; δ 157.61; δ 136.94; δ 132.66; δ 128.98; δ 128.81; δ 128.47; δ 128.10; δ 126.64; δ 124.02; δ 122.35; δ 121.63; δ 113.73; δ 70.35. MS (ESI<sup>+</sup>) *m/z*: 334 [M+Na]<sup>+</sup>.

*(Z)*-5-((2,3-dihydrobenzo[*b*][1,4]dioxin-6-yl)methylene)thiazolidine-2,4-dione (**32**). The title compound **32** was obtained as a pale yellow solid, according to general procedure using 2,3-dihydrobenzo[*b*][1,4]dioxine-6-carbaldehyde (**32a**). Yield 75%. <sup>1</sup>H-NMR (401 MHz, DMSO-*d*<sub>6</sub>): δ 12.52 (br s, 1H); δ 7.69 (s, 1H); δ 7.12-7.10 (m, 2H); δ 7.02 (dd, *J* = 7.6, 1.2, 1H); δ 4.30-4.25 (m, 4H). <sup>13</sup>C-NMR (101 MHz, DMSO-*d*<sub>6</sub>): δ 168.40; δ 168.01; δ 146.04; δ 144.13; δ 131.99; δ 126.78; δ 124.21; δ 121.60; δ 119.16; δ 118.42; δ 64.89; δ 64.41. MS (ESI<sup>-</sup>) *m/z*: 262 [M-H]<sup>-</sup>.

*(Z)*-5-((7-methoxybenzo[*d*][1,3]dioxol-5-yl)methylene)thiazolidine-2,4-dione (**33**). The title compound **33** was obtained as a yellow solid, according to general procedure using 7-methoxybenzo[*d*][1,3]dioxole-5-carbaldehyde (**33a**). Yield 58%. <sup>1</sup>H-NMR (401

MHz, DMSO-*d*<sub>6</sub>): δ 12.55 (br s, 1H); δ 7.72 (s, 1H); δ 6.97 (s, 1H); δ 6.82 (s, 1H); δ 6.11 (s, 2H); δ 3.87 (s, 3H). <sup>13</sup>C-NMR (101 MHz, DMSO-*d*<sub>6</sub>): δ 168.33; δ 167.98; δ 149.56; δ 143.91; δ 137.43; δ 132.28; δ 128.02; δ 122.08; δ 111.80; δ 103.44; δ 102.68; δ 56.82. MS (ESI<sup>-</sup>) *m/z*: 278 [M-H]<sup>-</sup>.

*(Z)*-5-((2-chloroquinolin-3-yl)methylene)thiazolidine-2,4-dione (**34**). The title compound **34** was obtained as a pale yellow solid, according to general procedure using 2-chloroquinoline-3-carbaldehyde (**34a**). Yield 45%. <sup>1</sup>H-NMR (401 MHz, DMSO-*d*<sub>6</sub>): δ 12.87 (br s, 1H); δ 8.55 (s, 1H); δ 8.24 (d, *J* = 8.1, 1H); δ 8.00-7.88 (m, 3H); δ 7.73 (t, *J* = 7.2, 1H). <sup>13</sup>C-NMR (101 MHz, DMSO-*d*<sub>6</sub>): δ 167.91; δ 167.26; δ 149.81; δ 146.90; δ 138.45; δ 132.88; δ 129.42; δ 128.63; δ 128.11; δ 126.92; δ 126.29; δ 125.85. MS (ESI<sup>-</sup>) *m/z*: 290 [M-H]<sup>-</sup>.

*(Z)*-5-((2-chloro-6-methoxyquinolin-3-yl)methylene)thiazolidine-2,4-dione (**35**). The title compound **35** was obtained as a yellow solid, according to general procedure using 2-chloro-6-methoxyquinoline-3-carbaldehyde (**35a**). Yield 32%. <sup>1</sup>H-NMR (401 MHz, DMSO-*d*<sub>6</sub>): δ 12.85 (br s, 1H); δ 8.44 (s, 1H); δ 7.94 (s, 1H); δ 7.89 (d, *J* = 9.2, 1H); δ 7.69 (d, *J* = 2.5, 1H); δ 7.52 (dd, *J* = 9.1, 2.7, 1H); δ 3.92 (s, 3H). <sup>13</sup>C-NMR (101 MHz, DMSO-*d*<sub>6</sub>): δ 167.96; δ 167.33; δ 158.75; δ 147.17; δ 142.93; δ 137.08; δ 129.52; δ 129.19; δ 128.33; δ 126.21; δ 125.88; δ 125.19; δ 107.20; δ 56.26. MS (ESI<sup>-</sup>) *m/z*: 320 [M-H]<sup>-</sup>.

**Synthesis of 2-(*N,N*-Dimethylamino)benzaldehyde (11a).** To a solution of 2-fluorobenzaldehyde (0.800 g, 6.44 mmol) in dry DMF (14 mL), was added a solution of dimethylamine (5.6M) in EtOH (1.73 mL) and K<sub>2</sub>CO<sub>3</sub> (0.896 g). The mixture was warmed at reflux temperature for 14 h. The mixture was poured on to ice to give a yellow oil and then diluted with water and extracted with ethyl acetate. The organic solvent was removed and the residual oil purified through column chromatography using CH<sub>2</sub>Cl<sub>2</sub> (10) to obtain **11a**, 0.548 g (57%), as a yellow oil. <sup>1</sup>H-NMR (401 MHz, CDCl<sub>3</sub>): δ 10.25 (br s, 1H); δ 7.80-7.76 (m, 1H); δ 7.49 (t, *J* = 8.8, 1H); δ 7.09-7.02 (m, 2H); δ 2.95 (s, 6H).

**Synthesis of 3-(*N,N*-Dimethylamino)benzaldehyde (12a).** Dry DMSO (0.94 mL, 13.24 mmol) was added to oxalyl chloride (0.336 mL, 3.97 mmol) in CH<sub>2</sub>Cl<sub>2</sub> (15 mL) at -78 °C. After 15 min a solution of the alcohol (0.500 g, 3.31 mmol) in CH<sub>2</sub>Cl<sub>2</sub> (10 mL) was

added dropwise. After 25 min triethylamine (2.31 mL, 16.55 mmol) was added dropwise, and the mix was allowed to warm to RT for 30 min. Then the reaction was diluted with CH<sub>2</sub>Cl<sub>2</sub> and washed with water. The organic extracts were concentrated in vacuo and purified through column chromatography with CH<sub>2</sub>Cl<sub>2</sub>/MeOH/toluene (8.5:0.5:1) to give **12a** (0.483 g, 98%) as a yellow solid. <sup>1</sup>H-NMR (401 MHz, CDCl<sub>3</sub>): δ 9.94 (br s, 1H); δ 7.37 (t, *J* = 7.6, 1H); δ 7.19-7.17 (m, 2H); δ 6.96 (dd, *J* = 9.62, 5.21, 1H); δ 2.99 (s, 6H).

### 7.1.2 K18 aggregation and inhibition studies

K18 (kindly provided by E. De Cecco, SISSA) aggregations were performed in a black 96-well optical flat bottom plate (Thermoscientific) with a basic reaction mix (BRM) prepared as follow: 21 μM K18, heparin 0.015 mg/mL, 0.1 mM DTT, 10 μM ThT in PBS 1X. Five different experimental conditions were assessed: (1) BRM alone to assess the kinetic of tauK18 self-assembly; BRM supplemented with **27** at the final concentration of (2) 1 μM; (3) 5 μM; and (4) 10 μM; (5) BRM supplemented with 1% DMSO. Each experimental condition was prepared and analyzed in triplicate. The plate was sealed with a sealing film, inserted into a FLUOstar OPTIMA microplate reader (BMG Labtech) and subjected to cycles of shaking (1 minute at 300 rpm - double orbital) and incubation (14 minutes) at 37°C. Fluorescence readings (480 nm) were taken every 15 minutes (30 flashes per well at 450 nm).

### 7.1.3 Full-length 2N4R tau aggregation and inhibition studies

TauFL 2N4R (kindly provided by E. De Cecco, SISSA) aggregation was performed in a black 96-well optical flat bottom plate (Thermoscientific) with a basic reaction mix (BRM) prepared as follow: 20 μM tauFL (2N4R), heparin 0.02 mg/mL, 0.5 mM DTT, 10 μM ThT in PBS 1X. Three different experimental conditions were assessed: (1) BRM alone to assess the kinetic of TauFL 2N4R self-assembly; (2) BRM supplemented with



**27** at the final concentration of 10  $\mu\text{M}$ ; (3) BRM supplemented with 1% DMSO as control for the reaction. The plate was then inserted into a FLUOstar OPTIMA microplate reader (BMG Labtech) and subjected to cycles of shaking (1 minute at 600 rpm - single orbital) and incubation (1 minute) at 42°C. Fluorescence readings (480 nm) were taken every two minutes (100 flashes per well at 450 nm).

## **7.2 Fluorescent bivalent ligands with combined therapeutic and diagnostic activities against Alzheimer's disease**

### **7.2.1 Chemistry**

All the commercial available reagents and solvents were purchased from Sigma-Aldrich, Alpha Aesar, and VWR, and used without further purification. Reactions were followed by analytical thin layer chromatography (TLC), on pre-coated TLC plates (layer 0.20 mm silica gel60 with a fluorescent indicator UV254, from Sigma-Aldrich). Developed plates were air-dried and analyzed under a UV lamp (UV 254/365 nm). CEM Discover SP focused microwave reactor was used for microwave mediated reactions. Nuclear magnetic resonance (NMR) experiments were run on Varian VXR 400 (400 MHz for  $^1\text{H}$ , 100 MHz for  $^{13}\text{C}$ ).  $^1\text{H}$  and  $^{13}\text{C}$  NMR spectra were acquired at 300 K using deuterated dimethyl sulfoxide ( $(\text{CD}_3)_2\text{SO}$ ) and chloroform ( $\text{CDCl}_3$ ) as solvents. Chemical shifts ( $\delta$ ) are reported in parts per million (ppm) relative to tetramethylsilane (TMS) as internal reference, and coupling constants (J) are reported in hertz (Hz). The spin multiplicities are reported as s (singlet), br s (broad singlet), d (doublet), t (triplet), q (quartet), and m (multiplet). Mass spectra were recorded on a VG707EH-F apparatus, and electrospray ionization (ESI) both in positive and negative mode was applied. Compounds were named following IUPAC rules as applied by ChemBioDraw Ultra (version 14.0). All of the final compounds showed  $\geq 95\%$  purity by analytical HPLC.

### **General procedure for the synthesis of compounds 36-47 and 54-59.**

The corresponding dialdehydes (1 mmol) were reacted with the corresponding TZD derivative (3 mmol), using EDDA (0.5 mmol) under microwave irradiation at  $100^\circ\text{C}$  for 45 minutes. The reaction mixture was diluted with water and the solid was collected by filtration. After washing it with water all the final compounds were purified through crystallization or column chromatography.

*(5Z,5'Z)-5,5'-(1,4-phenylenebis(methanylylidene))bis(thiazolidine-2,4-dione)* (**36**). The title compound **36** was obtained as a yellow solid, according to general procedure using dialdehyde **65** and **TZD**. Yield 75%. <sup>1</sup>H-NMR (401 MHz, d<sub>6</sub>-DMSO): δ 7.79 (s, 2H); δ 7.72 (s, 4H). <sup>13</sup>C-NMR (101 MHz, DMSO-*d*<sub>6</sub>): δ 168.53; δ 168.21; δ 134.41; δ 131.07; δ 130.85; δ 130.51. MS (ESI<sup>-</sup>) *m/z*: 331 [M-H]<sup>-</sup>.

*(5Z,5'Z)-5,5'-([1,1'-biphenyl]-4,4'-diylbis(methanylylidene))bis(thiazolidine-2,4-dione)* (**37**). The title compound **37** was obtained as a yellow solid, according to general procedure using dialdehyde **66** and **TZD**. Yield 57%. <sup>1</sup>H-NMR (401 MHz, DMSO-*d*<sub>6</sub>): δ 12.63 (br s, 2H); δ 7.93 (d, *J* = 8.1, 4H); δ 7.84 (s, 2H); δ 7.71 (d, *J* = 8.1, 4H). <sup>13</sup>C-NMR (101 MHz, DMSO-*d*<sub>6</sub>): δ 168.32; δ 168.02; δ 140.70; δ 133.29; δ 131.38; δ 131.19; δ 127.96; δ 124.46. MS (ESI<sup>-</sup>) *m/z*: 407 [M-H]<sup>-</sup>.

*(5Z,5'Z)-5,5'-((methylenebis(4,1-phenylene))bis(methanylylidene))bis(thiazolidine-2,4-dione)* (**38**). The title compound **38** was obtained as a white solid, according to general procedure using dialdehyde **67** and **TZD**. Yield 59%. <sup>1</sup>H-NMR (401 MHz, DMSO-*d*<sub>6</sub>): δ 7.71 (s, 2H); δ 7.53 (d, *J* = 8.1, 4H); δ 7.40 (d, *J* = 8.1, 4H); δ 4.06 (s, 2H). <sup>13</sup>C-NMR (101 MHz, DMSO-*d*<sub>6</sub>): δ 168.86; δ 168.82; δ 143.60; δ 131.69; δ 131.30; δ 130.69; δ 130.10; δ 41.05. MS (ESI<sup>-</sup>) *m/z*: 421 [M-H]<sup>-</sup>.

*(5Z,5'Z)-5,5'-((9H-carbazole-3,6-diyl)bis(methanylylidene))bis(thiazolidine-2,4-dione)* (**39**). The title compound **39** was obtained as a dark yellow solid, according to general procedure using dialdehyde **68** and **TZD**. Yield 57%. <sup>1</sup>H-NMR (401 MHz, DMSO-*d*<sub>6</sub>): δ 12.43 (br s, 2H); δ 12.07 (s, 1H); δ 8.48 (s, 2H); δ 7.97 (s, 2H); δ 7.68 (s, 4H). <sup>13</sup>C-NMR (101 MHz, DMSO-*d*<sub>6</sub>): δ 168.75; δ 168.24; δ 141.75; δ 133.47; δ 128.75; δ 125.09; δ 124.16; δ 123.31; δ 120.46; δ 112.90. MS (ESI<sup>-</sup>) *m/z*: 420 [M-H]<sup>-</sup>.

*(5Z,5'Z)-5,5'-((9,9-dimethyl-9H-fluorene-2,7-diyl)bis(methanylylidene))bis(thiazolidine-2,4-dione)* (**40**). The title compound **40** was obtained as a dark yellow solid, according to general procedure using dialdehyde **69** and **TZD**. Yield 40%. <sup>1</sup>H-NMR (401 MHz, DMSO-*d*<sub>6</sub>): δ 12.57 (br s, 2H); δ 8.06 (d, *J* = 8.0, 2H); δ 7.86 (s, 2H); δ 7.80 (s, 2H); δ 7.63 (dd, *J* = 8.0, 1.2, 2H); δ 1.51 (s, 6H). <sup>13</sup>C-NMR (101 MHz, DMSO-*d*<sub>6</sub>): δ 168.51; δ 168.20; δ 155.28; δ 140.00; δ 133.60; δ 132.05; δ 129.92; δ 125.03; δ 124.10; δ 122.21; δ 55.33; δ 47.16; δ 26.91. MS (ESI<sup>-</sup>) *m/z*: 447 [M-H]<sup>-</sup>.

(5Z,5'Z)-5,5'-([2,2'-bithiophene]-5,5'-diylbis(methanylylidene))bis(thiazolidine-2,4-dione) (**41**). The title compound **41** was obtained as a red solid, according to general procedure using dialdehyde **70** and **TZD**. Yield 25%. <sup>1</sup>H-NMR (401 MHz, DMSO-*d*<sub>6</sub>): δ 12.61 (br s, 2H); δ 8.03 (s, 2H); δ 7.67 (s, 4H). MS (ESI<sup>-</sup>) *m/z*: 419 [M-H]<sup>-</sup>.

diethyl 2,2'-((5Z,5'Z)-(1,4-phenylenebis(methanylylidene))bis(2,4-dioxothiazolidin-3-yl-5-ylidene))diacetate (**42**). The title compound **42** was obtained as a yellow solid, according to general procedure using dialdehyde **65** and **TZD-1**. Yield 69%. <sup>1</sup>H-NMR (401 MHz, DMSO-*d*<sub>6</sub>): δ 8.05 (s, 2H); δ 7.83 (s, 4H); δ 4.52 (s, 4H); δ 4.19 (q, *J* = 7.1, 4H); δ 1.22 (t, *J* = 7.1, 6H). <sup>13</sup>C-NMR (101 MHz, DMSO-*d*<sub>6</sub>): δ 166.75; δ 166.03; δ 165.28; δ 134.88; δ 132.73; δ 130.80; δ 123.15; δ 62.21; δ 42.22; δ 14.05. MS (ESI<sup>+</sup>) *m/z*: 527 [M+Na]<sup>+</sup>.

diethyl 2,2'-((5Z,5'Z)-([1,1'-biphenyl]-4,4'-diylbis(methanylylidene))bis(2,4-dioxothiazolidin-3-yl-5-ylidene))diacetate (**43**). The title compound **43** was obtained as a yellow solid, according to general procedure using dialdehyde **66** and **TZD-1**. Yield 30%. <sup>1</sup>H-NMR (401 MHz, CDCl<sub>3</sub>): δ 7.97 (s, 2H); δ 7.76 (d, *J* = 8.3, 4H); δ 7.63 (d, *J* = 8.3, 4H); δ 4.50 (s, 4H); δ 4.26 (q, *J* = 7.1, 4H); δ 1.31 (t, *J* = 7.1, 6H). <sup>13</sup>C-NMR (101 MHz, CDCl<sub>3</sub>): δ 167.17; δ 166.15; δ 165.48; δ 141.64; δ 133.72; δ 132.83; δ 130.93; δ 127.78; δ 121.43; δ 62.16; δ 42.16; δ 14.06. MS (ESI<sup>+</sup>) *m/z*: 603 [M+Na]<sup>+</sup>.

diethyl 2,2'-((5Z,5'Z)-((methylenebis(4,1-phenylene))bis(methanylylidene))bis(2,4-dioxothiazolidin-3-yl-5-ylidene))diacetate (**44**). The title compound **44** was obtained as a white solid, according to general procedure using dialdehyde **67** and **TZD-1**. Yield 60%. <sup>1</sup>H-NMR (401 MHz, CDCl<sub>3</sub>): δ 7.91 (s, 2H); δ 7.47 (d, *J* = 8.1, 4H); δ 7.31 (d, *J* = 8.1, 4H); δ 4.47 (s, 4H); δ 4.24 (q, *J* = 7.1, 4H); δ 4.08 (s, 2H); δ 1.30 (t, *J* = 7.1, 6H). <sup>13</sup>C-NMR (101 MHz, CDCl<sub>3</sub>): δ 167.34; δ 166.17; δ 165.55; δ 143.15; δ 134.21; δ 131.37; δ 130.65; δ 129.82; δ 120.59; δ 62.12; δ 42.10; δ 41.69; δ 14.04. MS (ESI<sup>+</sup>) *m/z*: 617 [M+Na]<sup>+</sup>.

diethyl 2,2'-((5Z,5'Z)-((9H-carbazole-3,6-diyl)bis(methanylylidene))bis(2,4-dioxothiazolidin-3-yl-5-ylidene))diacetate (**45**). The title compound **45** was obtained as a yellow solid, according to general procedure using dialdehyde **68** and **TZD-1**. Yield 37%. <sup>1</sup>H-NMR (401 MHz, CDCl<sub>3</sub>): δ 9.08 (br s, 1H); δ 7.98 (s, 2H); δ 7.94 (s, 2H); δ 7.62-7.43 (m, 4H); δ 4.52 (s, 4H); δ 4.31 (q, *J* = 7.1, 4H); δ 1.35 (t, *J* = 7.1, 6H). <sup>13</sup>C-NMR (101 MHz, CDCl<sub>3</sub>): δ 167.52; δ 166.78; δ 165.62; δ 141.18; δ 135.37; δ 129.31; δ 125.46; δ

123.54;  $\delta$  123.16;  $\delta$  117.73;  $\delta$  112.00;  $\delta$  62.26;  $\delta$  42.11;  $\delta$  14.09. MS (ESI<sup>+</sup>) m/z: 616 [M+Na]<sup>+</sup>.

*diethyl 2,2'-((5Z,5'Z)-((9,9-dimethyl-9H-fluorene-2,7-diyl)bis(methanylylidene))bis(2,4-dioxothiazolidin-3-yl-5-ylidene))diacetate (46)*. The title compound **46** was obtained as a yellow solid, according to general procedure using dialdehyde **69** and **TZD-1**. Yield 55%. <sup>1</sup>H-NMR (401 MHz, CDCl<sub>3</sub>):  $\delta$  8.03 (s, 2H);  $\delta$  7.86 (d, *J* = 8.0, 2H);  $\delta$  7.60 (s, 2H);  $\delta$  7.55 (d, *J* = 8.0, 2H);  $\delta$  4.50 (s, 4H);  $\delta$  4.26 (q, *J* = 7.1, 4H);  $\delta$  1.56 (s, 6H);  $\delta$  1.31 (t, *J* = 7.1, 6H). <sup>13</sup>C-NMR (101 MHz, CDCl<sub>3</sub>):  $\delta$  167.27;  $\delta$  166.16;  $\delta$  165.52;  $\delta$  155.21;  $\delta$  140.50;  $\delta$  134.64;  $\delta$  133.18;  $\delta$  129.99;  $\delta$  124.57;  $\delta$  121.46;  $\delta$  120.72;  $\delta$  62.13;  $\delta$  47.12;  $\delta$  42.15;  $\delta$  26.89;  $\delta$  14.06. MS (ESI<sup>+</sup>) m/z: 643 [M+Na]<sup>+</sup>.

*diethyl 2,2'-((5Z,5'Z)-([2,2'-bithiophene]-5,5'-diylbis(methanylylidene))bis(2,4-dioxothiazolidin-3-yl-5-ylidene))diacetate (47)*. The title compound **47** was obtained as a red solid, according to general procedure using dialdehyde **70** and **TZD-1**. Yield 24%. <sup>1</sup>H-NMR (401 MHz, DMSO-*d*<sub>6</sub>):  $\delta$  8.28 (s, 2H);  $\delta$  7.78 (dd, *J* = 13.8, 3.7, 4H);  $\delta$  4.50 (s, 4H);  $\delta$  4.18 (q, *J* = 6.9, 4H);  $\delta$  1.23 (t, *J* = 7.0, 6H). MS (ESI<sup>+</sup>) m/z: 615 [M+Na]<sup>+</sup>.

*(5Z,5'Z)-5,5'-(1,4-phenylenebis(methanylylidene))bis(3-(2-(dimethylamino)ethyl)thiazolidine-2,4-dione) (54)*. The title compound **54** was obtained as a pale yellow solid, according to general procedure using dialdehyde **65** and **TZD-3**. Yield 27%. <sup>1</sup>H-NMR (401 MHz, CDCl<sub>3</sub>):  $\delta$  7.87 (s, 2H);  $\delta$  7.59 (s, 4H);  $\delta$  3.88 (t, *J* = 6.5, 4H);  $\delta$  2.58 (t, *J* = 6.5, 4H);  $\delta$  2.28 (s, 12H). <sup>13</sup>C-NMR (101 MHz, CDCl<sub>3</sub>):  $\delta$  167.25;  $\delta$  166.10;  $\delta$  134.90;  $\delta$  131.86;  $\delta$  130.68;  $\delta$  123.57;  $\delta$  56.24;  $\delta$  45.47;  $\delta$  39.92. MS (ESI<sup>+</sup>) m/z: 497 [M+Na]<sup>+</sup>.

*(5Z,5'Z)-5,5'-([1,1'-biphenyl]-4,4'-diylbis(methanylylidene))bis(3-(2-(dimethylamino)ethyl)thiazolidine-2,4-dione) (55)*. The title compound **55** was obtained as a yellow solid, according to general procedure using dialdehyde **66** and **TZD-3**. Yield 21%. <sup>1</sup>H-NMR (401 MHz, CDCl<sub>3</sub>):  $\delta$  7.92 (s, 2H);  $\delta$  7.73 (d, *J* = 8.3, 4H);  $\delta$  7.60 (d, *J* = 8.4, 4H);  $\delta$  3.88 (t, *J* = 6.5, 4H);  $\delta$  2.59 (t, *J* = 6.5, 4H);  $\delta$  2.29 (s, 12H). <sup>13</sup>C-NMR (101 MHz, CDCl<sub>3</sub>):  $\delta$  167.65;  $\delta$  166.29;  $\delta$  141.41;  $\delta$  133.02;  $\delta$  132.76;  $\delta$  130.83;  $\delta$  127.68;  $\delta$  121.98;  $\delta$  56.29;  $\delta$  45.51;  $\delta$  39.85. MS (ESI<sup>+</sup>) m/z: 573 [M+Na]<sup>+</sup>.

*(5Z,5'Z)-5,5'-((methylenebis(4,1-phenylene))bis(methanylylidene))bis(3-(2-(dimethylamino)ethyl)thiazolidine-2,4-dione) (56)*. The title compound **56** was obtained

as a pale yellow solid, according to general procedure using dialdehyde **67** and **TZD-3**. Yield 20%. <sup>1</sup>H-NMR (401 MHz, CDCl<sub>3</sub>): δ 7.86 (s, 2H); δ 7.45 (d, *J* = 8.0, 4H); δ 7.28 (d, *J* = 8.0, 4H); δ 4.06 (s, 2H); δ 3.87 (t, *J* = 6.5, 4H); δ 2.59 (t, *J* = 6.4, 4H); δ 2.29 (s, 12H). <sup>13</sup>C-NMR (101 MHz, CDCl<sub>3</sub>): δ 167.82; δ 166.35; δ 142.89; δ 133.27; δ 131.58; δ 130.55; δ 129.75; δ 121.15; δ 56.24; δ 45.43; δ 41.67; δ 39.68. MS (ESI<sup>+</sup>) *m/z*: 587 [M+Na]<sup>+</sup>.

(5*Z*,5'*Z*)-5,5'-((9*H*-carbazole-3,6-diyl)bis(methanylylidene))bis(3-(2-(dimethylamino)ethyl)thiazolidine-2,4-dione) (**57**). The title compound **57** was obtained as a yellow solid, according to general procedure using dialdehyde **68** and **TZD-3**. Yield 18%. <sup>1</sup>H-NMR (401 MHz, CDCl<sub>3</sub>): δ 10.80 (s, 1H); δ 7.77 (s, 2H); δ 7.68 (s, 2H); δ 7.41 (dd, *J* = 25.1, 8.0, 4H); δ 3.94 (s, 4H); δ 2.78 (s, 4H); δ 2.45 (s, 12H). <sup>13</sup>C-NMR (101 MHz, CDCl<sub>3</sub>): δ 168.03; δ 166.28; δ 141.79; δ 134.43; δ 129.70; δ 124.74; δ 123.41; δ 122.12; δ 116.93; δ 111.83; δ 56.38; δ 45.28; δ 39.23. MS (ESI<sup>+</sup>) *m/z*: 586 [M+Na]<sup>+</sup>.

(5*Z*,5'*Z*)-5,5'-((9,9-dimethyl-9*H*-fluorene-2,7-diyl)bis(methanylylidene))bis(3-(2-(dimethylamino)ethyl)thiazolidine-2,4-dione) (**58**). The title compound **58** was obtained as a dark yellow solid, according to general procedure using dialdehyde **69** and **TZD-3**. Yield 21%. <sup>1</sup>H-NMR (401 MHz, CDCl<sub>3</sub>): δ 7.98 (s, 2H); δ 7.84 (d, *J* = 8, 2H); δ 7.58 (s, 2H); δ 7.54 (d, *J* = 8.2, 2H); δ 3.92 (t, *J* = 6.4, 4H); δ 2.67 (t, *J* = 6.2, 4H); δ 2.35 (s, 12H); δ 1.54 (s, 6H). MS (ESI<sup>+</sup>) *m/z*: 613 [M+Na]<sup>+</sup>.

(5*Z*,5'*Z*)-5,5'-([2,2'-bithiophene]-5,5'-diyl)bis(methanylylidene))bis(3-(2-(dimethylamino)ethyl)thiazolidine-2,4-dione) (**59**). The title compound **59** was obtained as a red solid, according to general procedure using dialdehyde **70** and **TZD-3**. Yield 25%. <sup>1</sup>H-NMR (401 MHz, DMSO-*d*<sub>6</sub>): δ 8.20 (s, 2H); δ 7.73 (d, *J* = 4.3, 2H); δ 7.68 (d, *J* = 4.0, 2H); δ 4.01 (t, *J* = 5.6, 4H); δ 3.40 (t, *J* = 5.6, 4H); δ 2.87 (s, 12H). <sup>13</sup>C-NMR (101 MHz, DMSO-*d*<sub>6</sub>/TFA-*d*<sub>1</sub>): δ 167.14; δ 165.83; δ 142.11; δ 137.68; δ 136.87; δ 127.60; δ 126.13; δ 119.92; δ 54.27; δ 42.67; δ 37.25. MS (ESI<sup>+</sup>) *m/z*: 585 [M+Na]<sup>+</sup>.

### General procedure for the synthesis of compounds 48-53.

The corresponding ester-derivatives (0.1 mmol) were refluxed overnight in acetic acid (4 mL) and concentrated HCl (1 mL). The reaction mixture was filtered and the solid

was washed three times with water, methanol, and dichloromethane (DCM) to give the final compounds.

*2,2'-((5Z,5'Z)-(1,4-phenylenebis(methanylylidene))bis(2,4-dioxothiazolidin-3-yl-5-ylidene))diacetic acid (48)*. The title compound **48** was obtained as a pale yellow solid, according to the general procedure using **42**. Yield 86%. <sup>1</sup>H-NMR (401 MHz, DMSO-*d*<sub>6</sub>): δ 13.48 (br s, 2H); δ 8.04 (s, 2H); δ 7.83 (s, 4H); δ 4.40 (s, 4H). <sup>13</sup>C-NMR (101 MHz, DMSO-*d*<sub>6</sub>): δ 168.30; δ 167.07; δ 165.36; δ 135.04; δ 132.94; δ 131.38; δ 123.01; δ 42.88. MS (ESI<sup>-</sup>) *m/z*: 447 [M-H]<sup>-</sup>.

*2,2'-((5Z,5'Z)-([1,1'-biphenyl]-4,4'-diylbis(methanylylidene))bis(2,4-dioxothiazolidin-3-yl-5-ylidene))diacetic acid (49)*. The title compound **49** was obtained as a yellow solid, according to the general procedure using **43**. Yield 50%. <sup>1</sup>H-NMR (401 MHz, DMSO-*d*<sub>6</sub>): δ 13.42 (br s, 2H); δ 8.06 (s, 2H); δ 7.98 (d, *J* = 8.1, 4H); δ 7.79 (d, *J* = 8.1, 4H); δ 4.40 (s, 4H). <sup>13</sup>C-NMR (101 MHz, DMSO-*d*<sub>6</sub>): δ 168.36; δ 167.21; δ 165.44; δ 141.11; δ 133.65; δ 133.04; δ 131.45; δ 128.12; δ 121.37; δ 42.83. MS (ESI<sup>-</sup>) *m/z*: 523 [M-H]<sup>-</sup>.

*2,2'-((5Z,5'Z)-((methylenebis(4,1-phenylene))bis(methanylylidene))bis(2,4-dioxothiazolidin-3-yl-5-ylidene))diacetic acid (50)*. The title compound **50** was obtained as a white solid, according to the general procedure using **44**. Yield 33%. <sup>1</sup>H-NMR (401 MHz, DMSO-*d*<sub>6</sub>): δ 7.96 (s, 2H); δ 7.60 (d, *J* = 8.2, 4H); δ 7.45 (d, *J* = 8.2, 4H); δ 4.37 (s, 4H); δ 4.09 (s, 2H). <sup>13</sup>C-NMR (101 MHz, DMSO-*d*<sub>6</sub>): δ 168.37; δ 167.33; δ 165.46; δ 144.26; δ 134.11; δ 131.27; δ 131.03; δ 130.26; δ 120.46; δ 42.74; δ 41.10. MS (ESI<sup>-</sup>) *m/z*: 537 [M-H]<sup>-</sup>.

*2,2'-((5Z,5'Z)-((9H-carbazole-3,6-diyl)bis(methanylylidene))bis(2,4-dioxothiazolidin-3-yl-5-ylidene))diacetic acid (51)*. The title compound **51** was obtained as a yellow solid, according to the general procedure using **45**. Yield 50%. <sup>1</sup>H-NMR (401 MHz, DMSO-*d*<sub>6</sub>): δ 13.43 (br s, 2H); δ 12.17 (s, 1H); δ 8.55 (s, 2H); δ 8.16 (s, 2H); δ 7.75 - 7.79 (m, 4H); δ 4.40 (s, 4H). <sup>13</sup>C-NMR (101 MHz, DMSO-*d*<sub>6</sub>): δ 168.49; δ 167.64; δ 165.65; δ 142.08; δ 135.62; δ 129.03; δ 124.86; δ 124.71; δ 123.39; δ 117.30; δ 113.07; δ 42.70. MS (ESI<sup>-</sup>) *m/z*: 536 [M-H]<sup>-</sup>.

*2,2'-((5Z,5'Z)-((9,9-dimethyl-9H-fluorene-2,7-diyl)bis(methanylylidene))bis(2,4-dioxothiazolidin-3-yl-5-ylidene))diacetic acid (52)*. The title compound **52** was obtained

as a yellow solid, according to the general procedure using **46**. Yield 58%. <sup>1</sup>H-NMR (401 MHz, DMSO-*d*<sub>6</sub>): δ 8.11 (d, *J* = 8.0, 2H); δ 8.08 (s, 2H); δ 7.88 (s, 2H); δ 7.69 (d, *J* = 8.2, 2H); δ 4.41 (s, 4H); δ 1.53 (s, 6H). <sup>13</sup>C-NMR (101 MHz, DMSO-*d*<sub>6</sub>): δ 168.39; δ 167.32; δ 165.45; δ 155.44; δ 140.41; δ 134.43; δ 133.35; δ 130.13; δ 125.43; δ 122.45; δ 120.86; δ 47.27; δ 42.80; δ 26.84. MS (ESI<sup>-</sup>) *m/z*: 563 [M-H]<sup>-</sup>.

*2,2'-((5Z,5'Z)-([2,2'-bithiophene]-5,5'-diylbis(methanylylidene))bis(2,4-dioxothiazolidin-3-yl-5-ylidene))diacetic acid (53)*. The title compound **53** was obtained as a red solid, according to the general procedure using **47**. Yield 30%. <sup>1</sup>H-NMR (401 MHz, DMSO-*d*<sub>6</sub>/TFA-*d*<sub>1</sub>): δ 8.16 (s, 2H); δ 7.66 (d, *J* = 4.3, 2H); δ 7.61 (d, *J* = 4.0, 2H); δ 4.34 (s, 4H). MS (ESI<sup>+</sup>) *m/z*: 559 [M+Na]<sup>+</sup>.

**Ethyl 2-(2,4-dioxothiazolidin-3-yl)acetate (TZD-1)**. A mixture of 2,4-thiazolidinedione (2 mmol), ethyl bromoacetate (2 mmol), and anhydrous K<sub>2</sub>CO<sub>3</sub> (3 mmol) in acetone (12 mL), was react under microwave irradiation at 100°C for 50 minutes. After the reaction, K<sub>2</sub>CO<sub>3</sub> was removed by filtration, and the solvent was evaporated under reduced pressure. The crude product was purified by column chromatography eluting with DCM/ethyl acetate (9.6:0.4). Yield 87%. <sup>1</sup>H-NMR (401 MHz, CDCl<sub>3</sub>): δ 4.24 (s, 2H); δ 4.13 (q, *J* = 7.2, 2H); δ 3.97 (s, 2H); δ 1.20 (t, *J* = 7.1, 3H).

**Synthesis of 3-(2-(dimethylamino)ethyl)thiazolidine-2,4-dione (TZD-3)**. A mixture of 2,4-thiazolidinedione (2 mmol), 2-chloro-*N,N*-dimethylethan-1-amine (2 mmol), and Cs<sub>2</sub>CO<sub>3</sub> (2 mmol) in acetone (12 mL), was react under microwave irradiation at 100°C for 50 minutes. After the reaction, Cs<sub>2</sub>CO<sub>3</sub> was removed by filtration, and the solvent was evaporated under reduced pressure. The crude product was purified by column chromatography eluting with DCM/ethanol/NH<sub>4</sub><sup>+</sup>OH<sup>-</sup> (9.5:0.5:0.05). Yield 53%. <sup>1</sup>H-NMR (401 MHz, CDCl<sub>3</sub>): δ 4.87 (s, 2H); δ 3.89 (s, 2H); δ 3.65 (t, *J* = 6.5, 2H); δ 2.42 (t, *J* = 6.5, 2H); δ 2.17 (s, 6H).

**4,4'-methylenedibenzaldehyde (67)**. Diphenylmethane (12 mmol) and paraformaldehyde (42 mmol) were dissolved in 8 mL of glacial acetic acid containing



33% wt HBr. After being refluxed for 12 hours, the reaction flask was immersed in an ice bath. The white greasy solid was separated by decantation, and washed three times with water. Recrystallization from toluene afforded bis(4-(bromomethyl)phenyl)methane (yield 20%).  $^1\text{H-NMR}$  (401 MHz,  $\text{CDCl}_3$ ):  $\delta$  7.32 (d,  $J = 7.9$ , 4H);  $\delta$  7.15 (d,  $J = 8.0$ , 4H);  $\delta$  4.48 (s, 4H);  $\delta$  3.96 (s, 2H). Hexamethylenetetramine (6 mmol) and bis(4-(bromomethyl)phenyl)methane (2 mmol) were dissolved into separate 4 mL chloroform. The two solutions were mixed and refluxed for 6 hours. The white precipitate was filtered and dry in vacuum overnight. Then, it was dissolved in 7 mL 50% acetic acid and refluxed for 6 hours. 1 mL concentrated HCl was added and refluxed for other 2 hours. The reaction solution was extracted with ethyl ether and then washed with 5N NaOH. Concentration of the ether portion and recrystallization from ethanol give **67** as a white solid. Yield 42%.  $^1\text{H-NMR}$  (401 MHz,  $\text{CDCl}_3$ ):  $\delta$  9.99 (s, 2H);  $\delta$  7.83 (d,  $J = 8.0$ , 4H);  $\delta$  7.35 (d,  $J = 7.9$ , 4H);  $\delta$  4.14 (s, 2H).

#### **General procedure for the synthesis of dialdehydes 68-70.**

The corresponding dibromo starting materials (3 mmol) were dissolved in anhydrous THF (20 mL) and the solution was stirred in a dry ice/acetone bath. 8.5 mL of BuLi (2.5 mol/L in hexane) were slowly added. The cooling bath was removed for 1h and then replaced. After 10 min, anhydrous DMF (2.5 mL) was added dropwise. The cooling bath was removed, and the reaction was stirred for 90 min. After this period, 1M HCl (20 mL) was added and the reaction was extracted twice with ethyl acetate. The combined extract was washed with brine, dried over  $\text{Na}_2\text{SO}_4$  and concentrated. The final compounds were purified through column chromatography.

*9H-carbazole-3,6-dicarbaldehyde (68)*. The title compound **68** was obtained as a yellow solid, according to the general procedure using 3,6-dibromo-9H-carbazole. Column chromatography eluted with DCM/ethyl acetate/toluene 6:3:1 Yield 58%.  $^1\text{H-NMR}$  (401 MHz,  $\text{DMSO-}d_6$ ):  $\delta$  12.35 (br s, 1H);  $\delta$  10.09 (s, 2H);  $\delta$  8.88 (d,  $J = 1.2$ , 2H);  $\delta$  8.02 (dd,  $J = 8.5$ , 1.5, 2H);  $\delta$  7.72 (d,  $J = 8.5$ , 2H).  $^{13}\text{C-NMR}$  (101 MHz,  $\text{DMSO-}d_6$ ):  $\delta$  192.40;  $\delta$  144.68;  $\delta$  129.64;  $\delta$  127.61;  $\delta$  125.17;  $\delta$  123.13;  $\delta$  112.64.

*9,9-dimethyl-9H-fluorene-2,7-dicarbaldehyde (69)*. The title compound **69** was obtained as a yellow solid, according to the general procedure using 2,7-dibromo-9,9-dimethyl-9H-fluorene. Column chromatography eluted with DCM. Yield 45%. <sup>1</sup>H-NMR (401 MHz, CDCl<sub>3</sub>): δ 10.06 (s, 2H); δ 7.99 (s, 2H); δ 7.96 - 7.82 (m, 4H); δ 1.53 (s, 6H). <sup>13</sup>C-NMR (101 MHz, CDCl<sub>3</sub>): δ 191.92; δ 155.46; δ 143.70; δ 136.56; δ 130.34; δ 123.32; δ 121.56; δ 47.12; δ 26.66.

*[2,2'-bithiophene]-5,5'-dicarbaldehyde (70)*. The title compound **70** was obtained as a dark yellow solid, according to the general procedure using 5,5'-dibromo-2,2'-bithiophene. Column chromatography eluted with DCM/petroleum ether/toluene/ethyl acetate 5:3:1.5:0.5. Yield 57%. <sup>1</sup>H-NMR (401 MHz, CDCl<sub>3</sub>): δ 9.91 (s, 2H); δ 7.72 (d, *J* = 4.0, 2H); δ 7.42 (d, *J* = 4.0, 2H). <sup>13</sup>C-NMR (101 MHz, CDCl<sub>3</sub>): δ 182.50; δ 144.79; δ 143.84; δ 136.86; δ 126.44.

### 7.2.2 Native fluorescent studies

*General information.* All the spectra were recorded using an UV/VIS spectrophotometer Jasco V530 and a spectrofluorometer, equipped with the control and data acquisition software V-350 and FP-750, respectively. Both excitation and emission slits were set up at 5 nm bandwidth, and 1 cm quartz cells were employed.

*General procedure.* Accurately weighed amounts of the studied compounds were dissolved using ethanol or DMF, to obtain 0.5 mM stock solutions. From these stocks, intermediate dilutions in ethanol were prepared as required.

## **7.3 Development of a focused library of antiprion compounds built around Compound 1**

### **7.3.1 Chemistry**

All the commercial available reagents and solvents were purchased from Sigma-Aldrich, TCI and Acros Organics, and used without further purification. Reactions were followed by analytical thin layer chromatography (TLC), on pre-coated TLC plates (layer 0.20 mm silica gel60 with a fluorescent indicator UV254, from Sigma-Aldrich). Developed plates were air-dried and analyzed under a UV lamp (UV 254/365 nm). CEM Discover SP focused microwave reactor was used for microwave mediated reactions. Nuclear magnetic resonance (NMR) experiments were run on Varian VXR 400 (400 MHz for  $^1\text{H}$ , 100 MHz for  $^{13}\text{C}$ ).  $^1\text{H}$  and  $^{13}\text{C}$  NMR spectra were acquired at 300 K using chloroform ( $\text{CDCl}_3$ ), methanol ( $\text{CD}_3\text{OD}$ ), and dimethyl sulfoxide ( $(\text{CD}_3)_2\text{SO}$ ) as solvents. Chemical shifts ( $\delta$ ) are reported in parts per million (ppm) relative to tetramethylsilane (TMS) as internal reference and coupling constants ( $J$ ) are reported in hertz (Hz). The spin multiplicities are reported as s (singlet), d (doublet), t (triplet), q (quartet), and m (multiplet). Compounds were named following IUPAC rules as applied by ChemBioDraw Ultra (version 14.0). Compounds purity was assessed by LC-MS using a SB-C18 RP column (100 x 2.1 mm I.D., 3.5  $\mu\text{m}$ ) as the stationary phase and a mixture of 0.1% formic acid in water and 0.1% formic acid in acetonitrile (60/40, V/V), in isocratic mode at a flow rate of 100  $\mu\text{L}/\text{min}$ . Acquisition was performed by total ion current (TIC) and ESI+. Compound 1 showed a purity  $\geq 98.1\%$ . All the final compounds **60-64** showed a purity  $>95\%$ .

**Synthesis of 7-chloro-4-hydrazynilquinoline (71).** A suspension of 4,7-dichloroquinoline (500 mg) and hydrazine monohydrate 65% (2 eq) was irradiated in a sealed tube at 150 W for 5 min ( $T = 150^\circ\text{C}$ ,  $P = 200$  psi, Power max = on). After cooling, the resulting solid was diluted with water, washed, and isolated by filtration. The final compound was purified through crystallization from ethanol, affording a pale yellow solid. Yield: 69%.  $^1\text{H}$ -NMR (401 MHz,  $\text{CD}_3\text{OD}$ ):  $\delta$  8.41 (d,  $J = 5.6$  Hz, 1H);  $\delta$  8.00 (d,  $J = 9.0$  Hz, 1H);  $\delta$  7.80 (d,  $J = 1.8$  Hz, 1H);  $\delta$  7.40 (dd,  $J = 9.0, 2.0$  Hz, 1H);  $\delta$  6.99 (d,  $J = 5.6$  Hz,

1H). <sup>13</sup>C-NMR (101 MHz, CD<sub>3</sub>OD): δ 158.55; δ 143.28; δ 140.69; δ 140.05; δ 128.23; δ 125.54; δ 120.16; δ 114.92; δ 99.67.

**Synthesis of (Z)-2-(1-(2-(7-chloroquinolin-4-yl)hydrazono)ethyl)-10H-phenothiazine (Compound 1).** To a solution of **71** (2.60 mmol) in ethanol (20 mL), 2-acetylphenothiazine (7.80 mmol) and acetic acid (2.5 mL) were added in sequence at room temperature. The solution was refluxed for 24h, and then evaporated under vacuum. The crude product was purified by column chromatography on silica gel (DCM/MeOH/NH<sub>3</sub> 9.2:0.8:0.08), affording Compound 1 as a dark yellow solid. Yield: 81%. <sup>1</sup>H-NMR (401 MHz, DMSO-*d*<sub>6</sub>): δ 8.69 (s, 1H); δ 8.40 (d, *J* = 8.7 Hz, 1H); δ 7.61 (s, 1H); δ 7.36 (t, *J* = 11.5 Hz, 2H); δ 7.24 (dd, *J* = 8.1, 1.8 Hz, 1H); δ 7.08 - 6.81 (m, 4H); δ 6.79 - 6.55 (m, 2H); δ 2.40 (s, 3H).

#### General procedure for the synthesis of compounds 60-64.

To a solution of **71** (0.3 mmol) in ethanol (3 mL), the corresponding phenothiazine derivatives **72-76** (0.3 mmol) and acetic acid (50 μL) were added in sequence at room temperature. The solution was refluxed for 24h, and then evaporated under vacuum. All the final compounds were purified through column chromatography on silica gel (ethyl acetate/ethanol/toluene/NH<sub>3</sub> 6.8:0.2:3:0.02).

*(E)*-2-(2-(1-(2-(7-chloroquinolin-4-yl)hydrazono)ethyl)-10H-phenothiazin-10-yl)-*N,N*-dimethylethan-1-amine (**60**). The title compound **60** was obtained as a yellow solid, according to the general procedure using **72**. Yield 50%. <sup>1</sup>H-NMR (401 MHz, CDCl<sub>3</sub>): δ 8.62 (s, 1H); δ 8.01 (s, 1H); δ 7.87 (d, *J* = 8.9, 1H); δ 7.55 (s, 1H); δ 7.48 (d, *J* = 5.4, 1H); δ 7.44 (dd, *J* = 8.9, 2.0, 1H); δ 7.35 (d, *J* = 7.9, 1H); δ 7.21-7.15 (m, 3H); δ 6.98-6.95 (m, 2H); δ 4.28 (s, 2H); δ 3.00 (s, 2H); δ 2.53 (s, 6H); δ 2.44 (s, 3H).

*(E)*-3-(2-(1-(2-(7-chloroquinolin-4-yl)hydrazono)ethyl)-10H-phenothiazin-10-yl)-*N,N*-dimethylpropan-1-amine (**61**). The title compound **61** was obtained as a yellow solid, according to the general procedure using **73**. Yield 35%. <sup>1</sup>H-NMR (401 MHz, CDCl<sub>3</sub>): δ 8.63 (s, 1H); δ 7.99 (s, 1H); δ 7.77 (d, *J* = 8.8, 1H); δ 7.43 (d, *J* = 7.1, 3H); δ 7.29 (d, *J* = 7.9, 1H); δ 7.24 (s, 1H); δ 7.15 (dd, *J* = 15.8, 8.0, 3H); δ 6.92 (d, *J* = 7.0, 2H); δ 4.03 (t, *J* =

6.3, 2H);  $\delta$  2.66-2.48 (m, 2H);  $\delta$  2.39 (s, 3H);  $\delta$  2.28 (s, 6H);  $\delta$  2.15-1.99 (m, 2H).  $^{13}\text{C}$ -NMR (101 MHz,  $\text{CDCl}_3$ ):  $\delta$  206.87;  $\delta$  145.20;  $\delta$  144.72;  $\delta$  137.49;  $\delta$  135.13;  $\delta$  127.48;  $\delta$  127.15;  $\delta$  125.89;  $\delta$  124.75;  $\delta$  122.74;  $\delta$  120.48;  $\delta$  115.79;  $\delta$  112.75;  $\delta$  102.53;  $\delta$  56.91;  $\delta$  53.38;  $\delta$  45.38;  $\delta$  45.02;  $\delta$  30.88;  $\delta$  29.66;  $\delta$  29.32;  $\delta$  24.42;  $\delta$  22.65;  $\delta$  14.08;  $\delta$  12.61.

*(E)*-2-(1-(2-(7-chloroquinolin-4-yl)hydrazono)ethyl)-10-(2-(piperidin-1-yl)ethyl)-10H-phenothiazine (**62**) The title compound **62** was obtained as a yellow solid, according to the general procedure using **74**. Yield 22%.  $^1\text{H}$ -NMR (401 MHz,  $\text{CDCl}_3$ ):  $\delta$  8.65 (s, 1H);  $\delta$  8.02 (s, 1H);  $\delta$  7.78 (d,  $J = 8.6$ , 1H);  $\delta$  7.53 (s, 1H);  $\delta$  7.45 (dd,  $J = 13.6$ , 6.8, 2H);  $\delta$  7.35 (d,  $J = 8.1$ , 1H);  $\delta$  7.22-7.05 (m, 3H);  $\delta$  6.95 (dd,  $J = 15.8$ , 7.8, 3H);  $\delta$  4.23 (s, 2H);  $\delta$  2.91 (s, 2H);  $\delta$  2.65 (s, 4H);  $\delta$  2.42 (s, 3H);  $\delta$  1.77 (d,  $J = 59.7$ , 4H);  $\delta$  1.48 (s, 2H).  $^{13}\text{C}$ -NMR (101 MHz,  $\text{CDCl}_3$ ):  $\delta$  144.82;  $\delta$  144.48;  $\delta$  137.57;  $\delta$  135.12;  $\delta$  127.61;  $\delta$  127.45;  $\delta$  127.14;  $\delta$  125.90;  $\delta$  122.83;  $\delta$  120.54;  $\delta$  115.51;  $\delta$  112.68;  $\delta$  102.58;  $\delta$  55.69;  $\delta$  54.85;  $\delta$  29.67;  $\delta$  25.30;  $\delta$  23.74;  $\delta$  12.64.

*(E)*-4-(2-(2-(1-(2-(7-chloroquinolin-4-yl)hydrazono)ethyl)-10H-phenothiazin-10-yl)ethyl)morpholine (**63**) The title compound **63** was obtained as a dark yellow solid, according to the general procedure using **75**. Yield 91%.  $^1\text{H}$ -NMR (401 MHz,  $\text{CDCl}_3$ ):  $\delta$  8.53 (d,  $J = 5.0$ , 1H);  $\delta$  8.01 (d,  $J = 2.0$ , 1H);  $\delta$  7.94 (d,  $J = 8.9$ , 1H);  $\delta$  7.51 (d,  $J = 1.6$ , 1H);  $\delta$  7.48-7.40 (m, 2H);  $\delta$  7.37 (dd,  $J = 8.0$ , 1.7, 1H);  $\delta$  7.22-7.14 (m, 3H);  $\delta$  6.98-6.94 (m, 2H);  $\delta$  4.15 (t,  $J = 6.7$  Hz, 2H);  $\delta$  3.75-3.73 (m, 4H);  $\delta$  2.87 (t, 2H);  $\delta$  2.67-2.56 (m, 4H);  $\delta$  2.50 (s, 3H).  $^{13}\text{C}$ -NMR (101 MHz,  $\text{CDCl}_3$ ):  $\delta$  150.54;  $\delta$  148.22;  $\delta$  147.68;  $\delta$  146.90;  $\delta$  144.93;  $\delta$  144.55;  $\delta$  137.38;  $\delta$  135.32;  $\delta$  127.90;  $\delta$  127.50;  $\delta$  127.39;  $\delta$  127.05;  $\delta$  126.46;  $\delta$  125.87;  $\delta$  124.08;  $\delta$  122.72;  $\delta$  120.92;  $\delta$  120.45;  $\delta$  115.92;  $\delta$  115.46;  $\delta$  112.56;  $\delta$  102.35;  $\delta$  66.89;  $\delta$  55.93;  $\delta$  54.02;  $\delta$  45.98;  $\delta$  12.69.

*(E)*-2-(1-(2-(7-chloroquinolin-4-yl)hydrazono)ethyl)-10-(2-(4-methylpiperazin-1-yl)ethyl)-10H-phenothiazine (**64**) The title compound **64** was obtained as a dark yellow solid, according to the general procedure using **76**. Yield 37%.  $^1\text{H}$ -NMR (401 MHz,  $\text{CDCl}_3$ ):  $\delta$  8.59 (s, 1H);  $\delta$  7.98 (s, 1H);  $\delta$  7.83 (d,  $J = 8.5$ , 1H);  $\delta$  7.49 (s, 1H);  $\delta$  7.42-7.32 (m, 2H);  $\delta$  7.30 (d,  $J = 8$ , 1H);  $\delta$  7.18-7.11 (m, 3H);  $\delta$  6.94-6.92 (m, 2H);  $\delta$  4.12 (t,  $J = 6.8$ , 2H);  $\delta$  2.87 (t,  $J = 6.8$ , 2H);  $\delta$  2.71-2.60 (m, 8H);  $\delta$  2.38 (s, 3H);  $\delta$  2.35 (s, 3H).  $^{13}\text{C}$ -NMR (101 MHz,  $\text{CDCl}_3$ ):  $\delta$  142.38;  $\delta$  142.05;  $\delta$  134.88;  $\delta$  132.81;  $\delta$  125.03;  $\delta$  124.96;  $\delta$  124.87;  $\delta$  124.55;  $\delta$  124.13;  $\delta$  124.10;  $\delta$  123.38;  $\delta$  121.69;  $\delta$  120.21;  $\delta$  118.40;  $\delta$  117.97;  $\delta$  113.15;

$\delta$  112.98;  $\delta$  110.10;  $\delta$  108.23;  $\delta$  99.82;  $\delta$  97.86;  $\delta$  63.24;  $\delta$  52.55;  $\delta$  52.13;  $\delta$  50.15;  $\delta$  43.47;  $\delta$  42.83;  $\delta$  10.25.

### General procedure for the synthesis of phenothiazine derivatives **72-76**.

To a solution of 2-acetylphenothiazine (1 mmol) in anhydrous DMF (12 mL) was added NaH (4.5 eq) in portions, and the mixture was stirred for 30 min at room temperature. Then, the corresponding chloro-derivatives **77-81** were added, and the mixture was stirred for 5 hours at 50°C. The solution was then concentrated under vacuum and the residue was purified through column chromatography (7.3:0.2:2.5:0.02 DCM/ethanol/toluene/NH<sub>3</sub>).

*1-(10-(2-(dimethylamino)ethyl)-10H-phenothiazin-2-yl)ethan-1-one* (**72**). The title compound **72** was obtained as a yellowish oil, according to the general procedure using **77**. Yield 14%. <sup>1</sup>H-NMR (401 MHz, CDCl<sub>3</sub>):  $\delta$  7.52 (s, 1H);  $\delta$  7.44 (d, *J* = 7.9, 1H);  $\delta$  7.13 (dd, *J* = 15.5, 7.8, 2H);  $\delta$  7.06 (d, *J* = 7.8, 1H);  $\delta$  6.94-6.85 (m, 2H);  $\delta$  4.00 (t, *J* = 6.7, 2H);  $\delta$  2.70 (t, *J* = 6.6, 2H);  $\delta$  2.54 (s, 3H);  $\delta$  2.31 (s, 6H). <sup>13</sup>C-NMR (101 MHz, CDCl<sub>3</sub>):  $\delta$  197.26;  $\delta$  145.06;  $\delta$  144.19;  $\delta$  136.31;  $\delta$  131.45;  $\delta$  127.74;  $\delta$  127.33;  $\delta$  126.91;  $\delta$  123.13;  $\delta$  122.91;  $\delta$  122.83;  $\delta$  115.45;  $\delta$  114.04;  $\delta$  56.43;  $\delta$  46.61;  $\delta$  45.79;  $\delta$  26.50.

*1-(10-(3-(dimethylamino)propyl)-10H-phenothiazin-2-yl)ethan-1-one* (**73**). The title compound **73** was obtained as a yellow oil, according to the general procedure using **78**. Yield 22%. <sup>1</sup>H-NMR (401 MHz, CDCl<sub>3</sub>):  $\delta$  7.43 (d, *J* = 7.8, 2H);  $\delta$  7.20-7.00 (m, 3H);  $\delta$  6.89 (dd, *J* = 10.7, 8.1, 2H);  $\delta$  3.94 (t, *J* = 6.8, 2H);  $\delta$  2.54 (d, *J* = 9.9, 3H);  $\delta$  2.42 (t, *J* = 7.0, 2H);  $\delta$  2.20 (s, 6H);  $\delta$  1.94 (dt, *J* = 13.6, 6.9, 2H). <sup>13</sup>C-NMR (101 MHz, CDCl<sub>3</sub>):  $\delta$  197.58;  $\delta$  145.47;  $\delta$  144.50;  $\delta$  136.32;  $\delta$  132.24;  $\delta$  127.75;  $\delta$  127.53;  $\delta$  127.09;  $\delta$  123.84;  $\delta$  123.14;  $\delta$  122.83;  $\delta$  115.96;  $\delta$  114.05;  $\delta$  56.93;  $\delta$  45.40;  $\delta$  26.61;  $\delta$  24.82;  $\delta$  22.65.

*1-(10-(2-(piperidin-1-yl)ethyl)-10H-phenothiazin-2-yl)ethan-1-one* (**74**). The title compound **74** was obtained as a yellowish oil, according to the general procedure using **79**. Yield 52%. <sup>1</sup>H-NMR (401 MHz, CDCl<sub>3</sub>):  $\delta$  7.53 (s, 1H);  $\delta$  7.46 (dd, *J* = 7.9, 1.6, 1H);  $\delta$  7.15 (d, *J* = 7.9, 2H);  $\delta$  7.08 (dd, *J* = 7.6, 1.4, 1H);  $\delta$  6.95-6.90 (m, 2H);  $\delta$  4.09-4.06 (m, 2H);  $\delta$  2.75 (t, *J* = 6.5, 2H);  $\delta$  2.56 (s, 3H);  $\delta$  2.52 (s, 4H);  $\delta$  1.65-1.62 (m, 4H);  $\delta$  1.48-1.45 (m, 2H). <sup>13</sup>C-NMR (101 MHz, CDCl<sub>3</sub>):  $\delta$  197.66;  $\delta$  145.48;  $\delta$  144.59;  $\delta$  136.71;  $\delta$

131.84;  $\delta$  128.08;  $\delta$  127.67;  $\delta$  127.26;  $\delta$  123.53;  $\delta$  123.24;  $\delta$  123.18;  $\delta$  115.95;  $\delta$  114.54;  $\delta$  56.47;  $\delta$  55.31;  $\delta$  46.51;  $\delta$  26.93;  $\delta$  26.18;  $\delta$  24.43.

*1-(10-(2-morpholinoethyl)-10H-phenothiazin-2-yl)ethan-1-one (75)*. The title compound **75** was obtained as a light brown oil, according to the general procedure using **80**. Yield 28%.  $^1\text{H-NMR}$  (401 MHz,  $\text{CDCl}_3$ ):  $\delta$  7.52 (s, 1H);  $\delta$  7.47 (d,  $J = 7.9$ , 1H);  $\delta$  7.18 (t,  $J = 6.8$ , 2H);  $\delta$  7.11 (d,  $J = 7.9$ , 1H);  $\delta$  6.94 (t,  $J = 7.3$ , 2H);  $\delta$  4.10 (s, 2H);  $\delta$  3.75 (s, 4H);  $\delta$  2.81 (s, 2H);  $\delta$  2.59 (s, 4H);  $\delta$  2.57 (s, 3H).  $^{13}\text{C-NMR}$  (101 MHz,  $\text{CDCl}_3$ ):  $\delta$  144.87;  $\delta$  144.54;  $\delta$  137.53;  $\delta$  135.10;  $\delta$  127.57;  $\delta$  127.41;  $\delta$  127.11;  $\delta$  125.91;  $\delta$  122.77;  $\delta$  120.49;  $\delta$  115.49;  $\delta$  112.66;  $\delta$  102.61;  $\delta$  54.92;  $\delta$  50.81;  $\delta$  29.66;  $\delta$  23.78;  $\delta$  12.57.

*1-(10-(2-(4-methylpiperazin-1-yl)ethyl)-10H-phenothiazin-2-yl)ethan-1-one (76)*. The title compound **76** was obtained as a pale yellow oil, according to the general procedure using **81**. Yield 23%.  $^1\text{H-NMR}$  (401 MHz,  $\text{CDCl}_3$ ):  $\delta$  7.53 (d,  $J = 1.6$ , 1H);  $\delta$  7.46 (dd,  $J = 7.9$ , 1.7, 1H);  $\delta$  7.18-7.14 (m, 2H);  $\delta$  7.08 (dd,  $J = 7.5$ , 1.5, 1H);  $\delta$  6.94-6.89 (m, 2H);  $\delta$  4.04 (t,  $J = 6.8$ , 2H);  $\delta$  2.79 (m,  $J = 6.8$ , 2H);  $\delta$  2.63 (br s, 4H);  $\delta$  2.56 (s, 6H);  $\delta$  2.34 (s, 4H).  $^{13}\text{C-NMR}$  (101 MHz,  $\text{CDCl}_3$ ):  $\delta$  197.28;  $\delta$  145.15;  $\delta$  144.19;  $\delta$  136.32;  $\delta$  131.70;  $\delta$  127.71;  $\delta$  127.37;  $\delta$  126.93;  $\delta$  123.34;  $\delta$  123.05;  $\delta$  122.89;  $\delta$  115.58;  $\delta$  114.10;  $\delta$  55.30;  $\delta$  54.89;  $\delta$  53.07;  $\delta$  46.22;  $\delta$  45.73;  $\delta$  26.59.

**Synthesis of 4-(2-chloroethyl)morpholine (80)**. Morpholine (17 mmol) was added to a solution of  $\text{K}_2\text{CO}_3$  (20 mmol) in acetonitrile (70 mL). Then, 1-bromo-2-chloroethane (34 mmol) was added dropwise. The resulting mixture was stirred at room temperature overnight. The suspension was then filtered, and the filtrate was evaporated. The crude product was purified through column chromatography of silica gel (DCM/ethanol/ $\text{NH}_3$  9.8:0.2:0.02), affording the target compound **80** as a colorless oil. Yield 20%.  $^1\text{H-NMR}$  (401 MHz,  $\text{CDCl}_3$ ):  $\delta$  3.59 (s, 4H);  $\delta$  3.47 (t,  $J = 6.8$ , 2H);  $\delta$  2.60 (t,  $J = 6.8$ , 2H);  $\delta$  2.39 (s, 4H).  $^{13}\text{C-NMR}$  (101 MHz,  $\text{CDCl}_3$ ):  $\delta$  66.68;  $\delta$  60.04;  $\delta$  53.50;  $\delta$  40.56.

**Synthesis of 1-(2-chloroethyl)-4-methylpiperazine (81)**. To a stirred solution of 1-methylpiperazine (10 mmol) and 2-bromoethanol (20 mmol) in acetonitrile (10 mL),  $\text{K}_2\text{CO}_3$  (30 mmol) was added and the reaction was stirred at 75°C for 16 h. Upon

completion, the reaction mixture was filtered and the filtrate was concentrated under reduced pressure. The crude product was then dissolved in dry dichloromethane (10 mL), and  $\text{SOCl}_2$  (5 mL) was added and stirred at  $80^\circ\text{C}$  for 16 h. The reaction mixture was filtrated and the solid residue was triturated with diethyl ether and methanol, filtered and dried to afford the target compound **81** as a colorless oil. Yield 43%.  $^1\text{H-NMR}$  (401 MHz,  $\text{CD}_3\text{OD}$ ):  $\delta$  4.00 (t,  $J = 6.1$ , 2H);  $\delta$  3.73 (br s, 8H);  $\delta$  3.66 (t,  $J = 6.1$ , 2H);  $\delta$  3.30-3.28 (m, 3H).  $^{13}\text{C-NMR}$  (101 MHz,  $\text{CD}_3\text{OD}$ ):  $\delta$  57.12;  $\delta$  49.82;  $\delta$  48.63;  $\delta$  41.94;  $\delta$  36.57.





## **Appendix 1**

### **Supplementary Experimental Part**

#### **1. Chapter III**

##### **1.1 Kinases assays**

###### *1.1.1 Inhibition of GSK-3 $\beta$ : Kinase-Glo luminescent assay*

Human recombinant GSK-3 $\beta$  was purchased from Millipore (Millipore Iberica S.A.U.). The prephosphorylated polypeptide substrate was purchased from Millipore (Millipore Iberica SAU). Kinase-Glo Luminescent Kinase Assay was obtained from Promega (Promega Biotech Iberica, SL). ATP and all other reagents were from Sigma-Aldrich (St. Louis, MO). Assay buffer contained 50 mM HEPES (pH 7.5), 1 mM EDTA, 1 mM EGTA, and mM magnesium acetate. The method of Baki et al.<sup>40</sup> was followed to analyze the inhibition of GSK-3 $\beta$ . Kinase-Glo assays were performed in assay buffer using white 96-well plates. In a typical assay, 10  $\mu$ L (10  $\mu$ M) of the tested compound (dissolved in DMSO at mM concentration and diluted in advance in assay buffer to the desired concentration) and 10  $\mu$ L (20 ng) of enzyme were added to each well followed by 20  $\mu$ L of assay buffer containing 25  $\mu$ M substrate (GS-2 peptide) and 1  $\mu$ M ATP. The final DMSO concentration in the reaction mixture did not exceed 1%. After a 30 min incubation at 30 °C, the enzymatic reaction was stopped with 40  $\mu$ L of Kinase-Glo reagent. Glow-type luminescence was recorded after 10 min using a Fluoroskan Ascent multimode reader. The activity is proportional to the difference of the total and consumed ATP. The inhibitory activities were calculated on the basis of maximal kinase and luciferase activities measured in the absence of inhibitor and in the presence of a reference compound inhibitor (TDZD8, Sigma Aldrich, IC<sub>50</sub> = 0.69  $\mu$ M) at total inhibition concentration, respectively. The linear regression parameters were determined and the IC<sub>50</sub> extrapolated (GraphPad Prism 4.0, GraphPad Software Inc.).

### 1.1.2 Mechanism of action on GSK3 $\beta$ . Kinetic studies

To investigate the inhibitory mechanism of **25** and **27** on GSK-3 $\beta$ , kinetic experiments were performed. Lineweaver-Burk plots of enzyme kinetics varying both ATP (from 1 to 50 mM) and inhibitor concentrations were performed. The intercept of the plot in the vertical axis (1/V) does not change when the inhibitors concentration increases. These results would suggest that inhibitors act as competitive inhibitors of ATP binding.

### 1.1.3 Inhibition of GSK-3 $\beta$ : TR-FRET assay

The assays were performed in white Optiplate-384 at room temperature (22 °C) in a final volume of 25  $\mu$ L, using the following Kinase Buffer: 50 mM HEPES pH 7.5, 1 mM EGTA, 10 mM MgCl<sub>2</sub>, 2 mM DTT and 0.01% Tween-20. The compounds were dissolved in DMSO and then diluted in Kinase Buffer, keeping constant the concentration of DMSO (3%) in each well. In each assay, the compound SB216763 was used as positive control (IC<sub>50</sub> 11.4 $\pm$ 2.1 nM), while DMSO was used as reference. GSK-3 $\beta$  (0.5 nM, final concentration) was first incubated with the two compounds for 30 minutes, then a mixture of ATP (10  $\mu$ M, final concentration) and ULight-GS (Ser641/pSer657) Peptide (50 nM, final concentration) was added. The reaction was incubated for 1 h, afterwards the kinase reaction was stopped by adding 24 mM EDTA and 2 nM (final concentration) of Eu-anti-phospho-GS (Ser641) antibody, both diluted in Detection Buffer 1X. After an incubation of 1 h, the TR-FRET signal was read with the EnSight Multimode Plate Reader (excitation at 320 nm and emissions at 615 and 665 nm). The compounds were tested in 10-dose IC<sub>50</sub> mode with two-fold serial dilutions. Data were analysed using Excel and GraphPad Prism software (version 6.0, GraphPad) for IC<sub>50</sub> curve fits using sigmoidal dose-response (variable slope) equation. Values obtained for each compound are the means  $\pm$  SD determined for at least two separate experiments. Compounds **25** and **27** are soluble in the assay conditions as determined at the maximum concentration tested (nephelometry determination) and do not interfere with the readout of the assay (no absorption at 320 nm and no emission at 615 and 665 nm).

#### *1.1.4 Jump Dilution assay*

The overall procedure and the reagents were the same as the one used for TR-FRET GSK-3 $\beta$  Kinase Assay. Before proceeding with the enzymatic reaction, 5  $\mu$ L of a 100 $\times$  solution containing GSK-3 $\beta$  (50 nM) was pre-incubated with 2.5  $\mu$ L of a 10 $\times$  the biochemical IC<sub>50</sub> of **27** (55  $\mu$ M) for 30 minutes, and then this solution was diluted 100-fold into the buffer containing substrate and cofactor, starting the reaction of phosphorylation. This dilution creates a 1 $\times$  solution of the protein while it dilutes the compound from 10 $\times$  to 0.1 $\times$  the IC<sub>50</sub> value. The residual enzymatic activity was determined and values are reported as percentage values (mean values  $\pm$  SD of two separate experiments) compared to the reaction performed with the vehicle.

#### *1.1.5 Inhibition of casein kinase 1 (CK1) $\delta$ and $\epsilon$*

Human recombinant CK1 $\delta$  and CK1 $\epsilon$  were purchased from Millipore (Millipore Iberica S.A.U.). Casein solution from bovine milk, 5%, was purchased from Sigma-Aldrich (St. Louis, MO). ATP and all other reagents were from Sigma-Aldrich (St. Louis, MO). Assay buffer contained 50 mM HEPES, pH 7.5, 0.01% Brij-35, 10 mM Cl<sub>2</sub>Mg, 1 mM EGTA, and 0.01% NaN<sub>3</sub>. Kinase-Glo Kit from Promega was used to test compounds **25** and **27** for activity against CK-1. The Kinase-Glo assays were performed in the above mentioning assay buffer using black 96-well plates. Typically, 10  $\mu$ L of test compound (dissolved in DMSO at 1 mM concentration and diluted in advance in assay buffer to 10  $\mu$ M) and 10  $\mu$ L (16 ng) of enzyme were added to each well followed by 20  $\mu$ L of assay buffer containing 0.1% casein as substrate and 4  $\mu$ M ATP. The final DMSO concentration in the reaction mixture did not exceed 1%. After 60 min incubation at 30  $^{\circ}$ C the enzymatic reaction was stopped with 40  $\mu$ L of Kinase-Glo reagent. Glow-type luminescence was recorded after 10 min using a FLUOstar Optima (BMG Labtechnologies GmbH, Offenburg, Germany) multimode reader. The activity is proportional to the difference of the total and consumed ATP. The inhibitory activities were calculated on the basis of maximal activities measured in the absence of inhibitor. The IC<sub>50</sub> was defined as the concentration of each compound that reduces to 50% the enzymatic activity with respect to that without inhibitors. Each value is the mean of two independent experiments.

### *1.1.6 Inhibition of cell division cycle 7 (Cdc7)*

The ADP-Glo™ Kinase Assay + CDC7 / DBF4 Kinase Enzyme System (catalogue no. V5089) from Promega was used to screen compounds for activity against Cdc7. ATP and other reagents were purchased from Sigma-Aldrich (St. Louis, MO). The assays were performed in a buffer solution using 96-well plates. Compounds **25** and **27** (5  $\mu$ L, 40  $\mu$ M dissolved in 4% DMSO) were added to each well followed by the enzyme (5  $\mu$ L, 25 ng / well), ATP (5  $\mu$ L, final concentration in the well 10  $\mu$ M) and PDKtidE (5  $\mu$ L, 4  $\mu$ g / well) as substrate. Then it was allowed to incubate for 60 min at room temperature and ADP-Glo™ reagent (20  $\mu$ L) was added and incubate again for 40 min at room temperature. After the incubation, the kinase detection agent (40  $\mu$ L) was added and allowed to incubate for 30 min at room temperature. Finally, the luminescence was recorded using a FLUOstar Optima (BMG Labtechnologies GmbH, Offenburg, Germany) multimode reader. The inhibition activities were calculated based on the maximum activity, measured in the absence of inhibitor.

## **1.2 Docking studies**

(a) Ligands preparation. Ligand molecules were sketched in 2D using Maestro and prepared in 3D using LigPrep module. Ligands were ionized at pH=7.6 $\pm$ 0.2 using Epik and OPLS3 force field. After this step, ligands were exported into Autodock v4.2, Gasteiger charges were added and Autodock specific atom types were assigned. (b) Target preparation. Target structure was extracted from the Protein Data Bank [www.rcsb.org](http://www.rcsb.org) (PDB ID 1Q3W).<sup>417</sup> The structure corresponds to GSK-3 $\beta$  complexed with alsterpaullone, which is an ATP competitive inhibitor. For the target structure preparation, the Protein Preparation Wizard tool, implemented on Maestro was used. All ions and ligands were removed, hydrogen atoms were added, missing residues (121-124, 288-291) were modelled using Prime, residues were ionized at pH=7.6 using PROPKA and a restrained minimization of the heavy atoms was carried out using OPLS3 force field and RMSD converge criteria of 0.3 $\text{\AA}$ . The prepared structure was exported into Autodock v4.2 and prepared adding Gasteiger charges and specific autodock atom types. (c) Docking protocol. Using Autodock v4.2, a grid of 50x50x70 (x,y,z) points with a spacing of 0.375 $\text{\AA}$  was calculated, taking as center the centroid of the crystallized

ligand, alsterpauillone. In this case, the center corresponds to 38.457, 6.618, 35.326 coordinates (x,y,z). Docking parameters were set in order to search for 200 total ligand-target poses, individuals in population was set as 150, 250000 as the maximum number of energy evaluations. The docking analysis was performed clustering the poses into RMS clusters of 2.0Å and the best docking solutions were selected by visual inspection, searching for specific ligand-target interactions with Asp133 and Val135.

### **1.3 Blood Brain Barrier permeation**

Prediction of the brain penetration was evaluated using a PAMPA-BBB.<sup>418</sup> Ten commercial drugs, phosphate buffer saline solution at pH 7.4 (PBS), ethanol and dodecane were purchased from Sigma Aldrich, Acros organics, Merck, and Fluka. The porcine polar brain lipid (PBL) (catalog no. 141101) was from Avanti Polar Lipids. The donor plate was a 96-well filtrate plate (Multiscreen® IP Sterile Plate PDVF membrane, pore size is 0.45 µM, catalog no. MAIPS4510) and the acceptor plate was an indented 96-well plate (Multiscreen®, catalog no. MAMCS9610) both from Millipore. Filter PDVF membrane units (diameter 30 mm, pore size 0.45 µm) from Symta were used to filter the samples. A 96-well plate UV reader (Thermoscientific, Multiskan spectrum) was used for the UV measurements. Test compounds [(3-5 mg of Caffeine, Enoxacin, Hydrocortisone, Desipramine, Ofloxacin, Piroxicam, Testosterone), (12 mg of Promazine) and 25 mg of Verapamil and Atenolol] were dissolved in EtOH (1000 µL). 100 µL of this compound stock solution were taken; 1400 µL of EtOH and 3500 µL of PBS pH = 7.4 buffer were then added to reach 30% of EtOH concentration in the experiment. These solutions were filtered. The acceptor 96-well microplate was filled with 180 µL of PBS/EtOH (70/30). The donor 96-well plate was coated with 4 µL of porcine brain lipid in dodecane (20 mg/mL) and after 5 minutes, 180 µL of each compound solution was added. 1-2 mg of each compound were dissolved in 1500 µL of EtOH and 3500 µL of PBS pH =7.4 buffer, filtered and then added to the donor 96-well plate to be determined their ability to pass the brain barrier. Then, the donor plate was carefully put on the acceptor plate to form a “sandwich”, which was left undisturbed for 2h and 30 min at 25°C. During this time the compounds diffused from the donor plate through the brain lipid membrane into the acceptor plate. After incubation, the donor plate was removed. UV plate reader determined the

concentration of compounds and commercial drugs in the acceptor and the donor wells. Every sample was analyzed at three to five wavelengths, in 3 wells and in two independent runs. Results are given as the mean [standard deviation (SD)] and the average of the two runs is reported. Ten quality control compounds (previously mentioned) of known BBB permeability were included in each experiment to validate the analysis set.

#### **1.4 Neuro- and hepato-toxicity assessment**

Primary cultures of CGNs were prepared from 7 day-old pups of the same rat strain, as previously described.<sup>419, 420</sup> All animal experiments were authorized by the University of Bologna bioethical committee (Protocol n° 17-72-1212) and performed according to Italian and European Community laws on the use of animals for experimental purposes. For cerebellar granule cultures, cells were dissociated from cerebella and plated on 96 well plates, previously coated with 10 µg/mL poly-L-lysine, at a density of  $3 \times 10^5$  cells/0.2 mL medium/well in BME supplemented with 100 mL/L heat-inactivated FBS (Life technologies), 2 mM glutamine, 100 µM gentamicin sulphate and 25 mM KCl (all from Sigma-Aldrich). 16 h later, 10 µM cytosine arabino-furanoside (Sigma-Aldrich) was added to avoid glial proliferation. After 7 days in vitro, differentiated neurons were shifted to serum free BME medium containing 25 mM KCl without serum and different treatments were performed.

HepG2 cells (human hepatocellular liver carcinoma cell line from American Type Culture Collection, ATCC), were grown in DMEM supplemented with 10% FBS and 50 units/mL of penicillin/ streptomycin (Life Technologies) at 37 °C in a humidified atmosphere containing 5% CO<sub>2</sub>. For the experiments, cells ( $0.5 \times 10^5$  cells/well) were seeded in 96-well plate in complete medium; after 24 h, the medium was removed, and cells were exposed to the increasing concentrations of previously selected non-neurotoxic compounds (0, 10, 25, and 50 µM) in DMEM with no serum for further 24 h and survival was measured through MTT assay.

The viability of the different cell types (CGNs and HepG2) exposed to increasing concentrations of the studied compounds (0, 5, 25 and 50 µM) for 24 h was evaluated

through the MTT assay. Briefly, thiazolyl blue was added to the culture medium at a final concentration of 0.1 mg/mL. Following a 20 min incubation for CGNs and 10 min for HepG2 cells at 37 °C in the dark, the MTT precipitate was dissolved in 0.1 M Tris-HCl pH 7.5 buffer containing 5% Triton X-100 (all from Sigma-Aldrich) and absorbance was read at 570 nm in a multiplate spectrophotometric reader (Bio-Rad).

### **1.5 AcPHF6 aggregation and inhibition studies by ThT fluorescence**

ThT fluorescence assays were performed as described previously by Lunven *et al.*<sup>259</sup> with some variations. AcPHF6 (Celtek Peptides) was initially dissolved in 1,1,1,3,3,3-hexafluoro-2-propanol, kept at room temperature overnight, aliquoted and dried. Stock solutions of AcPHF6 (0.5 mM) were then prepared in ultrapure water immediately prior to fluorescence assays. Stock solutions of all tested compounds (2 mM) were prepared in DMSO, while stock solution of ThT (0.5 mM) was prepared in 50 mM phosphate buffer pH 7.4. AcPHF6 aggregation was monitored using standard 96-well plates and an EnSpire plate reader (PerkinElmer) setting the excitation and emission wavelengths at 446 and 490 nm, respectively. Samples were prepared by diluting stock solutions in 50 mM phosphate buffer pH 7.4 to a final AcPHF6 concentration of 50  $\mu$ M with 20  $\mu$ M ThT and 10  $\mu$ M test compound (maximum final DMSO content: 0.5%, v/v); the final volume was 100  $\mu$ L. Assays were performed at 25°C. Fluorescence data were recorded every minute over 120 min with 10 s shaking (400 rpm) prior to each reading. Each condition was assayed at least in triplicate and values were averaged. Estimation of the inhibitory potency (%) was carried out by comparing fluorescence values at the plateau (average fluorescence intensity value in the 70-80 min range).

### **1.6 CD spectroscopy**

CD spectra were measured in the 260–200 nm spectral range on a Jasco J-810 spectropolarimeter (Tokyo, Japan) equipped with a PTC-423S Peltier-type temperature control system. Measurements were carried out at 25 °C using quartz cells with 1 mm pathlength (Hellma, Milan, Italy), a 50 nm min<sup>-1</sup> scanning speed, a 2 nm response, a 2



nm spectral bandwidth and an accumulation cycle of 3. Stock solutions of AcPHF6 (1 mM) were prepared in water immediately prior to CD measurements, while stock solutions of compounds **25** and **27** (2 mM) were prepared in methanol/DMSO (95:5, v/v). Samples were prepared by diluting stock solutions in phosphate buffer 50 mM (pH 7.4) to a final AcPHF6 concentration of 100  $\mu$ M with 20  $\mu$ M test compound (final DMSO content: 0.05%, v/v). The spectral contribution of solvents and test compounds was subtracted to derive the CD spectra of AcPHF6, then data were converted to molar units per residue ( $\Delta\epsilon_{res}$ ) and plotted using the Bezier smoothing algorithm provided by the Gnuplot software (version 5.2.2, <http://gnuplot.sourceforge.net>).

### 1.7 Atomic force microscopy

Atomic Force Microscopy imaging was performed in PeakForce™ tapping-mode on a Nanoscope Multimode 8 (Bruker, U.S.A.) with ScanAsyst Air probes (Bruker). Peptide specimens were prepared by quickly diluting a freshly-prepared 500  $\mu$ M aliquot of AcPHF6 peptide in water to 50  $\mu$ M concentration in 50 mM phosphate buffer (pH 7.4) or in the same buffer additionally containing 10  $\mu$ M of either compound **25** or **27**, briefly vortexing and then subjecting the specimens to the same incubation procedure detailed for ThT fluorescence measurements (briefly, incubation at 25°C for 80 min with 400 rpm shaking for 10 s every minute). At the end of the incubation, the peptide solutions were immediately filtered through Microcon centrifuge ultrafiltration devices (MWCO 30 kDa, Millipore) to separate the small MW fraction from the polymerized peptide fraction. Additional runs on the same Microcons were performed in order to exchange the different buffers with ultrapure water. 5  $\mu$ L aliquots of the high-molecular weight retentate fractions were layered on discs of freshly cleaved muscovite mica (EMS, U.S.A.) and allowed to dry while protected from ambient contamination. The recorded micrographs were only processed by flattening with Bruker's Nanoscope Analysis software (version 1.8).

### **1.8 Okadaic acid-induced tau hyperphosphorylation cell model**

Human SH-SY5Y cells were grown in DMEM supplemented with 10% FBS and 1% penicillin-streptomycin at 37 °C and 5% CO<sub>2</sub> in an incubator. SH-SY5Y cells were seeded onto 96-well plate at 60000 cells per well. 48 hours later, cells were pre-incubated with the compounds at the desired concentration for 1 hour and after that time OA (acquired from Sigma Aldrich, catalogue number: 09381) was added at a concentration of 30nM and incubated for another 24 hours. Afterwards, cells were incubated with 0.5mg/mL MTT solution for at least 4 hours at 37 °C and 5% CO<sub>2</sub>. Then culture media was removed and the formazan crystals attached to the bottom of the plate were dissolved with 200µL of DMSO. Finally, UV-absorbance was measured at 595nM in a microplate reader (Varioskan Flash Microplate reader, Thermo Scientific).

## **2. Chapter IV**

### **2.1 Aβ<sub>42</sub> and tau anti-aggregating activities in *Escherichia coli* cells**

*Cloning and over-expression of Aβ<sub>42</sub> peptide. Escherichia coli* competent cells BL21 (DE3) were transformed with the pET28a vector (Novagen, Inc., Madison, WI, USA) carrying the DNA sequence of Aβ<sub>42</sub>. Because of the addition of the initiation codon ATG in front of both genes, the overexpressed peptide contains an additional methionine residue at its N terminus. For overnight culture preparation, an amount of 10 mL of M9 minimal medium containing 50 µg/mL of kanamycin was inoculated with a colony of BL21 (DE3) bearing the plasmid to be expressed at 37°C. For expression of the Aβ<sub>42</sub> peptide, the required volume of overnight culture to obtain 1:500 dilution was added into fresh M9 minimal medium containing 50 µg/mL of kanamycin and 250 µM ThS. The bacterial culture was grown at 37°C and 250 rpm. When the cell density reached OD<sub>600</sub> = 0.6, 980 µL of culture were transferred into Eppendorf tubes of 1.5 mL with 10 µL of each compound to be tested in DMSO and 10 µL of isopropyl 1-thio-β-D-galactopyranoside (IPTG) at 100 mM. The final concentration of the tested compounds was fixed at 20 µM. The samples were grown overnight at 37°C and 1400

rpm using a Thermomixer (Eppendorf, Hamburg, Germany). As negative control (maximal amyloid presence) the same amount of DMSO without compounds was added in the sample. In parallel, non-induced samples (in absence of IPTG) were also prepared and used as positive controls (non-amyloid presence). In addition, these samples were used to assess the potential intrinsic toxicity of the compounds, and to confirm the correct bacterial growth.

*Cloning and Overexpression of Tau Protein.* *E. coli* BL21 (DE3) competent cells were transformed with pTARA containing the RNA-polymerase gen of T7 phage (T7RP) under the control of the promoter PBAD. *E. coli* BL21 (DE3) with pTARA competent cells were transformed with pRKT42 vector encoding four repeats of tau protein in two inserts. For overnight culture preparation, 10 mL of M9 medium containing 0.5% of glucose, 50 µg/mL of ampicillin, and 12.5 µg/mL of chloramphenicol were inoculated with a colony of BL21 (DE3) bearing the plasmids to be expressed at 37 °C. For expression of tau protein, the required volume of overnight culture to obtain 1:500 dilution was added to fresh M9 minimal medium containing 0.5% of glucose, 50 µg/mL of ampicillin, 12.5 µg/mL of chloramphenicol, and 250 µM ThS. The bacterial culture was grown at 37 °C and 250 rpm. When the cell density reached OD600 = 0.6, 980 µL of culture were transferred into Eppendorf tubes of 1.5 mL with 10 µL of each compound to be tested in DMSO and 10 µL of arabinose at 25%. The final concentration of the compounds was fixed at 20 µM. The samples were grown overnight at 37 °C and 1400 rpm using a Thermomixer (Eppendorf, Hamburg, Germany). As negative control (maximal presence of tau), the same amount of DMSO without compounds was added in the sample. In parallel, non-induced samples (in absence of arabinose) were also prepared and used as positive controls (absence of tau). In addition, these samples were used to assess the potential intrinsic toxicity of the compounds and to confirm the correct bacterial growth.

*Thioflavin S Steady-State Fluorescence.* ThS (T1892) and other chemical reagents were purchased from Sigma (St. Louis, MO). ThS stock solution (2500 mM) was prepared in double-distilled water purified through a Milli-Q system (Millipore, USA). For the fluorescence assay, the ThS spectra were measured on an Aminco Bowman series 2 luminescence spectrophotometer (Aminco-Bowman AB2, SLM Aminco, Rochester, NY,

USA) from 460 to 600 nm at 25 °C using an excitation wavelength of 440 nm and slit widths of 4 nm. The emission at 485 nm (ThS peak fluorescence in the presence of amyloids) was recorded. In order to normalize the ThS fluorescence as a function of the bacterial concentration, OD600 was obtained using a Shimadzu UV-2401 PC UV-Vis spectrophotometer (Shimadzu, Japan). Note that the fluorescence normalization was carried out considering as 100% the ThS fluorescence of the bacterial cells expressing the peptide or protein in the absence of tested compounds, and 0% the ThS fluorescence of the bacterial cells non-expressing the protein.

## **Bibliography**

1. Chiti, F.; Dobson, C. M. Protein misfolding, functional amyloid, and human disease. *Annu Rev Biochem* **2006**, *75*, 333-66.
2. Soto, C. Protein misfolding and disease; protein refolding and therapy. *FEBS Letters* **2001**, *498*, 204-207.
3. Soto, C. Alzheimer's and prion disease as disorders of protein conformation: implications for the design of novel therapeutic approaches. *Journal of Molecular Medicine* **1999**, *77*, 412-418.
4. Westermarck, P.; Benson, M. D.; Buxbaum, J. N.; Cohen, A. S.; Frangione, B.; Ikeda, S.; Masters, C. L.; Merlini, G.; Saraiva, M. J.; Sipe, J. D. Amyloid: toward terminology clarification. Report from the Nomenclature Committee of the International Society of Amyloidosis. *Amyloid* **2005**, *12*, 1-4.
5. Soto, C. Unfolding the role of protein misfolding in neurodegenerative diseases. *Nature Reviews Neuroscience* **2003**, *4*, 49.
6. Prusiner, S. B. Biology and genetics of prions causing neurodegeneration. *Annu Rev Genet* **2013**, *47*, 601-23.
7. Chiti, F.; Dobson, C. M. Protein Misfolding, Amyloid Formation, and Human Disease: A Summary of Progress Over the Last Decade. *Annu Rev Biochem* **2017**, *86*, 27-68.
8. Goedert, M.; Clavaguera, F.; Tolnay, M. The propagation of prion-like protein inclusions in neurodegenerative diseases. *Trends Neurosci* **2010**, *33*, 317-25.
9. Eisenberg, D.; Jucker, M. The amyloid state of proteins in human diseases. *Cell* **2012**, *148*, 1188-203.
10. Sunde, M.; Serpell, L. C.; Bartlam, M.; Fraser, P. E.; Pepys, M. B.; Blake, C. C. F. Common core structure of amyloid fibrils by synchrotron X-ray diffraction. Edited by F. E. Cohen. *Journal of Molecular Biology* **1997**, *273*, 729-739.
11. Goldsbury, C.; Kistler, J.; Aebi, U.; Arvinte, T.; Cooper, G. J. Watching amyloid fibrils grow by time-lapse atomic force microscopy. *J Mol Biol* **1999**, *285*, 33-9.
12. Jimenez, J. L.; Guijarro, J. I.; Orlova, E.; Zurdo, J.; Dobson, C. M.; Sunde, M.; Saibil, H. R. Cryo-electron microscopy structure of an SH3 amyloid fibril and model of the molecular packing. *Embo j* **1999**, *18*, 815-21.
13. Serpell, L. C.; Sunde, M.; Benson, M. D.; Tennent, G. A.; Pepys, M. B.; Fraser, P. E. The protofilament substructure of amyloid fibrils. *J Mol Biol* **2000**, *300*, 1033-9.
14. Paravastu, A. K.; Leapman, R. D.; Yau, W. M.; Tycko, R. Molecular structural basis for polymorphism in Alzheimer's beta-amyloid fibrils. *Proc Natl Acad Sci U S A* **2008**, *105*, 18349-54.
15. Wasmer, C.; Lange, A.; Van Melckebeke, H.; Siemer, A. B.; Riek, R.; Meier, B. H. Amyloid fibrils of the HET-s(218-289) prion form a beta solenoid with a triangular hydrophobic core. *Science* **2008**, *319*, 1523-6.
16. Nilsson, M. R. Techniques to study amyloid fibril formation in vitro. *Methods* **2004**, *34*, 151-60.
17. Dobson, C. M. Protein misfolding, evolution and disease. *Trends Biochem Sci* **1999**, *24*, 329-32.

18. Knowles, T. P.; Fitzpatrick, A. W.; Meehan, S.; Mott, H. R.; Vendruscolo, M.; Dobson, C. M.; Welland, M. E. Role of intermolecular forces in defining material properties of protein nanofibrils. *Science* **2007**, 318, 1900-3.
19. Greenwald, J.; Riek, R. Biology of Amyloid: Structure, Function, and Regulation. *Structure* **2010**, 18, 1244-1260.
20. Rambaran, R. N.; Serpell, L. C. Amyloid fibrils: abnormal protein assembly. *Prion* **2008**, 2, 112-7.
21. Knowles, T. P.; Waudby, C. A.; Devlin, G. L.; Cohen, S. I.; Aguzzi, A.; Vendruscolo, M.; Terentjev, E. M.; Welland, M. E.; Dobson, C. M. An analytical solution to the kinetics of breakable filament assembly. *Science* **2009**, 326, 1533-7.
22. Arosio, P.; Cukalevski, R.; Frohm, B.; Knowles, T. P.; Linse, S. Quantification of the concentration of Abeta42 propagons during the lag phase by an amyloid chain reaction assay. *J Am Chem Soc* **2014**, 136, 219-25.
23. Meisl, G.; Yang, X.; Hellstrand, E.; Frohm, B.; Kirkegaard, J. B.; Cohen, S. I.; Dobson, C. M.; Linse, S.; Knowles, T. P. Differences in nucleation behavior underlie the contrasting aggregation kinetics of the Abeta40 and Abeta42 peptides. *Proc Natl Acad Sci U S A* **2014**, 111, 9384-9.
24. Jucker, M.; Walker, L. C. Self-propagation of pathogenic protein aggregates in neurodegenerative diseases. *Nature* **2013**, 501, 45.
25. Collinge, J.; Clarke, A. R. A General Model of Prion Strains and Their Pathogenicity. *Science* **2007**, 318, 930-936.
26. Benilova, I.; Karran, E.; De Strooper, B. The toxic Abeta oligomer and Alzheimer's disease: an emperor in need of clothes. *Nat Neurosci* **2012**, 15, 349-57.
27. Roberts, H. L.; Brown, D. R. Seeking a mechanism for the toxicity of oligomeric alpha-synuclein. *Biomolecules* **2015**, 5, 282-305.
28. Guerrero-Munoz, M. J.; Gerson, J.; Castillo-Carranza, D. L. Tau Oligomers: The Toxic Player at Synapses in Alzheimer's Disease. *Front Cell Neurosci* **2015**, 9, 464.
29. Mannini, B.; Cascella, R.; Zampagni, M.; van Waarde-Verhagen, M.; Meehan, S.; Roodveldt, C.; Campioni, S.; Boninsegna, M.; Penco, A.; Relini, A.; Kampinga, H. H.; Dobson, C. M.; Wilson, M. R.; Cecchi, C.; Chiti, F. Molecular mechanisms used by chaperones to reduce the toxicity of aberrant protein oligomers. *Proc Natl Acad Sci U S A* **2012**, 109, 12479-84.
30. World Health Organization. <http://www.who.int/en/news-room/fact-sheets/detail/dementia> (September, 10th 2018).
31. Cummings, J.; Lee, G.; Ritter, A.; Zhong, K. Alzheimer's disease drug development pipeline: 2018. *Alzheimer's & Dementia: Translational Research & Clinical Interventions* **2018**, 4, 195-214.
32. Prusiner, S. B. Prions. *Proceedings of the National Academy of Sciences* **1998**, 95, 13363-13383.
33. Aisen, P. S.; Cummings, J.; Jack, C. R.; Morris, J. C.; Sperling, R.; Frölich, L.; Jones, R. W.; Dowsett, S. A.; Matthews, B. R.; Raskin, J.; Scheltens, P.; Dubois, B. On the path to 2025: understanding the Alzheimer's disease continuum. *Alzheimer's Research & Therapy* **2017**, 9, 60.
34. World Alzheimer Report 2018. <https://www.alz.co.uk/research/WorldAlzheimerReport2018.pdf> (September, 27th 2018).

35. Vradenburg, G. A pivotal moment in Alzheimer's disease and dementia: how global unity of purpose and action can beat the disease by 2025. *Expert Rev Neurother* **2015**, *15*, 73-82.
36. Cummings, J.; Aisen, P. S.; DuBois, B.; Frölich, L.; Jack, C. R.; Jones, R. W.; Morris, J. C.; Raskin, J.; Dowsett, S. A.; Scheltens, P. Drug development in Alzheimer's disease: the path to 2025. *Alzheimer's Research & Therapy* **2016**, *8*, 39.
37. Cummings, J.; Lee, G.; Mortsdorf, T.; Ritter, A.; Zhong, K. Alzheimer's disease drug development pipeline: 2017. *Alzheimer's & Dementia: Translational Research & Clinical Interventions* **2017**, *3*, 367-384.
38. Schneider, L. S.; Mangialasche, F.; Andreasen, N.; Feldman, H.; Giacobini, E.; Jones, R.; Mantua, V.; Mecocci, P.; Pani, L.; Winblad, B.; Kivipelto, M. Clinical trials and late-stage drug development for Alzheimer's disease: an appraisal from 1984 to 2014. *J Intern Med* **2014**, *275*, 251-83.
39. Cummings, J. L.; Morstorf, T.; Zhong, K. Alzheimer's disease drug-development pipeline: few candidates, frequent failures. *Alzheimers Res Ther* **2014**, *6*, 37.
40. Baki, A.; Bielik, A.; Molnar, L.; Szendrei, G.; Keseru, G. M. A high throughput luminescent assay for glycogen synthase kinase-3beta inhibitors. *Assay Drug Dev Technol* **2007**, *5*, 75-83.
41. Sugino, H.; Watanabe, A.; Amada, N.; Yamamoto, M.; Ohgi, Y.; Kostic, D.; Sanchez, R. Global Trends in Alzheimer Disease Clinical Development: Increasing the Probability of Success. *Clin Ther* **2015**, *37*, 1632-42.
42. Andrieu, S.; Coley, N.; Lovestone, S.; Aisen, P. S.; Vellas, B. Prevention of sporadic Alzheimer's disease: lessons learned from clinical trials and future directions. *Lancet Neurol* **2015**, *14*, 926-944.
43. Bird, T. D. Genetic aspects of Alzheimer disease. *Genet Med* **2008**, *10*, 231-9.
44. Iqbal, K.; Grundke-Iqbal, I. Alzheimer Disease, a Multifactorial Disorder Seeking Multi-therapies. *Alzheimer's & dementia : the journal of the Alzheimer's Association* **2010**, *6*, 420-424.
45. Walker, L. C.; Schelle, J.; Jucker, M. The Prion-Like Properties of Amyloid-beta Assemblies: Implications for Alzheimer's Disease. *Cold Spring Harb Perspect Med* **2016**, *6*.
46. McDonald, R. J. Multiple combinations of co-factors produce variants of age-related cognitive decline: a theory. *Can J Exp Psychol* **2002**, *56*, 221-39.
47. Bartus, R. T.; Dean, R. L., 3rd; Beer, B.; Lippa, A. S. The cholinergic hypothesis of geriatric memory dysfunction. *Science* **1982**, *217*, 408-14.
48. Bartus, R. T. On neurodegenerative diseases, models, and treatment strategies: lessons learned and lessons forgotten a generation following the cholinergic hypothesis. *Exp Neurol* **2000**, *163*, 495-529.
49. Hardy, J.; Higgins, G. Alzheimer's disease: the amyloid cascade hypothesis. *Science* **1992**, *256*, 184-185.
50. Hardy, J.; Selkoe, D. J. The amyloid hypothesis of Alzheimer's disease: progress and problems on the road to therapeutics. *Science* **2002**, *297*, 353-6.
51. Haass, C.; Kaether, C.; Thinakaran, G.; Sisodia, S. Trafficking and proteolytic processing of APP. *Cold Spring Harb Perspect Med* **2012**, *2*, a006270.
52. Bolognesi, M. L. 1.04 - From Imaging Agents to Theranostic Drugs in Alzheimer's Disease. In *Comprehensive Medicinal Chemistry III*, Chackalamannil, S.; Rotella, D.; Ward, S. E., Eds. Elsevier: Oxford, 2017; pp 74-106.

53. Jack, C. R., Jr.; Knopman, D. S.; Jagust, W. J.; Shaw, L. M.; Aisen, P. S.; Weiner, M. W.; Petersen, R. C.; Trojanowski, J. Q. Hypothetical model of dynamic biomarkers of the Alzheimer's pathological cascade. *Lancet Neurol* **2010**, *9*, 119-28.
54. Holtzman, D. M.; Morris, J. C.; Goate, A. M. Alzheimer's disease: the challenge of the second century. *Sci Transl Med* **2011**, *3*, 77sr1.
55. Selkoe, D. J. Resolving controversies on the path to Alzheimer's therapeutics. *Nat Med* **2011**, *17*, 1060-5.
56. Jucker, M.; Walker, L. C. Pathogenic protein seeding in Alzheimer disease and other neurodegenerative disorders. *Ann Neurol* **2011**, *70*, 532-40.
57. Tanzi, R. E.; Bertram, L. Twenty years of the Alzheimer's disease amyloid hypothesis: a genetic perspective. *Cell* **2005**, *120*, 545-55.
58. Walsh, D. M.; Klyubin, I.; Fadeeva, J. V.; Cullen, W. K.; Anwyl, R.; Wolfe, M. S.; Rowan, M. J.; Selkoe, D. J. Naturally secreted oligomers of amyloid beta protein potently inhibit hippocampal long-term potentiation in vivo. *Nature* **2002**, *416*, 535-9.
59. Stefani, M.; Dobson, C. M. Protein aggregation and aggregate toxicity: new insights into protein folding, misfolding diseases and biological evolution. *J Mol Med (Berl)* **2003**, *81*, 678-99.
60. Varadarajan, S.; Yatin, S.; Aksenova, M.; Butterfield, D. A. Review: Alzheimer's amyloid beta-peptide-associated free radical oxidative stress and neurotoxicity. *J Struct Biol* **2000**, *130*, 184-208.
61. Sakono, M.; Zako, T. Amyloid oligomers: formation and toxicity of Abeta oligomers. *Febs j* **2010**, *277*, 1348-58.
62. Karran, E.; Mercken, M.; De Strooper, B. The amyloid cascade hypothesis for Alzheimer's disease: an appraisal for the development of therapeutics. *Nat Rev Drug Discov* **2011**, *10*, 698-712.
63. Villemagne, V. L.; Furumoto, S.; Fodero-Tavoletti, M.; Harada, R.; Mulligan, R. S.; Kudo, Y.; Masters, C. L.; Yanai, K.; Rowe, C. C.; Okamura, N. The challenges of tau imaging. *Future Neurology* **2012**, *7*, 409-421.
64. Weingarten, M. D.; Lockwood, A. H.; Hwo, S. Y.; Kirschner, M. W. A protein factor essential for microtubule assembly. *Proceedings of the National Academy of Sciences* **1975**, *72*, 1858-1862.
65. Drubin, D.; Kirschner, M. Tau protein function in living cells. *The Journal of Cell Biology* **1986**, *103*, 2739-2746.
66. Iqbal, K.; Liu, F.; Gong, C. X. Tau and neurodegenerative disease: the story so far. *Nat Rev Neurol* **2016**, *12*, 15-27.
67. Goedert, M.; Spillantini, M. G. A Century of Alzheimer's Disease. *Science* **2006**, *314*, 777-781.
68. Dolan, P. J.; Johnson, G. V. The role of tau kinases in Alzheimer's disease. *Curr Opin Drug Discov Devel* **2010**, *13*, 595-603.
69. Holmes, B. B.; Diamond, M. I. Prion-like properties of Tau protein: the importance of extracellular Tau as a therapeutic target. *J Biol Chem* **2014**, *289*, 19855-61.
70. Clavaguera, F.; Bolmont, T.; Crowther, R. A.; Abramowski, D.; Frank, S.; Probst, A.; Fraser, G.; Stalder, A. K.; Beibel, M.; Staufenbiel, M.; Jucker, M.; Goedert, M.; Tolnay, M. Transmission and spreading of tauopathy in transgenic mouse brain. *Nat Cell Biol* **2009**, *11*, 909-13.
71. Blennow, K.; de Leon, M. J.; Zetterberg, H. Alzheimer's disease. *The Lancet* **2006**, *368*, 387-403.



72. Cavalli, A.; Bolognesi, M. L.; Minarini, A.; Rosini, M.; Tumiatti, V.; Recanatini, M.; Melchiorre, C. Multi-target-directed ligands to combat neurodegenerative diseases. *J Med Chem* **2008**, *51*, 347-72.
73. Caughey, B.; Baron, G. S. Prions and their partners in crime. *Nature* **2006**, *443*, 803-10.
74. Prusiner, S. B.; DeArmond, S. J. Prion diseases and neurodegeneration. *Annu Rev Neurosci* **1994**, *17*, 311-39.
75. Saá, P.; Harris, D. A.; Cervenakova, L. Mechanisms of prion-induced neurodegeneration. *Expert Reviews in Molecular Medicine* **2016**, *18*, e5.
76. Hauw, J. J.; Haik, S.; Brandel, J. P. History of Prions and transmission of protein misfolding. *Bull Acad Natl Med* **2015**, *199*, 787-796.
77. Prusiner, S. B. Novel proteinaceous infectious particles cause scrapie. *Science* **1982**, *216*, 136-44.
78. Fraser, P. E. Prions and Prion-like Proteins. *Journal of Biological Chemistry* **2014**, *289*, 19839-19840.
79. Aguzzi, A. Prion diseases of humans and farm animals: epidemiology, genetics, and pathogenesis. *Journal of Neurochemistry* **2006**, *97*, 1726-1739.
80. Aguzzi, A.; Polymenidou, M. Mammalian prion biology: one century of evolving concepts. *Cell* **2004**, *116*, 313-27.
81. Cobb, N. J.; Surewicz, W. K. Prion Diseases and Their Biochemical Mechanisms. *Biochemistry* **2009**, *48*, 2574-2585.
82. M., G.; G., C.; A., L. C.; J., M.; T., W. H. J.; E., H. P.; G., W. R. A retrospective case note review of deceased recipients of vCJD-implicated blood transfusions. *Vox Sanguinis* **2009**, *97*, 211-218.
83. Wroe, S. J.; Pal, S.; Siddique, D.; Hyare, H.; Macfarlane, R.; Joiner, S.; Linehan, J. M.; Brandner, S.; Wadsworth, J. D.; Hewitt, P.; Collinge, J. Clinical presentation and pre-mortem diagnosis of variant Creutzfeldt-Jakob disease associated with blood transfusion: a case report. *Lancet* **2006**, *368*, 2061-7.
84. Bueler, H.; Fischer, M.; Lang, Y.; Bluethmann, H.; Lipp, H. P.; DeArmond, S. J.; Prusiner, S. B.; Aguet, M.; Weissmann, C. Normal development and behaviour of mice lacking the neuronal cell-surface PrP protein. *Nature* **1992**, *356*, 577-82.
85. Manson, J. C.; Clarke, A. R.; Hooper, M. L.; Aitchison, L.; McConnell, I.; Hope, J. 129/Ola mice carrying a null mutation in PrP that abolishes mRNA production are developmentally normal. *Molecular Neurobiology* **1994**, *8*, 121-127.
86. Aguzzi, A.; Baumann, F.; Bremer, J. The prion's elusive reason for being. *Annu Rev Neurosci* **2008**, *31*, 439-77.
87. Zahn, R.; Liu, A.; Luhrs, T.; Riek, R.; von Schroetter, C.; Lopez Garcia, F.; Billeter, M.; Calzolari, L.; Wider, G.; Wuthrich, K. NMR solution structure of the human prion protein. *Proc Natl Acad Sci U S A* **2000**, *97*, 145-50.
88. Roucou, X.; Gains, M.; LeBlanc, A. C. Neuroprotective functions of prion protein. *Journal of Neuroscience Research* **2004**, *75*, 153-161.
89. Oh, J. M.; Shin, H. Y.; Park, S. J.; Kim, B. H.; Choi, J. K.; Choi, E. K.; Carp, R. I.; Kim, Y. S. The involvement of cellular prion protein in the autophagy pathway in neuronal cells. *Mol Cell Neurosci* **2008**, *39*, 238-47.
90. Schmitt-Ulms, G.; Ehsani, S.; Watts, J. C.; Westaway, D.; Wille, H. Evolutionary Descent of Prion Genes from the ZIP Family of Metal Ion Transporters. *PLOS ONE* **2009**, *4*, e7208.

91. Brandner, S.; Isenmann, S.; Raeber, A.; Fischer, M.; Sailer, A.; Kobayashi, Y.; Marino, S.; Weissmann, C.; Aguzzi, A. Normal host prion protein necessary for scrapie-induced neurotoxicity. *Nature* **1996**, *379*, 339-43.
92. Mallucci, G.; Dickinson, A.; Linehan, J.; Klöhn, P.-C.; Brandner, S.; Collinge, J. Depleting Neuronal PrP in Prion Infection Prevents Disease and Reverses Spongiosis. *Science* **2003**, *302*, 871-874.
93. Harris, D. A.; True, H. L. New Insights into Prion Structure and Toxicity. *Neuron* **2006**, *50*, 353-357.
94. Brown, D. R.; Herms, J.; Kretzschmar, H. A. Mouse cortical cells lacking cellular PrP survive in culture with a neurotoxic PrP fragment. *Neuroreport* **1994**, *5*, 2057-60.
95. Chesebro, B.; Trifilo, M.; Race, R.; Meade-White, K.; Teng, C.; LaCasse, R.; Raymond, L.; Favara, C.; Baron, G.; Priola, S.; Caughey, B.; Masliah, E.; Oldstone, M. Anchorless prion protein results in infectious amyloid disease without clinical scrapie. *Science* **2005**, *308*, 1435-9.
96. Sweeney, P.; Park, H.; Baumann, M.; Dunlop, J.; Frydman, J.; Kopito, R.; McCampbell, A.; Leblanc, G.; Venkateswaran, A.; Nurmi, A.; Hodgson, R. Protein misfolding in neurodegenerative diseases: implications and strategies. *Translational Neurodegeneration* **2017**, *6*, 6.
97. Denny, R. A.; Gavrin, L. K.; Saiah, E. Recent developments in targeting protein misfolding diseases. *Bioorg Med Chem Lett* **2013**, *23*, 1935-44.
98. Bose, S.; Cho, J. Targeting chaperones, heat shock factor-1, and unfolded protein response: Promising therapeutic approaches for neurodegenerative disorders. *Ageing Res Rev* **2017**, *35*, 155-175.
99. Liu, Y. H.; Han, Y. L.; Song, J.; Wang, Y.; Jing, Y. Y.; Shi, Q.; Tian, C.; Wang, Z. Y.; Li, C. P.; Han, J.; Dong, X. P. Heat shock protein 104 inhibited the fibrillization of prion peptide 106-126 and disassembled prion peptide 106-126 fibrils in vitro. *Int J Biochem Cell Biol* **2011**, *43*, 768-74.
100. DeSantis, M. E.; Leung, E. H.; Sweeny, E. A.; Jackrel, M. E.; Cushman-Nick, M.; Neuhaus-Follini, A.; Vashist, S.; Sochor, M. A.; Knight, M. N.; Shorter, J. Operational plasticity enables hsp104 to disaggregate diverse amyloid and nonamyloid clients. *Cell* **2012**, *151*, 778-93.
101. Deane, R.; Bell, R. D.; Sagare, A.; Zlokovic, B. V. Clearance of amyloid-beta peptide across the blood-brain barrier: implication for therapies in Alzheimer's disease. *CNS Neurol Disord Drug Targets* **2009**, *8*, 16-30.
102. Watt, A. D.; Crespi, G. A.; Down, R. A.; Ascher, D. B.; Gunn, A.; Perez, K. A.; McLean, C. A.; Villemagne, V. L.; Parker, M. W.; Barnham, K. J.; Miles, L. A. Do current therapeutic anti-Aβ antibodies for Alzheimer's disease engage the target? *Acta Neuropathol* **2014**, *127*, 803-10.
103. European Medicines Agency.  
[http://www.ema.europa.eu/ema/index.jsp?curl=pages/medicines/human/orphans/2009/11/human\\_orphan\\_000690.jsp&murl=menus/medicines/medicines.jsp&mid=WC0b01ac058001d12b&jenabled=true](http://www.ema.europa.eu/ema/index.jsp?curl=pages/medicines/human/orphans/2009/11/human_orphan_000690.jsp&murl=menus/medicines/medicines.jsp&mid=WC0b01ac058001d12b&jenabled=true) (September, 10th 2018).
104. Johnson, S. M.; Connelly, S.; Fearn, C.; Powers, E. T.; Kelly, J. W. The Transthyretin Amyloidoses: From Delineating the Molecular Mechanism of Aggregation Linked to Pathology to a Regulatory Agency Approved Drug. *Journal of Molecular Biology* **2012**, *421*, 185-203.

105. Hammarstrom, P.; Wiseman, R. L.; Powers, E. T.; Kelly, J. W. Prevention of transthyretin amyloid disease by changing protein misfolding energetics. *Science* **2003**, 299, 713-6.
106. Bulawa, C. E.; Connelly, S.; DeVit, M.; Wang, L.; Weigel, C.; Fleming, J. A.; Packman, J.; Powers, E. T.; Wiseman, R. L.; Foss, T. R.; Wilson, I. A.; Kelly, J. W.; Labaudinière, R. Tafamidis, a potent and selective transthyretin kinetic stabilizer that inhibits the amyloid cascade. *Proceedings of the National Academy of Sciences of the United States of America* **2012**, 109, 9629-9634.
107. Coelho, T.; Merlini, G.; Bulawa, C. E.; Fleming, J. A.; Judge, D. P.; Kelly, J. W.; Maurer, M. S.; Plante-Bordeneuve, V.; Labaudiniere, R.; Mundayat, R.; Riley, S.; Lombardo, I.; Huertas, P. Mechanism of Action and Clinical Application of Tafamidis in Hereditary Transthyretin Amyloidosis. *Neurol Ther* **2016**, 5, 1-25.
108. Pankevich, D. E.; Altevogt, B. M.; Dunlop, J.; Gage, F. H.; Hyman, S. E. Improving and Accelerating Drug Development for Nervous System Disorders. *Neuron* **2014**, 84, 546-553.
109. Rankovic, Z. CNS Drug Design: Balancing Physicochemical Properties for Optimal Brain Exposure. *Journal of Medicinal Chemistry* **2015**, 58, 2584-2608.
110. Bolognesi, M. L. Polypharmacology in a single drug: multitarget drugs. *Curr Med Chem* **2013**, 20, 1639-45.
111. Morphy, R.; Rankovic, Z. Fragments, network biology and designing multiple ligands. *Drug Discov Today* **2007**, 12, 156-60.
112. Hopkins, A. L. Network pharmacology: the next paradigm in drug discovery. *Nat Chem Biol* **2008**, 4, 682-90.
113. Morphy, R.; Rankovic, Z. Designed Multiple Ligands. An Emerging Drug Discovery Paradigm. *Journal of Medicinal Chemistry* **2005**, 48, 6523-6543.
114. Woodgett, J. R. Molecular cloning and expression of glycogen synthase kinase-3/factor A. *Embo j* **1990**, 9, 2431-8.
115. Leroy, K.; Brion, J. P. Developmental expression and localization of glycogen synthase kinase-3beta in rat brain. *J Chem Neuroanat* **1999**, 16, 279-93.
116. Doble, B. W.; Woodgett, J. R. GSK-3: tricks of the trade for a multi-tasking kinase. *J Cell Sci* **2003**, 116, 1175-86.
117. Salas, T. R.; Reddy, S. A.; Clifford, J. L.; Davis, R. J.; Kikuchi, A.; Lippman, S. M.; Menter, D. G. Alleviating the Suppression of Glycogen Synthase Kinase-3 $\beta$  by Akt Leads to the Phosphorylation of cAMP-response Element-binding Protein and Its Transactivation in Intact Cell Nuclei. *Journal of Biological Chemistry* **2003**, 278, 41338-41346.
118. Hooper, C.; Markevich, V.; Plattner, F.; Killick, R.; Schofield, E.; Engel, T.; Hernandez, F.; Anderton, B.; Rosenblum, K.; Bliss, T.; Cooke, S. F.; Avila, J.; Lucas, J. J.; Giese, K. P.; Stephenson, J.; Lovestone, S. Glycogen synthase kinase-3 inhibition is integral to long-term potentiation. *Eur J Neurosci* **2007**, 25, 81-6.
119. Peineau, S.; Taghibiglou, C.; Bradley, C.; Wong, T. P.; Liu, L.; Lu, J.; Lo, E.; Wu, D.; Saule, E.; Bouschet, T.; Matthews, P.; Isaac, J. T.; Bortolotto, Z. A.; Wang, Y. T.; Collingridge, G. L. LTP inhibits LTD in the hippocampus via regulation of GSK3beta. *Neuron* **2007**, 53, 703-17.
120. Bax, B.; Carter, P. S.; Lewis, C.; Guy, A. R.; Bridges, A.; Tanner, R.; Pettman, G.; Mannix, C.; Culbert, A. A.; Brown, M. J.; Smith, D. G.; Reith, A. D. The structure of phosphorylated GSK-3beta complexed with a peptide, FRATtide, that inhibits beta-catenin phosphorylation. *Structure* **2001**, 9, 1143-52.

121. Dajani, R.; Fraser, E.; Roe, S. M.; Young, N.; Good, V.; Dale, T. C.; Pearl, L. H. Crystal structure of glycogen synthase kinase 3 beta: structural basis for phosphate-primed substrate specificity and autoinhibition. *Cell* **2001**, 105, 721-32.
122. ter Haar, E.; Coll, J. T.; Austen, D. A.; Hsiao, H. M.; Swenson, L.; Jain, J. Structure of GSK3beta reveals a primed phosphorylation mechanism. *Nat Struct Biol* **2001**, 8, 593-6.
123. Johnson, L. N.; Noble, M. E.; Owen, D. J. Active and inactive protein kinases: structural basis for regulation. *Cell* **1996**, 85, 149-58.
124. Fiol, C. J.; Wang, A.; Roeske, R. W.; Roach, P. J. Ordered multisite protein phosphorylation. Analysis of glycogen synthase kinase 3 action using model peptide substrates. *Journal of Biological Chemistry* **1990**, 265, 6061-6065.
125. Imahori, K.; Hoshi, M.; Ishiguro, K.; Sato, K.; Takahashi, M.; Shiurba, R.; Yamaguchi, H.; Takashima, A.; Uchida, T. Possible Role of Tau Protein Kinases in Pathogenesis of Alzheimer's Disease. *Neurobiology of Aging* **1998**, 19, S93-S98.
126. Plattner, F.; Angelo, M.; Giese, K. P. The Roles of Cyclin-dependent Kinase 5 and Glycogen Synthase Kinase 3 in Tau Hyperphosphorylation. *Journal of Biological Chemistry* **2006**, 281, 25457-25465.
127. Hooper, C.; Killick, R.; Lovestone, S. The GSK3 hypothesis of Alzheimer's disease. *J Neurochem* **2008**, 104, 1433-9.
128. de la Monte, S. M.; Tong, M.; Lester-Coll, N.; Plater, M., Jr.; Wands, J. R. Therapeutic rescue of neurodegeneration in experimental type 3 diabetes: relevance to Alzheimer's disease. *J Alzheimers Dis* **2006**, 10, 89-109.
129. Hoshi, M.; Takashima, A.; Noguchi, K.; Murayama, M.; Sato, M.; Kondo, S.; Saitoh, Y.; Ishiguro, K.; Hoshino, T.; Imahori, K. Regulation of mitochondrial pyruvate dehydrogenase activity by tau protein kinase I/glycogen synthase kinase 3beta in brain. *Proceedings of the National Academy of Sciences of the United States of America* **1996**, 93, 2719-2723.
130. Turenne, G. A.; Price, B. D. Glycogen synthase kinase3 beta phosphorylates serine 33 of p53 and activates p53's transcriptional activity. *BMC Cell Biology* **2001**, 2, 12.
131. Hansen, T. v. O.; Rehfeld, J. F.; Nielsen, F. C. GSK-3 $\beta$  reduces cAMP-induced cholecystokinin gene expression by inhibiting CREB binding. *NeuroReport* **2004**, 15, 841-845.
132. Noble, W.; Planel, E.; Zehr, C.; Olm, V.; Meyerson, J.; Suleman, F.; Gaynor, K.; Wang, L.; LaFrancois, J.; Feinstein, B.; Burns, M.; Krishnamurthy, P.; Wen, Y.; Bhat, R.; Lewis, J.; Dickson, D.; Duff, K. Inhibition of glycogen synthase kinase-3 by lithium correlates with reduced tauopathy and degeneration *in vivo*. *Proceedings of the National Academy of Sciences of the United States of America* **2005**, 102, 6990-6995.
133. Rockenstein, E.; Torrance, M.; Adame, A.; Mante, M.; Bar-on, P.; Rose, J. B.; Crews, L.; Masliah, E. Neuroprotective effects of regulators of the glycogen synthase kinase-3beta signaling pathway in a transgenic model of Alzheimer's disease are associated with reduced amyloid precursor protein phosphorylation. *J Neurosci* **2007**, 27, 1981-91.
134. Martinez, A.; Perez, D. I.; Gil, C. Lessons learnt from glycogen synthase kinase 3 inhibitors development for Alzheimer's disease. *Curr Top Med Chem* **2013**, 13, 1808-19.

135. Stambolic, V.; Ruel, L.; Woodgett, J. R. Lithium inhibits glycogen synthase kinase-3 activity and mimics wingless signalling in intact cells. *Curr Biol* **1996**, *6*, 1664-8.
136. Klein, P. S.; Melton, D. A. A molecular mechanism for the effect of lithium on development. *Proceedings of the National Academy of Sciences* **1996**, *93*, 8455-8459.
137. Zhang, F.; Phiel, C. J.; Spece, L.; Gurvich, N.; Klein, P. S. Inhibitory phosphorylation of glycogen synthase kinase-3 (GSK-3) in response to lithium. Evidence for autoregulation of GSK-3. *J Biol Chem* **2003**, *278*, 33067-77.
138. Kirshenboim, N.; Plotkin, B.; Shlomo, S. B.; Kaidanovich-Beilin, O.; Eldar-Finkelman, H. Lithium-mediated phosphorylation of glycogen synthase kinase-3beta involves PI3 kinase-dependent activation of protein kinase C-alpha. *J Mol Neurosci* **2004**, *24*, 237-45.
139. Alvarez, G.; Muñoz-Montaña, J. R.; Satrústegui, J.; Avila, J.; Bogónez, E.; Díaz-Nido, J. Lithium protects cultured neurons against  $\beta$ -amyloid-induced neurodegeneration. *FEBS Letters* **1999**, *453*, 260-264.
140. Caccamo, A.; Oddo, S.; Tran, L. X.; LaFerla, F. M. Lithium reduces tau phosphorylation but not A beta or working memory deficits in a transgenic model with both plaques and tangles. *Am J Pathol* **2007**, *170*, 1669-75.
141. Avila, J.; Wandosell, F.; Hernandez, F. Role of glycogen synthase kinase-3 in Alzheimer's disease pathogenesis and glycogen synthase kinase-3 inhibitors. *Expert Rev Neurother* **2010**, *10*, 703-10.
142. Macdonald, A.; Briggs, K.; Poppe, M.; Higgins, A.; Velayudhan, L.; Lovestone, S. A feasibility and tolerability study of lithium in Alzheimer's disease. *International Journal of Geriatric Psychiatry* **2008**, *23*, 704-711.
143. Ilouz, R.; Kaidanovich, O.; Gurwitz, D.; Eldar-Finkelman, H. Inhibition of glycogen synthase kinase-3beta by bivalent zinc ions: insight into the insulin-mimetic action of zinc. *Biochem Biophys Res Commun* **2002**, *295*, 102-6.
144. Ryves, W. J.; Dajani, R.; Pearl, L.; Harwood, A. J. Glycogen synthase kinase-3 inhibition by lithium and beryllium suggests the presence of two magnesium binding sites. *Biochem Biophys Res Commun* **2002**, *290*, 967-72.
145. Ring, D. B.; Johnson, K. W.; Henriksen, E. J.; Nuss, J. M.; Goff, D.; Kinnick, T. R.; Ma, S. T.; Reeder, J. W.; Samuels, I.; Slabiak, T.; Wagman, A. S.; Hammond, M. E.; Harrison, S. D. Selective glycogen synthase kinase 3 inhibitors potentiate insulin activation of glucose transport and utilization in vitro and in vivo. *Diabetes* **2003**, *52*, 588-95.
146. Coghlan, M. P.; Culbert, A. A.; Cross, D. A.; Corcoran, S. L.; Yates, J. W.; Pearce, N. J.; Rausch, O. L.; Murphy, G. J.; Carter, P. S.; Roxbee Cox, L.; Mills, D.; Brown, M. J.; Haigh, D.; Ward, R. W.; Smith, D. G.; Murray, K. J.; Reith, A. D.; Holder, J. C. Selective small molecule inhibitors of glycogen synthase kinase-3 modulate glycogen metabolism and gene transcription. *Chem Biol* **2000**, *7*, 793-803.
147. Hu, S.; Begum, A. N.; Jones, M. R.; Oh, M. S.; Beech, W. K.; Beech, B. H.; Yang, F.; Chen, P.; Ubeda, O. J.; Kim, P. C.; Davies, P.; Ma, Q.; Cole, G. M.; Frautschy, S. A. GSK3 inhibitors show benefits in an Alzheimer's disease (AD) model of neurodegeneration but adverse effects in control animals. *Neurobiol Dis* **2009**, *33*, 193-206.
148. Bhat, R.; Xue, Y.; Berg, S.; Hellberg, S.; Ormö, M.; Nilsson, Y.; Radesäter, A.-C.; Jerning, E.; Markgren, P.-O.; Borgegård, T.; Nylöf, M.; Giménez-Cassina, A.; Hernández, F.; Lucas, J. J.; Díaz-Nido, J.; Avila, J. Structural Insights and Biological Effects of

- Glycogen Synthase Kinase 3-specific Inhibitor AR-A014418. *Journal of Biological Chemistry* **2003**, 278, 45937-45945.
149. Koh, S. H.; Kim, Y.; Kim, H. Y.; Hwang, S.; Lee, C. H.; Kim, S. H. Inhibition of glycogen synthase kinase-3 suppresses the onset of symptoms and disease progression of G93A-SOD1 mouse model of ALS. *Exp Neurol* **2007**, 205, 336-46.
150. Selenica, M. L.; Jensen, H. S.; Larsen, A. K.; Pedersen, M. L.; Helboe, L.; Leist, M.; Lotharius, J. Efficacy of small-molecule glycogen synthase kinase-3 inhibitors in the postnatal rat model of tau hyperphosphorylation. *Br J Pharmacol* **2007**, 152, 959-79.
151. Schultz, C.; Link, A.; Leost, M.; Zaharevitz, D. W.; Gussio, R.; Sausville, E. A.; Meijer, L.; Kunick, C. Paullones, a Series of Cyclin-Dependent Kinase Inhibitors: Synthesis, Evaluation of CDK1/Cyclin B Inhibition, and in Vitro Antitumor Activity. *Journal of Medicinal Chemistry* **1999**, 42, 2909-2919.
152. Leost, M.; Schultz, C.; Link, A.; Wu, Y. Z.; Biernat, J.; Mandelkow, E. M.; Bibb, J. A.; Snyder, G. L.; Greengard, P.; Zaharevitz, D. W.; Gussio, R.; Senderowicz, A. M.; Sausville, E. A.; Kunick, C.; Meijer, L. Paullones are potent inhibitors of glycogen synthase kinase-3beta and cyclin-dependent kinase 5/p25. *Eur J Biochem* **2000**, 267, 5983-94.
153. Phiel, C. J.; Wilson, C. A.; Lee, V. M.; Klein, P. S. GSK-3alpha regulates production of Alzheimer's disease amyloid-beta peptides. *Nature* **2003**, 423, 435-9.
154. Ding, S.; Wu, T. Y. H.; Brinker, A.; Peters, E. C.; Hur, W.; Gray, N. S.; Schultz, P. G. Synthetic small molecules that control stem cell fate. *Proceedings of the National Academy of Sciences* **2003**, 100, 7632-7637.
155. Khanfar, M. A.; Hill, R. A.; Kaddoumi, A.; El Sayed, K. A. Discovery of novel GSK-3beta inhibitors with potent in vitro and in vivo activities and excellent brain permeability using combined ligand- and structure-based virtual screening. *J Med Chem* **2010**, 53, 8534-45.
156. Saitoh, M.; Kunitomo, J.; Kimura, E.; Iwashita, H.; Uno, Y.; Onishi, T.; Uchiyama, N.; Kawamoto, T.; Tanaka, T.; Mol, C. D.; Dougan, D. R.; Textor, G. P.; Snell, G. P.; Takizawa, M.; Itoh, F.; Kori, M. 2-{3-[4-(Alkylsulfinyl)phenyl]-1-benzofuran-5-yl}-5-methyl-1,3,4-oxadiazole Derivatives as Novel Inhibitors of Glycogen Synthase Kinase-3 $\beta$  with Good Brain Permeability. *Journal of Medicinal Chemistry* **2009**, 52, 6270-6286.
157. Xie, H.; Wen, H.; Zhang, D.; Liu, L.; Liu, B.; Liu, Q.; Jin, Q.; Ke, K.; Hu, M.; Chen, X. Designing of dual inhibitors for GSK-3beta and CDK5: Virtual screening and in vitro biological activities study. *Oncotarget* **2017**, 8, 18118-18128.
158. Arfeen, M.; Bhagat, S.; Patel, R.; Prasad, S.; Roy, I.; Chakraborti, A. K.; Bharatam, P. V. Design, synthesis and biological evaluation of 5-benzylidene-2-iminothiazolidin-4-ones as selective GSK-3beta inhibitors. *Eur J Med Chem* **2016**, 121, 727-736.
159. Martinez, A.; Alonso, M.; Castro, A.; Pérez, C.; Moreno, F. J. First Non-ATP Competitive Glycogen Synthase Kinase 3  $\beta$  (GSK-3 $\beta$ ) Inhibitors: Thiadiazolidinones (TDZD) as Potential Drugs for the Treatment of Alzheimer's Disease. *Journal of Medicinal Chemistry* **2002**, 45, 1292-1299.
160. Dominguez, J. M.; Fuertes, A.; Orozco, L.; del Monte-Millan, M.; Delgado, E.; Medina, M. Evidence for irreversible inhibition of glycogen synthase kinase-3beta by tideglusib. *J Biol Chem* **2012**, 287, 893-904.
161. Lovestone, S.; Boada, M.; Dubois, B.; Hull, M.; Rinne, J. O.; Huppertz, H. J.; Calero, M.; Andres, M. V.; Gomez-Carrillo, B.; Leon, T.; del Ser, T. A phase II trial of tideglusib in Alzheimer's disease. *J Alzheimers Dis* **2015**, 45, 75-88.

162. Perez, D. I.; Conde, S.; Perez, C.; Gil, C.; Simon, D.; Wandosell, F.; Moreno, F. J.; Gelpi, J. L.; Luque, F. J.; Martinez, A. Thienylhalomethylketones: Irreversible glycogen synthase kinase 3 inhibitors as useful pharmacological tools. *Bioorg Med Chem* **2009**, *17*, 6914-25.
163. Conde, S.; Pérez, D. I.; Martínez, A.; Perez, C.; Moreno, F. J. Thienyl and Phenyl  $\alpha$ -Halomethyl Ketones: New Inhibitors of Glycogen Synthase Kinase (GSK-3 $\beta$ ) from a Library of Compound Searching. *Journal of Medicinal Chemistry* **2003**, *46*, 4631-4633.
164. Eldar-Finkelman, H.; Licht-Murava, A.; Pietrokovski, S.; Eisenstein, M. Substrate competitive GSK-3 inhibitors - strategy and implications. *Biochim Biophys Acta* **2010**, *1804*, 598-603.
165. Eldar-Finkelman, H.; Eisenstein, M. Peptide inhibitors targeting protein kinases. *Curr Pharm Des* **2009**, *15*, 2463-70.
166. Palomo, V.; Perez, D. I.; Perez, C.; Morales-Garcia, J. A.; Soteras, I.; Alonso-Gil, S.; Encinas, A.; Castro, A.; Campillo, N. E.; Perez-Castillo, A.; Gil, C.; Martinez, A. 5-Imino-1,2,4-Thiadiazoles: First Small Molecules As Substrate Competitive Inhibitors of Glycogen Synthase Kinase 3. *Journal of Medicinal Chemistry* **2012**, *55*, 1645-1661.
167. Hamann, M.; Alonso, D.; Martín-Aparicio, E.; Fuertes, A.; Pérez-Puerto, M. J.; Castro, A.; Morales, S.; Navarro, M. L.; del Monte-Millán, M.; Medina, M.; Pennaka, H.; Balaiah, A.; Peng, J.; Cook, J.; Wahyuono, S.; Martínez, A. Glycogen Synthase Kinase-3 (GSK-3) Inhibitory Activity and Structure–Activity Relationship (SAR) Studies of the Manzamine Alkaloids. Potential for Alzheimer’s Disease. *Journal of Natural Products* **2007**, *70*, 1397-1405.
168. Palomo, V.; Soteras, I.; Perez, D. I.; Perez, C.; Gil, C.; Campillo, N. E.; Martinez, A. Exploring the Binding Sites of Glycogen Synthase Kinase 3. Identification and Characterization of Allosteric Modulation Cavities. *Journal of Medicinal Chemistry* **2011**, *54*, 8461-8470.
169. Bidon-Chanal, A.; Fuertes, A.; Alonso, D.; Perez, D. I.; Martinez, A.; Luque, F. J.; Medina, M. Evidence for a new binding mode to GSK-3: allosteric regulation by the marine compound palinurin. *Eur J Med Chem* **2013**, *60*, 479-89.
170. Mandelkow, E. M.; Mandelkow, E. Biochemistry and cell biology of tau protein in neurofibrillary degeneration. *Cold Spring Harb Perspect Med* **2012**, *2*, a006247.
171. Goedert, M.; Spillantini, M. G.; Jakes, R.; Rutherford, D.; Crowther, R. A. Multiple isoforms of human microtubule-associated protein tau: sequences and localization in neurofibrillary tangles of Alzheimer's disease. *Neuron* **1989**, *3*, 519-26.
172. Goedert, M.; Spillantini, M. G. Propagation of Tau aggregates. *Molecular Brain* **2017**, *10*, 18.
173. Schweers, O.; Schonbrunn-Hanebeck, E.; Marx, A.; Mandelkow, E. Structural studies of tau protein and Alzheimer paired helical filaments show no evidence for beta-structure. *J Biol Chem* **1994**, *269*, 24290-7.
174. Mukrasch, M. D.; Bibow, S.; Korukottu, J.; Jeganathan, S.; Biernat, J.; Griesinger, C.; Mandelkow, E.; Zweckstetter, M. Structural polymorphism of 441-residue tau at single residue resolution. *PLoS Biol* **2009**, *7*, e34.
175. Morris, M.; Knudsen, G. M.; Maeda, S.; Trinidad, J. C.; Ioanoviciu, A.; Burlingame, A. L.; Mucke, L. Tau post-translational modifications in wild-type and human amyloid precursor protein transgenic mice. *Nature Neuroscience* **2015**, *18*, 1183.
176. Guo, T.; Noble, W.; Hanger, D. P. Roles of tau protein in health and disease. *Acta Neuropathologica* **2017**, *133*, 665-704.

177. Rodriguez-Martin, T.; Cuchillo-Ibanez, I.; Noble, W.; Nyenya, F.; Anderton, B. H.; Hanger, D. P. Tau phosphorylation affects its axonal transport and degradation. *Neurobiol Aging* **2013**, *34*, 2146-57.
178. Kopke, E.; Tung, Y. C.; Shaikh, S.; Alonso, A. C.; Iqbal, K.; Grundke-Iqbal, I. Microtubule-associated protein tau. Abnormal phosphorylation of a non-paired helical filament pool in Alzheimer disease. *J Biol Chem* **1993**, *268*, 24374-84.
179. Alonso Adel, C.; Mederlyova, A.; Novak, M.; Grundke-Iqbal, I.; Iqbal, K. Promotion of hyperphosphorylation by frontotemporal dementia tau mutations. *J Biol Chem* **2004**, *279*, 34873-81.
180. Kolarova, M.; Garc; #xed; a-Sierra, F.; Bartos, A.; Ricny, J.; Ripova, D. Structure and Pathology of Tau Protein in Alzheimer Disease. *International Journal of Alzheimer&#x2019;s Disease* **2012**, *2012*, 13.
181. Ludolph, A. C.; Kassubek, J.; Landwehrmeyer, B. G.; Mandelkow, E.; Mandelkow, E. M.; Burn, D. J.; Caparros-Lefebvre, D.; Frey, K. A.; de Yebenes, J. G.; Gasser, T.; Heutink, P.; Höglinger, G.; Jamrozik, Z.; Jellinger, K. A.; Kazantsev, A.; Kretschmar, H.; Lang, A. E.; Litvan, I.; Lucas, J. J.; McGeer, P. L.; Melquist, S.; Oertel, W.; Otto, M.; Paviour, D.; Reum, T.; Saint-Raymond, A.; Steele, J. C.; Tolnay, M.; Tumani, H.; van Swieten, J. C.; Vanier, M. T.; Vonsattel, J. P.; Wagner, S.; Wszolek, Z. K.; for the Reisensburg Working Group for Tauopathies With, P. Tauopathies with parkinsonism: clinical spectrum, neuropathologic basis, biological markers, and treatment options. *European journal of neurology : the official journal of the European Federation of Neurological Societies* **2009**, *16*, 297-309.
182. Martin, L.; Latypova, X.; Terro, F. Post-translational modifications of tau protein: implications for Alzheimer's disease. *Neurochem Int* **2011**, *58*, 458-71.
183. Alonso, A. C.; Zaidi, T.; Grundke-Iqbal, I.; Iqbal, K. Role of abnormally phosphorylated tau in the breakdown of microtubules in Alzheimer disease. *Proceedings of the National Academy of Sciences of the United States of America* **1994**, *91*, 5562-5566.
184. Alonso, A. d. C.; Grundke-Iqbal, I.; Barra, H. S.; Iqbal, K. Abnormal phosphorylation of tau and the mechanism of Alzheimer neurofibrillary degeneration: Sequestration of microtubule-associated proteins 1 and 2 and the disassembly of microtubules by the abnormal tau. *Proceedings of the National Academy of Sciences of the United States of America* **1997**, *94*, 298-303.
185. Li, B.; Chohan, M. O.; Grundke-Iqbal, I.; Iqbal, K. Disruption of microtubule network by Alzheimer abnormally hyperphosphorylated tau. *Acta Neuropathologica* **2007**, *113*, 501-511.
186. Berriman, J.; Serpell, L. C.; Oberg, K. A.; Fink, A. L.; Goedert, M.; Crowther, R. A. Tau filaments from human brain and from *in vitro* assembly of recombinant protein show cross- $\beta$  structure. *Proceedings of the National Academy of Sciences* **2003**, *100*, 9034-9038.
187. Ballatore, C.; Lee, V. M.; Trojanowski, J. Q. Tau-mediated neurodegeneration in Alzheimer's disease and related disorders. *Nat Rev Neurosci* **2007**, *8*, 663-72.
188. Spillantini, M. G.; Goedert, M. Tau pathology and neurodegeneration. *Lancet Neurol* **2013**, *12*, 609-22.
189. Maeda, S.; Sahara, N.; Saito, Y.; Murayama, S.; Ikai, A.; Takashima, A. Increased levels of granular tau oligomers: an early sign of brain aging and Alzheimer's disease. *Neurosci Res* **2006**, *54*, 197-201.



190. Patterson, K. R.; Remmers, C.; Fu, Y.; Brooker, S.; Kanaan, N. M.; Vana, L.; Ward, S.; Reyes, J. F.; Philibert, K.; Glucksman, M. J.; Binder, L. I. Characterization of Prefibrillar Tau Oligomers in Vitro and in Alzheimer Disease. *Journal of Biological Chemistry* **2011**, *286*, 23063-23076.
191. Lasagna-Reeves, C. A.; Castillo-Carranza, D. L.; Sengupta, U.; Sarmiento, J.; Troncoso, J.; Jackson, G. R.; Kaye, R. Identification of oligomers at early stages of tau aggregation in Alzheimer's disease. *FASEB J* **2012**, *26*, 1946-59.
192. Lasagna-Reeves, C. A.; Castillo-Carranza, D. L.; Sengupta, U.; Clos, A. L.; Jackson, G. R.; Kaye, R. Tau oligomers impair memory and induce synaptic and mitochondrial dysfunction in wild-type mice. *Mol Neurodegener* **2011**, *6*, 39.
193. Chirita, C. N.; Congdon, E. E.; Yin, H.; Kuret, J. Triggers of Full-Length Tau Aggregation: A Role for Partially Folded Intermediates. *Biochemistry* **2005**, *44*, 5862-5872.
194. Sahara, N.; Maeda, S.; Murayama, M.; Suzuki, T.; Dohmae, N.; Yen, S. H.; Takashima, A. Assembly of two distinct dimers and higher-order oligomers from full-length tau. *Eur J Neurosci* **2007**, *25*, 3020-9.
195. Ballatore, C.; Brunden, K. R.; Hurn, D. M.; Trojanowski, J. Q.; Lee, V. M. Y.; Smith, A. B. Microtubule Stabilizing Agents as Potential Treatment for Alzheimer's Disease and Related Neurodegenerative Tauopathies. *Journal of medicinal chemistry* **2012**, *55*, 8979-8996.
196. Bulic, B.; Pickhardt, M.; Mandelkow, E. Progress and developments in tau aggregation inhibitors for Alzheimer disease. *J Med Chem* **2013**, *56*, 4135-55.
197. Palomo, V.; Martinez, A. Glycogen synthase kinase 3 (GSK-3) inhibitors: a patent update (2014-2015). *Expert Opin Ther Pat* **2017**, *27*, 657-666.
198. Bulic, B.; Pickhardt, M.; Mandelkow, E. M.; Mandelkow, E. Tau protein and tau aggregation inhibitors. *Neuropharmacology* **2010**, *59*, 276-89.
199. Wischik, C. M.; Edwards, P. C.; Lai, R. Y.; Roth, M.; Harrington, C. R. Selective inhibition of Alzheimer disease-like tau aggregation by phenothiazines. *Proc Natl Acad Sci U S A* **1996**, *93*, 11213-8.
200. Schirmer, R. H.; Adler, H.; Pickhardt, M.; Mandelkow, E. "Lest we forget you--methylene blue...". *Neurobiol Aging* **2011**, *32*, 2325.e7-16.
201. Wischik, C. M.; Staff, R. T.; Wischik, D. J.; Bentham, P.; Murray, A. D.; Storey, J. M.; Kook, K. A.; Harrington, C. R. Tau aggregation inhibitor therapy: an exploratory phase 2 study in mild or moderate Alzheimer's disease. *J Alzheimers Dis* **2015**, *44*, 705-20.
202. Open-Label Study of TRx0237 in Subjects With Alzheimer's Disease or Behavioral Variant Frontotemporal Dementia (bvFTD).  
<https://clinicaltrials.gov/ct2/show/study/NCT02245568>
203. Wilcock, G. K.; Gauthier, S.; Frisoni, G. B.; Jia, J.; Hardlund, J. H.; Moebius, H. J.; Bentham, P.; Kook, K. A.; Schelter, B. O.; Wischik, D. J.; Davis, C. S.; Staff, R. T.; Vuksanovic, V.; Ahearn, T.; Bracoud, L.; Shamsi, K.; Marek, K.; Seibyl, J.; Riedel, G.; Storey, J. M. D.; Harrington, C. R.; Wischik, C. M. Potential of Low Dose Leuco-Methylthionium Bis(Hydromethanesulphonate) (LMTM) Monotherapy for Treatment of Mild Alzheimer's Disease: Cohort Analysis as Modified Primary Outcome in a Phase III Clinical Trial. *J Alzheimers Dis* **2018**, *61*, 435-457.
204. Nacula, M.; Chirita, C. N.; Kuret, J. Cyanine dye N744 inhibits tau fibrillization by blocking filament extension: implications for the treatment of tauopathic neurodegenerative diseases. *Biochemistry* **2005**, *44*, 10227-37.

205. Congdon, E. E.; Figueroa, Y. H.; Wang, L.; Toneva, G.; Chang, E.; Kuret, J.; Conrad, C.; Duff, K. E. Inhibition of Tau Polymerization with a Cyanine Dye in Two Distinct Model Systems. *Journal of Biological Chemistry* **2009**, *284*, 20830-20839.
206. Taniguchi, S.; Suzuki, N.; Masuda, M.; Hisanaga, S.; Iwatsubo, T.; Goedert, M.; Hasegawa, M. Inhibition of heparin-induced tau filament formation by phenothiazines, polyphenols, and porphyrins. *J Biol Chem* **2005**, *280*, 7614-23.
207. Pickhardt, M.; Gazova, Z.; von Bergen, M.; Khlistunova, I.; Wang, Y.; Hascher, A.; Mandelkow, E. M.; Biernat, J.; Mandelkow, E. Anthraquinones inhibit tau aggregation and dissolve Alzheimer's paired helical filaments in vitro and in cells. *J Biol Chem* **2005**, *280*, 3628-35.
208. Khlistunova, I.; Biernat, J.; Wang, Y.; Pickhardt, M.; von Bergen, M.; Gazova, Z.; Mandelkow, E.; Mandelkow, E.-M. Inducible Expression of Tau Repeat Domain in Cell Models of Tauopathy: AGGREGATION IS TOXIC TO CELLS BUT CAN BE REVERSED BY INHIBITOR DRUGS. *Journal of Biological Chemistry* **2006**, *281*, 1205-1214.
209. Pickhardt, M.; Larbig, G.; Khlistunova, I.; Coksezen, A.; Meyer, B.; Mandelkow, E.-M.; Schmidt, B.; Mandelkow, E. Phenylthiazolyl-Hydrazide and Its Derivatives Are Potent Inhibitors of  $\tau$  Aggregation and Toxicity in Vitro and in Cells. *Biochemistry* **2007**, *46*, 10016-10023.
210. Bulic, B.; Pickhardt, M.; Khlistunova, I.; Biernat, J.; Mandelkow, E.-M.; Mandelkow, E.; Waldmann, H. Rhodanine-Based Tau Aggregation Inhibitors in Cell Models of Tauopathy. *Angewandte Chemie International Edition* **2007**, *46*, 9215-9219.
211. Messing, L.; Decker, J. M.; Joseph, M.; Mandelkow, E.; Mandelkow, E. M. Cascade of tau toxicity in inducible hippocampal brain slices and prevention by aggregation inhibitors. *Neurobiol Aging* **2013**, *34*, 1343-1354.
212. Crowe, A.; Huang, W.; Ballatore, C.; Johnson, R. L.; Hogan, A.-M. L.; Huang, R.; Wichterman, J.; McCoy, J.; Hury, D.; Auld, D. S.; Smith, A. B.; Inglese, J.; Trojanowski, J. Q.; Austin, C. P.; Brunden, K. R.; Lee, V. M. Y. The Identification of Aminothienopyridazine Inhibitors of Tau Assembly by Quantitative High-Throughput Screening. *Biochemistry* **2009**, *48*, 7732-7745.
213. Ballatore, C.; Brunden, K. R.; Piscitelli, F.; James, M. J.; Crowe, A.; Yao, Y.; Hyde, E.; Trojanowski, J. Q.; Lee, V. M. Y.; Smith, A. B. Discovery of Brain-Penetrant, Orally Bioavailable Aminothienopyridazine Inhibitors of Tau Aggregation. *Journal of Medicinal Chemistry* **2010**, *53*, 3739-3747.
214. Ballatore, C.; Crowe, A.; Piscitelli, F.; James, M.; Lou, K.; Rossidivito, G.; Yao, Y.; Trojanowski, J. Q.; Lee, V. M. Y.; Brunden, K. R.; Smith, A. B. Aminothienopyridazine inhibitors of tau aggregation: Evaluation of structure-activity relationship leads to selection of candidates with desirable in vivo properties. *Bioorganic & medicinal chemistry* **2012**, *20*, 4451-4461.
215. Crowe, A.; James, M. J.; Lee, V. M.; Smith, A. B., 3rd; Trojanowski, J. Q.; Ballatore, C.; Brunden, K. R. Aminothienopyridazines and methylene blue affect Tau fibrillization via cysteine oxidation. *J Biol Chem* **2013**, *288*, 11024-37.
216. Fatouros, C.; Pir, G. J.; Biernat, J.; Koushika, S. P.; Mandelkow, E.; Mandelkow, E. M.; Schmidt, E.; Baumeister, R. Inhibition of tau aggregation in a novel *Caenorhabditis elegans* model of tauopathy mitigates proteotoxicity. *Hum Mol Genet* **2012**, *21*, 3587-603.
217. Kiss, R.; Csizmadia, G.; Solti, K.; Keresztes, A.; Zhu, M.; Pickhardt, M.; Mandelkow, E.; Toth, G. Structural Basis of Small Molecule Targetability of Monomeric Tau Protein. *ACS Chem Neurosci* **2018**.

218. de los Ríos, C.; Egea, J.; Marco-Contelles, J.; León, R.; Samadi, A.; Iriepa, I.; Moraleda, I.; Gálvez, E.; García, A. G.; López, M. G.; Villarroja, M.; Romero, A. Synthesis, Inhibitory Activity of Cholinesterases, and Neuroprotective Profile of Novel 1,8-Naphthyridine Derivatives. *Journal of Medicinal Chemistry* **2010**, *53*, 5129-5143.
219. Lorrio, S.; Romero, A.; Gonzalez-Lafuente, L.; Lajarin-Cuesta, R.; Martinez-Sanz, F. J.; Estrada, M.; Samadi, A.; Marco-Contelles, J.; Rodriguez-Franco, M. I.; Villarroja, M.; Lopez, M. G.; de los Rios, C. PP2A ligand ITH12246 protects against memory impairment and focal cerebral ischemia in mice. *ACS Chem Neurosci* **2013**, *4*, 1267-77.
220. Pérez-Areales, F. J.; Di Pietro, O.; Espargaró, A.; Vallverdú-Queralt, A.; Galdeano, C.; Ragusa, I. M.; Viayna, E.; Guillou, C.; Clos, M. V.; Pérez, B.; Sabaté, R.; Lamuela-Raventós, R. M.; Luque, F. J.; Muñoz-Torrero, D. Shogaol–huprine hybrids: Dual antioxidant and anticholinesterase agents with  $\beta$ -amyloid and tau anti-aggregating properties. *Bioorganic & Medicinal Chemistry* **2014**, *22*, 5298-5307.
221. Mariano, M.; Schmitt, C.; Miralinaghi, P.; Catto, M.; Hartmann, R. W.; Carotti, A.; Engel, M. First selective dual inhibitors of tau phosphorylation and Beta-amyloid aggregation, two major pathogenic mechanisms in Alzheimer's disease. *ACS Chem Neurosci* **2014**, *5*, 1198-202.
222. Fuse, S.; Matsumura, K.; Fujita, Y.; Sugimoto, H.; Takahashi, T. Development of dual targeting inhibitors against aggregations of amyloid- $\beta$  and tau protein. *European Journal of Medicinal Chemistry* **2014**, *85*, 228-234.
223. Prati, F.; De Simone, A.; Bisignano, P.; Armirotti, A.; Summa, M.; Pizzirani, D.; Scarpelli, R.; Perez, D. I.; Andrisano, V.; Perez-Castillo, A.; Monti, B.; Massenzio, F.; Polito, L.; Racchi, M.; Favia, A. D.; Bottegoni, G.; Martinez, A.; Bolognesi, M. L.; Cavalli, A. Multitarget drug discovery for Alzheimer's disease: triazinones as BACE-1 and GSK-3beta inhibitors. *Angew Chem Int Ed Engl* **2015**, *54*, 1578-82.
224. Okuda, M.; Hijikuro, I.; Fujita, Y.; Teruya, T.; Kawakami, H.; Takahashi, T.; Sugimoto, H. Design and synthesis of curcumin derivatives as tau and amyloid  $\beta$  dual aggregation inhibitors. *Bioorganic & Medicinal Chemistry Letters* **2016**, *26*, 5024-5028.
225. Lajarín-Cuesta, R.; Nanclares, C.; Arranz-Tagarro, J.-A.; González-Lafuente, L.; Arribas, R. L.; Araujo de Brito, M.; Gandía, L.; de los Ríos, C. Gramine Derivatives Targeting Ca<sup>2+</sup> Channels and Ser/Thr Phosphatases: A New Dual Strategy for the Treatment of Neurodegenerative Diseases. *Journal of Medicinal Chemistry* **2016**, *59*, 6265-6280.
226. Di Martino, R. M.; De Simone, A.; Andrisano, V.; Bisignano, P.; Bisi, A.; Gobbi, S.; Rampa, A.; Fato, R.; Bergamini, C.; Perez, D. I.; Martinez, A.; Bottegoni, G.; Cavalli, A.; Belluti, F. Versatility of the Curcumin Scaffold: Discovery of Potent and Balanced Dual BACE-1 and GSK-3beta Inhibitors. *J Med Chem* **2016**, *59*, 531-44.
227. Cornec, A. S.; Monti, L.; Kovalevich, J.; Makani, V.; James, M. J.; Vijayendran, K. G.; Oukoloff, K.; Yao, Y.; Lee, V. M.; Trojanowski, J. Q.; Smith, A. B., 3rd; Brunden, K. R.; Ballatore, C. Multitargeted Imidazoles: Potential Therapeutic Leads for Alzheimer's and Other Neurodegenerative Diseases. *J Med Chem* **2017**, *60*, 5120-5145.
228. Panek, D.; Wieckowska, A.; Jonczyk, J.; Godyn, J.; Bajda, M.; Wichur, T.; Pasięka, A.; Knez, D.; Pislár, A.; Korabecny, J.; Soukup, O.; Sepsova, V.; Sabate, R.; Kos, J.; Gobec, S.; Malawska, B. Design, Synthesis, and Biological Evaluation of 1-Benzylamino-2-hydroxyalkyl Derivatives as New Potential Disease-Modifying Multifunctional Anti-Alzheimer's Agents. *ACS Chem Neurosci* **2018**.

229. Duran-Frigola, M.; Siragusa, L.; Ruppin, E.; Barril, X.; Cruciani, G.; Aloy, P. Detecting similar binding pockets to enable systems polypharmacology. *PLoS Computational Biology* **2017**, *13*, e1005522.
230. Prati, F.; Cavalli, A.; Bolognesi, M. L. Navigating the Chemical Space of Multitarget-Directed Ligands: From Hybrids to Fragments in Alzheimer's Disease. *Molecules* **2016**, *21*, 466.
231. Ono, M.; Hayashi, S.; Matsumura, K.; Kimura, H.; Okamoto, Y.; Ihara, M.; Takahashi, R.; Mori, H.; Saji, H. Rhodanine and thiohydantoin derivatives for detecting tau pathology in Alzheimer's brains. *ACS Chem Neurosci* **2011**, *2*, 269-75.
232. Mendgen, T.; Steuer, C.; Klein, C. D. Privileged scaffolds or promiscuous binders: a comparative study on rhodanines and related heterocycles in medicinal chemistry. *J Med Chem* **2012**, *55*, 743-53.
233. Baell, J. B. Observations on screening-based research and some concerning trends in the literature. *Future Med Chem* **2010**, *2*, 1529-46.
234. Baell, J. B.; Ferrins, L.; Falk, H.; Nikolakopoulos, G. PAINS: Relevance to Tool Compound Discovery and Fragment-Based Screening. *Australian Journal of Chemistry* **2013**, *66*, 1483-1494.
235. Pouliot, M.; Jeanmart, S. Pan Assay Interference Compounds (PAINS) and Other Promiscuous Compounds in Antifungal Research. *J Med Chem* **2016**, *59*, 497-503.
236. Biomarker Qualification for Risk of Mild Cognitive Impairment (MCI) Due to Alzheimer's Disease (AD) and Safety and Efficacy Evaluation of Pioglitazone in Delaying Its Onset (TOMORROW).  
<https://www.clinicaltrials.gov/ct2/show/NCT01931566?term=pioglitazone%2C+alzheim&rank=1>
237. Cisek, K.; Cooper, G. L.; Huseby, C. J.; Kuret, J. Structure and mechanism of action of tau aggregation inhibitors. *Current Alzheimer research* **2014**, *11*, 918-927.
238. Reinke, A. A.; Gestwicki, J. E. Insight into amyloid structure using chemical probes. *Chem Biol Drug Des* **2011**, *77*, 399-411.
239. Bhat, B. A.; Ponnala, S.; Sahu, D. P.; Tiwari, P.; Tripathi, B. K.; Srivastava, A. K. Synthesis and antihyperglycemic activity profiles of novel thiazolidinedione derivatives. *Bioorg Med Chem* **2004**, *12*, 5857-64.
240. Zhang, Y.; Zhou, Z. A Solvent-Free Protocol for the Green Synthesis of 5-Arylidene-2,4-thiazolidinediones Using Ethylenediamine Diacetate as Catalyst. *Organic Chemistry International* **2012**, *2012*, 5.
241. Mao, F.; Huang, L.; Luo, Z.; Liu, A.; Lu, C.; Xie, Z.; Li, X. O-Hydroxyl- or o-amino benzylamine-tacrine hybrids: multifunctional biometals chelators, antioxidants, and inhibitors of cholinesterase activity and amyloid-beta aggregation. *Bioorg Med Chem* **2012**, *20*, 5884-92.
242. Qabaja, G.; Jones, G. B. Annulation Strategies for Benzo[b]fluorene Synthesis: Efficient Routes to the Kinafluorenone and WS-5995 Antibiotics. *The Journal of Organic Chemistry* **2000**, *65*, 7187-7194.
243. Perez, D. I.; Palomo, V.; Perez, C.; Gil, C.; Dans, P. D.; Luque, F. J.; Conde, S.; Martinez, A. Switching reversibility to irreversibility in glycogen synthase kinase 3 inhibitors: clues for specific design of new compounds. *J Med Chem* **2011**, *54*, 4042-56.
244. Copeland, R. A. Drug-target residence time. In *Evaluation of Enzyme Inhibitors in Drug Discovery*, 2nd ed.; Wiley, Hoboken: 2013; pp 318-325.
245. Pande, V.; Ramos, M. J. Structural basis for the GSK-3 $\beta$  binding affinity and selectivity against CDK-2 of 1-(4-aminofurazan-3-yl)-5-dialkylaminomethyl-1H-[1,2,3]

- triazole-4-carboxylic acid derivatives. *Bioorganic & Medicinal Chemistry Letters* **2005**, 15, 5129-5135.
246. Feng, L.; Geisselbrecht, Y.; Blanck, S.; Wilbuer, A.; Atilla-Gokcumen, G. E.; Filippakopoulos, P.; Kräling, K.; Celik, M. A.; Harms, K.; Maksimoska, J.; Marmorstein, R.; Frenking, G.; Knapp, S.; Essen, L.-O.; Meggers, E. Structurally Sophisticated Octahedral Metal Complexes as Highly Selective Protein Kinase Inhibitors. *Journal of the American Chemical Society* **2011**, 133, 5976-5986.
247. Fu, G.; Sivaprakasam, P.; Dale, O. R.; Manly, S. P.; Cutler, S. J.; Doerksen, R. J. Pharmacophore Modeling, Ensemble Docking, Virtual Screening, and Biological Evaluation on Glycogen Synthase Kinase-3beta. *Mol Inform* **2014**, 33, 610-26.
248. Cardoso, F. L.; Brites, D.; Brito, M. A. Looking at the blood-brain barrier: molecular anatomy and possible investigation approaches. *Brain Res Rev* **2010**, 64, 328-63.
249. van Asperen, J.; Mayer, U.; van Tellingen, O.; Beijnen, J. H. The functional role of P-Glycoprotein in the blood–Brain barrier. *Journal of Pharmaceutical Sciences* **1997**, 86, 881-884.
250. Crivori, P.; Cruciani, G.; Carrupt, P. A.; Testa, B. Predicting blood-brain barrier permeation from three-dimensional molecular structure. *J Med Chem* **2000**, 43, 2204-16.
251. Contestabile, A. Cerebellar granule cells as a model to study mechanisms of neuronal apoptosis or survival in vivo and in vitro. *Cerebellum* **2002**, 1, 41-55.
252. Willson, T. M.; Brown, P. J.; Sternbach, D. D.; Henke, B. R. The PPARs: From Orphan Receptors to Drug Discovery. *Journal of Medicinal Chemistry* **2000**, 43, 527-550.
253. von Bergen, M.; Friedhoff, P.; Biernat, J.; Heberle, J.; Mandelkow, E.-M.; Mandelkow, E. Assembly of  $\tau$  protein into Alzheimer paired helical filaments depends on a local sequence motif (<sup>306</sup>VQIVYK<sup>311</sup>) forming  $\beta$  structure. *Proceedings of the National Academy of Sciences* **2000**, 97, 5129-5134.
254. Bulic, B.; Pickhardt, M.; Schmidt, B.; Mandelkow, E. M.; Waldmann, H.; Mandelkow, E. Development of tau aggregation inhibitors for Alzheimer's disease. *Angew Chem Int Ed Engl* **2009**, 48, 1740-52.
255. Li, W.; Sperry, J. B.; Crowe, A.; Trojanowski, J. Q.; Smith, A. B., 3rd; Lee, V. M. Inhibition of tau fibrillization by oleocanthal via reaction with the amino groups of tau. *J Neurochem* **2009**, 110, 1339-51.
256. Zheng, J.; Liu, C.; Sawaya, M. R.; Vadla, B.; Khan, S.; Woods, R. J.; Eisenberg, D.; Goux, W. J.; Nowick, J. S. Macrocyclic  $\beta$ -Sheet Peptides That Inhibit the Aggregation of a Tau-Protein-Derived Hexapeptide. *Journal of the American Chemical Society* **2011**, 133, 3144-3157.
257. Mohamed, T.; Hoang, T.; Jelokhani-Niaraki, M.; Rao, P. P. N. Tau-Derived-Hexapeptide 306VQIVYK311 Aggregation Inhibitors: Nitrocatechol Moiety as A Pharmacophore In Drug Design. *ACS Chemical Neuroscience* **2013**, 4, 1559-1570.
258. Frenkel-Pinter, M.; Tal, S.; Scherzer-Attali, R.; Abu-Hussien, M.; Alyagor, I.; Eisenbaum, T.; Gazit, E.; Segal, D. Naphthoquinone-Tryptophan Hybrid Inhibits Aggregation of the Tau-Derived Peptide PHF6 and Reduces Neurotoxicity. *J Alzheimers Dis* **2016**, 51, 165-78.
259. Lunven, L.; Bonnet, H.; Yahiaoui, S.; Yi, W.; Da Costa, L.; Peuchmaur, M.; Boumendjel, A.; Chierici, S. Disruption of Fibers from the Tau Model AcPHF6 by

- Naturally Occurring Aurones and Synthetic Analogues. *ACS Chemical Neuroscience* **2016**, 7, 995-1003.
260. Wang, C. K.; Northfield, S. E.; Huang, Y. H.; Ramos, M. C.; Craik, D. J. Inhibition of tau aggregation using a naturally-occurring cyclic peptide scaffold. *Eur J Med Chem* **2016**, 109, 342-9.
261. Fitzpatrick, A. W. P.; Falcon, B.; He, S.; Murzin, A. G.; Murshudov, G.; Garringer, H. J.; Crowther, R. A.; Ghetti, B.; Goedert, M.; Scheres, S. H. W. Cryo-EM structures of tau filaments from Alzheimer's disease. *Nature* **2017**, 547, 185-190.
262. Biancalana, M.; Koide, S. Molecular mechanism of Thioflavin-T binding to amyloid fibrils. *Biochim Biophys Acta* **2010**, 1804, 1405-12.
263. Wille, H.; Drewes, G.; Biernat, J.; Mandelkow, E. M.; Mandelkow, E. Alzheimer-like paired helical filaments and antiparallel dimers formed from microtubule-associated protein tau in vitro. *The Journal of Cell Biology* **1992**, 118, 573-584.
264. Paudel, H. K.; Li, W. Heparin-induced Conformational Change in Microtubule-associated Protein Tau as Detected by Chemical Cross-linking and Phosphopeptide Mapping. *Journal of Biological Chemistry* **1999**, 274, 8029-8038.
265. Wilham, J. M.; Orrú, C. D.; Bessen, R. A.; Atarashi, R.; Sano, K.; Race, B.; Meade-White, K. D.; Taubner, L. M.; Timmes, A.; Caughey, B. Rapid End-Point Quantitation of Prion Seeding Activity with Sensitivity Comparable to Bioassays. *PLOS Pathogens* **2010**, 6, e1001217.
266. Fernandez, M. T.; Zitko, V.; Gascon, S.; Novelli, A. The marine toxin okadaic acid is a potent neurotoxin for cultured cerebellar neurons. *Life Sci* **1991**, 49, P157-62.
267. Leira, F.; Alvarez, C.; Vieites, J. M.; Vieytes, M. R.; Botana, L. M. Characterization of distinct apoptotic changes induced by okadaic acid and yessotoxin in the BE(2)-M17 neuroblastoma cell line. *Toxicol In Vitro* **2002**, 16, 23-31.
268. Wang, J.-z.; Tung, Y. C.; Wang, Y.; Li, X. T.; Iqbal, K.; Grundke-Iqbal, I. Hyperphosphorylation and accumulation of neurofilament proteins in Alzheimer disease brain and in okadaic acid-treated SY5Y cells. *FEBS Letters* **2001**, 507, 81-87.
269. Zhang, Z.; Simpkins, J. W. An okadaic acid-induced model of tauopathy and cognitive deficiency. *Brain Res* **2010**, 1359, 233-46.
270. Chen, Z.; Chen, B.; Xu, W. F.; Liu, R. F.; Yang, J.; Yu, C. X. Effects of PTEN inhibition on regulation of tau phosphorylation in an okadaic acid-induced neurodegeneration model. *Int J Dev Neurosci* **2012**, 30, 411-9.
271. Swords, R.; Mahalingam, D.; O'Dwyer, M.; Santocanale, C.; Kelly, K.; Carew, J.; Giles, F. Cdc7 kinase - a new target for drug development. *Eur J Cancer* **2010**, 46, 33-40.
272. Singh, T. J.; Grundke-Iqbal, I.; Iqbal, K. Phosphorylation of tau protein by casein kinase-1 converts it to an abnormal Alzheimer-like state. *J Neurochem* **1995**, 64, 1420-3.
273. Sabbagh, M. N.; Lue, L. F.; Fayard, D.; Shi, J. Increasing Precision of Clinical Diagnosis of Alzheimer's Disease Using a Combined Algorithm Incorporating Clinical and Novel Biomarker Data. *Neurol Ther* **2017**, 6, 83-95.
274. Drug Development Tools Glossary.  
<https://www.fda.gov/Drugs/DevelopmentApprovalProcess/DrugDevelopmentToolsQualificationProgram/ucm284395.htm>
275. Pike, K. E.; Savage, G.; Villemagne, V. L.; Ng, S.; Moss, S. A.; Maruff, P.; Mathis, C. A.; Klunk, W. E.; Masters, C. L.; Rowe, C. C. Beta-amyloid imaging and memory in non-demented individuals: evidence for preclinical Alzheimer's disease. *Brain* **2007**, 130, 2837-44.

276. Moyer, B. R.; Barrett, J. A. Biomarkers and imaging: physics and chemistry for noninvasive analyses. *Bioanalysis* **2009**, *1*, 321-56.
277. Sperling, R. A.; Aisen, P. S.; Beckett, L. A.; Bennett, D. A.; Craft, S.; Fagan, A. M.; Iwatsubo, T.; Jack, C. R., Jr.; Kaye, J.; Montine, T. J.; Park, D. C.; Reiman, E. M.; Rowe, C. C.; Siemers, E.; Stern, Y.; Yaffe, K.; Carrillo, M. C.; Thies, B.; Morrison-Bogorad, M.; Wagster, M. V.; Phelps, C. H. Toward defining the preclinical stages of Alzheimer's disease: recommendations from the National Institute on Aging-Alzheimer's Association workgroups on diagnostic guidelines for Alzheimer's disease. *Alzheimers Dement* **2011**, *7*, 280-92.
278. Jack, C. R., Jr.; Knopman, D. S.; Jagust, W. J.; Petersen, R. C.; Weiner, M. W.; Aisen, P. S.; Shaw, L. M.; Vemuri, P.; Wiste, H. J.; Weigand, S. D.; Lesnick, T. G.; Pankratz, V. S.; Donohue, M. C.; Trojanowski, J. Q. Tracking pathophysiological processes in Alzheimer's disease: an updated hypothetical model of dynamic biomarkers. *Lancet Neurol* **2013**, *12*, 207-16.
279. Zhang, L.; Villalobos, A. Chapter Eight - Recent Advances in the Development of PET and SPECT Tracers for Brain Imaging. In *Annual Reports in Medicinal Chemistry*, Desai, M. C., Ed. Academic Press: 2012; Vol. 47, pp 105-119.
280. Piel, M.; Vernaleken, I.; Rösch, F. Positron Emission Tomography in CNS Drug Discovery and Drug Monitoring. *Journal of Medicinal Chemistry* **2014**, *57*, 9232-9258.
281. Mier, W.; Mier, D. Advantages in functional imaging of the brain. *Front Hum Neurosci* **2015**, *9*, 249.
282. Sabri, O.; Seibyl, J.; Rowe, C.; Barthel, H. Beta-amyloid imaging with florbetaben. *Clin Transl Imaging* **2015**, *3*, 13-26.
283. Yang, L.; Rieves, D.; Ganley, C. Brain amyloid imaging--FDA approval of florbetapir F18 injection. *N Engl J Med* **2012**, *367*, 885-7.
284. Hatashita, S.; Yamasaki, H.; Suzuki, Y.; Tanaka, K.; Wakebe, D.; Hayakawa, H. [18F]Flutemetamol amyloid-beta PET imaging compared with [11C]PIB across the spectrum of Alzheimer's disease. *Eur J Nucl Med Mol Imaging* **2014**, *41*, 290-300.
285. Nordberg, A. The use of amyloid imaging in clinical praxis: a critical review. *Clinical and Translational Imaging* **2015**, *3*, 7-11.
286. Patterson, A. P.; Booth, S. A.; Saba, R. The Emerging Use of In Vivo Optical Imaging in the Study of Neurodegenerative Diseases. *BioMed Research International* **2014**, 2014, 14.
287. Weissleder, R.; Nahrendorf, M. Advancing biomedical imaging. *Proceedings of the National Academy of Sciences* **2015**, *112*, 14424-14428.
288. Raymond, S. B.; Kumar, A. T.; Boas, D. A.; Bacskai, B. J. Optimal parameters for near infrared fluorescence imaging of amyloid plaques in Alzheimer's disease mouse models. *Phys Med Biol* **2009**, *54*, 6201-16.
289. Khurana, R.; Coleman, C.; Ionescu-Zanetti, C.; Carter, S. A.; Krishna, V.; Grover, R. K.; Roy, R.; Singh, S. Mechanism of thioflavin T binding to amyloid fibrils. *J Struct Biol* **2005**, *151*, 229-38.
290. Howie, A. J.; Brewer, D. B. Optical properties of amyloid stained by Congo red: history and mechanisms. *Micron* **2009**, *40*, 285-301.
291. Bacskai, B. J.; Kajdasz, S. T.; Christie, R. H.; Carter, C.; Games, D.; Seubert, P.; Schenk, D.; Hyman, B. T. Imaging of amyloid- $\beta$  deposits in brains of living mice permits direct observation of clearance of plaques with immunotherapy. *Nature Medicine* **2001**, *7*, 369.

292. Hintersteiner, M.; Enz, A.; Frey, P.; Jatton, A. L.; Kinzy, W.; Kneuer, R.; Neumann, U.; Rudin, M.; Staufenbiel, M.; Stoeckli, M.; Wiederhold, K. H.; Gremlich, H. U. In vivo detection of amyloid-beta deposits by near-infrared imaging using an oxazine-derivative probe. *Nat Biotechnol* **2005**, *23*, 577-83.
293. Nesterov, E. E.; Skoch, J.; Hyman, B. T.; Klunk, W. E.; Bacskai, B. J.; Swager, T. M. In vivo optical imaging of amyloid aggregates in brain: design of fluorescent markers. *Angew Chem Int Ed Engl* **2005**, *44*, 5452-6.
294. Ran, C.; Xu, X.; Raymond, S. B.; Ferrara, B. J.; Neal, K.; Bacskai, B. J.; Medarova, Z.; Moore, A. Design, Synthesis, and Testing of Difluoroboron-Derivatized Curcumins as Near-Infrared Probes for in Vivo Detection of Amyloid- $\beta$  Deposits. *Journal of the American Chemical Society* **2009**, *131*, 15257-15261.
295. Zhang, X.; Tian, Y.; Li, Z.; Tian, X.; Sun, H.; Liu, H.; Moore, A.; Ran, C. Design and Synthesis of Curcumin Analogues for in Vivo Fluorescence Imaging and Inhibiting Copper-Induced Cross-Linking of Amyloid Beta Species in Alzheimer's Disease. *Journal of the American Chemical Society* **2013**, *135*, 16397-16409.
296. Okamura, N.; Mori, M.; Furumoto, S.; Yoshikawa, T.; Harada, R.; Ito, S.; Fujikawa, Y.; Arai, H.; Yanai, K.; Kudo, Y. In vivo detection of amyloid plaques in the mouse brain using the near-infrared fluorescence probe THK-265. *J Alzheimers Dis* **2011**, *23*, 37-48.
297. Schmidt, A.; Pahnke, J. Efficient near-infrared in vivo imaging of amyloid-beta deposits in Alzheimer's disease mouse models. *J Alzheimers Dis* **2012**, *30*, 651-64.
298. Cui, M.; Ono, M.; Watanabe, H.; Kimura, H.; Liu, B.; Saji, H. Smart Near-Infrared Fluorescence Probes with Donor-Acceptor Structure for in Vivo Detection of  $\beta$ -Amyloid Deposits. *Journal of the American Chemical Society* **2014**, *136*, 3388-3394.
299. Fu, H.; Cui, M.; Tu, P.; Pan, Z.; Liu, B. Evaluation of molecules based on the electron donor-acceptor architecture as near-infrared  $\beta$ -amyloid-targeting probes. *Chemical Communications* **2014**, *50*, 11875-11878.
300. Fu, H.; Cui, M.; Zhao, L.; Tu, P.; Zhou, K.; Dai, J.; Liu, B. Highly Sensitive Near-Infrared Fluorophores for in Vivo Detection of Amyloid- $\beta$  Plaques in Alzheimer's Disease. *Journal of Medicinal Chemistry* **2015**, *58*, 6972-6983.
301. Zhou, K.; Fu, H.; Feng, L.; Cui, M.; Dai, J.; Liu, B. The synthesis and evaluation of near-infrared probes with barbituric acid acceptors for in vivo detection of amyloid plaques. *Chemical Communications* **2015**, *51*, 11665-11668.
302. Kim, D.; Moon, H.; Baik, S. H.; Singha, S.; Jun, Y. W.; Wang, T.; Kim, K. H.; Park, B. S.; Jung, J.; Mook-Jung, I.; Ahn, K. H. Two-Photon Absorbing Dyes with Minimal Autofluorescence in Tissue Imaging: Application to in Vivo Imaging of Amyloid- $\beta$  Plaques with a Negligible Background Signal. *Journal of the American Chemical Society* **2015**, *137*, 6781-6789.
303. Cheng, Y.; Zhu, B.; Deng, Y.; Zhang, Z. In vivo detection of cerebral amyloid fibrils with smart dicyanomethylene-4H-pyran-based fluorescence probe. *Anal Chem* **2015**, *87*, 4781-7.
304. Garin, D.; Virgone-Carlotta, A.; Gözel, B.; Oukhatar, F.; Perret, P.; Marti-Battle, D.; Touret, M.; Millet, P.; Dubois-Dauphin, M.; Meyronet, D.; Streichenberger, N.; Laferla, F. M.; Demeunynck, M.; Chierici, S.; Sallanon, M. M.; Ghezzi, C. COB231 targets amyloid plaques in post-mortem human brain tissue and in an Alzheimer mouse model. *Journal of Neurochemistry* **2015**, *132*, 609-618.



305. Teoh, C. L.; Su, D.; Sahu, S.; Yun, S.-W.; Drummond, E.; Prelli, F.; Lim, S.; Cho, S.; Ham, S.; Wisniewski, T.; Chang, Y.-T. Chemical Fluorescent Probe for Detection of A $\beta$  Oligomers. *Journal of the American Chemical Society* **2015**, *137*, 13503-13509.
306. Maruyama, M.; Shimada, H.; Suhara, T.; Shinotoh, H.; Ji, B.; Maeda, J.; Zhang, M. R.; Trojanowski, J. Q.; Lee, V. M.; Ono, M.; Masamoto, K.; Takano, H.; Sahara, N.; Iwata, N.; Okamura, N.; Furumoto, S.; Kudo, Y.; Chang, Q.; Saido, T. C.; Takashima, A.; Lewis, J.; Jang, M. K.; Aoki, I.; Ito, H.; Higuchi, M. Imaging of tau pathology in a tauopathy mouse model and in Alzheimer patients compared to normal controls. *Neuron* **2013**, *79*, 1094-108.
307. Harada, R.; Okamura, N.; Furumoto, S.; Yoshikawa, T.; Arai, H.; Yanai, K.; Kudo, Y. Use of a benzimidazole derivative BF-188 in fluorescence multispectral imaging for selective visualization of tau protein fibrils in the Alzheimer's disease brain. *Mol Imaging Biol* **2014**, *16*, 19-27.
308. Boländer, A.; Kieser, D.; Voss, C.; Bauer, S.; Schön, C.; Burgold, S.; Bittner, T.; Hölzer, J.; Heyny-von Haußen, R.; Mall, G.; Goetschy, V.; Czech, C.; Knust, H.; Berger, R.; Herms, J.; Hilger, I.; Schmidt, B. Bis(arylvinyl)pyrazines, -pyrimidines, and -pyridazines As Imaging Agents for Tau Fibrils and  $\beta$ -Amyloid Plaques in Alzheimer's Disease Models. *Journal of Medicinal Chemistry* **2012**, *55*, 9170-9180.
309. Seo, Y.; Park, K. S.; Ha, T.; Kim, M. K.; Hwang, Y. J.; Lee, J.; Ryu, H.; Choo, H.; Chong, Y. A Smart Near-Infrared Fluorescence Probe for Selective Detection of Tau Fibrils in Alzheimer's Disease. *ACS Chem Neurosci* **2016**, *7*, 1474-1481.
310. Anumala, U. R.; Gu, J.; Lo Monte, F.; Kramer, T.; Heyny-von Haußen, R.; Hölzer, J.; Goetschy-Meyer, V.; Schön, C.; Mall, G.; Hilger, I.; Czech, C.; Herms, J.; Schmidt, B. Fluorescent rhodanine-3-acetic acids visualize neurofibrillary tangles in Alzheimer's disease brains. *Bioorganic & Medicinal Chemistry* **2013**, *21*, 5139-5144.
311. Bolognesi, M. L.; Gandini, A.; Prati, F.; Uliassi, E. From Companion Diagnostics to Theranostics: A New Avenue for Alzheimer's Disease? *J Med Chem* **2016**, *59*, 7759-70.
312. Kelkar, S. S.; Reineke, T. M. Theranostics: combining imaging and therapy. *Bioconjug Chem* **2011**, *22*, 1879-903.
313. Chen, X. S. Introducing Theranostics Journal - From the Editor-in-Chief. *Theranostics* **2011**, *1*, 1-2.
314. Kojima, R.; Aubel, D.; Fussenegger, M. Novel theranostic agents for next-generation personalized medicine: small molecules, nanoparticles, and engineered mammalian cells. *Curr Opin Chem Biol* **2015**, *28*, 29-38.
315. Prati, F. B., M. L. Tackling neurodegeneration with multi-target and theranostic small molecules. In *2015 Medicinal Chemistry Reviews*, ACS, Ed. 2015; Vol. 50, pp 347-356.
316. Cui, M. Past and recent progress of molecular imaging probes for beta-amyloid plaques in the brain. *Curr Med Chem* **2014**, *21*, 82-112.
317. Yang, W.; Wong, Y.; Ng, O. T.; Bai, L. P.; Kwong, D. W.; Ke, Y.; Jiang, Z. H.; Li, H. W.; Yung, K. K.; Wong, M. S. Inhibition of beta-amyloid peptide aggregation by multifunctional carbazole-based fluorophores. *Angew Chem Int Ed Engl* **2012**, *51*, 1804-10.
318. Staderini, M.; Aulic, S.; Bartolini, M.; Tran, H. N.; Gonzalez-Ruiz, V.; Perez, D. I.; Cabezas, N.; Martinez, A.; Martin, M. A.; Andrisano, V.; Legname, G.; Menendez, J. C.; Bolognesi, M. L. A Fluorescent Styrylquinoline with Combined Therapeutic and Diagnostic Activities against Alzheimer's and Prion Diseases. *ACS Med Chem Lett* **2013**, *4*, 225-9.

319. Li, Q.; Min, J.; Ahn, Y. H.; Namm, J.; Kim, E. M.; Lui, R.; Kim, H. Y.; Ji, Y.; Wu, H.; Wisniewski, T.; Chang, Y. T. Styryl-based compounds as potential in vivo imaging agents for beta-amyloid plaques. *Chembiochem* **2007**, *8*, 1679-87.
320. Zhang, X.; Tian, Y.; Yuan, P.; Li, Y.; Yaseen, M. A.; Grutzendler, J.; Moore, A.; Ran, C. A bifunctional curcumin analogue for two-photon imaging and inhibiting crosslinking of amyloid beta in Alzheimer's disease. *Chemical Communications* **2014**, *50*, 11550-11553.
321. Ahmed, M.; Davis, J.; Aucoin, D.; Sato, T.; Ahuja, S.; Aimoto, S.; Elliott, J. I.; Van Nostrand, W. E.; Smith, S. O. Structural conversion of neurotoxic amyloid-beta(1-42) oligomers to fibrils. *Nat Struct Mol Biol* **2010**, *17*, 561-7.
322. Tian, Y.; Zhang, X.; Li, Y.; Shoup, T. M.; Teng, X.; Elmaleh, D. R.; Moore, A.; Ran, C. Crown ethers attenuate aggregation of amyloid beta of Alzheimer's disease. *Chemical Communications* **2014**, *50*, 15792-15795.
323. Yang, T.; Wang, X.; Zhang, C.; Ma, X.; Wang, K.; Wang, Y.; Luo, J.; Yang, L.; Yao, C.; Wang, X. Specific self-monitoring of metal-associated amyloid- $\beta$  peptide disaggregation by a fluorescent chelator. *Chemical Communications* **2016**, *52*, 2245-2248.
324. Bolognin, S.; Drago, D.; Messori, L.; Zatta, P. Chelation therapy for neurodegenerative diseases. *Med Res Rev* **2009**, *29*, 547-70.
325. Dao, P.; Ye, F.; Liu, Y.; Du, Z. Y.; Zhang, K.; Dong, C. Z.; Meunier, B.; Chen, H. Development of Phenothiazine-Based Theranostic Compounds That Act Both as Inhibitors of  $\beta$ -Amyloid Aggregation and as Imaging Probes for Amyloid Plaques in Alzheimer's Disease. *ACS Chemical Neuroscience* **2017**, *8*, 798-806.
326. Dao, P.; Ye, F.; Du, Z. Y.; Chen, Q.; Zhang, K.; Dong, C. Z.; Meunier, B.; Chen, H. Design and synthesis of new theranostic agents for near-infrared imaging of  $\beta$ -amyloid plaques and inhibition of  $\beta$ -amyloid aggregation in Alzheimer's disease. *Dyes and Pigments* **2017**, *147*, 130-140.
327. Dobson, C. M. Protein folding and misfolding. *Nature* **2003**, *426*, 884-90.
328. Kranjc, A.; Bongarzone, S.; Rossetti, G.; Biarnés, X.; Cavalli, A.; Bolognesi, M. L.; Roberti, M.; Legname, G.; Carloni, P. Docking Ligands on Protein Surfaces: The Case Study of Prion Protein. *Journal of Chemical Theory and Computation* **2009**, *5*, 2565-2573.
329. Jin, L.; Wang, W.; Fang, G. Targeting protein-protein interaction by small molecules. *Annu Rev Pharmacol Toxicol* **2014**, *54*, 435-56.
330. Staderini, M.; Legname, G.; Bolognesi, M. L.; Menendez, J. C. Modulation of prion by small molecules: from monovalent to bivalent and multivalent ligands. *Curr Top Med Chem* **2013**, *13*, 2491-503.
331. Portoghese, P. S. From Models to Molecules: Opioid Receptor Dimers, Bivalent Ligands, and Selective Opioid Receptor Probes. *Journal of Medicinal Chemistry* **2001**, *44*, 2259-2269.
332. Gandini, A.; Bartolini, M.; Tedesco, D.; Martinez-Gonzalez, L.; Roca, C.; Campillo, N. E.; Zaldivar-Diez, J.; Perez, C.; Zuccheri, G.; Miti, A.; Feoli, A.; Castellano, S.; Petralla, S.; Monti, B.; Rossi, M.; Moda, F.; Legname, G.; Martinez, A.; Bolognesi, M. L. Tau-Centric Multitarget Approach for Alzheimer's Disease: Development of First-in-Class Dual Glycogen Synthase Kinase 3 $\beta$  and Tau-Aggregation Inhibitors. *Journal of Medicinal Chemistry* **2018**, *61*, 7640-7656.
333. Zhang, X.; Wang, Y.; Wang, S.-n.; Chen, Q.-h.; Tu, Y.-l.; Yang, X.-h.; Chen, J.-k.; Yan, J.-w.; Pi, R.-b.; Wang, Y. Discovery of a novel multifunctional carbazole-

- aminoquinoline dimer for Alzheimer's disease: copper selective chelation, anti-amyloid aggregation, and neuroprotection. *Medicinal Chemistry Research* **2018**, *27*, 777-784.
334. Hong, H. S.; Maezawa, I.; Budamagunta, M.; Rana, S.; Shi, A.; Vassar, R.; Liu, R.; Lam, K. S.; Cheng, R. H.; Hua, D. H.; Voss, J. C.; Jin, L. W. Candidate anti-A beta fluorene compounds selected from analogs of amyloid imaging agents. *Neurobiol Aging* **2010**, *31*, 1690-9.
335. Petrlova, J.; Kálai, T.; Maezawa, I.; Altman, R.; Harishchandra, G.; Hong, H.-S.; Bricarello, D. A.; Parikh, A. N.; Lorigan, G. A.; Jin, L.-W.; Hideg, K.; Voss, J. C. The Influence of Spin-Labeled Fluorene Compounds on the Assembly and Toxicity of the A $\beta$  Peptide. *PLOS ONE* **2012**, *7*, e35443.
336. Aslund, A.; Sigurdson, C. J.; Klingstedt, T.; Grathwohl, S.; Bolmont, T.; Dickstein, D. L.; Glimsdal, E.; Prokop, S.; Lindgren, M.; Konradsson, P.; Holtzman, D. M.; Hof, P. R.; Heppner, F. L.; Gandy, S.; Jucker, M.; Aguzzi, A.; Hammarstrom, P.; Nilsson, K. P. Novel pentameric thiophene derivatives for in vitro and in vivo optical imaging of a plethora of protein aggregates in cerebral amyloidoses. *ACS Chem Biol* **2009**, *4*, 673-84.
337. Cui, M. C.; Li, Z. J.; Tang, R. K.; Liu, B. L. Synthesis and evaluation of novel benzothiazole derivatives based on the bithiophene structure as potential radiotracers for beta-amyloid plaques in Alzheimer's disease. *Bioorg Med Chem* **2010**, *18*, 2777-84.
338. Ashok, D.; Vanaja, B. Synthesis and anticancer activity evaluation of (E)-3-[[5-(aryl)-1,3,4-oxadiazol-2-yl]methyl]-5-(3,4,5-trimethoxybenzylidene)thiazolidine-2,4-diones. *Russian Journal of General Chemistry* **2016**, *86*, 681-685.
339. Peng, K.-Y.; Chen, S.-A.; Fann, W.-S. Efficient Light Harvesting by Sequential Energy Transfer across Aggregates in Polymers of Finite Conjugational Segments with Short Aliphatic Linkages. *Journal of the American Chemical Society* **2001**, *123*, 11388-11397.
340. Angyal, S. J.; Rassack, R. C. The Sommelet Reaction. *Nature* **1948**, *161*, 723.
341. Folmer-Andersen, J. F.; Buhler, E.; Candau, S.-J.; Joulie, S.; Schmutz, M.; Lehn, J.-M. Cooperative, bottom-up generation of rigid-rod nanostructures through dynamic polymer chemistry. *Polymer International* **2010**, *59*, 1477-1491.
342. Lu, B.; Vogel, H. Drosophila models of neurodegenerative diseases. *Annu Rev Pathol* **2009**, *4*, 315-42.
343. Moloney, A.; Sattelle, D. B.; Lomas, D. A.; Crowther, D. C. Alzheimer's disease: insights from Drosophila melanogaster models. *Trends Biochem Sci* **2010**, *35*, 228-35.
344. Newman, T.; Sinadinos, C.; Johnston, A.; Sealey, M.; Mudher, A. Using Drosophila models of neurodegenerative diseases for drug discovery. *Expert Opin Drug Discov* **2011**, *6*, 129-40.
345. Pratim Bose, P.; Chatterjee, U.; Nerelius, C.; Govender, T.; Norstrom, T.; Gogoll, A.; Sandegren, A.; Gothelid, E.; Johansson, J.; Arvidsson, P. I. Poly-N-methylated amyloid beta-peptide (A $\beta$ ) C-terminal fragments reduce A $\beta$  toxicity in vitro and in Drosophila melanogaster. *J Med Chem* **2009**, *52*, 8002-9.
346. Scherzer-Attali, R.; Pellarin, R.; Convertino, M.; Frydman-Marom, A.; Egoz-Matia, N.; Peled, S.; Levy-Sakin, M.; Shalev, D. E.; Caflish, A.; Gazit, E.; Segal, D. Complete phenotypic recovery of an Alzheimer's disease model by a quinone-tryptophan hybrid aggregation inhibitor. *PLoS One* **2010**, *5*, e11101.
347. Caesar, I.; Jonson, M.; Nilsson, K. P.; Thor, S.; Hammarstrom, P. Curcumin promotes A-beta fibrillation and reduces neurotoxicity in transgenic Drosophila. *PLoS One* **2012**, *7*, e31424.

348. McKoy, A. F.; Chen, J.; Schupbach, T.; Hecht, M. H. A novel inhibitor of amyloid beta (Abeta) peptide aggregation: from high throughput screening to efficacy in an animal model of Alzheimer disease. *J Biol Chem* **2012**, *287*, 38992-9000.
349. Frenkel-Pinter, M.; Tal, S.; Scherzer-Attali, R.; Abu-Hussien, M.; Alyagor, I.; Eisenbaum, T.; Gazit, E.; Segal, D. Cl-NQTrp Alleviates Tauopathy Symptoms in a Model Organism through the Inhibition of Tau Aggregation-Engendered Toxicity. *Neurodegener Dis* **2017**, *17*, 73-82.
350. Crowther, D. C.; Kinghorn, K. J.; Miranda, E.; Page, R.; Curry, J. A.; Duthie, F. A.; Gubb, D. C.; Lomas, D. A. Intraneuronal Abeta, non-amyloid aggregates and neurodegeneration in a Drosophila model of Alzheimer's disease. *Neuroscience* **2005**, *132*, 123-35.
351. Jonson, M.; Nystrom, S.; Sandberg, A.; Carlback, M.; Michno, W.; Hanrieder, J.; Starkenberg, A.; Nilsson, K. P. R.; Thor, S.; Hammarstrom, P. Aggregated Abeta1-42 Is Selectively Toxic for Neurons, Whereas Glial Cells Produce Mature Fibrils with Low Toxicity in Drosophila. *Cell Chem Biol* **2018**, *25*, 595-610.e5.
352. Wittmann, C. W.; Wszolek, M. F.; Shulman, J. M.; Salvaterra, P. M.; Lewis, J.; Hutton, M.; Feany, M. B. Tauopathy in Drosophila: neurodegeneration without neurofibrillary tangles. *Science* **2001**, *293*, 711-4.
353. Villar-Piqué, A.; Ventura, S. Modeling amyloids in bacteria. *Microbial Cell Factories* **2012**, *11*, 166.
354. Ami, D.; Natalello, A.; Lotti, M.; Doglia, S. M. Why and how protein aggregation has to be studied in vivo. *Microbial Cell Factories* **2013**, *12*, 17.
355. Pouplana, S.; Espargaro, A.; Galdeano, C.; Viayna, E.; Sola, I.; Ventura, S.; Munoz-Torrero, D.; Sabate, R. Thioflavin-S staining of bacterial inclusion bodies for the fast, simple, and inexpensive screening of amyloid aggregation inhibitors. *Curr Med Chem* **2014**, *21*, 1152-9.
356. Espargaró, A.; Medina, A.; Di Pietro, O.; Muñoz-Torrero, D.; Sabate, R. Ultra rapid in vivo screening for anti-Alzheimer anti-amyloid drugs. *Scientific Reports* **2016**, *6*, 23349.
357. Viayna, E.; Sola, I.; Bartolini, M.; De Simone, A.; Tapia-Rojas, C.; Serrano, F. G.; Sabaté, R.; Juárez-Jiménez, J.; Pérez, B.; Luque, F. J.; Andrisano, V.; Clos, M. V.; Inestrosa, N. C.; Muñoz-Torrero, D. Synthesis and Multitarget Biological Profiling of a Novel Family of Rhein Derivatives As Disease-Modifying Anti-Alzheimer Agents. *Journal of Medicinal Chemistry* **2014**, *57*, 2549-2567.
358. Di Pietro, O.; Pérez-Areales, F. J.; Juárez-Jiménez, J.; Espargaró, A.; Clos, M. V.; Pérez, B.; Lavilla, R.; Sabaté, R.; Luque, F. J.; Muñoz-Torrero, D. Tetrahydrobenzo[h][1,6]naphthyridine-6-chlorotacrine hybrids as a new family of anti-Alzheimer agents targeting  $\beta$ -amyloid, tau, and cholinesterase pathologies. *European Journal of Medicinal Chemistry* **2014**, *84*, 107-117.
359. Perez-Areales, F. J.; Di Pietro, O.; Espargaro, A.; Vallverdu-Queralt, A.; Galdeano, C.; Ragusa, I. M.; Viayna, E.; Guillou, C.; Clos, M. V.; Perez, B.; Sabate, R.; Lamuela-Raventos, R. M.; Luque, F. J.; Munoz-Torrero, D. Shogaol-huprine hybrids: dual antioxidant and anticholinesterase agents with beta-amyloid and tau anti-aggregating properties. *Bioorg Med Chem* **2014**, *22*, 5298-307.
360. Sola, I.; Aso, E.; Frattini, D.; López-González, I.; Espargaró, A.; Sabaté, R.; Di Pietro, O.; Luque, F. J.; Clos, M. V.; Ferrer, I.; Muñoz-Torrero, D. Novel Levetiracetam Derivatives That Are Effective against the Alzheimer-like Phenotype in Mice: Synthesis,

- in Vitro, ex Vivo, and in Vivo Efficacy Studies. *Journal of Medicinal Chemistry* **2015**, 58, 6018-6032.
361. Wang, S. N.; Li, Q.; Jing, M. H.; Alba, E.; Yang, X. H.; Sabate, R.; Han, Y. F.; Pi, R. B.; Lan, W. J.; Yang, X. B.; Chen, J. K. Natural Xanthenes from *Garcinia mangostana* with Multifunctional Activities for the Therapy of Alzheimer's Disease. *Neurochem Res* **2016**, 41, 1806-17.
362. Perez-Areales, F. J.; Betari, N.; Viayna, A.; Pont, C.; Espargaro, A.; Bartolini, M.; De Simone, A.; Rinaldi Alvarenga, J. F.; Perez, B.; Sabate, R.; Lamuela-Raventos, R. M.; Andrisano, V.; Luque, F. J.; Munoz-Torrero, D. Design, synthesis and multitarget biological profiling of second-generation anti-Alzheimer rhein-huprine hybrids. *Future Med Chem* **2017**, 9, 965-981.
363. Gandini, A.; Bolognesi, M. L. Therapeutic Approaches to Prion Diseases. *Prog Mol Biol Transl Sci* **2017**, 150, 433-453.
364. Nicoll, A. J.; Collinge, J. Preventing prion pathogenicity by targeting the cellular prion protein. *Infect Disord Drug Targets* **2009**, 9, 48-57.
365. Thompson, A. G.; Lowe, J.; Fox, Z.; Lukic, A.; Porter, M. C.; Ford, L.; Gorham, M.; Gopalakrishnan, G. S.; Rudge, P.; Walker, A. S.; Collinge, J.; Mead, S. The Medical Research Council prion disease rating scale: a new outcome measure for prion disease therapeutic trials developed and validated using systematic observational studies. *Brain* **2013**, 136, 1116-27.
366. Sanders, W. L.; Dunn, T. L. Creutzfeldt-Jakob disease treated with amantidine. A report of two cases. *J Neurol Neurosurg Psychiatry* **1973**, 36, 581-4.
367. Sanders, W. L. Short report: Creutzfeldt-Jakob disease treated with amantidine. *Journal of Neurology, Neurosurgery, and Psychiatry* **1979**, 42, 960-961.
368. Kovanen, J.; Haltia, M.; Cantell, K. Failure of interferon to modify Creutzfeldt-Jakob disease. *Br Med J* **1980**, 280, 902.
369. Furlow, T. W., Jr.; Whitley, R. J.; Wilmes, F. J. Repeated suppression of Creutzfeldt-Jakob disease with vidarabine. *Lancet* **1982**, 2, 564-5.
370. David, A.; Grant, R.; Ballantyne, J. UNSUCCESSFUL TREATMENT OF CREUTZFELDT-JAKOB DISEASE WITH ACYCLOVIR. *The Lancet* **1984**, 323, 512-513.
371. Newman, P. K. Acyclovir in Creutzfeldt-Jakob disease. *Lancet* **1984**, 1, 793.
372. Masullo, C.; Macchi, G.; Xi, Y. G.; Pocchiari, M. Failure to ameliorate Creutzfeldt-Jakob disease with amphotericin B therapy. *J Infect Dis* **1992**, 165, 784-5.
373. Dervaux, A.; Vicart, S.; Lopes, F.; Le Borgne, M. H. [Psychiatric manifestations of a new variant of Creutzfeldt-Jakob disease. Apropos of a case]. *Encephale* **2001**, 27, 194-7.
374. Korth, C.; May, B. C.; Cohen, F. E.; Prusiner, S. B. Acridine and phenothiazine derivatives as pharmacotherapeutics for prion disease. *Proc Natl Acad Sci U S A* **2001**, 98, 9836-41.
375. Furukawa, H.; Takahashi, M.; Nakajima, M.; Yamada, T. [Prospects of the therapeutic approaches to Creutzfeldt-Jakob disease: a clinical trial of antimalarial, quinacrine]. *Nihon Rinsho* **2002**, 60, 1649-57.
376. Collinge, J.; Gorham, M.; Hudson, F.; Kennedy, A.; Keogh, G.; Pal, S.; Rossor, M.; Rudge, P.; Siddique, D.; Spyer, M.; Thomas, D.; Walker, S.; Webb, T.; Wroe, S.; Darbyshire, J. Safety and efficacy of quinacrine in human prion disease (PRION-1 study): a patient-preference trial. *Lancet Neurology* **2009**, 8, 334-344.
377. Geschwind, M. D.; Kuo, A. L.; Wong, K. S.; Haman, A.; Devereux, G.; Raudabaugh, B. J.; Johnson, D. Y.; Torres-Chae, C. C.; Finley, R.; Garcia, P.; Thai, J. N.;

- Cheng, H. Q.; Neuhaus, J. M.; Forner, S. A.; Duncan, J. L.; Possin, K. L.; Dearmond, S. J.; Prusiner, S. B.; Miller, B. L. Quinacrine treatment trial for sporadic Creutzfeldt-Jakob disease. *Neurology* **2013**, *81*, 2015-23.
378. Ghaemmaghami, S.; Ahn, M.; Lessard, P.; Giles, K.; Legname, G.; DeArmond, S. J.; Prusiner, S. B. Continuous Quinacrine Treatment Results in the Formation of Drug-Resistant Prions. *PLOS Pathogens* **2009**, *5*, e1000673.
379. Benito-Leon, J. Combined quinacrine and chlorpromazine therapy in fatal familial insomnia. *Clin Neuropharmacol* **2004**, *27*, 201-3.
380. Martínez-Lage, J. F.; Rábano, A.; Bermejo, J.; Martínez Pérez, M.; Guerrero, M. C.; Contreras, M. A.; Lunar, A. Creutzfeldt-Jakob disease acquired via a dural graft: failure of therapy with quinacrine and chlorpromazine. *World Neurosurgery* **2005**, *64*, 542-545.
381. Floel, A.; Reilmann, R.; Frese, A.; Ludemann, P. Anticonvulsants for Creutzfeldt-Jakob disease? *Lancet* **2003**, *361*, 224.
382. Arruda, W. O.; Bordignon, K. C.; Milano, J. B.; Ramina, R. [Creutzfeldt-Jakob disease, Heidenhain variant: case report with MRI (DWI) findings]. *Arq Neuropsiquiatr* **2004**, *62*, 347-52.
383. Perovic, S.; Schroder, H. C.; Pergande, G.; Ushijima, H.; Muller, W. E. Effect of flupirtine on Bcl-2 and glutathione level in neuronal cells treated in vitro with the prion protein fragment (PrP106-126). *Exp Neurol* **1997**, *147*, 518-24.
384. Otto, M.; Cepek, L.; Ratzka, P.; Doehlinger, S.; Boekhoff, I.; Wiltfang, J.; Irle, E.; Pergande, G.; Eilers-Lenz, B.; Windl, O.; Kretschmar, H. A.; Poser, S.; Prange, H. Efficacy of flupirtine on cognitive function in patients with CJD: A double-blind study. *Neurology* **2004**, *62*, 714-8.
385. Ehlers, B.; Diringer, H. Dextran sulphate 500 delays and prevents mouse scrapie by impairment of agent replication in spleen. *J Gen Virol* **1984**, *65* ( Pt 8), 1325-30.
386. Doh-ura, K.; Ishikawa, K.; Murakami-Kubo, I.; Sasaki, K.; Mohri, S.; Race, R.; Iwaki, T. Treatment of transmissible spongiform encephalopathy by intraventricular drug infusion in animal models. *J Virol* **2004**, *78*, 4999-5006.
387. Appleby, B. S.; Lyketsos, C. G. Rapidly progressive dementias and the treatment of human prion diseases. *Expert Opin Pharmacother* **2011**, *12*, 1-12.
388. Todd, N. V.; Morrow, J.; Doh-ura, K.; Dealler, S.; O'Hare, S.; Farling, P.; Duddy, M.; Rainov, N. G. Cerebroventricular infusion of pentosan polysulphate in human variant Creutzfeldt-Jakob disease. *J Infect* **2005**, *50*, 394-6.
389. Whittle, I. R.; Knight, R. S.; Will, R. G. Unsuccessful intraventricular pentosan polysulphate treatment of variant Creutzfeldt-Jakob disease. *Acta Neurochir (Wien)* **2006**, *148*, 677-9; discussion 679.
390. Parry, A.; Baker, I.; Stacey, R.; Wimalaratna, S. Long term survival in a patient with variant Creutzfeldt-Jakob disease treated with intraventricular pentosan polysulphate. *J Neurol Neurosurg Psychiatry* **2007**, *78*, 733-4.
391. Rainov, N. G.; Tsuboi, Y.; Krolak-Salmon, P.; Vighetto, A.; Doh-Ura, K. Experimental treatments for human transmissible spongiform encephalopathies: is there a role for pentosan polysulfate? *Expert Opin Biol Ther* **2007**, *7*, 713-26.
392. Bone, I.; Belton, L.; Walker, A. S.; Darbyshire, J. Intraventricular pentosan polysulphate in human prion diseases: an observational study in the UK. *Eur J Neurol* **2008**, *15*, 458-64.

393. Tsuboi, Y.; Doh-Ura, K.; Yamada, T. Continuous intraventricular infusion of pentosan polysulfate: clinical trial against prion diseases. *Neuropathology* **2009**, *29*, 632-6.
394. De Luigi, A.; Colombo, L.; Diomede, L.; Capobianco, R.; Mangieri, M.; Miccolo, C.; Limido, L.; Forloni, G.; Tagliavini, F.; Salmona, M. The Efficacy of Tetracyclines in Peripheral and Intracerebral Prion Infection. *PLOS ONE* **2008**, *3*, e1888.
395. Zerr, I. Therapeutic trials in human transmissible spongiform encephalopathies: recent advances and problems to address. *Infect Disord Drug Targets* **2009**, *9*, 92-9.
396. Haik, S.; Marcon, G.; Mallet, A.; Tettamanti, M.; Welaratne, A.; Giaccone, G.; Azimi, S.; Pietrini, V.; Fabreguettes, J. R.; Imperiale, D.; Cesaro, P.; Buffa, C.; Aucan, C.; Lucca, U.; Peckeu, L.; Suardi, S.; Tranchant, C.; Zerr, I.; Houillier, C.; Redaelli, V.; Vespignani, H.; Campanella, A.; Sellal, F.; Krasnianski, A.; Seilhean, D.; Heinemann, U.; Sedel, F.; Canovi, M.; Gobbi, M.; Di Fede, G.; Laplanche, J. L.; Pocchiari, M.; Salmona, M.; Forloni, G.; Brandel, J. P.; Tagliavini, F. Doxycycline in Creutzfeldt-Jakob disease: a phase 2, randomised, double-blind, placebo-controlled trial. *Lancet Neurol* **2014**, *13*, 150-8.
397. Forloni, G.; Tettamanti, M.; Lucca, U.; Albanese, Y.; Quaglio, E.; Chiesa, R.; Erbetta, A.; Villani, F.; Redaelli, V.; Tagliavini, F.; Artuso, V.; Roiter, I. Preventive study in subjects at risk of fatal familial insomnia: Innovative approach to rare diseases. *Prion* **2015**, *9*, 75-9.
398. Clinical trials. <https://www.clinicaltrialsregister.eu/ctr-search/trial/2010-022233-28/IT>
399. Ghaemmaghami, S.; Russo, M.; Renslo, A. R. Successes and challenges in phenotype-based lead discovery for prion diseases. *J Med Chem* **2014**, *57*, 6919-29.
400. Kawasaki, Y.; Kawagoe, K.; Chen, C.-j.; Teruya, K.; Sakasegawa, Y.; Doh-ura, K. Orally Administered Amyloidophilic Compound Is Effective in Prolonging the Incubation Periods of Animals Cerebrally Infected with Prion Diseases in a Prion Strain-Dependent Manner. *Journal of Virology* **2007**, *81*, 12889-12898.
401. Wagner, J.; Ryazanov, S.; Leonov, A.; Levin, J.; Shi, S.; Schmidt, F.; Prix, C.; Pan-Montojo, F.; Bertsch, U.; Mitteregger-Kretzschmar, G.; Geissen, M.; Eiden, M.; Leidel, F.; Hirschberger, T.; Deeg, A. A.; Krauth, J. J.; Zinth, W.; Tavan, P.; Pilger, J.; Zweckstetter, M.; Frank, T.; Bähr, M.; Weishaupt, J. H.; Uhr, M.; Urlaub, H.; Teichmann, U.; Samwer, M.; Bötzel, K.; Groschup, M.; Kretzschmar, H.; Griesinger, C.; Giese, A. Anle138b: a novel oligomer modulator for disease-modifying therapy of neurodegenerative diseases such as prion and Parkinson's disease. *Acta Neuropathologica* **2013**, *125*, 795-813.
402. Berry, D. B.; Lu, D.; Geva, M.; Watts, J. C.; Bhardwaj, S.; Oehler, A.; Renslo, A. R.; DeArmond, S. J.; Prusiner, S. B.; Giles, K. Drug resistance confounding prion therapeutics. *Proceedings of the National Academy of Sciences* **2013**, *110*, E4160-E4169.
403. Herrmann, U. S.; Schütz, A. K.; Shirani, H.; Huang, D.; Saban, D.; Nuvolone, M.; Li, B.; Ballmer, B.; Åslund, A. K. O.; Mason, J. J.; Rushing, E.; Budka, H.; Nyström, S.; Hammarström, P.; Böckmann, A.; Cafilisch, A.; Meier, B. H.; Nilsson, K. P. R.; Hornemann, S.; Aguzzi, A. Structure-based drug design identifies polythiophenes as antiprion compounds. *Science Translational Medicine* **2015**, *7*, 299ra123-299ra123.

404. Ishibashi, D.; Nakagaki, T.; Ishikawa, T.; Atarashi, R.; Watanabe, K.; Cruz, F. A.; Hamada, T.; Nishida, N. Structure-Based Drug Discovery for Prion Disease Using a Novel Binding Simulation. *EBioMedicine* **2016**, *9*, 238-249.
405. Giles, K.; Berry, D. B.; Condello, C.; Dugger, B. N.; Li, Z.; Oehler, A.; Bhardwaj, S.; Elepano, M.; Guan, S.; Silber, B. M.; Olson, S. H.; Prusiner, S. B. Optimization of Aryl Amides that Extend Survival in Prion-Infected Mice. *Journal of Pharmacology and Experimental Therapeutics* **2016**, *358*, 537-547.
406. Silber, B. M.; Gever, J. R.; Li, Z.; Gallardo-Godoy, A.; Renslo, A. R.; Widjaja, K.; Irwin, J. J.; Rao, S.; Jacobson, M. P.; Ghaemmaghami, S.; Prusiner, S. B. Antiprion compounds that reduce PrP(Sc) levels in dividing and stationary-phase cells. *Bioorg Med Chem* **2013**, *21*, 7999-8012.
407. Krejciova, Z.; Alibhai, J.; Zhao, C.; Krencik, R.; Rzechorzek, N. M.; Ullian, E. M.; Manson, J.; Ironside, J. W.; Head, M. W.; Chandran, S. Human stem cell-derived astrocytes replicate human prions in a <em>PRNP</em> genotype-dependent manner. *The Journal of Experimental Medicine* **2017**.
408. Ghose, A. K.; Herbertz, T.; Hudkins, R. L.; Dorsey, B. D.; Mallamo, J. P. Knowledge-Based, Central Nervous System (CNS) Lead Selection and Lead Optimization for CNS Drug Discovery. *ACS Chemical Neuroscience* **2012**, *3*, 50-68.
409. Gemma, S.; Kukreja, G.; Tripaldi, P.; Altarelli, M.; Bernetti, M.; Franceschini, S.; Savini, L.; Campiani, G.; Fattorusso, C.; Butini, S. Microwave-assisted synthesis of 4-quinolyhydrazines followed by nickel boride reduction: a convenient approach to 4-aminoquinolines and derivatives. *Tetrahedron Letters* **2008**, *49*, 2074-2077.
410. Zhu, S.-J.; Ying, H.-Z.; Wu, Y.; Qiu, N.; Liu, T.; Yang, B.; Dong, X.-W.; Hu, Y.-Z. Design, synthesis and biological evaluation of novel podophyllotoxin derivatives bearing 4 $\beta$ -disulfide/trisulfide bond as cytotoxic agents. *RSC Advances* **2015**, *5*, 103172-103183.
411. EMMERSON, C. J. HETEROCYCLE SUBSTITUTED AMINO-PYRIDINE COMPOUNDS AND METHODS OF USE THEREOF 2017.
412. Maccari, R.; Ottana, R.; Curinga, C.; Vigorita, M. G.; Rakowitz, D.; Steindl, T.; Langer, T. Structure-activity relationships and molecular modelling of 5-arylidene-2,4-thiazolidinediones active as aldose reductase inhibitors. *Bioorg Med Chem* **2005**, *13*, 2809-23.
413. Aldrich, C.; Bertozzi, C.; Georg, G. I.; Kiessling, L.; Lindsley, C.; Liotta, D.; Merz, K. M., Jr.; Schepartz, A.; Wang, S. The Ecstasy and Agony of Assay Interference Compounds. *J Med Chem* **2017**, *60*, 2165-2168.
414. Avonto, C.; Tagliatela-Scafati, O.; Pollastro, F.; Minassi, A.; Di Marzo, V.; De Petrocellis, L.; Appendino, G. An NMR spectroscopic method to identify and classify thiol-trapping agents: revival of Michael acceptors for drug discovery? *Angew Chem Int Ed Engl* **2011**, *50*, 467-71.
415. Torres, J. L.; Lozano, C.; Julia, L.; Sanchez-Baeza, F. J.; Anglada, J. M.; Centelles, J. J.; Cascante, M. Cysteinyl-flavan-3-ol conjugates from grape procyanidins. Antioxidant and antiproliferative properties. *Bioorg Med Chem* **2002**, *10*, 2497-509.
416. Arsovska, E.; Trontelj, J.; Zidar, N.; Tomasic, T.; Masic, L. P.; Kikelj, D.; Plavec, J.; Zega, A. Evaluation of Michael-type acceptor reactivity of 5-benzylidenebarbiturates, 5-benzylidenerhodanines, and related heterocycles using NMR. *Acta Chim Slov* **2014**, *61*, 637-44.



417. Bertrand, J. A.; Thieffine, S.; Vulpetti, A.; Cristiani, C.; Valsasina, B.; Knapp, S.; Kalisz, H. M.; Flocco, M. Structural characterization of the GSK-3beta active site using selective and non-selective ATP-mimetic inhibitors. *J Mol Biol* **2003**, 333, 393-407.
418. Di, L.; Kerns, E. H.; Fan, K.; McConnell, O. J.; Carter, G. T. High throughput artificial membrane permeability assay for blood-brain barrier. *Eur J Med Chem* **2003**, 38, 223-32.
419. Polazzi, E.; Mengoni, I.; Caprini, M.; Pena-Altamira, E.; Kurtys, E.; Monti, B. Copper-zinc superoxide dismutase (SOD1) is released by microglial cells and confers neuroprotection against 6-OHDA neurotoxicity. *Neurosignals* **2013**, 21, 112-28.
420. Peña-Altamira, E.; Polazzi, E.; Moretto, E.; Lauriola, M.; Monti, B. The transcription factor CCAAT enhancer-binding protein  $\beta$  protects rat cerebellar granule neurons from apoptosis through its transcription-activating isoforms. *European Journal of Neuroscience* **2014**, 39, 176-185.